

**Fabrication of a Superconducting Hot-Electron Bolometer Receiver
with Micromachined Waveguide Components**

A Dissertation

Presented to

the Faculty of the School of Engineering and Applied Science

University of Virginia

In Partial Fulfillment

of the Requirements for the Degree of

Doctor of Philosophy in Electrical and Computer Engineering

by

Aaron Michael Datesman

August 2005

Approval Sheet

This thesis is submitted in partial fulfillment of the requirements for the degree of
Doctor of Philosophy in Electrical and Computer Engineering by:

Aaron Michael Datesman

This thesis has been read and approved by the examining committee:

N. Scott Barker, Chairman

Arthur W. Lichtenberger, Dissertation Advisor

Thomas W. Crowe

Bascom S. Deaver

Robert M. Weikle

Accepted for the School of Engineering and Applied Science:

Dean, School of Engineering
and Applied Science

August 2005

ABSTRACT

This dissertation discusses the construction of a 1x5 heterodyne receiver array intended for operation at 1450 GHz. The receiver incorporates niobium superconducting hot-electron bolometer mixers and inexpensive waveguide components micromachined from silicon, and is intended to fly on a NASA mission called SOFIA (the Stratospheric Observatory for Infrared Astronomy). The mixers are fabricated on thin membranes of silicon nitride, which allows the array of devices to exist on a single silicon chip.

The hot-electron bolometer mixers examined during the course of this research are 100 Å thick microbridges of niobium in intimate contact with thick, normally conducting gold pads at each end. The lateral dimensions of the microbridges are quite small (about 0.22 μm long by 0.10 μm wide, or less). These devices were fabricated individually using focused-ion beam pattern definition, and finished by inert argon ion etching of gold. This dissertation examines materials issues relating to the fabrication process, discusses the applicability of the focused-ion beam instrument to the patterning of small structures, and presents the measured characteristics of finished and passivated devices.

The yield of this fabrication process is quite high (perhaps more than 90%), and the HEB devices which result seem to be quite robust and stable. FIB-manufactured HEB devices possess I-V characteristics which are similar to those published in the literature for devices fabricated by other means (typically EBL), with the exception that they do not exhibit negative differential resistance or hysteresis (down to 4.2 Kelvins). The devices absorb 10 GHz radiation appropriately, and demonstration of their operation as terahertz hot-spot mixers is expected.

ACKNOWLEDGMENTS

TABLE OF CONTENTS

LIST OF FIGURES	3
LIST OF TABLES	6
LIST OF SYMBOLS AND ABBREVIATIONS	7
1. INTRODUCTION	10
2. THEORY	
1. Introduction.....	13
2. Heterodyne Receivers.....	13
3. Application to Astronomical Research.....	17
4. Mixing Elements for Submillimeter Wave Receivers.....	20
5. Electron Gas Bolometers.....	23
6. Superconducting Diffusion-Cooled HEB Device Operation.....	32
3. DESIGN OF THE RECEIVER ARRAY	
1. Overview.....	37
2. Feedhorn Block.....	38
3. Design and Operation of the Semicircular Waveguide Probe.....	43
4. Effects of Probe Misalignment.....	47
5. IF Circuit Design.....	49
6. Cross-Talk Between Array Elements.....	50
7. Photonic Crystal Junctions and the Shape of the Backshort Block Pedestals.....	52
8. Conclusion.....	54
4. DESIGN AND FABRICATION OF THE BACKSHORT BLOCK	
1. Overview.....	56
2. Design of the Backshort Block Masks.....	56
3. Anisotropic Wet Etching of Silicon & Corner Compensation.....	65
4. Fabrication of the Backshort Block.....	70
5. Results.....	72
6. Conclusion.....	73
5. DESIGN AND FABRICATION OF THE HEB BLOCK	
1. Overview.....	75
2. Design of the HEB Block Masks.....	75
3. Etching Silicon to Release the Si ₃ N ₄ Membranes.....	79
4. Fabrication of the HEB Block.....	83
5. Conclusion.....	90
6. HOT-ELECTRON BOLOMETER FABRICATION	
1. Introduction.....	91
2. FIB1-3 Process.....	92

3. Film Stress.	102
4. Gallium Implantation	109
5. Further Materials Issues.	117
7. FABRICATION RESULTS	
1. Overview.	125
2. BtA/BtB Process.	126
3. 300 Volt Argon Bridge Etch - Samples on Si/Si ₃ N ₄ Substrates.	130
4. 150 Volt Argon Bridge Etch - Samples on Quartz Substrates.	144
5. 150 Volt Argon Bridge Etch - Samples on Si/Si ₃ N ₄ Substrates.	152
6. Resistance Ratio.	155
7. Results & Analysis.	160
8. Conclusion.	170
8. ANOMALOUS RESULTS WITH 10 nm NIOBIUM FILMS	
1. Introduction.	173
2. Description of the Experimental Technique.	173
3. Theoretical Analysis Using SRIM.	175
4. Experimental Results.	177
5. Conclusion.	184
9. CONCLUSIONS.	185
A. RECEIVER NOISE TEMPERATURE CHARACTERIZATION.	190
B. PROCESS SHEETS.	193
C. SUGGESTIONS FOR FABRICATION PROCESS ENHANCEMENT.	204
D. PRELIMINARY RESULTS REGARDING THE ANOMALOUS.	209
BEHAVIOR OF THIN Nb/Au FILMS	
BIBLIOGRAPHY.	214

LIST OF FIGURES

- 2.1 Heterodyne receiver schematic diagram
- 2.2 Rotational energy levels of molecules commonly found in the ISM
- 2.3 CO J=4-3 map of the interstellar object NCG-6334
- 2.4 Noise temperatures of receivers utilizing different types of mixing elements
- 2.5 Wavelength coverage of first-light SOFIA instruments
- 2.6 Bolometer schematic diagram
- 2.7 PHEB and DHEB schematic diagrams
- 2.8 Calculated DHEB microbridge temperature distribution
- 2.9 Hot-spot mixing
- 3.1 850 GHz 1x4 DHEB receiver array diagram
- 3.2 1450 GHz feedhorn half fabricated by LMM
- 3.3 Power coupling efficiency from 50 Ω HEB to feedhorn block
- 3.4 Detail of one 1450 GHz pixel in the assembled receiver
- 3.5 Input return loss of the 1450 GHz probe design
- 3.6 Detail of one HEB block 1450 GHz pixel
- 3.7 Design of the IF waveguide probe tap and probe throat
- 3.8 Electromagnetic simulation of the waveguide probe performance
- 3.9 Return loss of the membrane-based semicircular waveguide probe
- 3.10 Simulated effect of probe misalignment
- 3.11 IF circuit detail
- 3.12 Simulation of cross-talk between array pixels
- 3.13 Backshort pedestal
- 3.14 Coupling efficiency simulations for different backshort pedestal designs
- 3.15 Backshort and HEB blocks installed in receiver mount
- 4.1 Assembly of backshort and HEB blocks
- 4.2 Illustration of backshort block-HEB block alignment schemes
- 4.3 Ruby bearing in an etched pit
- 4.4 Hole positions for sapphire rods
- 4.5 Undercut backshort block pyramidal stub
- 4.6 Compensation scheme

- 4.7 Finished pyramidal stub
- 5.1 Close-up view of the mixer circuitry
- 5.2 Radial probe, kernel, and output line tap of a 1450 GHz pixel
- 5.3 Probe transition sculpted by focused-ion beam
- 5.4 Frontside wafer protection jig
- 5.5 Meniscus etching jig
- 5.6 850 GHz mixer looking through the membrane
- 6.1 Schematic diagram of a superconducting diffusion-cooled HEB
- 6.2 FEI Inc. Series 200 FIB
- 6.3 The FIB1, FIB2, and FIB3 steps
- 6.4 Alignment of the FIB3 pattern to the kernel
- 6.5 FIB image of a microbridge kernel
- 6.6 Summary of stress results on Si/Si₃N₄ substrates
- 6.7 SRIM simulation of the implantation of 30 keV gallium ions into gold
- 6.8 Microbridge scale diagram detailing gallium contamination
- 6.9 Critical temperature vs. gallium dose
- 6.10 FIB-milled patterns demonstrating the poor material characteristics of gold films
- 6.11 HEB microbridges demonstrating the non-uniformity of the bridge etch
- 6.12 SEM picture which shows that the microbridge is shorter than its desired length
- 6.13 HEB microbridges illustrating an incomplete bridge etch
- 6.14 Critical temperature vs. argon RIE etch time at 300 Volts
- 7.1 BtA and BtB FIB patterns
- 7.2 HEB microbridge fabricated using the BtA/BtB process
- 7.3 Formation of voids in an FIB-milled gold film
- 7.4 Results of the 300 Volt bridge etch tests
- 7.5 Time evolution of the resistance of wide and narrow microbridges
- 7.6 HEB devices fabricated with a 300 Volt bridge etch
- 7.7 HEB device on quartz fabricated with a 150 Volt bridge etch
- 7.8 Results of the 150 Volt bridge edge of the M2747B sets
- 7.9 HEB device on a silicon nitride membrane fabricated with a 150 Volt bridge etch
- 7.10 Resistive transition of a niobium sample implanted with gallium

- 7.11 Resistance ratio vs. HEB device resistance
- 7.12 Resistive transitions of devices “B” and “C”
- 7.13 I-V curves of devices “A” - “C”
- 7.14 I-V traces for device “C” at different temperatures
- 7.15 I-V traces for device “C” with different amounts of 10 GHz RF power applied
- 8.1 FIB screen shot during gallium implantation
- 8.2 Capture percentages of incident gallium flux
- 8.3 Distribution of implanted gallium
- 8.4 Results of the implantation experiments on masked samples
- 8.5 Results of the implantation experiments on unmasked samples
- 8.6 I-V curve of an implanted sample
- 8.7 Summary of the gallium implantation experimental results
- A.1 Schematics illustrating equivalent noise power and the Y-factor measurement
- D.1 Results of gallium implantation experiments on grounded samples
- D.2 Results of low-dose gallium implantation
- D.3 Example of anomalous behavior caused by etching with low-voltage argon ions

LIST OF TABLES

- 3.1 Probe tap dimensions for the 850 GHz and 1450 GHz receiver designs
- 4.1 Backshort block pyramidal stub dimensions
- 4.2 Outline of the backshort block fabrication process
- 5.1 Outline of the HEB block fabrication process
- 5.2 Illustration of a Nb-Ge reaction at 160° C
- 6.1 Summary of niobium stress runs
- 6.2 Ion implantation ranges and straggles for 30 keV gallium ions
- 6.3 Gold etch rates in the UVML Semi-RIE
- 7.1 Effect of argon bombardment upon the sheet resistance of thin niobium films
- 7.2 Results of the 150 Volt bridge etch for HEB devices on quartz substrates
- 7.3 Results of a resistance vs. microbridge width experiment
- 7.4 Results of the 150 Volt bridge etch for HEB devices on silicon nitride
- 8.1 Summary of the gallium implantation experiments on masked samples

LIST OF SYMBOLS AND ABBREVIATIONS

BtA-B	First and second steps of an alternative FIB HEB fabrication process
C	heat capacity
CAD	Computer-Assisted Drafting
CASIMIR	CAItech Submillimeter Interstellar Medium Investigations Receiver
CO	carbon monoxide
CPW	Co-Planar Waveguide
D	diffusion constant
DAC	Digital-Analog Converter
DHEB	Diffusion-cooled Hot-Electron Bolometer
EBL	Electron-Beam Lithography
ED	Etch Depth
EDP	ethylene diamine pyrochatechol, a silicon etchant
ESD	Electrostatic Discharge
FIB	Focused-Ion Beam
FIB1-3	First-third steps of the FIB HEB fabrication process
f_{RF}	same as the signal frequency f_{sig}
f_{sig}	signal frequency; identical to f_{RF}
f_{3dB}	-3 dB frequency IF bandwidth
G	thermal conductance
GREAT	German REceiver for Astronomy at Terahertz frequencies
HEB	Hot-Electron Bolometer
HFSS	High Frequency Structure Simulator
HIFI	Heterodyne Instrument for the Far-Infrared
IF	Intermediate Frequency
InSb	indium antimonide
IPA	isopropyl alcohol
IR	Infrared
K	thermal conductivity
KAO	Kuiper Airborne Observatory
KOH	potassium hydroxide, a silicon etchant

kx	1,000 times magnification
l	electronic mean free path
L	length, of a microbridge or of a compensation structure
L_{e-e}	characteristic electron-electron interaction length
L_{e-ph}	characteristic electron-phonon interaction length
L_H	hot spot length
LMM	Laser Micromachining
LO	Local Oscillator
LOR	Lift-Off Resist
LPCVD	Low-Pressure Chemical Vapor Deposition
NDR	Negative Differential Resistance
NMP	N-methyl-2-pyrrolidinone, a photoresist stripper
NRAO	National Radio Astronomy Observatory
PCJ	Photonic Crystal Junction
PECVD	Plasma-Enhanced Chemical Vapor Deposition
PHEB	Phonon-cooled Hot-Electron Bolometer
P_{in}	input power absorbed by the device
P_{LO}	power absorbed from the local oscillator signal
P_{RF}	power absorbed from the RF signal or signal of interest
R	Ion range; also, resistance
RIE	Reactive Ion Etch/Etcher/Etching
RF	Radio Frequency
RRR	Residual Resistance Ratio
SEM	Scanning Electron Microscope
SIS	Superconductor-Insulator-Superconductor
SOFIA	Stratospheric Observatory for Infrared Astronomy
T_{bath}	bath temperature
T_C	critical temperature of a superconductor
T_e	electron temperature
TELIS	TErahertz and submillimeter LIMb Sounder
TMAH	tetra-methyl ammonium hydroxide, a silicon etchant

T_p	phonon or lattice temperature
TTV	Total Thickness Variation
UVML	University of Virginia Microfabrication Laboratory
w	microbridge width
w_{pixels}	microbridge width, measured in its specification in FIB2 pixels
YBCO	Yttrium Barium Copper Oxide, a ceramic high- T_C superconductor
Δ	superconducting energy gap
ΔR	Ion straggle
ρ	resistivity
σ	conductivity; also, thin film stress
τ_{e-e}	characteristic electron-electron interaction time
τ_{eff}	effective thermal time constant
τ_{e-ph}	characteristic electron-phonon interaction time
τ_{esc}	characteristic thermal time constant for phonon escape to the substrate
τ_{th}	thermal time constant
ω_{3dB}	-3 dB angular frequency IF bandwidth

CHAPTER 1 - INTRODUCTION

This dissertation details the fabrication of a 1x5 heterodyne receiver array operating at 1450 GHz for application to research in the field of radio astronomy. The array utilizes hot-electron bolometer (HEB) mixers fabricated from very thin (100 Å) films of superconducting niobium, integrated with inexpensive waveguide components laser micromachined from silicon to build the receiver. The HEB devices, which are as small as 0.22 μm long by 0.07 μm wide, are fabricated by a three-step process using a gallium focused-ion beam (FIB), followed by selective etching of gold using a low-power argon plasma. As of this writing, focused-ion beam definition of such a small structure, or of a device fabricated from such a thin film of superconducting material, is unique to this research. How the FIB may be employed as a tool to pattern very small structures, and the consequences of its application, are important topics addressed in this work.

The array of mixers is arranged linearly on one chip, each supported by a 0.75 μm thick membrane of silicon nitride. This chip is referred to as the HEB block. The backshorts are cavities laser micromachined into pyramidal stubs which are themselves bulk micromachined using a wet etchant on another chip, referred to as the backshort block. The HEB block rests in the etched-out region of the backshort block, with the pyramidal stubs aligned beneath the membranes which support the HEB mixers. Details involving the design of the receiver array are contained in **Chapter 3**, while **Chapter 4** and **Chapter 5** discuss the design and fabrication of the backshort block and the HEB block, respectively. Although the first results with single-element HEB receivers were published in the literature about a decade ago, this work represents the first receiver array based upon superconducting HEBs which has ever been constructed.

The class of HEB devices described in this dissertation are known as diffusion-cooled hot-electron bolometers, or DHEBs. **Chapter 6** details the FIB1-3 process by which these devices were manufactured by the author, and examines several issues related to the fabrication process. These include attempts to control the niobium thin film stress, the effects of the implantation of gallium into the finished HEB device by the focused-ion beam, and the behavior of gold films and niobium thin films under bombardment with gallium and argon ions. **Chapter 7** surveys the results of the fabrication process after removal of the gold which covers the HEB microbridges, and presents cryogenic measurements of finished devices.

DHEBs are known to be quite fragile and very sensitive to destruction by electrostatic discharge (ESD), which presents significant fabrication challenges. Although a DHEB device is itself not a complicated structure - it is basically a thin, narrow, short strip of metal - very low yields are typical, and many good devices are lost during mounting and testing. One researcher reports that only about 5% of the devices fabricated in a run show the desired DC characteristics. [Ganzevles02] While it is possible to fabricate, assemble, and test a single-element receiver under this yield constraint, obviously the same cannot be said of the five-element receiver fabricated during the course of the research described in this dissertation. In fact, in order to have a 50% chance of success fabricating a five-element array, the single device yield must be 87%. The fabrication process described in **Chapter 6** and **Chapter 7** - including operator protocols intended to minimize the possibility of ESD damage - is promising in this regard.

Niobium is a refractory metal which oxidizes readily in atmosphere. Because DHEBs are fabricated from very thin films of niobium, and are very fragile, continued oxidation can degrade these devices, and eventually even cause them to open-circuit. During the course of this research, a very satisfactory passivation scheme utilizing films of sputtered germanium was developed and employed. Use of this material to passivate HEBs has not been described elsewhere.

Perhaps owing to external factors such as die size or choice of substrate, or perhaps due to the passivation material or to the fabrication process, FIB-manufactured DHEBs on Si/Si₃N₄ substrates are rather robust and stable. Along with the high yield which the process enjoys, this represents a very useful advance in the field. The niobium HEBs described in this dissertation were the first HEBs to be successfully fabricated from this material in the UVML.

Finally, **Chapter 8** discusses an interesting, but unexplained, effect relating to superconducting niobium thin films which was uncovered during the course of this research. It was found that implantation of gallium ions by FIB into a small portion of a test pad structure caused the transition temperature of implanted areas to decrease, which may be attributed to damage caused by implantation or to contamination of the niobium film. However, as a result of the implantation, the transition temperature of other sections of the sample, which were masked and had not been implanted, was simultaneously found to increase, which was wholly unexpected. This is termed the “anomalous increase of the contact pad transition temperature”, and is examined in **Chapter 8**.

CHAPTER 2 - THEORY

1. Introduction

This dissertation discusses the fabrication of a receiver array operating at 1.45 THz. The scientific application of this receiver involves the study of spectral lines in interstellar clouds of gas and dust, where stars are born and in which they are enveloped when they die. In order to accomplish these very sensitive measurements, the receiver is designed to operate in a heterodyne mode, and utilizes very fast, sensitive, state-of-the-art detectors known as superconducting hot-electron bolometer (HEB) mixers.

This chapter is intended to explain the interest of the radio astronomy community in this area of research (that is, to provide scientific motivation), to place the development of superconducting HEB mixers in their context historically and technologically, and to examine the operation of superconducting diffusion-cooled HEB mixers.

2. Heterodyne Receivers

The earliest radio transmitter built for this purpose by humankind was a tank circuit connected to a spark gap, from the 1887 experiments of Heinrich Hertz which verified the existence of self-propagating electromagnetic waves. (Hertz incidentally also uncovered the photoelectric effect at that time, laying the groundwork for quantum mechanics and for all which followed from it. This includes solid-state electronic devices and computers - virtually the whole of the modern practice of electrical engineering.) Maxwell had made his prediction in 1873.

Detoured only briefly by attempts to use the fresh brains of deceased human cadavers as radio receivers¹ [Collins02], what would be recognizable as a modern AM radio broadcast had occurred by 1906. Because a spark is a broadband emission, naturally this advance had required the development of more refined components: sine wave RF power transmitters (based upon the negative resistance of a glowing DC arc) and crystal detectors (of galena, caborundum, and silicon). Refinement from broad into narrow band transmission and reception continues into the present day.

One important advance, the “superheterodyne receiver”, was patented by Edwin Armstrong in 1917 (it used ten vacuum tubes). Armstrong was a member of the U.S. Army Signal Corps; his superhet receiver was intended to detect enemy planes by listening for electromagnetic transmissions from the spark plugs in their ignition systems [Lee98]. Heterodyne receivers are ubiquitous today, as an integral component of radios, televisions, and cell phones. A block diagram of a heterodyne receiver is shown in **Figure 2.1**. The central component of a heterodyne receiver is a non-linear circuit element called a mixer.

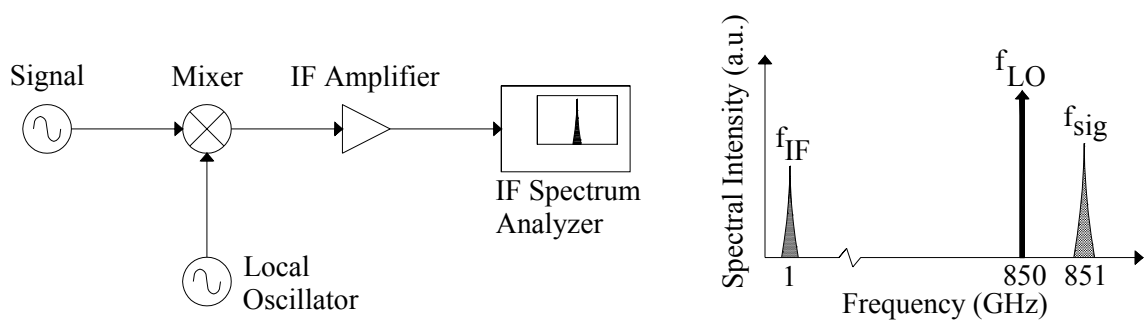


Figure 2.1. Block diagram of a heterodyne receiver (left) and a diagram setting forth its principle of operation (right). The signal of interest is combined with a monochromatic signal provided by the experimenter (the Local Oscillator, or LO) in a non-linear circuit element called a mixer. Among the harmonics which are produced is the intermediate frequency (IF), $f_{IF} = f_{sig} - f_{LO}$.

¹ True!

A heterodyne receiver is a means of extracting a replica at a low frequency of a signal of interest in a narrow bandwidth at a high frequency, as shown in **Figure 2.1**. The signal of interest (which might be a radio program, a radar signal, or even astronomical in origin) is combined in the mixer with a locally generated monochromatic source provided by the experimenter, called the local oscillator (LO). The LO frequency is chosen to nearly coincide with the signal frequency.

The output spectrum of a linear system does not contain any frequencies not found in the signal input to the system. By contrast, because the mixer includes a non-linear circuit element, such as a diode, the frequency spectrum of the mixer input is not preserved in its output, which includes harmonics of the signal and LO frequencies. One of these is the difference, or intermediate frequency (IF), $f_{IF} = f_{sig} - f_{LO}$. A distortion-free mixer also produces harmonics at $f_{IF} + nf_{LO}$ [**Saleh71**], although these undesired harmonics are easily filtered out. If the signal is properly conditioned and the bandwidth of the mixer is sufficient, the IF replica of the signal of interest contains the same phase and spectral information as the original signal, but within a frequency range where it may be easily amplified and analyzed, as shown in **Figure 2.1**. Further detailed information on the topic of mixer design and operation may be found in the monograph by Saleh [**Saleh71**], in the textbook by Pozar [**Pozar98**], and in the published papers of Held and Kerr [**Held78a,b**].

The astronomical application for which the receivers described in this dissertation are intended involves the heterodyne downconversion of signals in the frequency region near 1000 GHz down to a bandwidth of a few GHz. This requires the use of cutting-edge mixers, sources, amplifiers, and other equipment. Even so, the more accessible operation

of a conventional radio receiver, where the intermediate frequency is standardized at 455 kHz and the radio is tuned by changing the LO frequency of a resonant LC tank circuit, is precisely analogous.

The journey from spark gap transmitter to superheterodyne receiver represents a transition from incoherent to coherent detection. An incoherent, or direct, detector generates a DC signal proportional to the amount of radiation absorbed. In this case the particle description of electromagnetic radiation applies, and no phase information about the incoming photons is preserved. Because the response of an incoherent detector to every absorbed photon within the detector bandwidth is nearly identical, such a device cannot generally be used to obtain often desirable information such as spectra indicating atmospheric absorption and emission lines.

Coherent receivers, however, such as the heterodyne system just described, are sensitive not simply to the energy of absorbed photons, but rather to the incident electromagnetic field. Therefore a coherent receiver employs the wave description of electromagnetic radiation, and retains phase information about the incident signal. Because the superposed fields at every frequency are all orthogonal, a heterodyne receiver offers spectral discrimination within its operating bandwidth and is suited to spectrographic analysis. Furthermore, because the phase information is retained, a coherent receiver may be employed to perform interferometry among several different receivers spaced far apart.

The first radio astronomers were probably those looking unsuccessfully for radio emissions from the sun even prior to 1900 [Rohlf99], but the credit rightly goes to Karl Jansky in 1931. Working at 20 MHz - partially on the topic of interference caused by

lightning - he uncovered an extraterrestrial radio source, invisible in optical wavelengths, which lay in the constellation Sagittarius [**Jansky33**]. Astronomers had just recently determined that to be the location as well of the galactic core of the Milky Way galaxy. A scant twenty-five years after the first development of AM radio, more than fifteen years before the invention of the transistor, a vast new area of discovery had been opened up. Investigations continue.

3. Application to Astronomical Research

The galactic core happens to be invisible at optical wavelengths because it is obscured by vast quantities of small dust grains (about 1 μm in size) contained in the interstellar medium. Because these dust particles are much smaller than radio wavelengths, however, radio energy emanating from the galactic core is neither absorbed nor strongly scattered by the intervening dust cloud, and may be observed from earth. The fact that some astronomical objects may be observed only at radio wavelengths, and are not visible at all in other regions of the electromagnetic spectrum, continues to motivate much radio astronomy research.

Since radio observations may pierce clouds of dust and gas which are optically thick at shorter wavelengths, a great deal of cutting-edge research in radio astronomy naturally involves observations of these interstellar clouds, and of what lies within or behind them. Because many stars in the process of dying (planetary nebula) and all stars in the process of birth (stellar nurseries) are contained within clouds of gas and dust, this happens to be a very fruitful area of research. The astronomical receiver described in this dissertation, and fabricated by the author and his collaborators, could be applied to

scientific research involving the interstellar medium, protostellar collapse & disk processes, and circumstellar envelopes & planetary nebula. [SORAL]

Radio sources are broadly divided into thermal (blackbody) and non-thermal (synchrotron) types. Aside from these continuum emissions, however, it is often spectral lines corresponding to atomic, vibrational, and rotational transitions which are of interest. These signals are targets for coherent detection.

Atomic transitions (such as the Balmer, Lyman, and Paschen series for the hydrogen atom) generally occur in the infrared or shorter wavelengths, and so do not apply to this discussion. Molecular rotational transitions, however, possess lower energies and are richly represented in the submillimeter (above 300 GHz) and terahertz regimes. A list of the molecules found within circumstellar shells or within the interstellar medium as of 1998 [Rohlfs99] contains 122 separate molecules, some of which contain as many as 13 atoms. The list includes simple molecules such as H₂, CO, NO, H₂O, and NH₃, but also more complex species such as ethyl alcohol, CH₃CH₂OH, and formaldehyde, H₂CO.

The rotational spectrum of a rigid diatomic molecule may be easily obtained using two-body reduced coordinates and Schrödinger's Equation. The result for the rotational energy eigenvalues, assuming that the molecule is in the vibrational ground state, is

$$E_{rot} = \frac{\hbar^2}{2\Theta_e} J(J + 1), \quad (2.1)$$

where Θ_e is the moment of inertia of the molecule, and J is the quantum number of angular momentum, $J = 0, 1, 2, \dots$. The rotational energy levels of a few molecules commonly found in the interstellar medium are shown in **Figure 2.2**.

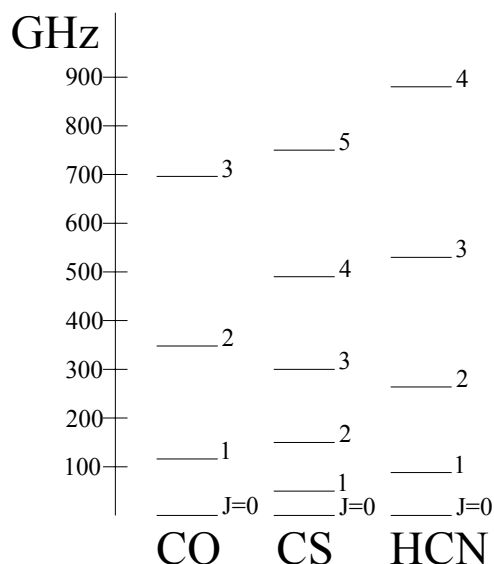


Figure 2.2. Rotational energy levels (in the vibrational ground state) of some linear molecules commonly found in the interstellar medium. The higher angular momentum transitions (such as CO J=3-2) lie within the submillimeter region. Only single-step transitions, that is, those from level J+1 to level J, occur.

The CO molecule is a common target of analysis in interstellar gas clouds, as it possesses strong transition lines and is present in relatively dense concentrations. The most prevalent species in interstellar clouds, H_2 , does not possess a dipole moment, and its rotational transitions cannot be detected. A map of the interstellar object NGC-6334 measured at the wavelength of the CO J=4-3 transition is shown in **Figure 2.3**. From spectroscopic analysis of interstellar gas clouds such information as the pressure, species concentration, chemical composition, density, temperature, and velocity distribution can be inferred. This data may subsequently be used to develop and refine models of star formation, and new phenomena revealed by these measurements may be modeled and investigated.

Finally, remote sensing of earth's atmosphere by satellite is another, very important, application of submillimeter and terahertz heterodyne spectroscopy. This has been a vital component of ongoing research involving the destruction of earth's ozone layer.

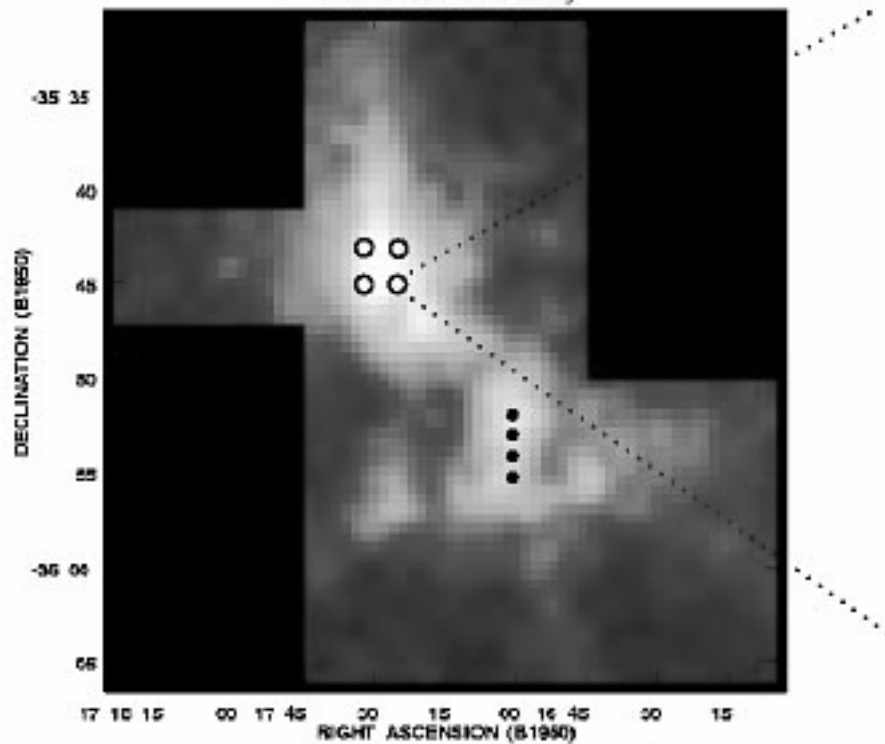


Figure 2.3. Map of the interstellar object NGC-6334, observed in the light of the ^{12}CO J=4-3 transition using the AST/RO telescope at the South Pole and the Arizona/CalTech 460/492 GHz receiver. The circles represent the spatial coverage of two HEB receiver arrays under consideration: an 810 GHz, 2x2 array (open), and a 1.5 THz, 1x4 array (closed). From [SORAL].

4. Mixing Elements for Submillimeter Wave Receivers

There are three types of devices in use today as mixers in submillimeter wave receivers: Schottky diodes, SIS (superconductor-insulator-superconductor) junctions, and superconducting hot-electron bolometers (HEBs). To a significant degree, these three choices represent complementary, and not competing, technologies. The two classes of superconductive devices require cryogenic cooling; when operation at helium temperature is either undesirable or impossible, Schottky diode mixers must be used. Choosing between the two types of superconducting devices, the operating frequency is

the principal criterion: SIS junctions work most efficiently below the gap frequency of the material from which they are fabricated, HEBs most efficiently above it.

The noise temperature (discussed in **Appendix A**) is the primary figure of merit for an astronomical receiver. A faint source may be resolved more easily by a receiver with a low noise temperature. In **Figure 2.4**, the noise temperatures of receivers based upon each of the three different types of mixing elements are compared. It is clear from the figure that HEBs compete with SIS devices on receiver noise temperature starting at about the gap frequency, and possess far lower noise temperatures than Schottky diode receivers above 1 THz.

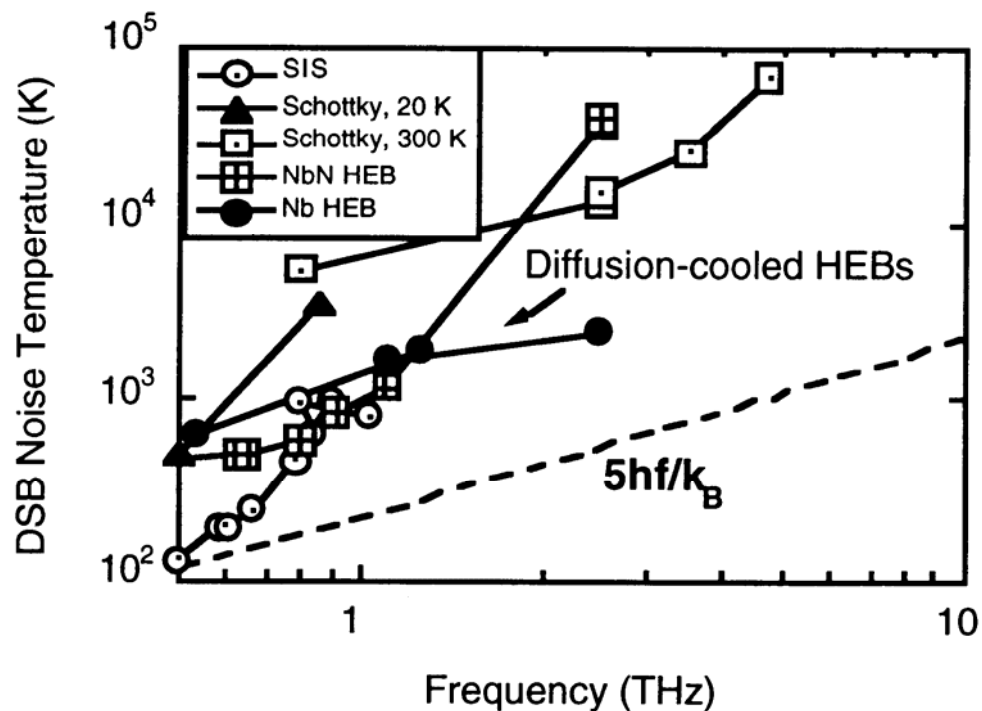


Figure 2.4. Comparison in the submillimeter wavelength region between the noise temperatures of receivers based upon Schottky diodes, SIS junctions, and NbN phonon- and Nb diffusion-cooled HEBs. SIS junction performance degrades strongly above the gap frequency of Nb (about 700 GHz), where HEBs begin to offer the best results. The graph is from 1998 [Karasik98a]. Currently phonon-cooled HEBs offer slightly better performance than diffusion-cooled devices [Baselmans03]. The dotted line indicates ten times the quantum noise limit.

Schottky diode and SIS junction mixers are well-established technologies, which is not true of HEB mixers, but in the last several years receivers employing phonon-cooled HEB devices (PHEBs) have been demonstrated on several ground-based telescopes [**Kawamura99, Gerecht04, Radford04**]. Diffusion-cooled HEBs (DHEBs) represent a second class of superconducting hot-electron bolometer devices. The devices discussed in this dissertation are diffusion-cooled HEBs. The differences between these two classes of HEBs are discussed in **Section 2.5**.

As of this writing, about ten labs in the United States and Europe are involved in superconducting HEB fabrication and testing, using both diffusion- and phonon-cooled devices [**Yngvesson03**]. Several receiver systems for airborne and space missions which will utilize HEBs are currently under development. These include HIFI band 6 (for the Herschel Space Telescope), GREAT (for SOFIA, the Stratospheric Observatory for Infrared Astronomy), and TELIS, all operating at frequencies above 1.4 THz.

SOFIA is a high-altitude observatory which operates from a specially fitted 747 aircraft. It succeeds the previous Kuiper Airborne Observatory (KAO). **Figure 2.5** illustrates the spectral coverage provided by the separate instrument packages intended to fly on SOFIA, including GREAT, which is planned to begin operation in 2005. The HEB receiver arrays described in this dissertation are also intended to fly on SOFIA.

The superconducting HEB mixer concept dates from 1990 [**Gershenson90**], and the diffusion-cooled superconducting HEB from 1993 [**Prober93**], but the basic idea developed around semiconducting electron-gas devices more than 20 years earlier. Development of semiconductor quantum-well devices which might compete with superconducting HEB mixers in fact continues [**Serapiglia04**].

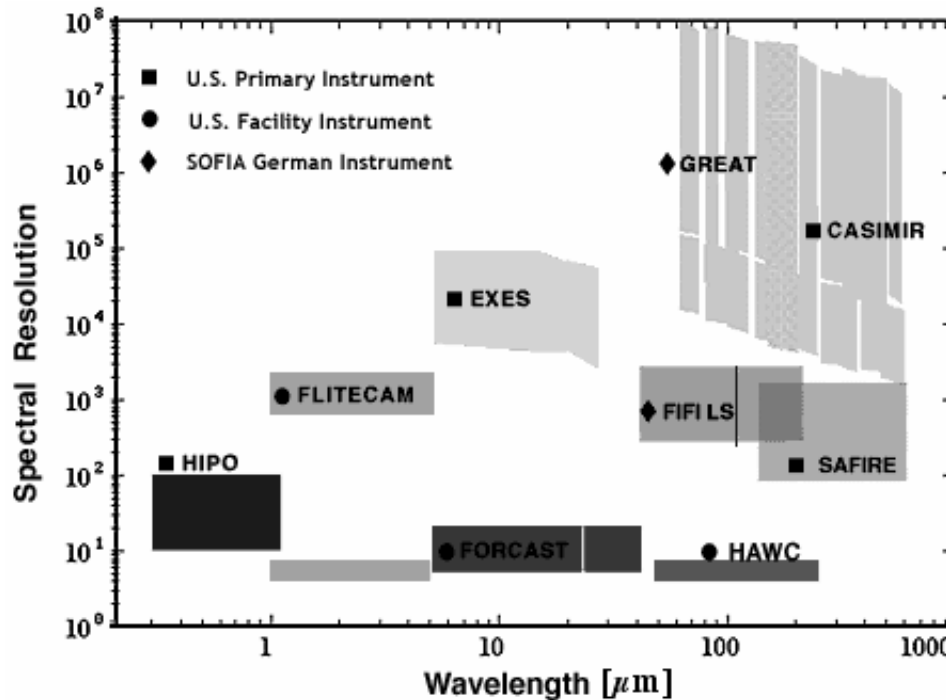


Figure 2.5. Spectral resolution vs. wavelength coverage of first-light SOFIA instruments [SOFIA]. The GREAT and CASIMIR receivers each include HEB devices. Cross-hatched areas represent goals for additional capabilities beyond the basic mission requirements. The submillimeter wavelength region between 1000 - 100 μm corresponds to frequencies from 300 GHz - 3 THz.

5. Electron Gas Bolometers

Radiation may be detected either through the heat it imparts to an absorbing object (thermal detection), or through the interaction between a single quantum of radiation and a single carrier in a bound state (photoelectric detection) [Smith65]. A bolometer belongs to the former class, and is pictured schematically in **Figure 2.6**. The use of bolometers as direct detectors of microwave and infrared radiation is longstanding and widespread [Richards94]. As incident power is absorbed by the device, the temperature of the absorbing element (which might be a thin metal film, a carbon resistor, or a semiconductor) increases. The magnitude of the incident power may be deduced

from this increase. Because the power available to be absorbed in the incident signal varies with the square of the incident field amplitude, bolometers are often referred to as square-law detectors.

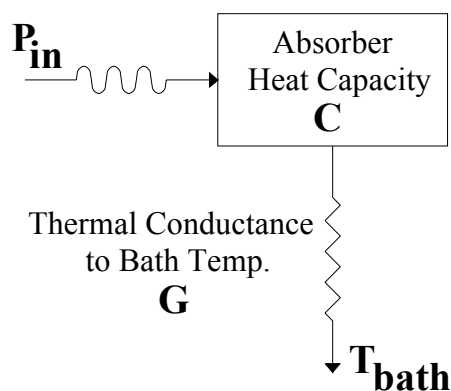


Figure 2.6. Schematic diagram of a bolometer, consisting of an absorber heat sunk to a thermal reservoir through a thermal conductance G . A separate, distinct thermometer is also a necessary component of the structure in many cases, but not when the absorber is a free electron gas, nor when the bolometer is intended to be used as a mixer.

By precise analogy to electrical circuit quantities, the thermal time constant of this system (ignoring electrothermal feedback [Burke97]) is

$$\tau_{th} = C/G \quad (2.2)$$

A fast bolometer detector may be obtained by minimizing the heat capacity of the absorbing element, either by reducing its physical volume, or by other means. Where the frequency (f) of the incident radiation nevertheless exceeds the speed of the detector ($f > 1/2\pi\tau_{th}$), the temperature of the absorber will not follow the rise and fall of the absorbed power, but instead begin to exhibit an elevated steady-state response.

As thermal, or total-power, detectors, bolometers are quite different from the whisker-contact crystal (i.e., Schottky) diodes which had by the 1960's already been in use as mixers for many years. Schottky diodes are photoelectric detectors which are useful as mixers due to their strongly non-linear I-V characteristics. (The same is true of SIS junctions.) Kinch and Rollin [Kinch63] nevertheless suggested using a square-law

bolometric detector made of high-purity n-type indium antimonide (InSb) as a mixer in 1963. Such a device was developed and installed in a receiver on the Kitt Peak telescope in 1973, and was used with great success [Phillips73]. Although the performance of InSb bolometer mixers no longer represents the state of the art, the details of their operation are analogous in many ways to the functioning of superconducting HEB mixers.

It is typical to consider the heat capacity of any material to include contributions from two sources, the phonon and electron gases [Kittel96]. The electrons and phonons interact and remain in thermal equilibrium with each other, so that the lattice (phonon) and electron temperatures are the same: $T_p = T_e$. In pure, high-mobility semiconductors at low (below 4.2 Kelvins) temperatures, however, the coupling between phonons and electrons can become quite weak [Putley65]. This situation, in which T_e may significantly exceed T_p , is known as a hot-electron distribution.

Because of the poor electron-phonon coupling, essentially only the electron gas interacts with, and is heated by, the power absorbed by the InSb device. Therefore, this device may be referred to as an electron-gas, or free-electron [Moore85], bolometer, in which the presence of the semiconductor lattice may be largely ignored. Since it is only the electron gas which acts as an absorber, it is solely the electronic heat capacity which should be used in Equation 2.2 to calculate the thermal time constant of the bolometer.

Since free carriers² act as the absorber in an electron-gas bolometer, only transitions within the conduction band are involved. Although these transitions do not change the number of carriers available, altering the distribution of carriers within the

² Typically highly compensated material is used, so that free carriers are present even at cryogenic temperatures.

band affects the conductivity by changing the average carrier mobility. The conductivity σ is found to depend upon the applied field according to the equation

$$\sigma = \sigma_0(1 + \beta E^2) \quad (2.3)$$

where σ_0 is the conductivity with no applied field (that is, for $T_p = T_e$), β is a non-linearity factor which increases with decreasing physical temperature, and E is the applied electric field (DC + RF). The increase in conductivity with applied field causes the InSb bolometer to exhibit a non-Ohmic I-V characteristic, and is actually a separate example of a hot-electron effect.

Arams et. al. [**Arams66**] were the first to demonstrate mixing in bulk InSb. In 1970, Whalen and Westgate [**Whalen70**] offered a comprehensive analysis of the performance of InSb mixers based upon a model in which the mixer resistance is a function only of the electron temperature, and the electron temperature is in turn determined by the total absorbed power. Phillips and Jefferts [**Phillips73**] used the same assumptions to develop a simplified, but largely accurate, description of mixing in an InSb electron-gas bolometer. The discussion following relies on their description.

If the voltage applied to the bolometer consists of DC, LO, and signal (RF) terms, then the power absorbed by the electron gas may be calculated according to $P=V^2/R$ and is approximately

$$P \approx I_0^2 R_0 + P_{LO} + 2\sqrt{P_{LO} P_{RF}} e^{j\omega_{IF} t} . \quad (2.4)$$

In this equation, I_0 is the DC bias current, R_0 is the bolometer resistance at the lattice temperature, $P_{LO}=V_{LO}^2/R_0$ is the absorbed power from the local oscillator, P_{RF} is defined similarly for the signal of interest, j is the imaginary unit, and $\omega_{IF} = \omega_{RF} - \omega_{LO}$ is the angular difference frequency. This result is obtained by noting that, although the voltage

impressed across the device follows the high frequency RF and LO signals, the temperature of the electron gas cannot - i.e., $\tau_{th} \gg 1/2\pi f_{RF}$ - and that the average value over one cycle $\langle e^{j\omega t} \rangle = 0$. Therefore the bolometer provides a steady-state DC response to LO heating. The power in the RF signal is small by comparison and is neglected.

According to the third term on the RHS of Equation 2.4, this square law detector mixes the LO and signal frequencies, modulating the temperature of the electron gas at the difference frequency. This will only be found to occur, however, if the device is fast enough to respond to the IF modulation; that is, if $\tau_{th} < 1/\omega_{3dB}$, where $\omega_{3dB}/2\pi$ is the -3 dB IF bandwidth. In this analysis, it is interesting to note that downconversion does not depend upon any non-linearity of the device I-V characteristic, but is instead a result of generating a signal within the device based upon the power absorbed by the device rather than from the voltage impressed across it. Therefore one expects from an electron gas bolometer neither an instantaneous response at the signal frequency, nor any harmonic response [McGrath95].

The result of Equation 2.4 is approximate because the resistance is a function of the electron temperature, which changes with the absorbed power. Phillips and Jefferts account for this electrothermal feedback phenomenon, and then balance the heat absorbed by the device with the heat outflow to the phonons (the bath) and the temperature increase of the electron gas, to solve for the voltage across the bolometer, V_b .

$$V_b = I_0 R_0 \left[1 - \frac{3 I_0^2 R_0 + P_{LO}}{2 G' T_p} - \frac{3 \sqrt{P_{LO} P_{RF}}}{G' T_p} \frac{e^{j\omega_{RF} t}}{1 + j\omega_{IF} \tau'} \right] \quad (2.5)$$

In this equation, $G' = G + 3(I_0^2 R_0 + P_{LO}) / 2T_0$ is the modified thermal conductance to bath, and $\tau' = C / G'$ is the modified thermal time constant (refer to Equation 2.2). These changes reflect the addition of electrothermal feedback effects into the model.

Of the three terms on the RHS of Equation 2.5, the first represents the Ohm's Law voltage, the second the deviation from Ohm's Law due to the hot-electron enhancement of the mobility, and the third is the IF signal term. The IF response rolls off with frequency according to a single-pole filter characteristic, based upon the modified thermal time constant.

The InSb mixer of Phillips and Jefferts [**Phillips73**], installed on the NRAO 11 meter antenna at Kitt Peak, operated at 120 GHz, with a noise temperature of 250 K and a useful IF bandwidth of 4 MHz ($\tau' = 0.25 \mu\text{s}$). This bandwidth is too narrow for the device to be considered useful today, so the discussion in this section moves on to the topic of thin-film superconducting electron-gas (today, called hot-electron) bolometer mixers.

Surface effects cause very thin metallic films to possess very high scattering rates. Writing about thermal conduction, Kumar and Vradis note that boundary scattering dominates the conduction process as the film thickness decreases to the order of the mean free path or less [**Kumar91**]. In metallic superconducting thin films, such as films of niobium, niobium nitride, aluminum, and tantalum, the electronic mean free path between collisions l is found to be very short indeed, between 1-10 nm. This represents an enhancement of the electron-electron interaction at the expense of the electron-phonon interaction [**Skalare96**]; specifically, it is found that $\tau_{e-e} \propto l$, while $\tau_{e-ph} \propto l^{-1}$ [**McGrath95**]. Because the electrons share energy between themselves very readily by

scattering from surface states, their interaction with the lattice is quite weak, and a hot-electron distribution may arise. Therefore a superconducting HEB is an electron-gas bolometer in the manner of the InSb bolometer, although the hot-electron effect arises for opposite reasons: these thin superconducting films operate with a very short mean free path in the dirty limit, while the InSb devices were fabricated from high-purity material with a large carrier mobility.

A comprehensive theory of superconducting HEB operation does not yet exist as of this writing, although substantial progress has been made [**Araujo98**, **Baubert03**, **Merkel01**, **Merkel02**, **Wilms Floet99a,b**, **Yngvesson03**]. The approach used to examine the operation of InSb devices does apply in its general outline, however: Equation 2.4 for the power absorbed by the bolometer continues to be valid, and in order to build a useful model of the superconducting HEB mixer element, it is still necessary to consider the heat balance equation. The two varieties of superconducting hot-electron bolometers, phonon-cooled (PHEBs) and diffusion-cooled (DHEBs), are illustrated in the schematic diagram of **Figure 2.7**.

It was noted in the analysis of the InSb electron gas bolometer that heat absorbed by the device flows either to the electron gas or to the lattice, so that the phonons act as the thermal reservoir to cool or re-set the absorber. How this cooling takes place is an integral aspect of the operation of a bolometer mixer. The different mechanisms of heat outflow illustrated in **Figure 2.7** comprise the basic distinction between phonon-cooled and diffusion-cooled HEB structures.

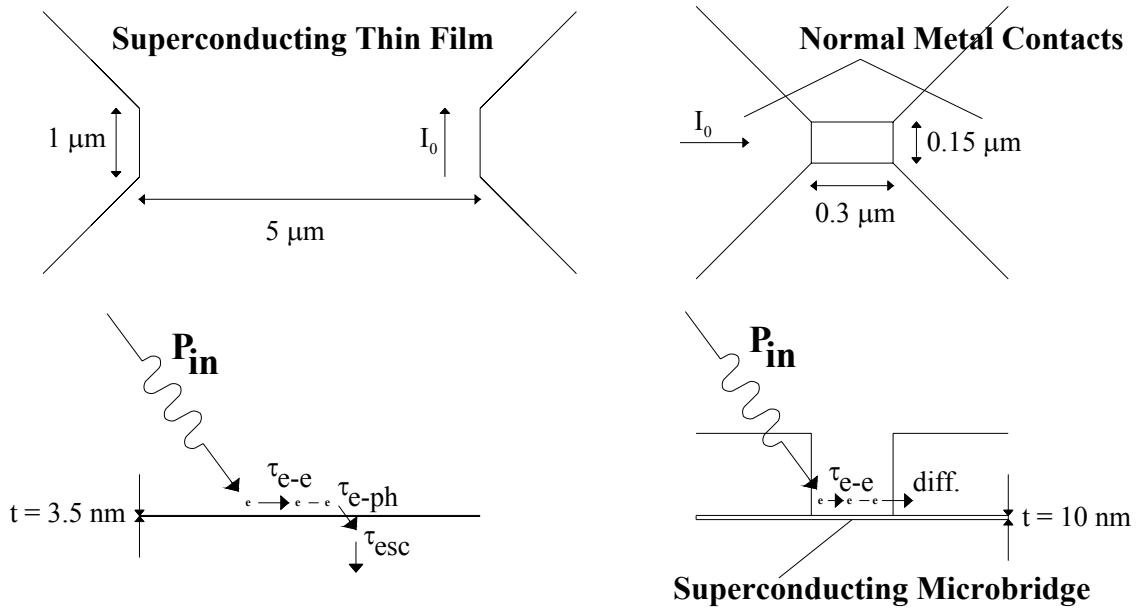


Figure 2.7. Schematic diagram of phonon-cooled (left, PHEB) and diffusion-cooled (DHEB) hot-electron bolometers, including typical dimensions and illustration of their thermal operation. τ_{e-e} , τ_{e-ph} , and τ_{esc} are the average electron-electron, electron-phonon, and lattice-to-substrate escape interaction times, respectively. The thickness of the thin superconducting films is t ; I_0 is the DC bias current.

When an RF photon is absorbed by a carrier³ in a PHEB, its energy is quickly shared with the electron gas, sustaining the hot-electron distribution. This heat escapes from the electron gas to the substrate through the lattice, so that in this case

$$\tau_{th} = \tau_{e-ph} + \tau_{esc}. \quad (2.6)$$

In order for this analysis to hold, it is necessary that $\tau_{e-e} < \tau_{e-ph}$, so that the electron gas thermalizes before absorbed heat is removed from the device, and also that $\tau_{esc} \ll \tau_{ph-e}$, so that energy removed to the lattice from the electron gas is not returned before it escapes to the substrate [Karasik98b]. Both of these conditions hold for typical superconducting thin films.

³ Below the gap frequency of the material, RF radiation is absorbed only by free carriers. Above the gap frequency, an incident photon can break a Cooper pair and so be readily absorbed.

If the film is very thin and the interface between the superconducting film and the substrate is transparent to the flow of heat [Frommberger01a], $\tau_{\text{esc}} \ll \tau_{\text{e-ph}}$, and according to Equation 2.6 the IF bandwidth will be determined solely by $\tau_{\text{e-ph}}$. For a niobium PHEB, $\tau_{\text{e-ph}} \approx 1$ ns, and $\omega_{3\text{dB}} \approx 160$ MHz. For a niobium nitride PHEB, however, $\tau_{\text{e-ph}} \approx 15$ ps, and $f_{3\text{dB}} \approx 10$ GHz [McGrath95, Yagoubov96]. While in practice, due to electrothermal feedback and other effects, the IF rolloff frequency is substantially less than this, values up to several gigahertz are typical. This bandwidth is quite wide enough to be of use in many modern submillimeter wave heterodyne receiver applications.

It is desired in a DHEB that the electron gas not interact with the lattice at all. Instead, after the RF radiation has been absorbed and the electron gas has thermalized, the absorbed heat escapes by diffusion out of the superconducting microbridge into the nearby normal metal contacts, which act as heat sinks held at the bath temperature. (This discussion involves the diffusion of heat, not carrier transport.) To prevent the escape of heat to the lattice, the length of the microbridge L is governed by the equation

$$L/2 < \sqrt{D\tau_{\text{e-ph}}} ; \quad (2.7)$$

that is, the characteristic length of heat diffusion must be less than the length scale associated with the electron-phonon interaction time.

For 10 nm niobium films, the diffusion constant $D \approx 1.6$ cm²/s [Wilms Floet01], and $\tau_{\text{e-ph}}$ may be determined from the relation [Gershenson91]

$$\tau_{\text{e-ph}} = \frac{10^{-8} \text{ sec}}{T^2} . \quad (2.8)$$

This corresponds to $\tau_{\text{e-ph}} = 0.6$ ns (Burke states $\tau_{\text{e-ph}} = 1$ ns [Burke97]), for a bridge length $L < 0.6$ μm . In practice a length of about 0.25 μm or less is typically selected by

researchers. This dimension equals about twice the characteristic electron-electron interaction length L_{e-e} , so that a carrier which absorbs a photon may be considered to share its energy with the electron gas in a time τ_{e-e} while moving a distance $L_{e-e}=L/2$ out of the microbridge.

The IF bandwidth of a diffusion-cooled device can be calculated with Equation 2.2, using the electron specific heat for the heat capacity C and the Wiedemann-Franz Law to calculate the thermal conductance G . McGrath obtains from this calculation a value of several gigahertz [McGrath95, Skalare95] for f_{3dB} , which is again usefully wide. A closer examination of diffusion-cooled HEBs, which are the subject of this dissertation, is the topic of **Section 2.6**.

6. Superconducting Diffusion-Cooled HEB Device Operation

According to the illustration of **Figure 2.7**, the process of photon absorption and heat outflow by phonon interaction in a superconducting PHEB is uniform throughout the device volume. Therefore, the electron temperature should be constant across the extent of the device. (This statement is not true in practice, as heat generated Ohmically by the DC bias current will create and sustain a resistive hot spot [Merkel01], discussed in the context of DHEBs shortly.) Because heat diffusion is driven by thermal gradients, however, a diffusion-cooled HEB microbridge must exhibit a non-uniform temperature distribution along its length: hottest in the center, and anchored at the bath temperature at its ends, as illustrated in **Figure 2.8**.

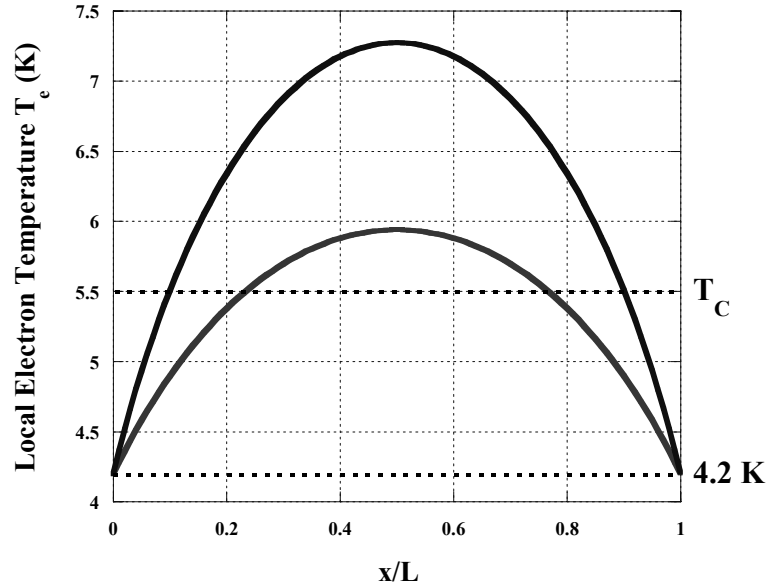


Figure 2.8. Temperature distribution along the length of a diffusion-cooled HEB microbridge for two different values of the absorbed power, assuming uniform DC heating and no heat outflow by way of phonon interactions. The central portion of the microbridge may be heated above the superconducting critical temperature, T_C .

Therefore, although a lumped element approach can provide useful insight, a diffusion-cooled HEB should be treated as a distributed element. As a result, Equations 2.2 for the thermal time constant and 2.4 for the power dissipated within the device should be regarded as only approximate. Assuming the HEB microbridge to be a metallic strip which undergoes uniform, weak, AC heating, Burke expresses the absorbed power in terms of its Fourier components and uses the time-dependent heat diffusion equation to solve for the electron temperature distribution along the length of the bridge. He obtains an effective thermal time constant [Burke97]

$$\tau_{eff} = \frac{L^2}{\pi^2 D}. \quad (2.9)$$

This result is different than that obtained using Equation 2.2, although it has the same functional dependence upon the microbridge length. Applying Equation 2.9, a diffusion-

cooled HEB microbridge 0.25 μm long should exhibit an IF 3 dB bandwidth of approximately 4 GHz.

From Equation 2.9, it is interesting to note that the characteristic time constants of thermal diffusion and electron-phonon interaction are equal, $\tau_{\text{eff}} = \tau_{\text{e-ph}}$, when the microbridge length

$$L = \pi L_{\text{e-ph}}. \quad (2.10)$$

This length, about 1.3 μm , represents the crossover between diffusion- and phonon-cooling. Because $2\pi f_{3\text{dB}} = 1/\tau_{\text{eff}}$, it also follows from Equation 2.9 that the IF bandwidth

$$f_{3\text{dB}} \propto \frac{1}{L^2} \quad (2.11)$$

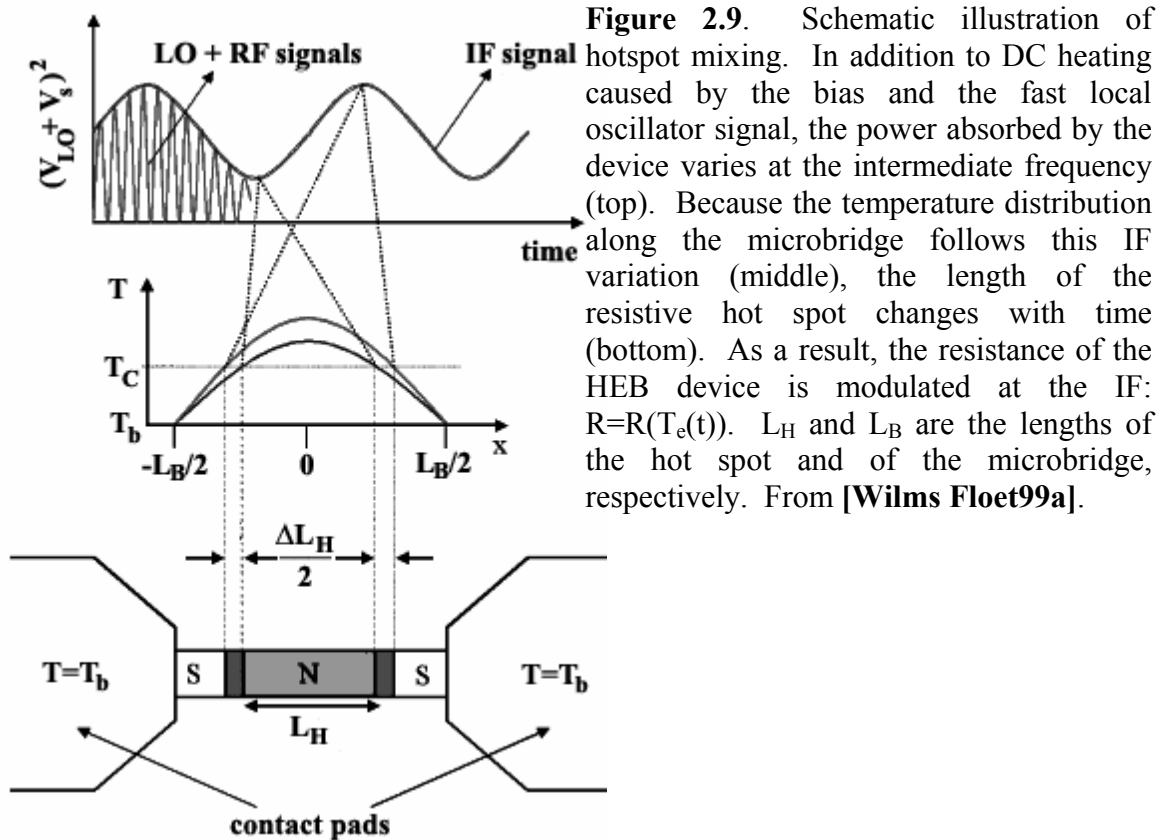
for diffusion-cooled devices. The predictions of Equations 2.10 and 2.11 were examined by Burke et. al. in 1996 and found to be correct within experimental uncertainty [Burke96].

The derivation of Equation 2.9 neglected the transfer of heat from electrons to phonons, assumed uniform absorption of power across the device, and utilized constant values of the thermal conductivity K and heat capacity C independent of the local electron temperature. While the first assumption is justified in a short microbridge where diffusion cooling dominates, the others are not justified in this case where a superconducting thin film is involved. **Figure 2.8** illustrates the reason why this is so.

For sufficiently large absorbed powers, as shown in **Figure 2.8**, the electron temperature in the central portion of the HEB microbridge exceeds the critical temperature at which the superconducting thin film reverts to its normally conducting, resistive state. The points where $T_e = T_C$ define the boundaries of a resistive hot spot which can grow or fade along with time variation of the power absorbed by the device.

Within the hot spot, the amount of power absorbed and the values of the material parameters C and K are quite different from their values in adjacent, superconducting regions of the microbridge. For instance, the DC bias provided to the mixer dissipates some heat in the device Ohmically, but only within the resistive hot spot. The resistance of the HEB microbridge follows changes in the length of this normally conducting region, as superconducting portions of the microbridge do not contribute to the resistance of the device.

Wilms Floet et. al. have proposed a physical model which explains heterodyne downconversion in a diffusion-cooled HEB mixer as a result of the modulation of the length of the resistive hot spot at the intermediate frequency, so-called “hotspot mixing” [Wilms Floet 99a]. This is illustrated schematically in **Figure 2.9**.



Equation 2.4 showed that the power absorbed by a square law detector used as a mixer includes both DC and intermediate frequency components, as long as the thermal time constant is quick enough to allow an IF response. This insight provides the foundation for the theory of hot spot mixing. Because τ_{eff} is quite short, the electron temperature distribution within the HEB microbridge responds not only to DC heating (the first and second terms of Equation 2.4), but also to the IF variation of the absorbed power. As a result, the length of the resistive hot spot (and the overall resistance of the HEB device) varies at the intermediate frequency

Since the generation of the intermediate frequency signal depends upon the modulation of the hot spot length, the DC voltage responsivity, S_0 , should be defined in terms of the hot spot length according to

$$S_0 = j\rho \frac{dL_H}{dP}, \quad (2.12)$$

where j is the bias current density, ρ the resistivity, L_H the hot spot length, and P the power absorbed by the device [Wilms Floet99a]. The output voltage signal at the IF developed across the HEB device is a downconverted replica of the original RF signal.

As of this writing, the performance of superconducting NbN phonon-cooled HEBs currently exceeds the performance of Nb diffusion-cooled devices. For instance, in recently published literature a PHEB operated at 2.5 THz exhibited a receiver noise temperature of 1050 Kelvins [Baselmans03], while a corresponding result with a Nb DHEB was 2500 Kelvins [Gerecht02]. Both receivers operated in a quasi-optical configuration; however, the DHEB result was uncorrected, and the experimental setup was not fully optimized. Development of both phonon- and diffusion-cooled HEBs continues, utilizing Nb, NbN, and other materials.

CHAPTER 3 - DESIGN OF THE RECEIVER ARRAY

1. Overview

The 850 and 1450 GHz receivers each consist of three pieces: a backshort block, an HEB block, and a feedhorn block. A drawing of an assembled 850 GHz 1x4 array is shown in **Figure 3.1**. Because the mixer rests on an electrically transparent membrane

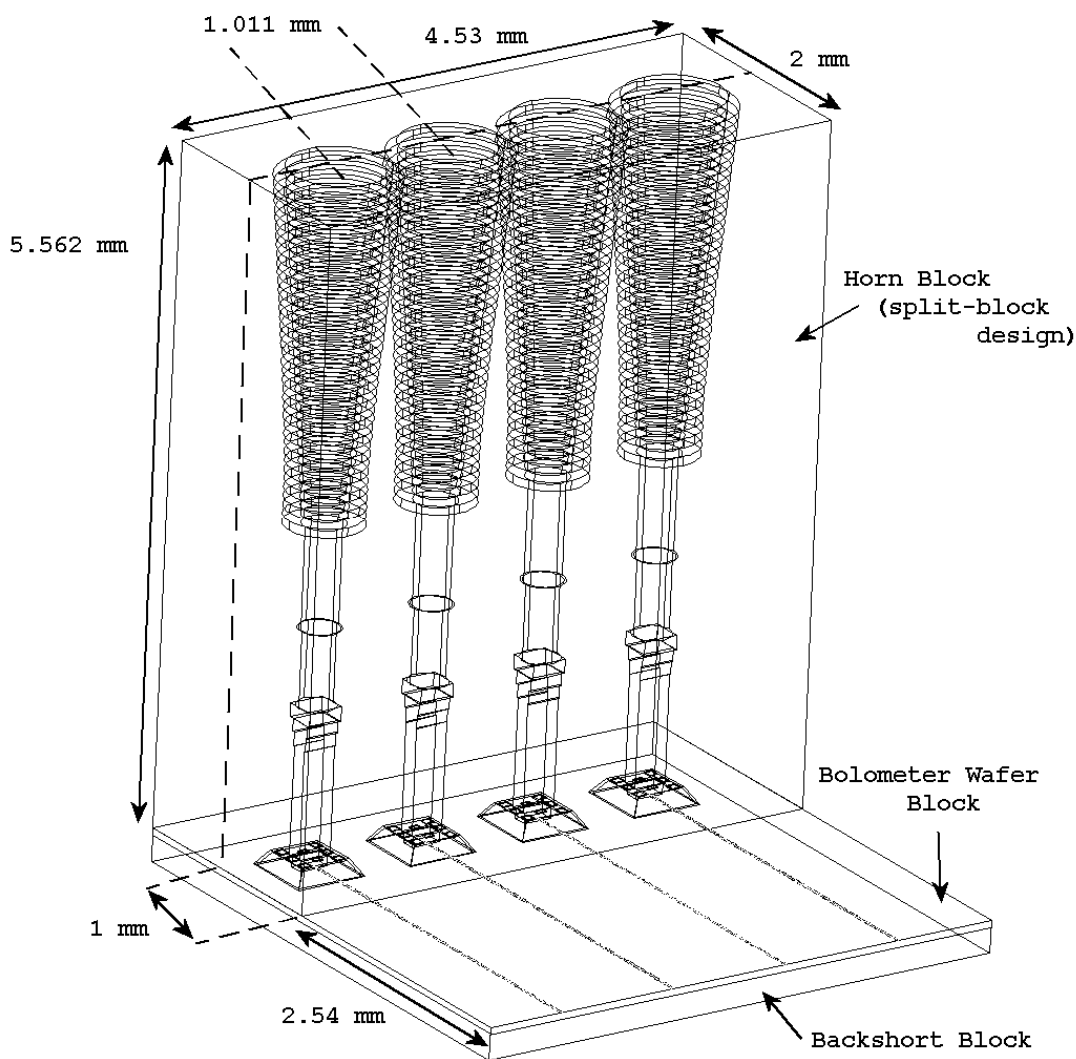


Figure 3.1. A diagram of an assembled 850 GHz 1x4 receiver array showing the three blocks, their dimensions, and how they fit together. The 1450 GHz 1x5 array is similar, although the dimensions of the micromachined feedhorns are smaller in that case and the pixel spacing is 3.600 mm rather than 1.011 mm.

of silicon nitride, it is possible in this design for the backshort to sit directly underneath the mixer. This allows several identical circuits to be replicated linearly on a single HEB chip, creating a receiver array in the simplest fashion possible.

This section is concerned with the overall design concept for the receiver array, the details of its intended operation, its electromagnetic design, and its predicted performance. The topics which follow illustrate many aspects of the design of all three blocks, along with information about the fabrication of the feedhorn block, which is underway at the University of Arizona and is not a principal topic of this dissertation. The fabrication of the backshort and HEB blocks is discussed in **Chapters 4-5**.

The work described in this section, though obviously integrally important to this dissertation, was mostly performed by scientists at California Institute of Technology (Jacob Kooi) and at the University of Arizona (Gopal Narayanan, Dathon Golish, and Chris Walker). The author wishes to re-iterate his gratitude to these co-workers.

2. Feedhorn Block

The feedhorns are constructed in a split-block design from a silicon wafer 1 mm thick using laser micromachining (LMM, which could perhaps more accurately be described as laser-assisted microchemical etching). [Walker97, Walker00] The corrugated feedhorn ridges, circular-to-rectangular waveguide transitions, waveguides, waveguide steps and alignment markers are all fabricated in mirror-image pairs using LMM. Since the array of horns are fabricated together on one piece of silicon, as a block, just as the mixers and backshorts are, the spacing and alignment of the individual horns

within the array are exact. An SEM photograph of one 1450 GHz feedhorn half is shown in **Figure 3.2**.

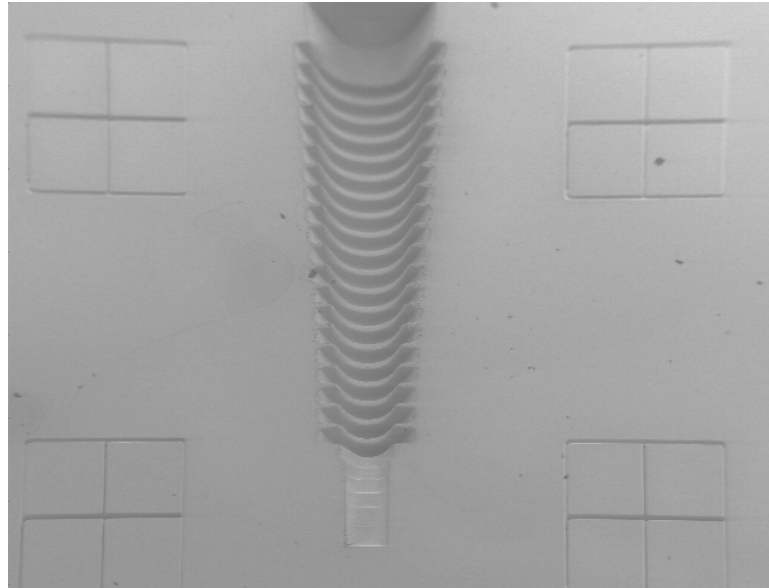


Figure 3.2. One 1450 GHz feedhorn half fabricated by LMM. The four quadrant patterns are markers intended for dicing and then to aid with alignment of the split-block halves. In this iteration, the circular-to-rectangular waveguide transition is not resolved well. The designed waveguide dimension is 140 μm wide by 70 μm deep.

The issue of aligning and assembling the split-block halves has been discussed, but not definitively addressed. A shim might serve this purpose adequately, and is required in any event in order to align the feedhorn block to the backshort block (see **Section 4.2**), but it is likely that an IR aligner will have to be utilized for this task. This means that a feedhorn block metallization mask, which includes patches of metallization for the feedhorns and metallized crosses for the IR alignment, must be created. This mask can easily be designed to register to marks placed on the silicon by LMM, such as the quadrant marks shown in **Figure 3.2**.

Returning to design issues, the principal concern the designer must address is the power coupling efficiency between the waveguide probe and the feedhorn (and, by

extension, the electromagnetic signal of interest propagating in free space). It may be seen in **Figure 3.3** that the coupling efficiency between a $50\ \Omega$ device and the horn block is predicted to be better than -0.5 dB from 1400 GHz to 1700 GHz and is rather flat. Contributions to this loss include conduction losses in the gold RF circuitry, losses due to RF mismatch, and leakage of energy in the airspace between the backshort and feedhorn blocks.

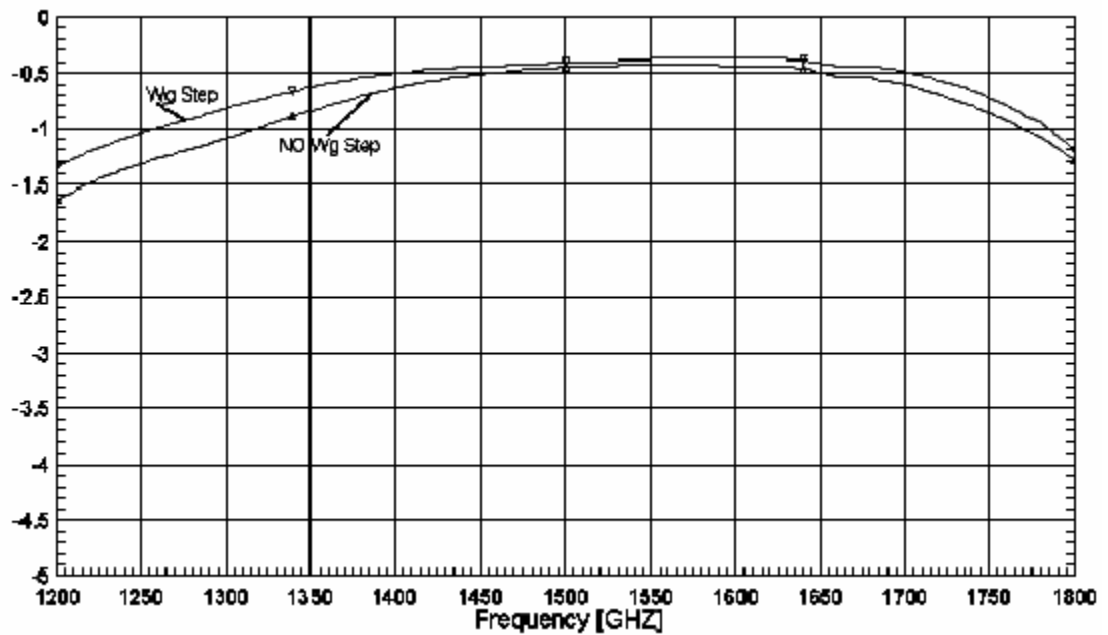


Figure 3.3. Power coupling efficiency from a $50\ \Omega$ HEB device to the horn block for the 1450 GHz design.

The performance just stated is achieved by adding a “waveguide step” to the feedhorn block design; that is, a small constriction in the waveguide a short distance above the mixer. The waveguide step improves the coupling efficiency by adding a shunt tuning capacitance [Kooi01a]. Since the waveguide itself is fabricated by LMM, this improvement is trivial to implement. In the 1450 GHz design, the waveguide step is $10\ \mu\text{m}$ narrower than the rest of the waveguide, i.e., $140\ \mu\text{m}$ wide by only $60\ \mu\text{m}$ deep. It is pictured in **Figure 3.4**.

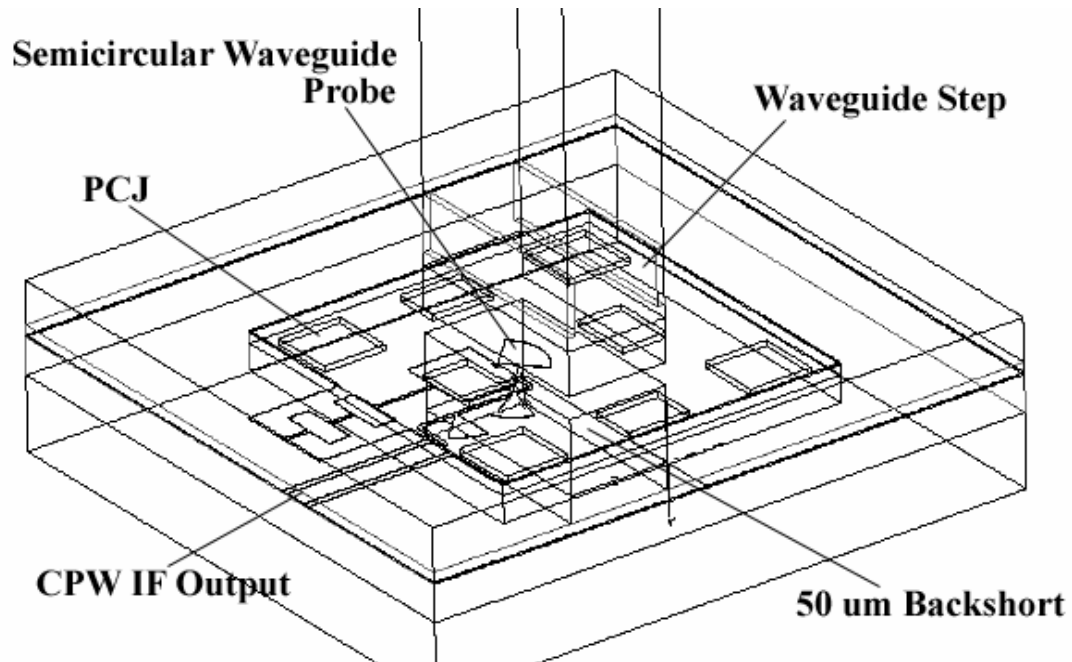


Figure 3.4. Wire frame drawing detailing the arrangement of one 1450 GHz pixel. The photonic crystal junctions on both the backshort pedestal and on the bottom edge of the feedhorn block are pictured.

Simulations of this design predict a return loss better than -20 dB from below 1200 to about 1650 GHz, as shown in **Figure 3.5**. Adding the capacitive tuning step to the waveguide design is clearly very beneficial to the operation of the receiver.

In addition to the in-plane features of the split-block halves (i.e., the fabrication of the corrugated feedhorn ridges, waveguides, etc.), the feedhorn block design includes features on the edges of the block halves (i.e., on the bottom surface of the feedhorn block as it is pictured in **Figure 3.1**). These features are necessary to prevent the field exiting the waveguide from leaking out into space (using a photonic crystal junction, or PCJ, discussed in more detail in **Section 4.2**), to accommodate the design of the IF lines, and to fabricate standoffs which maintain an air gap of 7 μm between the bottom edge of the feedhorn block and the HEB block.

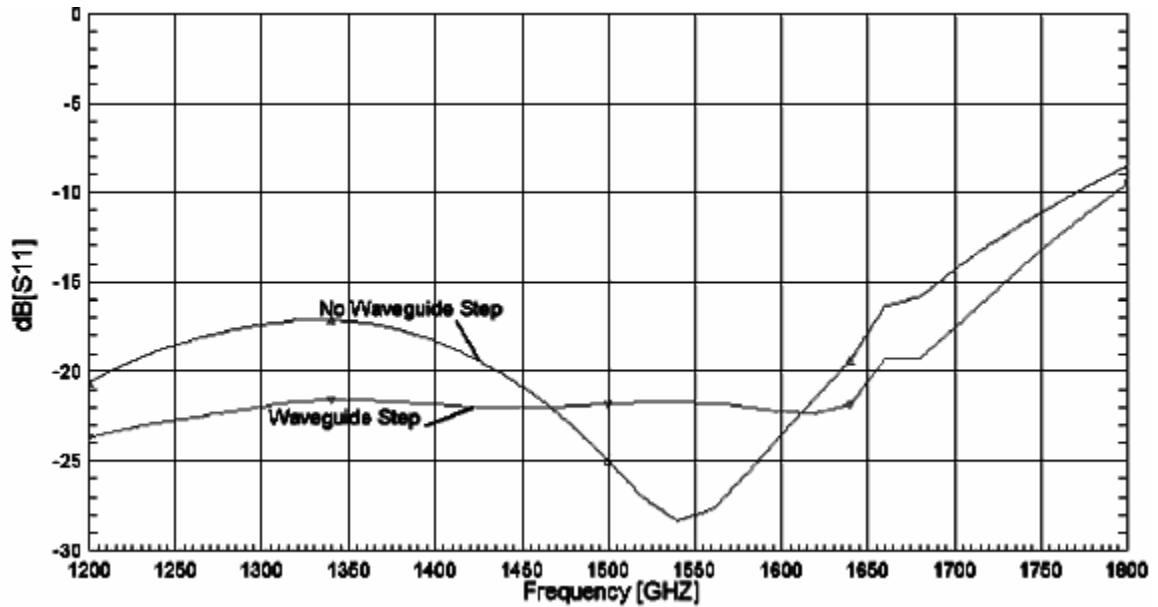


Figure 3.5. Input return loss of the 1450 GHz probe design, shown both with and without the waveguide step. In this case, the design of the waveguide step has been chosen to optimize the power coupling efficiency.

At present, a definitive plan for accomplishing these tasks by LMM has not been developed. Alternative methods may suffice. For instance, the PCJ lattice can likely be fabricated on the edge of the assembled feedhorn block by FIB deposition of platinum, and the 7 μm standoff can be accomplished fairly straightforwardly by plating up gold on the edges of the backshort block cradle (see **Figure 4.4**). The standoff might also be accomplished more elegantly using LMM to etch a deep hole during the in-plane fabrication of the feedhorns and waveguide structures. The space cutout necessary above the IF lines might also be possible using FIB, although the use of LMM would be far preferable in that case. However, neither the PCJ array nor the cutouts for the IF lines are absolutely necessary to the construction of a working receiver array, and both advances could be pursued in the course of subsequent improvements.

3. Design and Operation of the Semicircular Waveguide Probe

According to **Figure 3.5**, simulations predict that more than 99% of the RF energy in the band between 1200 GHz and 1650 GHz captured by the feedhorn will be guided to the HEB mixing element, where it should be absorbed by the electron gas in the superconducting niobium microbridge. This is a very satisfactory result, and the reader who wishes to know more about the operation of the waveguide probe in these regards is referred to the literature [**Kooi03**]. Two aspects of the probe design, however, have not been presented, and are of interest. These involve how the IF output line taps into the probe, and the detailed structure of the semicircular waveguide probe at its narrowest point, or “throat”. **Figure 3.6** details the design of one element in the receiver array.

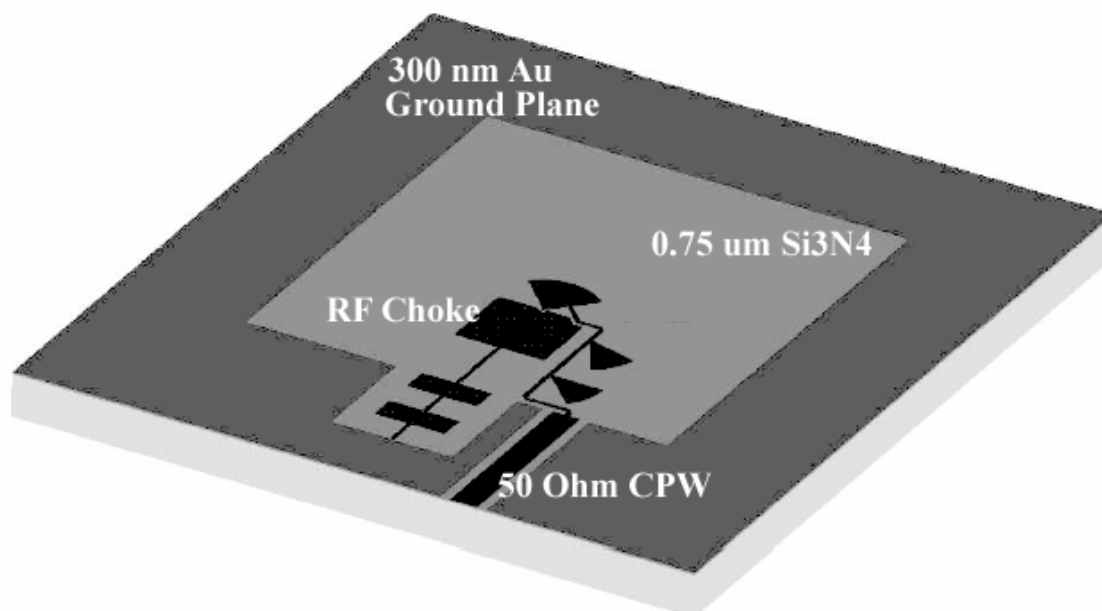


Figure 3.6. One element in the receiver array. Black (mixer circuitry) and dark gray (ground plane) both represent the same 300 nm layer of gold, deposited with an adhesion layer on top of a 0.75 μm film of silicon nitride (light gray) which covers the entire wafer. The silicon nitride membrane is simply the largest square area defined by the ground plane. The 50 Ω coplanar waveguide extracts the IF signal through a tap into the waveguide probe.

If this mixer design utilized a Schottky barrier diode or SIS junction mixer, rather than a superconducting HEB mixer, there might not be a compelling reason to consider tapping into the waveguide probe in the manner illustrated in **Figure 3.6**. Instead, since Schottky diodes and SIS junctions are formed stackwise, in those cases one could consider a symmetrical design in which the RF choke is covered with a layer of SiO₂, and the IF signal is extracted through a line deposited and patterned on top of that insulating layer. This arrangement would dispense with the asymmetrical configuration of the probe tap, microstrip line, chokes, and CPW line in the design under discussion.

A diffusion-cooled superconducting HEB, however, has a planar character and is much smaller than the other two types of mixing devices. For this reason, the symmetrical design built up vertically seemed unreasonably difficult to fabricate, and the design incorporating an asymmetrical tap into the waveguide probe was developed. A diagram of the waveguide probe IF tap and the probe throat appears in **Figure 3.7**; **Table 3.1** displays the relevant dimensions for both the 850 GHz and 1450 GHz designs.

Two interesting design decisions are illustrated in **Figure 3.7**. The first is the decision to set the probe throat back into the RF choke by one micron (allowing in addition an empty one micron space for placement of the HEB device). This forms a probe transition, seen in **Figure 5.3**, with the mixing element at its terminus. The second design decision involves the angled orientation of the first fan RF choke on the IF line. This was a compromise based upon the interplay of the fields in the waveguide and around the square RF choke at the base of the waveguide probe. [**Kooi01b**] Some sense of this design process may be gleaned from **Figure 3.8**, which shows the results of an HFSS calculation detailing the electromagnetic operation of the circuit structure.

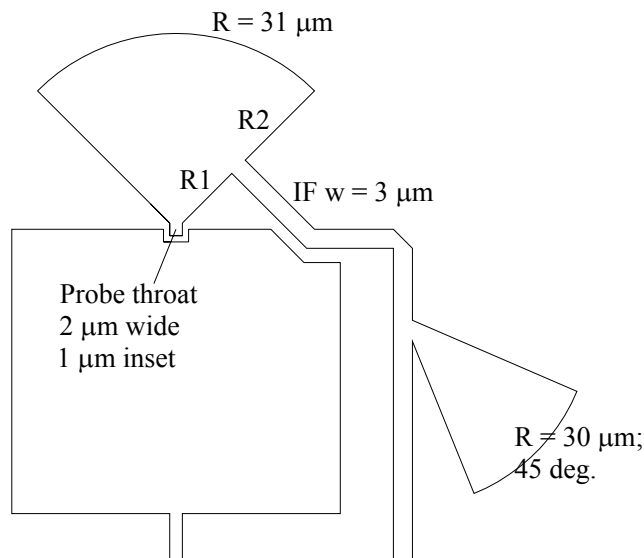


Figure 3.7. Design of the IF waveguide probe tap and probe throat. R1 is the distance from the center of the semicircular probe to the near edge of the IF line; R2 is the distance from the other edge of the IF line to the beginning of the arc. The dimensions given are for the 1450 GHz design; the probe throat design is unchanged in the 850 GHz design.

Design	R (μm)	R1 (μm)	w _{IF} (μm)	R2 (μm)
850 GHz	53	22	4	27
1450 GHz	31	12.5	3	15.5

Table 3.1. Probe tap dimensions for both the 850 GHz and 1450 GHz designs, referenced to **Figure 3.7**. The dimensions follow frequency scaling.

The most significant finding presented in **Figure 3.8** lies in the symmetry of the fields surrounding the waveguide probe. That the IF line which taps into the waveguide probe does not greatly disturb the field symmetry which would exist if the tap were absent implies that the tap has no adverse effect upon the operation of the probe. Therefore the design of the IF tap is satisfactory. The return loss of the final waveguide probe design in the frequency range between 1200 GHz and 1800 GHz is shown in **Figure 3.9**.



Figure 3.8. Electromagnetic simulation of the performance of the 850 GHz design at 900 GHz using HFSS. The magnitude of the electric field in the surface of the silicon nitride membrane is plotted. The field is greatest in the small space between the IF line, the RF choke, and the waveguide probe. The RF choke presents a short circuit at the waveguide wall.

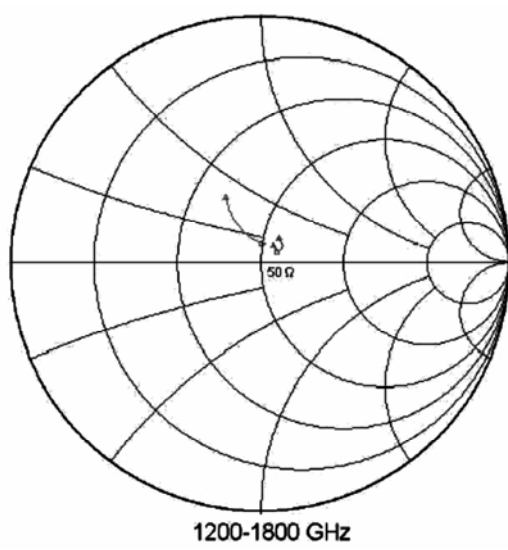


Figure 3.9. Return loss S_{11} of the membrane-based semicircular waveguide probe with IF tap. From 1200 GHz to 1700 GHz the impedance is nicely centered near 50 Ω .

4. Effects of Probe Misalignment

Because the feedhorn, HEB, and backshort blocks are all distinct pieces which must be aligned to each other and assembled, it is important to consider what effect improper positioning might have upon the performance of the waveguide probe. To answer this question, simulations of the 850 GHz design were conducted in which the waveguide probe was shifted 5% of the short waveguide dimension into, out of, and along the edge of the waveguide away from its intended position. **Figure 3.10** presents the results of these simulations.

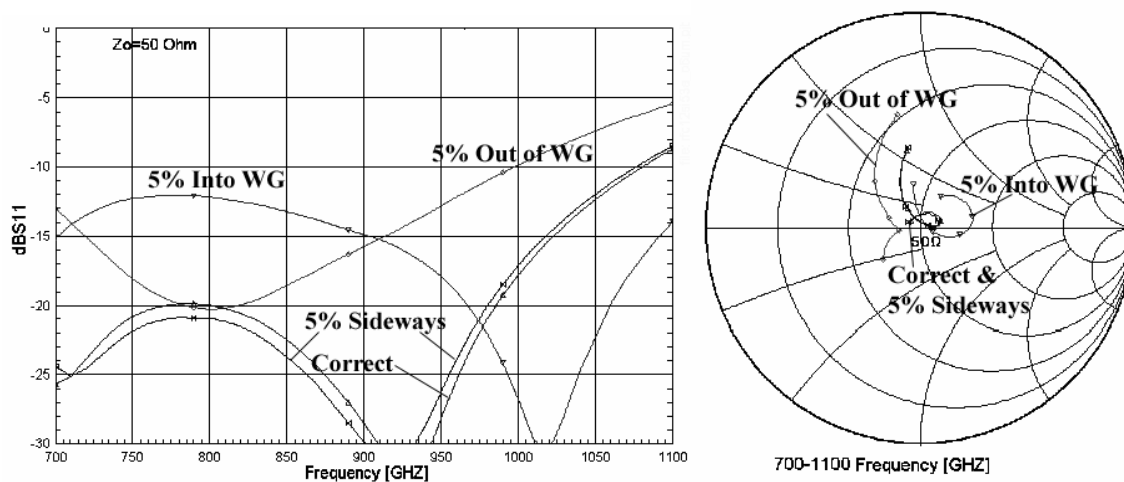


Figure 3.10. Simulated effect of probe misalignment in relation to the waveguide on the return loss S_{11} (left) and probe impedance (right) for the 850 GHz design. Since the waveguide dimensions are $240 \mu\text{m} \times 120 \mu\text{m}$, the distance the probe is shifted away from its intended position is $6 \mu\text{m}$. The simulated structure did not include the capacitive waveguide step.

According to these results, shifting the probe along the waveguide wall has basically no effect upon the impedance it presents, while the change caused by a shift parallel to the waveguide b-axis is significant. If the probe is shifted into the waveguide, its performance resembles that of a semicircular probe with a larger radius, while a probe shifted slightly out of the waveguide acts as would a probe of smaller radius [Kooi02a].

Although the misalignment tolerance shrinks to $3.5\ \mu\text{m}$ at 1450 GHz, in fact it should be possible to align the HEB block to the backshort block with an accuracy of about $1\ \mu\text{m}$ using an infrared aligner. The alignment of the feedhorn block to the other two components is much more problematic, since that assembly will be performed manually while peering with a microscope down through the feedhorn apertures to registration marks on the HEB block membrane. Even in the ideal case where the ends of the feedhorn block waveguides are perfectly rectangular and have precisely the correct $70\ \mu\text{m} \times 140\ \mu\text{m}$ dimensions, it would require extraordinary patience and skill to align the feedhorn block to the other components with $1\ \mu\text{m}$ accuracy.

In reality, the feedhorn block waveguides will be neither precisely dimensioned nor perfectly rectangular, and the registration marks on the HEB block membrane will be obscured by the feedhorn block waveguide step. Therefore to accomplish an alignment accuracy of even $3.5\ \mu\text{m}$ under realistic conditions using the method described may be very difficult. For that reason, each waveguide may suffer a significant discontinuity in the air space between the bottom of the feedhorn block and the top of the backshort block pedestal, although the alignment of the waveguide probe with respect to the backshort cavity should be quite good.

It is possible that the photonic crystal junctions will prevent this discontinuity from adversely affecting the return loss, as compensating for misaligned waveguide flanges is the function for which the concept was developed [Hesler01]. The case where the waveguide is discontinuous but the waveguide probe is properly aligned is not the one which has been modeled. It should be possible to exceed the modeled tolerance in the alignment of the waveguide probe to the backshort cavity.

5. IF Circuit Design

The output line which carries the intermediate frequency (IF) must transform the impedance of the probe tap operating in a microstrip mode to a $50\ \Omega$ coplanar waveguide (CPW) mode, pass the IF signal in a bandwidth of up to a few gigahertz, and block the high-frequency RF and LO signals captured by the waveguide probe. It also serves as part of the DC bias path to the HEB mixer. The circuit which accomplishes all of these tasks (in the 850 GHz receiver design), and its simulated performance, are shown in **Figure 3.11**.

Figure 3.11.

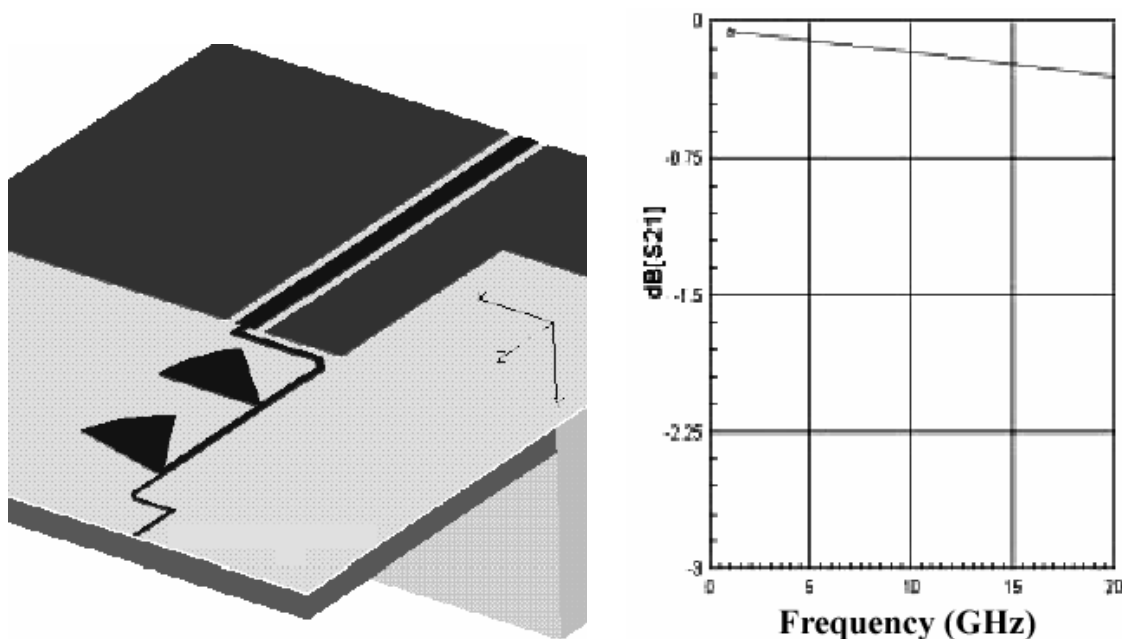


Figure 3.11. The IF circuit (left) and its simulated transmission loss s_{21} in the frequency range from 1 - 20 GHz (right). The impedance of the $4\ \mu\text{m}$ wide line at the probe tap is $148\ \Omega$ at 1 GHz, which is transformed by the IF circuit to $50\ \Omega$ at 1 GHz in the coplanar waveguide. The CPW consists of a center conductor $16\ \mu\text{m}$ wide bounded by symmetrical $4\ \mu\text{m}$ gaps. For intermediate frequencies below 5 GHz, the transmission loss is less than 0.2 dB.

The operation of the low-pass radial fan chokes can be inferred from **Figure 3.11**, where it is obvious that nearly the entire high-frequency signal is blocked by just the first choke. Simulations reveal that the transmission loss is greater than 30 dB at frequencies

above 700 GHz. The design effort involved in choosing the orientation of the radial fan choke has already been discussed.

The CPW does not operate simply in the open half-space pictured in **Figure 3.11**, since the mixer circuitry is separated from the bottom edge of the feedhorn block by only a small air gap (12 μm in the 850 GHz receiver design, 7 μm in the 1450 GHz design). Confinement alters the CPW mode, and changes the characteristic impedance of the line by a modest amount, from 50 Ω to 57 Ω . This problem may be surmounted by etching a channel (200 μm wide by 50 μm deep) in the edge of the feedhorn block in locations corresponding to the CPW lines. While this is an obvious application of laser micromachining, such a task has not been demonstrated as of this writing. A low noise receiver may be constructed successfully without this refinement.

6. Cross-talk Between Array Elements

One of the earliest issues addressed by the designer of the receiver was the possibility of cross-talk between separate elements in the array, which is a highly undesirable effect. The simulated structure which was used to investigate this pitfall, along with the results of the simulation, are shown in **Figure 3.12**.

In this simulation, an 850 GHz circuit design without an asymmetrical IF tap into the waveguide probe was used. The pixel spacing between the array elements was about 1.4 mm, and the membranes were about 700 μm across. These dimensions are somewhat larger than those used in the final design of the 850 GHz receiver, although the pixel spacing of the actual 1450 GHz 1x5 receiver is significantly greater, 3.6 mm. The

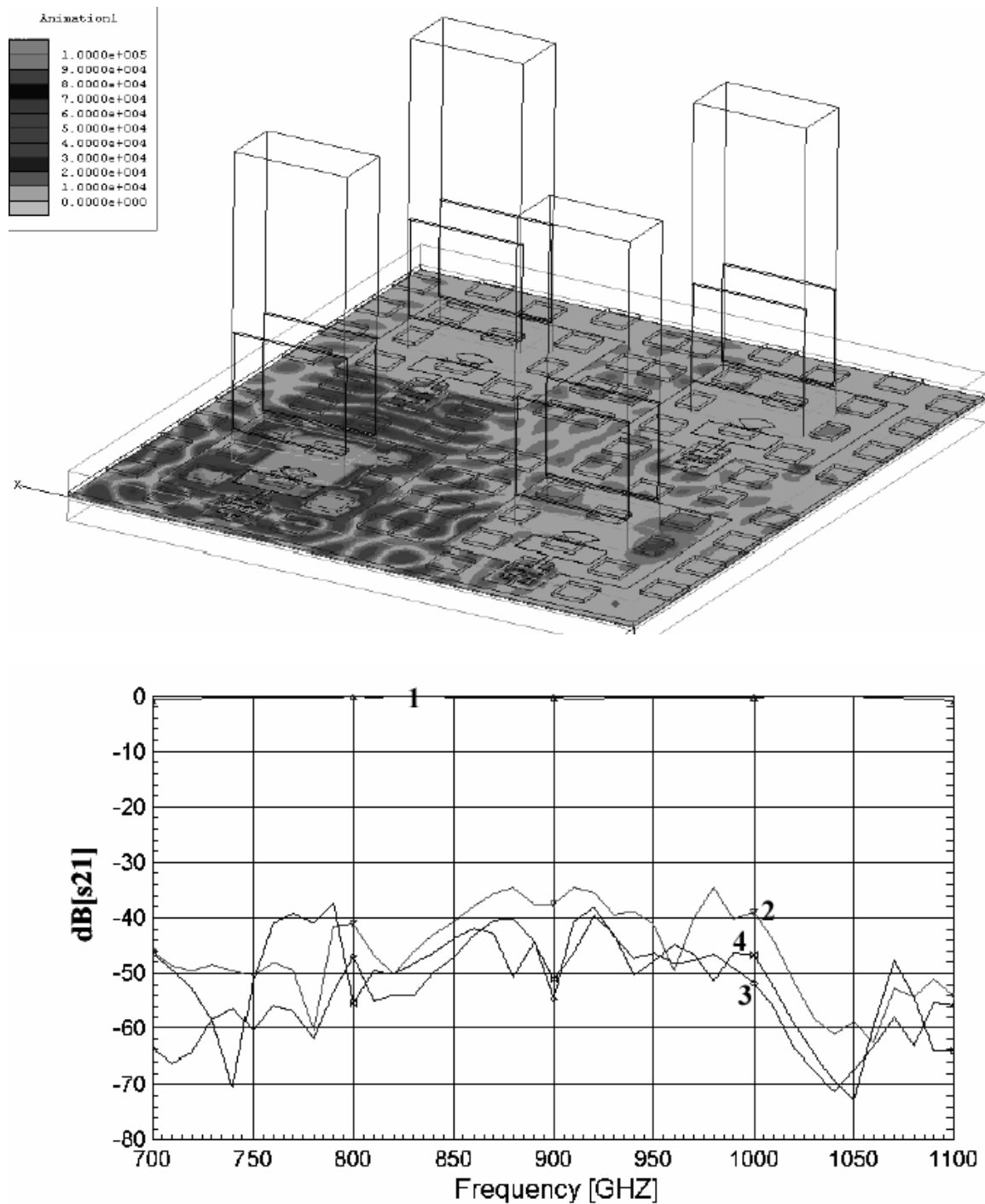


Figure 3.12. The simulated 2x2 array (top) and the transmission due to cross talk between the excited port (1) and the other elements of the array (bottom). The simulated design uses symmetrical mixer circuits without IF taps into the sides of the waveguide probes, and photonic crystal junctions. The action of the PCJs to disrupt the propagation of electromagnetic fields is apparent. Port 1 is leftmost. The cross-talk is lower than -35 dB over the entire band.

simulated design does use photonic crystal junctions, which clearly act very effectively to disperse the field.

The simulation reveals a transmission loss between array elements in all cases exceeding 35 dB, which means that cross-talk between pixels is not a significant concern.

7. Photonic Crystal Junctions and the Shape of the Backshort Block Pedestals

While the operation of the photonic crystal junctions may be inferred from the top half of **Figure 3.12**, it is possible to examine their performance quantitatively in the context of the backshort pedestals. The structure under discussion is shown in **Figure 3.13**.

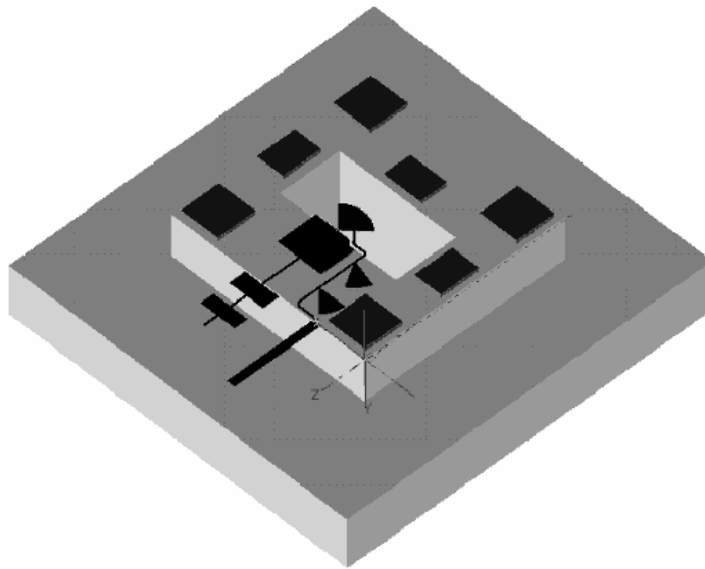


Figure 3.13. A backshort pedestal with vertical (not angled) walls and PCJs, along with the mixer circuitry on the membrane above.

Using this structure, simulations of the coupling efficiency of the 850 GHz receiver from 700 - 1100 GHz were performed for three distinct situations. Under the first condition, both the backshort pedestal and the matching membrane cavity in the HEB block were assumed to have vertical walls, so that the silicon pedestal filled the

cavity. Under the second condition, the backshort pedestal did not change, but the walls of the HEB block membrane cavity were given their actual slope following the $\{111\}$ planes. As a result, in this case the backshort pedestal failed to fill a portion of the empty cavity volume. In the third and final simulation, a photonic crystal junction was added to the backshort pedestal, which otherwise was not changed. The results of these calculations are shown in **Figure 3.14**.

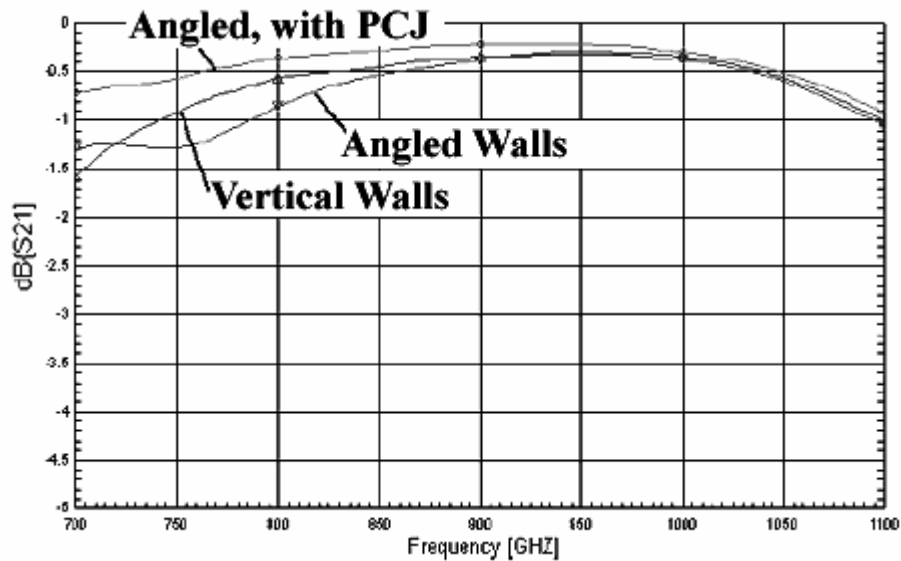


Figure 3.14. Simulations of the waveguide probe coupling efficiency for different designs of the HEB block membrane cavity (vertical or angled walls) and the backshort block pedestal (without or with a PCJ). The coupling efficiency is better if the pedestal fills the cavity space, but a photonic crystal junction, which prevents the field from leaking out into the empty volume of the cavity, is better still.

The results of these simulations are easy to interpret. The coupling efficiency suffers when it is possible for fields to leak out into an empty volume within the membrane cavity. Photonic crystal junctions minimize this leakage, and greatly improve the coupling efficiency, even compared to the hypothetical case where the walls of the membrane cavity are vertical (so that only a marginal volume is assumed to be empty).

In practice, the walls of the membrane cavity must follow the $\{111\}$ planes, and are therefore angled. Unlike the simulated situations just outlined, however, the actual backshort pedestals are also angled, so that they nearly fill the membrane cavities (see **Chapter 4**). The use of photonic crystal junctions still offers improvement in the coupling efficiency, as shown, but by corralling stray fields it also allows the designer the valuable freedom to loosen the mechanical tolerances.

8. Conclusion

To summarize, the designed 1450 GHz receiver (i.e., with the waveguide step and with PCJs both above and below the membrane) is predicted to perform as follows:

- Power coupling efficiency from feedhorn opening to device better than -0.5 dB from 1300 - 1725 GHz.
- Probe impedance nicely centered near 50Ω from 1200 - 1700 GHz.
- Input return loss less than -20 dB from 1290 - 1675 GHz.
- Cross-talk between elements below -35 dB.

The fabrication of the feedhorn block, which has been underway at the University of Arizona, was discussed, while the design and construction of the backshort and HEB blocks will be the subjects of the next two chapters. In addition to these silicon circuit components, mounting brackets, lens mounts, and other necessary structural components have been designed at the University of Arizona and machined. **Figure 3.15** shows the finished receiver mount, with a backshort block and HEB block set installed.

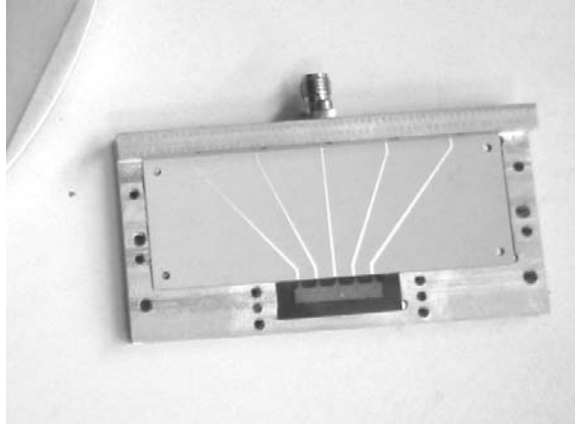


Figure 3.15. The mount for the 1x5 1450 GHz array receiver, machined from copper, showing the microstrip breakout board for the IF lines (only one SMA connector is installed) and the mounted backshort block/HEB block stack, at the bottom. The three holes on either side of the silicon components are for the lens mount, which will fit over the feedhorn block apertures.

CHAPTER 4 - DESIGN AND FABRICATION OF THE BACKSHORT BLOCK

1. Overview

The backshort block is fabricated from a 254 micron thick <100> silicon wafer, covered on both sides by LPCVD Si₃N₄, using front- and back-side lithography, reactive ion etching, and bulk chemical etching of silicon. The physical backshort underneath the HEB block membrane is a rectangular hole laser micromachined into the top surface of a pyramidal pedestal, five of which sit on one 1450 GHz backshort block die. The backshort block lithography mask includes a compensation scheme necessary to prevent undercutting of the exposed corners of the pedestals during the bulk etching of silicon. The pedestals themselves, exposed during this process as the surrounding material is etched away, stand in a field of etched silicon 127 microns deep, forming a cradle in which the HEB block rests. The border of the cradle also provides mechanical support and alignment for the feedhorn block. Finally, the completed backshort block contains several features intended to allow the backshort, HEB, and feedhorn blocks to be aligned to each other and assembled.

2. Design of the Backshort Block Masks

The component designs, based upon electromagnetic analyses performed by Jacob Kooi [Kooi02b], required that two separate sets of photolithography masks be designed and manufactured, one for the HEB block, and one for the backshort block, and additionally left open the question of how the components were to be aligned and assembled. The concern mentioned in the overview about undercutting at the corners of the pedestals, and the corresponding need to develop an adequate compensation scheme,

was discovered after the first iteration of the mask design. The following is a list of the issues which were considered by the author during the design of the backshort block lithography mask, along with some issues which arose subsequently:

1. The design calls for the fabrication of a photonic crystal junction (PCJ) [Hesler01] surrounding the backshort hole on the top of the pedestal. A PCJ is a ridged periodical structure which, if designed correctly, minimizes the leakage of electromagnetic energy out of a guiding structure into space. Such leakage occurs at the discontinuous joining of two waveguides, and the PCJ is necessary in this case to confine the submillimeter radiation propagating downward through the silicon nitride membrane. The PCJ pillars in this design are $4\ \mu\text{m}$ tall, $\pm 1.5\ \mu\text{m}$.

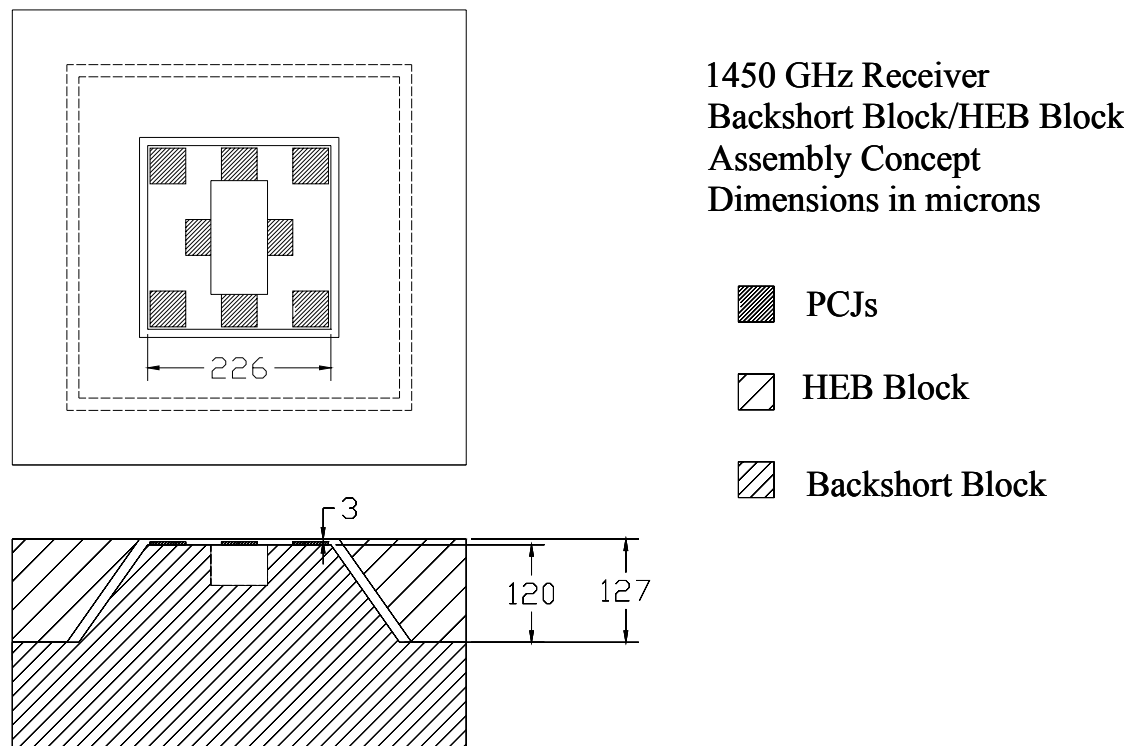


Figure 4.1. Concept drawing illustrating how the backshort block and HEB block are intended to fit together, maintaining a gap of $3\ \mu\text{m}$ between the membrane and the photonic crystal junctions. The arrangement of the PCJs is also shown.

2. The design specifies that there should be a gap of 3 μm between the HEB block membrane and the top of the PCJ pillar. (See **Figure 4.1**.) Since the HEB block wafer is 127 μm thick, and the PCJ pillars are 4 μm tall, the finished pedestal height is 120 μm . This dimension has a critical tolerance of $\pm 1.5 \mu\text{m}$.
3. The top surface of the pedestal, the PCJ pillars, and the backshort hole must be metallized, preferably with conformal sputtering of the same 3000 \AA of gold used for the HEB mixer circuitry. It is problematic, however, to cover the entire front side of the backshort block wafer with metal, as that would interfere with an important alignment scheme, described below.
4. All together, there are three separate schemes to help align the HEB block to the backshort block accurately. One involves features defined from the circuitry metallization on the HEB block membrane. A second uses pits, etched into the back of the HEB block, which will align to small holes laser micromachined into the etched surface of the backshort block. These holes are just large enough to accommodate a polished 6 mil ruby bearing, which should help to guide the two components together. The third alignment scheme uses IR alignment of metallized features on the front side of the HEB block to corresponding features on the bottom side of the backshort block. This cannot work if the front side of the backshort block die is entirely metallized.
5. The backshort block die should provide mechanical support for the feedhorn block, and some method of allowing the feedhorn block to be aligned with the other components, if possible.

6. Since the pedestals are bulk micromachined following the crystal planes, it is necessary to accurately align the backshort block mask to the wafer flat.
7. As has already been noted, the etch which exposes the pedestals reveals exotic crystal planes at their corners. Unlike the $\{111\}$ planes, which are relatively invulnerable, these planes are attacked by the etchant. This unwanted etching distorts the 850 GHz backshort block pyramidal stubs, and causes the smaller 1450 GHz stubs to be nearly etched away. A compensation scheme which addresses this problem was developed and successfully utilized.
8. It is desirable to fit backshort block die designs for both the 850 and 1450 GHz receivers on the same lithography mask, which minimizes expense.

How these issues were addressed by the ultimate mask design will now be discussed. The corresponding fabrication protocol will be the topic of a subsequent section.

It is impossible to consider using bulk micromachining to fabricate the photonic crystal junctions without somehow performing photolithography on the tops of the pedestals after they have already been etched nearly to completion. Another worthwhile idea, creating the PCJ pillars by plating following seed layer deposition and lithography, would offer a challenge of about the same degree of difficulty. For this project, however, the judgment was made that another method was available which would be simpler and much more flexible. Since the backshort cavity must be drilled in to the pedestal using laser micromachining anyway, the most elegant solution is to create the PCJ array by LMM at the same time that the backshort cavities are fabricated. (It would also be possible to build up the PCJ pillars by focused-ion beam deposition of platinum after the

backshort cavities have been machined and the backshort block die has been metallized, as explained in **Appendix C.**)

Since laser microchemical etching of silicon proceeds by removing material, it is necessary for the bulk silicon etch to leave behind enough material to allow PCJ fabrication by LMM. (That is, the pedestals must be etched somewhat taller than their ultimately specified height). The taper of the pedestals which results from the wet etch, however, adds a slight complication. In order to obtain the proper cross-sectional dimension at the proper height (226 μm across at a height of 120 μm , as illustrated in **Figure 4.1**), the size of the masked area must be determined based upon the target dimension, the 54.78° orientation of the crystal planes, and the depth of material which one intends to remove. This calculation is summarized in the last two rows of **Table 4.1**.

Receiver Design	850 GHz	1450 GHz
Pedestal Height (μm)	115 \pm 2	120 \pm 1.5
PCJ Pillar Height (μm)	8 +0/-2	4 \pm 1.5
Air Gap (μm)	4 \pm 2	3
Backshort Depth (μm)	82 \pm 3	50 \pm 2
Pedestal Width, Mask (μm)	383	216
Pedestal Width, Design (μm)	400	226

Table 4.1. Summary of the important backshort block pyramidal stub dimensions for both the 850 GHz and 1450 GHz designs. Refer to **Figure 4.1** for a visual definition of these dimensions. The dimensions listed for “Pedestal Width, Design” refer to the target size of the actual pedestal, while “Pedestal Width, Mask” is the size of the corresponding feature on the mask. The two dimensions differ due to the several microns of material intended to be shaved off of the top of the pyramidal stub by laser micromachining.

Table 4.1 also reveals that the pedestal heights for the 850 GHz receiver are not the same as those for the higher-frequency design. Laser micromachining allows for both

sets of backshort block dies to be fabricated on the same wafer, which would not be possible to accomplish using bulk chemical etching alone.

The mask design anticipates that the pedestals will be etched to a height of 127 μm , although to a certain extent that is an arbitrary choice. A depth of 124 μm would have been equally valid, since the sum of the pedestal height and the PCJ pillar height is about equal to this value for both designs. Choosing the deeper etch, however, allows for a small margin to compensate for variability in the pedestal heights across the surface of the wafer. The individual pedestals can be measured, and each adjusted by LMM to obtain best uniformity. Without this flexibility, it seems unlikely that a 1.5 μm tolerance on the 3 μm air gap could be achieved.

After etching the pedestals, stripping the Si_3N_4 mask off of the pedestals and the rest of the front of the backshort block wafer, and fabricating the backshort cavities and PCJs by LMM, it is necessary to metallize at least the top surfaces of the pyramidal stubs. It has already been noted, however, that this should not be accomplished simply by sputtering metal over the entire surface of the die, so that some variation of metal deposition, lithography, and etching or lift-off is required. Still, a very precise or artful lithography is not required. Therefore, it was chosen to cover the 1450 GHz backshort stubs with a patch of metallization 845 μm square (see **Figure 4.2**), and to cover the entire row of four 850 GHz stubs with a single patch 1011 μm wide x 4044 μm long. The actual dimensions which result from this lithography, where most of the wafer surface is more than 100 μm away from the mask, is of no consequence.

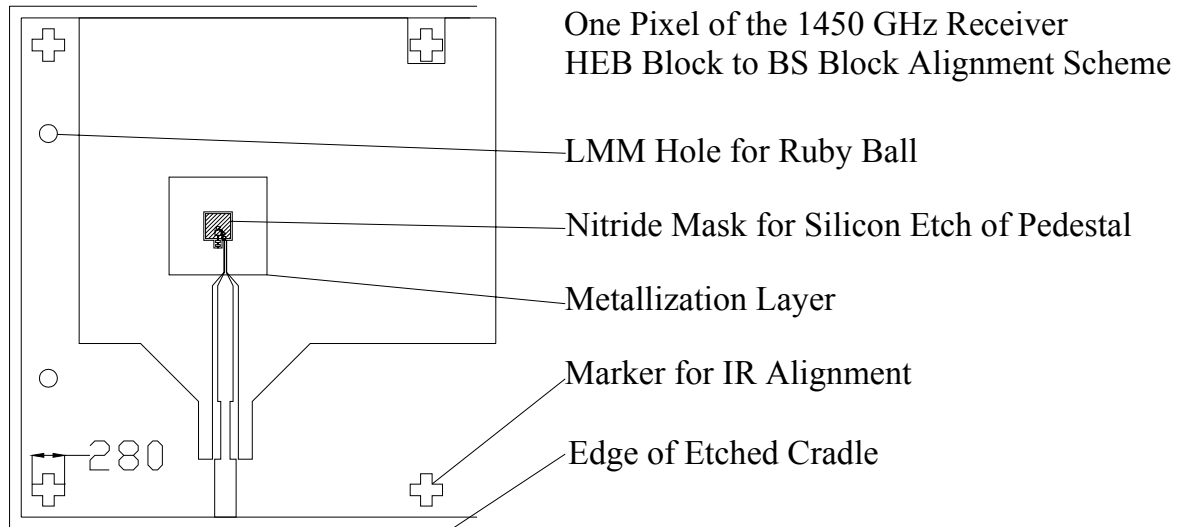


Figure 4.2. Illustration of the backshort block-HEB block alignment schemes involving the markers on the bottom side of the backshort block and the laser-micromachined holes for ruby bearings. The HEB mixer circuitry and outline of the backshort block metallization layer are also shown, along with the edges of the HEB block die and the borders of the etched cradle in the backshort block. The stated dimension of the alignment cross is 280 μm .

Alignment marks for the metallization lithography mask were not placed on the front side of the wafer, where they would have been destroyed during the etching of the cradle and pedestals, but on the bottom side of the backshort block wafer. The marks used for IR alignment of the HEB block to the backshort block are on the bottom side of the backshort block die for the same reason, and appear on the same mask. Hence the backshort block mask set includes three masks, in this order:

1. Front-side mask, defining the pyramidal backshorts, cradle edges, and alignment markers in silicon nitride.
2. Back-side mask, referred to the alignment markers on the front, defining alignment markers for the metallization mask and other markers for the IR alignment.
3. Front-side mask, referred to the new alignment markers on the back, for metallization.

The positions and size of the backshort block-HEB block alignment markers are illustrated in **Figure 4.2**.

The ruby bearings [SwissJewel] used in the second of the alignment schemes under discussion fit snugly into pits etched into the backside of the HEB block during the release of the silicon nitride membrane upon which the HEB rests. If the backshort block wafer can be aligned inside of the laser micromachining system with sufficient accuracy, then cylindrical holes etched into the backshort block which match the pits on the bottom side of the HEB block may allow for a quick and effective means of assembly. As of this writing, however, such an assembly has not been demonstrated. A picture of a ruby bearing in an etched pit is shown in **Figure 4.3**.

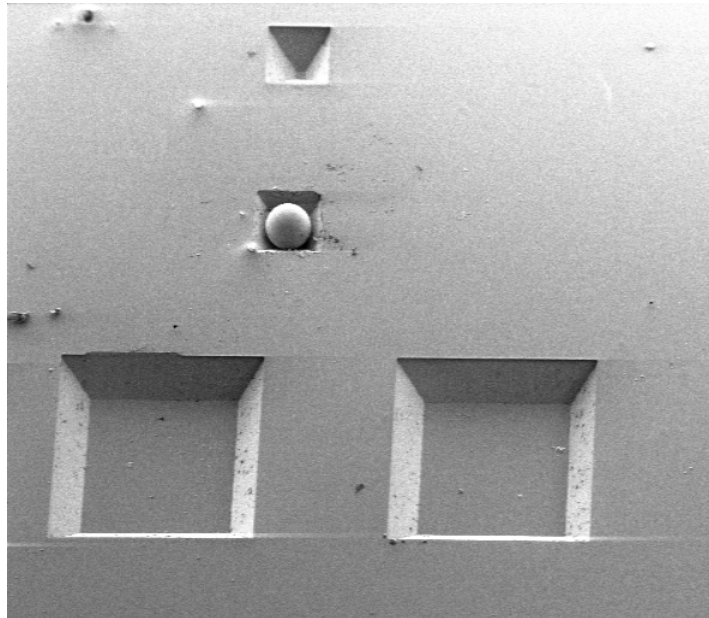
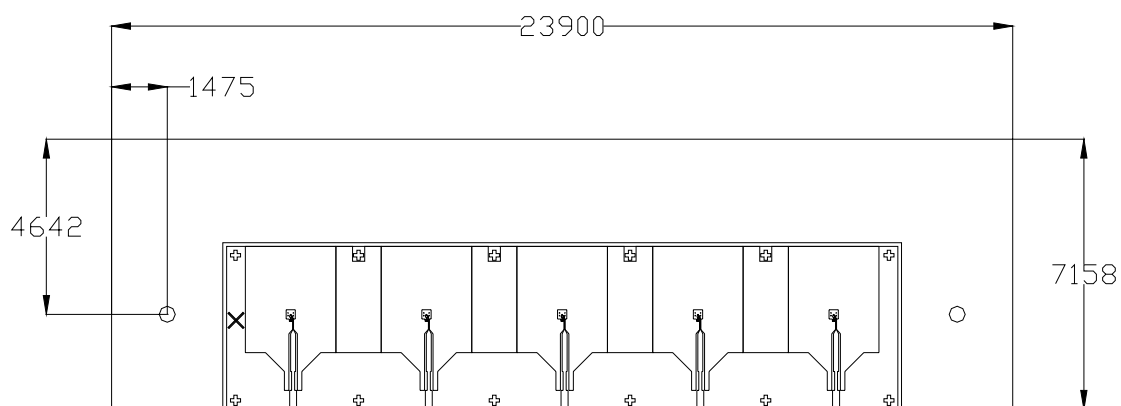


Figure 4.3. A 6 mil ruby bearing intended to serve as an alignment guide between the backshort and HEB blocks sits in a pit etched into the bottom side of the HEB block. The entire picture shows a portion of an 850 GHz 1x4 array; two released membranes are visible at the bottom of the picture.

A similar scheme utilizing a sapphire rod and two holes etched into the outer edge (i.e., the un-etched or raised edge) of the backshort cradle is intended to facilitate

mounting and alignment of the split-block feedhorns to the other components. If cylindrical grooves are etched into the feedhorn split-block dies at the same time that the feedhorns are machined, then a narrow sapphire rod can be used both as a shim to assemble the split halves of the feedhorn block, and as posts to guide the feedhorn block into its position resting on the backshort block. The positions of the mounting holes for the feedhorn block in relation to the backshort block and the HEB block are shown in

Figure 4.4.



1450 GHz Receiver Backshort Block Cradle Assembly Drawing
Indicates Positions of Holes LMM'd for Feedhorn Block
Dimensions in microns

Figure 4.4. Position of the 0.0175" holes in the backshort block die for the sapphire rods which guide the feedhorn block into place. Note that the fourth raised side of the backshort block cradle is removed by dicing, so that the CPW-to-microstrip transition on the HEB block comes right up to the edge of the assembly.

Currently, the smallest sapphire rods available seem to be 0.0175" in diameter, or about 425 μm , and this assembly has not yet been attempted. If smaller components, offering more precise alignment, become available in the future, it will be a simple matter to change the programming of the LMM system to accommodate this change.

In order to align the backshort block mask to the wafer's crystal planes, according to the advice of a colleague in the UVML [Hunt02] a long, narrow window on the edge

of the mask was designed to register to the wafer flat. This window consists of an opaque section 2 mm wide by 17 mm long, with a narrow, centered opening 30 microns wide by 15 mm long. It is quite simple to align the wafer flat roughly to the outside edge of the window, shift the visible edge of the flat into the narrow opening, and then complete the fine alignment.

3. Anisotropic Wet Etching of Silicon and Corner Compensation

The practice of bulk silicon micromachining, and the pertinent literature, is growing daily. Isotropic and anisotropic wet etchants, as well as plasma etch processes, are available. The anisotropic wet etchants, which include alkali hydroxide solutions, tetramethyl-ammonium hydroxide (TMAH), and ethylene diamine pyrochatechol (EDP), are crystal plane-selective. Solutions of potassium hydroxide (KOH), for instance, can show an etch selectivity between $\{111\}$ crystal planes and $\{100\}$ planes of 1:400. [Kovacs98] In general terms, this allows the design of etched structures bounded by $\{111\}$ planes, which are relatively invulnerable to the etchant. On a $\langle 100 \rangle$ silicon wafer, these $\{111\}$ crystal planes are oriented at an angle of 54.74° to the surface of the substrate.

The choice of etchant depends upon such considerations as process compatibility (KOH, for instance, is not CMOS-compatible, due to the presence of alkali ions), desired etch rate and surface roughness, etch stop characteristics, safety (EDP is a notably dangerous compound), available mask layers (silicon nitride and silicon dioxide being the most common), and others. For this work, using LPCVD silicon nitride as a mask layer, both TMAH and KOH etching solutions were examined. Ultimately, a solution of KOH

and isopropyl alcohol (IPA) was settled upon, as the surface roughness obtained with TMAH solutions was unacceptably poor.

With the information outlined above, etching away an enclosed area bounded by $\{111\}$ crystal planes is a relatively straightforward exercise. (In the terminology of this field, such a structure has four “concave” corners.) The pyramidal backshort stubs, however, possess four “convex” corners, and the manufacture of such protected features within large areas open to etching is not as simple as etching bounded areas. This is because, as the etch progresses, crystal planes other than the typical $\{100\}$, $\{110\}$, and $\{111\}$ planes are exposed at the convex corners of the structure (so-called “exotic” crystal planes, such as the $\{211\}$ and $\{212\}$ planes [Puers90]). These exotic crystal planes etch at rates comparable to the $\{100\}$ and $\{110\}$ etch rates, undercutting the intended structure. An illustration of this undercutting may be seen in **Figure 4.5**.

The method of accounting for this unwanted effect so that the desired structure may be obtained is known as corner compensation. Practical compensation schemes ([Wu89], [Puers90]) and parametrized algorithms for their generation [Long99] may be found in the literature, and even software which simulates the bulk etching of silicon [ACES] is available. Such information drawn from outside sources is difficult to use, however, because the solutions presented are only perfectly applicable to the process parameters, etchants, and geometries for which they were developed. Therefore, it was necessary to develop some practical expertise within the UVML in order to devise and implement a compensation scheme with good confidence in its success.

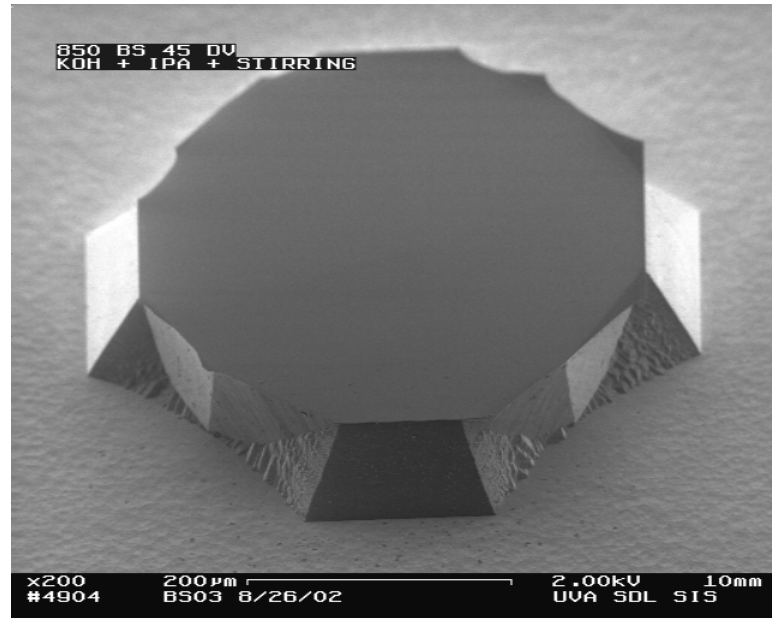


Figure 4.5. An 850 GHz backshort pyramidal stub etched under an LPCVD silicon nitride mask without a corner compensation scheme. The right-angled corners of the square original mask (at the $45^\circ + n90^\circ$ positions) broke away as the mask was undercut at those points. The etchant used was a mixture of KOH and IPA at 80°C .

In order to compensate for undesired etching, a corner compensation scheme adds sacrificial material to the desired right-angled corner. This extra silicon is consumed during the course of the etch, and ideally should vanish at the same moment that the desired etch depth is accomplished. The simplest compensation schemes add a triangular, rectangular, or square tab to a convex corner, although more complicated structures are not uncommon [Huang98]. Puers and Sanson [Puers90], for instance, describe a compensation scheme using a triangle with sides defined by the $\langle 120 \rangle$ directions, as well as shortened “flat triangle” and rectangular schemes based upon that triangle. The latter two schemes are desirable for cases where there is not enough space to accommodate the longer triangle. Puers and Sanson then demonstrated these compensation schemes with a mask set containing 72 different edge patterns.

Because of the flexibility offered by laser micromachining, for the pyramidal backshort stub application it was apparent that a compensation scheme which failed to produce a perfect corner (i.e., an unrounded corner, yet one without any unetched sacrificial material) but which was as simple and straightforward as possible would be entirely acceptable. In this context, a compensation scheme which could be produced and tested without the need to manufacture a test mask, perform sample etches, and interpret those tests, would be ideal. Such a compensation scheme was suggested and developed by Jon Schultz of the UVML under the author's direction [Schultz04].

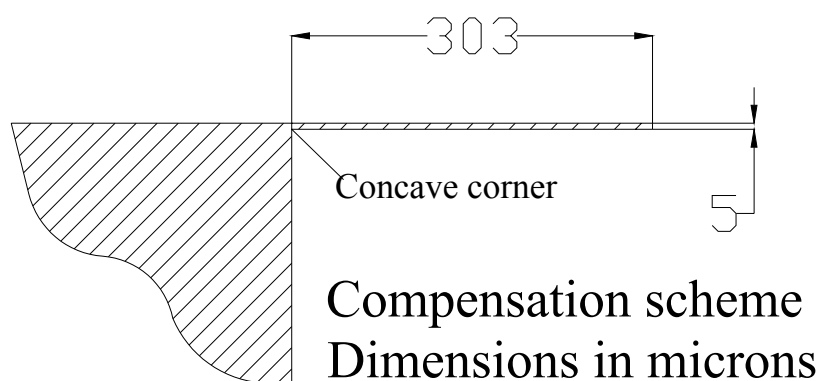


Figure 4.6. Diagram of the corner compensation scheme used for the pyramidal backshort stubs. Essentially the compensation bar replaces the desired right-angled convex corner with a concave corner on the one side and a preferred (111) plane on the other. The sacrificial bar is etched away from its end toward the desired corner.

The compensation structure shown in **Figure 4.6** can be fabricated using double exposure of the straight edges of features on existing masks. For the purposes of incorporating compensation structures into a mask design, it is of interest to know the ratio of the length of the compensation bar which is etched away (L) to the etch depth (ED). These structures, etched in the appropriate 4:1 solution of KOH 45%:IPA at 80° C, yield a value for that ratio of $L/ED = 2.15$. The vertical etch rate under these conditions is 0.69 $\mu\text{m}/\text{min}$.

For the intended etch depth of 127 μm , the measured ratio of L/ED calls for the compensation bar to be 273 μm long. The three variations chosen for the mask design, however, are 303, 323, and 348 μm long. Aside from the possibility of trimming the finished pyramidal stubs using LMM, another reason for this decision can be seen clearly in **Figure 4.1**. The hole in the HEB block beneath the membrane is significantly wider than the pyramidal stub - for the 1450 GHz receiver, a minimum of 30 μm wider. Therefore the design trade-offs in this case all weigh on the side of choosing the compensation structures to be longer than the minimum necessary.

The end of the compensation bar possesses two convex corners, which must etch inward in the manner of the uncompensated corners of **Figure 4.5** before the etch front begins to move along the length of the structure. Although this analysis suggests that the width of the bar merits consideration, in this case there is sufficient flexibility in the overall design that this width was specified somewhat arbitrarily. The 348 μm and 323 μm structures were designed with 5 μm widths, while the third variation on the mask was chosen to be 303 μm long by 10 μm wide. These widths were chosen because thinner structures of these lengths might pull up from the substrate after development of the photoresist pattern.

4. Fabrication of the Backshort Block

Process sheets for the backshort block fabrication can be found in **Appendix B**. In brief, however, the fabrication procedure is summarized in **Table 4.2**.

1. RCA Clean	5. Backside Markers	9. Metallization
2. Silicon Etch Litho.	6. Silicon Etch	10. Dicing
3. Si ₃ N ₄ Etch	7. Si ₃ N ₄ Removal	
4. Photoresist Removal	8. Laser μ Machining	

Table 4.2. Outline of the backshort block fabrication process

Since, as of this writing, laser micromachining of finished pyramidal stubs has not yet been attempted, a completed backshort block die with backside alignment markers and metallized backshorts has not yet been demonstrated. There are additionally some process incompatibility issues involving the metallic backside features and the silicon and silicon nitride wet etchants, which have not been fully addressed. It will be shown in the section on HEB block fabrication, however, that the HEB and backshort blocks can be aligned even if metal features on the bottom side of the backshort block cannot be preserved.

Following the published recipes of Li, French, and Wolffenbittel [Li95], a procedure for etching silicon nitride under AZ5214E-IR photoresist on UVML equipment using a plasma of CHF₃ and N₂ was successfully developed. Although the etched layer of silicon nitride is quite thick (as much as one micron), and the etch is correspondingly rather long (nearly one hour), the photoresist holds up well under these conditions. The process, unfortunately, is somewhat dirty, and it requires several hours in an oxygen plasma etcher to remove the photoresist after the silicon nitride etch is complete.

The lithography for the backside alignment markers has been demonstrated successfully using the EVG mask aligner in the UVML clean room. This allowed fabrication of these markers by a process of niobium deposition, AZ5214E-IR lithography, and RIE with a plasma of SF₆ + CHF₃ + N₂, followed by a photoresist strip. Potassium hydroxide at 80° C, however, etches niobium reasonably well, so that these

backside features will unfortunately be removed during the bulk silicon etch of the backshort block pedestals. This process incompatibly issue, and the possibilities for resolving it, are discussed in **Appendix C**.

Accuracy (i.e., achieving the target 127 μm etch depth) and uniformity are the principal concerns which the procedure devised to bulk micromachine the pyramidal backshort stubs must address. To avoid over-etching, it is necessary to remove the backshort block wafer from the etching pot several times in order to monitor the progress of the etch. This discourages the use of the frontside wafer protection jig designed for the HEB block membrane etch, since the large thermal mass of the jig causes the temperature of the etch bath, and therefore the etch rate, to vary by large amounts. Correspondingly, the best approach is simply to place the bare wafer on a pedestal in the etching solution. Ignoring the fate of the metal features on the bottom side of the wafer, this process gives excellent (quite uniform and accurate) results.

Removal of the silicon nitride masking layer from the front side of the backshort block wafer after the silicon etch is complete is necessary in order to perform laser micromachining. Either a wet etch using phosphoric acid at 180° C or RIE are acceptable for this task, although the phosphoric acid etch is somewhat preferable, as it is cleaner and totally selective to silicon (which the RIE etch is not). Unfortunately, this wet etchant is not compatible with the fabrication process which has been set forth. This is an additional topic of **Appendix C**.

Initial research involving silicon etching for this work used TMAH etch solutions and commercially available, 3000 Å, PECVD silicon nitride. TMAH was chosen at this stage because it is reported [**Kovacs98**] to treat Si_3N_4 layers more gently than KOH does;

the PECVD material, however, was full of pinholes no matter what etchant was chosen. Thereafter, although it was more difficult to obtain, only thicker, LPCVD, material was used. Low-stress LPCVD silicon nitride served robustly as a mask for silicon etching using both KOH and TMAH solutions.

Switching from a TMAH + IPA solution to a KOH + IPA solution reduced the surface roughness, measured approximately using a Tencor profilometer, from at least 8 μm to less than 0.1 μm . With an LPCVD silicon nitride mask layer which is robust to both etchants and with no concern about CMOS compatibility, therefore, better crystal plane selectivity and lower surface roughness both argue for the use of KOH over TMAH. The etchant settled on for this purpose was a solution of 45% KOH:IPA in a proportion of 4:1 by volume, heated to 80° C.

5. Results

The fabrication procedure described in the previous section and in **Table 4.2** does not allow for the survival of niobium alignment markers on the bottom side of the backshort block wafer, as described in **Appendix C**. The HEB block and backshort block can be aligned successfully without these marks, however, and the appendix suggests several alternate approaches which could be used to remedy this deficiency. All of these approaches have been demonstrated during the course of this research in other contexts.

The first wafer attempted with the compensation structures described herein was BS07. After 184 minutes of etching - sufficient to reach the target depth of 127 μm at the measured rate of 0.69 $\mu\text{m}/\text{min}$. - BS07 was removed from the etching pot, rinsed, and

measured using profilometry. The actual etch depth was approximately 124 μm , so the wafer was placed back into the etch bath for five additional minutes, removed, rinsed, and measured again. Measured at nine different points on the wafer, the etch depth was $127.1 \pm 0.3 \mu\text{m}$. A finished pyramidal stub is shown in **Figure 4.7**. Several other backshort block wafers were manufactured, with similar results.

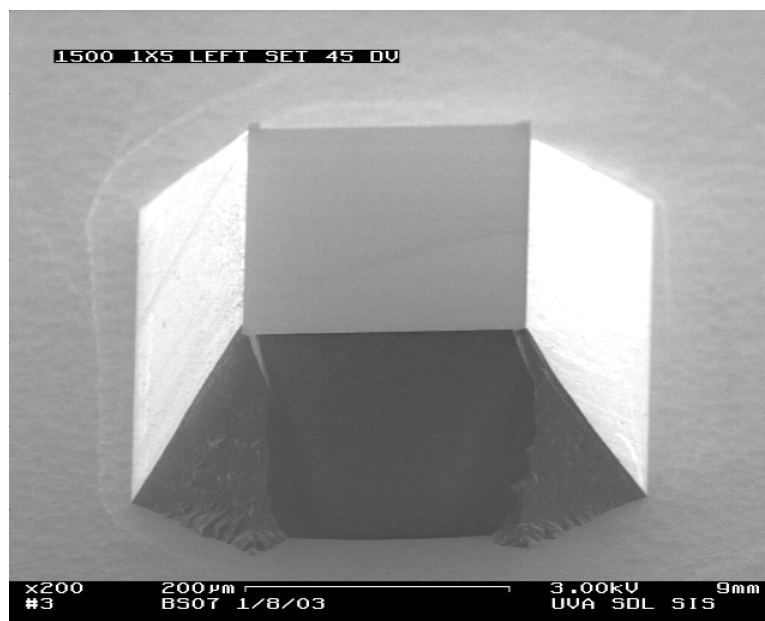


Figure 4.7. A 1450 GHz backshort pyramidal stub etched under an LPCVD silicon nitride mask using the corner compensation scheme outlined earlier. The orientation of the structure in this picture is the same as that of the undercut structure pictured in **Figure 4.5**. Although this scheme did not produce perfect corners, the flexibility offered by laser micromachining means that the result suffices for this application.

6. Conclusion

All of the eight concerns listed at the outset of this chapter were addressed by the mask design and fabrication procedure which were developed. Strategies for alignment of the backshort, HEB, and feedhorn blocks to each other were devised and incorporated into the mask designs and process flow, although some incompatibility issues, discussed in **Appendix C**, still remain somewhat unresolved. A simple compensation structure was

developed, tested, and - due to the flexibility offered by LMM and the wide mechanical tolerance - found to work very adequately. Finally, finished backshort block pyramidal stubs were found to be both accurate and uniform to a tolerance well within the design specifications. As of this writing, finished backshort block dies await laser micromachining of PCJs and backshort cavities at the University of Arizona.

CHAPTER 5 - DESIGN AND FABRICATION OF THE HEB BLOCK

1. Overview

The HEB block is fabricated from a <100> silicon wafer only 127 μm (5 mils) thick, covered on both sides by LPCVD Si_3N_4 0.75 μm thick. The microwave mixer circuitry is defined from films of niobium and gold deposited under a single vacuum on to a liftoff stencil; the actual hot-electron bolometer mixing elements are sculpted at a later time, one at a time, using a focused-ion beam. After fabrication of the circuitry on the front side of the wafer, backside alignment, lithography, and RIE are used to pattern the silicon nitride layer on the bottom side of the wafer. This layer masks the bulk silicon etch which subsequently releases the (front side) silicon nitride membrane supporting the mixer circuitry.

This section deals only with how the component designs which were provided were physically realized, and not with the characteristics or electrical performance of the devices which were fabricated. Although the design of the backshort block addressed many of the broadest issues, such as those involving alignment and assembly, there were still several interesting issues confronted during the design of the HEB block mask sets. These included concerns about wafer thickness variation, creating mirror-image masks for backside alignment, the patterning of very fine features, and protecting circuit features on the front side of an HEB block wafer during membrane-release silicon etching.

2. Design of the HEB Block Masks

Since the backshort block wafer lies at the bottom of a stack of components, and is the foundation upon which those components rest, its thickness and thickness

uniformity (TTV, i.e., total thickness variation) are not truly critical. Because the air gap between the backshort block PCJ pillars and the HEB block membrane is only 3 μm in the 1450 GHz design, however (see **Table 4.1**), and this dimension must be held across 5 pixels over a distance on the wafer exceeding 14 mm, this clearly cannot be said of the HEB block. In this case, both the thickness and TTV must be controlled as tightly as possible. Although it added greatly to the expense involved, for this work wafers with a thickness of $127 \pm 1 \mu\text{m}$, with a TTV $< 1 \mu\text{m}$, were specified.

Two of the three methods for aligning the backshort block die to the HEB block die - micromachined pits for ruby bearings, and IR alignment markers - were discussed earlier. The third alignment feature, incorporated into the HEB block mask, is illustrated in **Figure 5.1**. This is a set of four small markers which are intended to line up with the edges of the backshort cavity in the pyramidal stub underneath the membrane. At the least, this should allow for the quality of the alignment between the backshort and HEB blocks to be easily evaluated. It should also be possible to use these features to actually perform the alignment, in the event that a particular backshort block die lacks bottom side IR alignment markers.

An important issue for the mask designer is easy to illustrate at this point and deserves brief mention. Obviously the windows opened in the silicon nitride mask on the back side of the wafer are intended to line up with the appropriate membrane windows on the front side of the wafer. The mask designer accomplishes this by creating both front- and back-side masks as separate, overlapping, layers in the same AutoCad drawing. Since the wafer is flipped over when the backside lithography is performed, however, the backside mask should be registered not to the front-side mask, but to its mirror image.

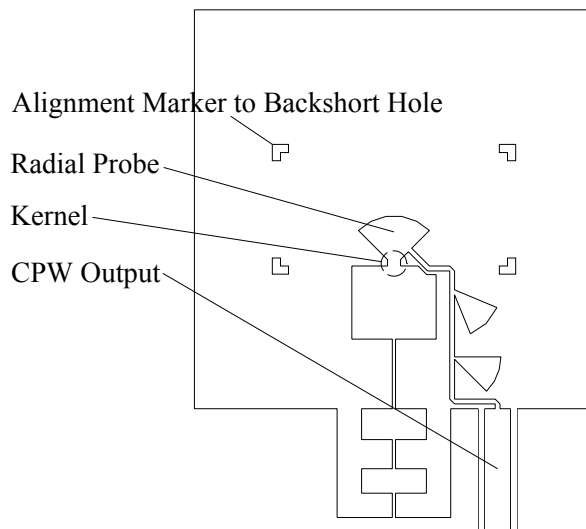


Figure 5.1. A close-up view of the mixer circuitry. The four alignment markers shown bracket the backshort cavity in the top surface of the backshort block pyramidal stub, which should be visible using a microscope to look through the membrane. The kernel (or probe throat) is an area from which the very fine features of the probe transition and the HEB will be sculpted, using the focused-ion beam.

In practice, this detail is handled by composing the masks in the manner described, and then mirror reflecting any backside layers once the designs are completed. Like the backshort block, the HEB block wafer must be aligned to the crystal planes, and the same long, rectangular feature at the right edge of the mask is used for this purpose. Reflecting the backside mask for the membrane windows across the line $y = 0$ moves this feature to the left side, which is a clear indication of the process to be followed. For backside alignment, it matters whether the wafer is turned over left to right or top to bottom.

The smallest feature shown in **Figure 5.1**, the tap into the radial probe, is a line 3 μm wide. Using the EVG aligner and a thin photoresist, AZ5206E, it is possible to fabricate this feature reliably by liftoff. The mixer design provided [Kooi02b], however, included even finer features at the probe throat, as shown in **Figure 5.2**. Given the approximately 3400 \AA thickness of the Nb/Au/Nb layer to be lifted off, these features

could not easily be created by deposition and liftoff, and it seemed best to consider fabricating the probe transition by FIB.

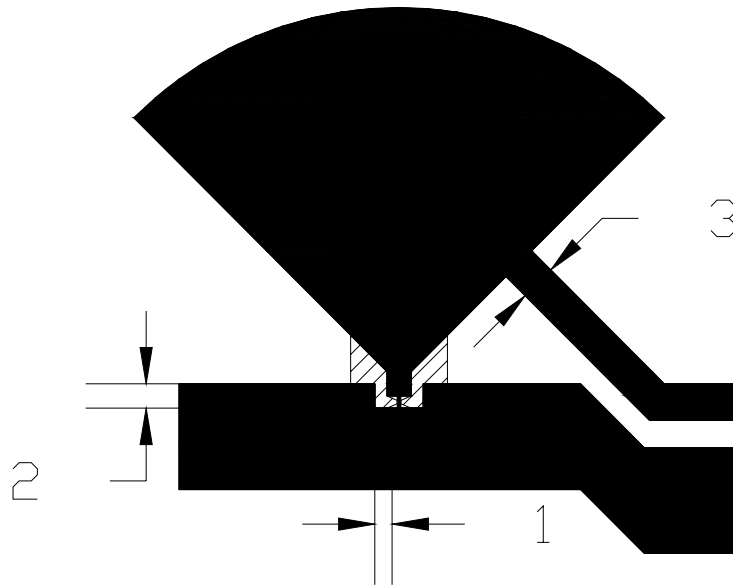


Figure 5.2. The radial probe, kernel, and output line tap design of a 1450 GHz pixel. The probe transition, which includes critical features as small as $1\ \mu\text{m}$, is sculpted using the focused-ion beam to mill away shaded portions of the kernel. Fabrication of this delicate feature is the first step of the focused-ion beam HEB fabrication process. The HEB itself is located at the throat of the probe. (Dimensions in microns.)

Manufacturing the probe transition by FIB does not add any additional steps to the HEB fabrication process, as the narrow dimensions of the device require that it be milled out of a larger “kernel” of material, no matter the specifics of a given electromagnetic design. Despite this flexibility, some consideration is still required, as choices regarding the size of the sacrificial kernel, how the pattern to be milled is to be registered to the features on the wafer, and whether other features (such as the tap into the probe) might beneficially be fabricated at the same time, must all be correct.

The kernel was chosen in this case to be $8\ \mu\text{m}$ across by $4\ \mu\text{m}$ tall. A larger pattern might in theory have made machine alignment of the stream file pattern to the wafer features slightly more accurate. Such a file, however, might not have been smaller

than the 250,000 pixel maximum which the FIB control software can accommodate. In practice, the shaded pattern shown in **Figure 5.2** aligns quite easily to the edges of the kernel and to the tapered sides of the radial probe. FIB fabrication of the probe transition was effective and successfully demonstrated, as may be seen in **Figure 5.3**.

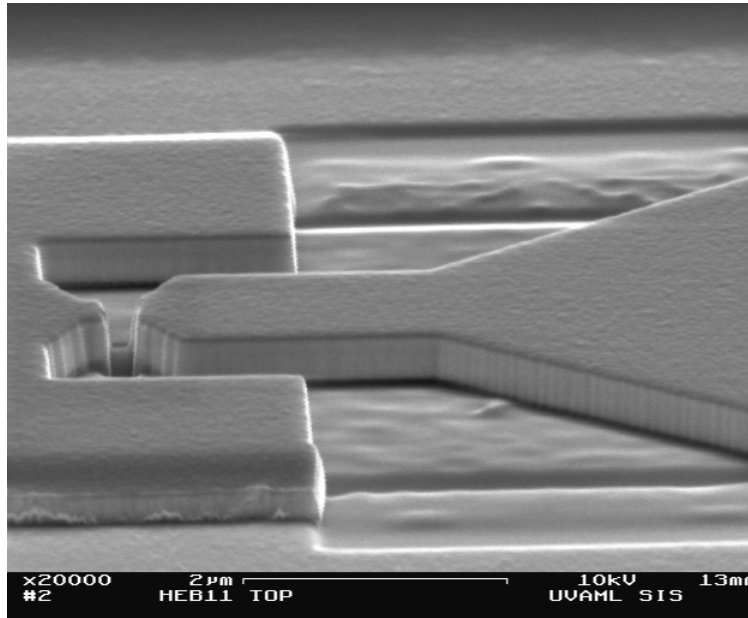


Figure 5.3. A probe transition sculpted by focused-ion beam. The probe extends out of this picture to the right, while the finished HEB sits nearly at the left edge.

The HEB block mask set includes three masks: the HEB Block, HEB Block Membrane Etch, and Passivation masks.

3. Silicon Etching to Release the Si_3N_4 Membranes

Because a great deal of information about the bulk micromachining of silicon has already been presented in earlier sections, this section focuses on only one issue: how the metal features on the front of the HEB block wafer are protected during the membrane etch. Hot KOH attacks and etches away the thin layer of microbridge niobium, which also serves as an adhesion layer for the 3000 Å of gold above it, if the front side of the

wafer is exposed. When this occurs, the HEB block wafer is ruined. Two methods of protecting the front side of the wafer were investigated - a stainless steel jig, which holds a 2" wafer and seals its top and bottom faces with O-rings, and meniscus etching.

[Schultz00] The wafer protection jig is shown in **Figure 5.4**.

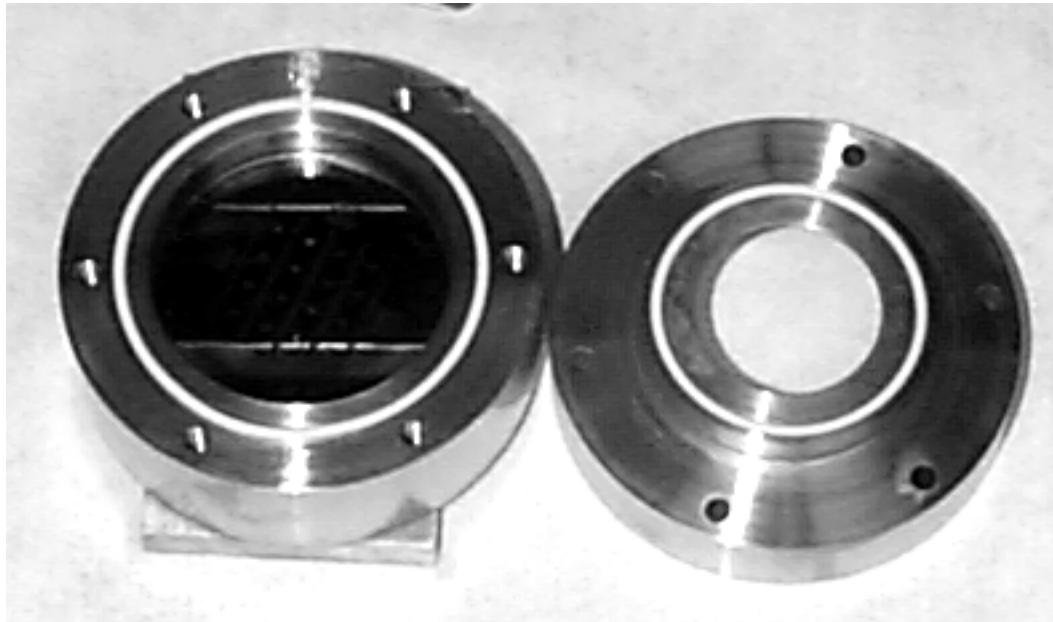


Figure 5.4. The frontside wafer protection jig for use during the membrane etch. O-rings seal the top (hidden beneath the wafer sitting in the jig, left) and bottom (shown on the right, in its position in the jig cap) surfaces of the wafer, with a third O-ring to seal between the two halves of the jig. The trade name of the O-ring material is Chemraz. [Greene-Tweed]

One obvious consequence of attempting to use a jig such as the one shown in **Figure 5.4** is that it becomes impossible to expose the entire wafer surface to the etchant. This restricts the placement of HEB block dies on the wafer surface, which is an issue that the mask designer must bear in mind. For this application, the largest suitable O-ring had an inner diameter of about 1.77". The hole in the jig cap is still less than that (1.25"), which prevented the HEB block mask design from including more than two 1x5 1450 GHz arrays. The wafer protection jig was not found to be suitable for the membrane etch in this case, but the mask design was conducted with these restrictions in mind.

The design of the wafer protection jig was fairly straightforward, except that it was not clear how much O-ring compression was necessary (to form a good seal) or desirable (to avoid breaking the wafer). With O-rings 70 mils (0.070") thick, compressions of 10-15 mils for the two O-rings touching the wafer, and of 25 mils for the O-ring sealing the two halves of the jig, were appropriate.

The wafer protection jig worked very well protecting the front side of a 10 mil silicon wafer (which was the original specification for the HEB block) during the membrane etch. It was only rarely successful, however, with 5 mil (127 μm thick, the current specification) wafers. Despite several modifications to the jig, nearly all of these wafers broke in the jig during the membrane etch, normally not until after two hours or more of etching had passed. That the wafers broke, not when the jig was tightened, but after an array of small holes in the wafer had been etched nearly through, indicates that the stress applied to the wafers by the jig broke them. Since the 127 μm silicon wafers were found to be quite fragile even under more gentle circumstances, another method of performing the membrane etch was developed.

Meniscus etching involves suspending the wafer above an open jar of heated etchant. Instead of submerging the wafer in the solution, in this case the level of the solution is raised up nearly to the bottom of the wafer by adding solution to the jar carefully with a dropper. Surface tension suffices for the last few millimeters, as the solution rises above its level, coats the bottom side of the wafer, and remains there. A picture of the meniscus etching jig used in this work is shown in **Figure 5.5**.



Figure 5.5. The meniscus etching jig. The wafer is held to the jig frame with a pair of clips made from shim stock. A Chemraz O-ring helps to prevent the etchant from splashing on to the front of the wafer. A temperature probe, which enters the solution at the rear of the photo, is connected to the hot plate controller.

In this case, meniscus etching is clearly preferable to the frontside wafer protection jig, as not one wafer of around ten which were etched in this way broke. However, if both possibilities could be pursued, then meniscus etching does suffer from some drawbacks by comparison. Briefly, among these drawbacks are: 1. the need to monitor the etch, periodically adding etchant (due to evaporation), 2. the inability to reflux evaporated etchant (changing the concentration of the etchant over time), 3. that the etchant cannot be stirred, 4. how easy it is for hot etchant to creep on to the front side of the wafer, which one wishes to protect, and finally 5. the tendency of the meniscus to cover one portion of the wafer surface but not another, due to the wafer being other than perfectly level. (This causes the etch rate across the wafer to appear to be highly non-uniform.) A picture of a membrane etched with this jig is shown in **Figure 5.6**.

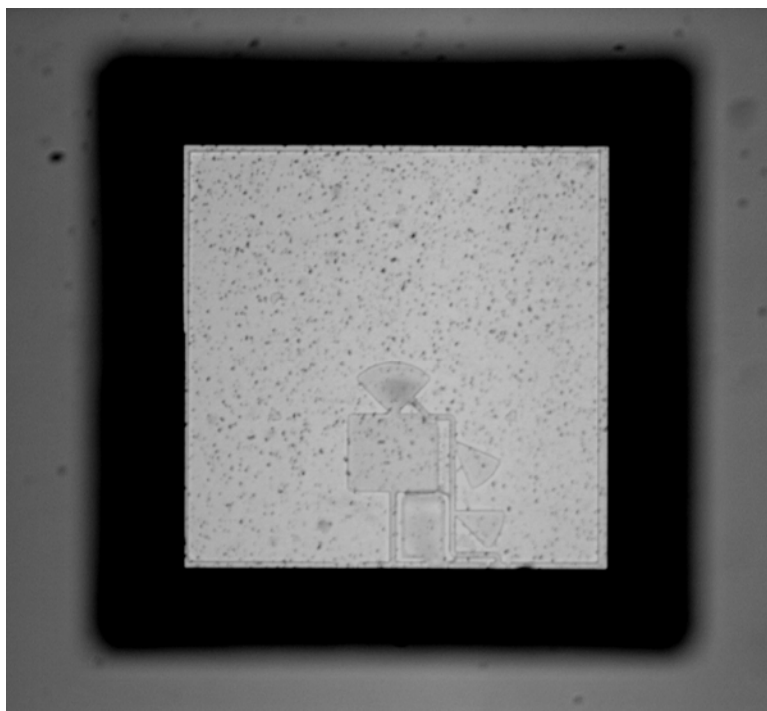


Figure 5.6. A photo of an 850 GHz mixer looking from the back side of the HEB block wafer through the membrane.

4. Fabrication of the HEB Block

Process sheets for the HEB block fabrication can be found in **Appendix B**. In brief, however, the fabrication procedure is summarized in **Table 5.1**.

- | | | |
|--|------------------------|------------------------|
| 1. RCA Clean | 6. Membrane Etch | 11. Germanium Depo. |
| 2. Liftoff Stencil Fab. | 7. Dicing | 12. Passivation Litho. |
| 3. Depo. & Liftoff | 8. Imaging Au Depo. | 13. Ge/Nb RIE Etch |
| 4. Membrane Etch Litho. | 9. FIB1-3 | 14. Packaging |
| 5. Si ₃ N ₄ Etch | 10. Bridge Etch & Msr. | |

Table 5.1. Outline of the HEB block fabrication process.

Niobium diffusion-cooled HEB microbridges are extremely sensitive to electrostatic discharge. Furthermore, even when ESD damage is avoided, the electrical characteristics of these devices often degrade over time due to oxidation resulting from exposure to the atmosphere. Because very little data regarding these issues is available in

the published literature, the development of appropriate methods of device passivation and of ESD control were important milestones during the research described in this dissertation.

The fabrication protocol described in **Table 5.1** has been demonstrated successfully. The steps are ordered as they are principally to minimize the possibility of harm caused to the finished HEBs by electrostatic discharge, but concerns about the fragile nature of the HEBs, the membranes, and the thin silicon wafers were also considered. While information about the actual HEB fabrication (steps 2, 3, 9, and 10) can be found in **Chapter 6**, some discussion of the manufacture of the HEB block dies follows.

The membrane etch lithography and silicon nitride etch are performed using the EVG aligner, AZ5214E-IR photoresist, and RIE in a plasma of CHF_3 and N_2 , with processes identical to those used for the backshort block already described. The accuracy of the backside alignment may be judged in **Figure 5.6**, where the edges of the membrane window on the front side of the wafer are seen to extend a few microns into the opening as viewed from the bottom side of the wafer. The top- and bottom-side windows are clearly aligned very well, even if the etched window is around $10\ \mu\text{m}$ too wide (probably the result of a non-zero $\{111\}$ etch rate and a large over-etch).

The membrane etch is performed using meniscus etching, as described, with the same solution of 4:1 KOH 45%:IPA at $80^\circ\ \text{C}$ which is used to etch the pyramidal backshort stubs. Compared to the immersive process used to etch the backshort block wafer, the meniscus etch proceeds at a slower average rate and requires some amount of over-etching in order to entirely clear the bottom surfaces of the membranes. This is

certainly due to evaporation, lack of agitation, and the need to continually replenish the etchant during the etch.

Unprotected membranes supporting 850 GHz mixers are generally destroyed by the jet of cooling water aimed at the dicing saw blade. Spinning liquid black wax on to the bottom side of the wafer prior to mounting and dicing solves this problem by providing the membranes mechanical support. While dicing cannot precede the membrane etch, the decision to fabricate the HEBs (steps 9-10) only after the membrane etch and after dicing was a deliberate choice intended to minimize the handling of completed devices.

Because of this choice, steps 8-13 are all performed, not on entire 2" wafers, but instead on individual dies which are rather small (4 mm square for the test samples, 18 mm by 4 mm for the 1450 GHz array), or sets of dies. After focused-ion beam processing (step 9), the array and test pad dies are held down to a clean glass slide carrier with tiny dabs of vacuum grease, and all of the subsequent steps are performed using that same carrier. Therefore, the dies containing finished HEBs are essentially never handled until after they are passivated, when they are removed from the carrier and packaged in conductive boxes designed to control ESD. Placing the dicing step in the middle of the fabrication process unfortunately makes it impossible to use the passivation lithography mask, which is discussed below, and limits the number of samples which may be conveniently fabricated, but it minimizes the risk of ESD damage to completed devices.

Among the materials examined as passivation layers during this work were thermally evaporated SiO, sputtered SiO₂, and sputtered germanium. Since the topography of the finished HEB device places the microbridge at a saddle point, although

the device is small, it is quite difficult to passivate. Even rather thick (1000 Å or more) layers of SiO often failed to cover the microbridges adequately. The more conformal coverage offered by sputtered films, however, seemed to work well for this application, although surprisingly large thicknesses were still required (1000 Å of Ge was used). The passivation layer is typically deposited immediately after the bridge etch, so that it covers not only the HEB device but also the 300 Å thick niobium mask layer which covers the waveguide probe and IF circuitry.

The principal basis for the choice of Ge over SiO₂ as a passivation material was that germanium is a semiconductor, while quartz is an insulator. It is likely that a semiconducting material at room temperature offers protection from ESD that an insulating material does not. The performance of the two materials at the operating temperature of 4.2 Kelvins, where any carriers which do exist in the semiconductor are frozen out, will be identically insulating. In practice, HEB microbridges passivated with germanium are rather robust and stable over long time periods (months).

The germanium films used as passivation layers in this work had two interesting characteristics. First, their adhesive qualities were quite poor, which prevented liftoff patterning of the passivation layer. The germanium layer was also quite difficult to pattern conventionally, as photoresist adhered to the passivation layer only very poorly. This was true of both 4000- and 5000-series AZ photoresists. An alternate process using an intermediate non-imaging organic layer, which adhered well to the germanium and is itself patterned by photoresist developer, solved this problem [Schultz03]. This extra organic layer (of “LOR”, or “Lift-Off Resist”) unfortunately requires a high-temperature bake (nominally 160° C).

The hard bake required for LOR processing caused an additional complication, which is detailed in **Table 5.2**. While it is clear from the table that passivated HEBs can be stable (i.e., not change in resistance) over long spans of time, the resistances of these same devices decreased dramatically when baked on a hot plate at a high temperature. Unpassivated devices subjected to this treatment either increase in resistance or show no change as a result.

Sample #	R(Ω), 1/14/04	R(Ω), 2/19/04	R(Ω) after 160° C bake
2	83	same	58
3	77	same	39
6	72	same	42
7	81	same	19

Table 5.2. Behavior of HEB microbridges passivated with germanium. These test samples from M2621C bottom (on a quartz substrate), were passivated with 1000 Å of germanium and were stable, showing no change in resistance after more than one month. A hot plate bake at 160° C for 5 minutes caused the resistances of these devices to decrease significantly.

The HEBs described in this work show a tendency to degrade toward open circuit over time if exposed to atmosphere, but are generally stable when passivated with germanium. This suggests that the passivation layer successfully shields the niobium microbridge from exposure to oxygen. If this is the case, however, then the decrease in resistance after the hot plate bake at 160° C shown in **Table 5.2** most likely represents the result of an interaction between the niobium microbridge and the passivation layer of germanium above it. This reaction takes place at a surprisingly low temperature.

There is strong support for this interpretation. Using films sputtered on to methyl cellulose substrates which were subsequently dissolved, T. Satow [Satow73] used

electron diffraction to show that 1000 Å films of amorphous sputtered germanium exhibit crystalline structure after annealing at only 167° C. According to the same article, the crystallization temperature of amorphous germanium is about 300° C.

The surface of an extremely thin niobium film is unfortunately an excellent substrate upon which to encourage the crystallization of amorphous germanium, since there exists a profusion of dangling bonds, and because the two elements are chemically compatible (Nb_3Ge is a well-known superconductor, with a transition temperature of 23 Kelvins). Although the reaction under discussion is undesired, it does confirm that there is intimate contact between the niobium microbridge and the passivating layer of germanium on top of it.

It turns out that a reasonably good passivation lithography is still possible if the LOR hard bake is reduced to 130° C, at which temperature no interaction between niobium and germanium appears to occur. Therefore, a suitable, stable passivation material for this work was identified, and the means to pattern it developed, so that no further investigation into the nature of the Nb-Ge interaction was undertaken.

The decision to dice the HEB block wafer before FIB fabrication, detailed in **Table 5.1**, leaves one detail involving this discussion of the passivation lithography unresolved. The passivation lithography mask designed in the course of this research was intended for use in a process flow where dicing was among the final steps, after the HEB devices were complete. Therefore the alignment markers for the passivation lithography sit in blank areas of the wafer, and not on individual HEB block dies (which measure 4.53 x 4.54 mm for the 850 GHz design, and 17.80 x 4.32 mm for the 1450 GHz design).

This means that the passivation mask cannot be used for the process flow which has been described.

A new mask set, which included a passivation mask with burnoff rectangles of the proper sizes, and an HEB mask with HEB block dies incorporating the proper alignment markers, would most likely resolve this issue. In the interim, spot exposure with an optical microscope works reasonably well, although it leaves a much larger patch of passivating material than originally planned (a circle of roughly 100 μm diameter, covering the semicircular probe). This has very little effect upon the performance of the mixer, according to electromagnetic simulations, but is not ideal. An alternative solution might be to use the FIB to deposit a small patch of SiO on top of the germanium layer to serve as the passivation lithography mask. Although simple in concept, this idea has not been tested. Some more discussion of this proposal may be found in **Appendix C**.

After the passivation lithography, unmasked germanium is removed from the entire wafer surface with a reactive ion etch. The $\text{SF}_6 + \text{CHF}_3 + \text{N}_2$ chemistry which is used for niobium also works very well for germanium, with the added benefit that it also removes the unwanted 30 nm layer of niobium underneath the germanium. This layer is no longer necessary after the RIE bridge etch (step 10), and must be removed so that the IF lines can be wire bonded. After this brief RIE etch, the glass slide carrier is heated at 130° C for a few minutes, which softens up the vacuum grease and allows the HEB block dies and test samples to be dismounted, cleaned, and packaged.

5. Conclusion

1x5 receiver arrays with completed, passivated HEB devices have been successfully fabricated, and await testing at the University of Arizona. Several developments discussed in this chapter contributed to that accomplishment. Among these, arranging the steps in the HEB block fabrication process in order to minimize the potential for ESD damage was of principal importance. The development of a passivation scheme using sputtered germanium films was also very significant. The use of this material for niobium HEB passivation has not been reported elsewhere, and may be responsible for the high yield of this fabrication process and for the robustness of the devices which result (discussed in **Chapter 7**).

Because the wafer protection jig designed for the membrane etch broke the 5 mil silicon wafers used for HEB block fabrication, the application of a meniscus etching technique was a vital process improvement. Finally, the use of the FIB to pattern fine features was suggested, demonstrated, and integrated into the FIB1-3 fabrication process, discussed in depth in **Section 6.2**. The results of the fabrication procedure described there and in this chapter are presented in depth in **Chapter 7**.

CHAPTER 6 - HOT-ELECTRON BOLOMETER FABRICATION

1. Introduction

A diffusion-cooled hot-electron bolometer (HEB) consists of a short bridge of a thin superconducting film in intimate contact with pads of normal metal at each end, as shown in **Figure 6.1**. Niobium was employed in this research, and is the most common choice of superconducting material, but films of YBCO [Harnack99], niobium nitride [Hajenius03], tantalum [Skalare03], and aluminum [Echternach99] have been employed by others. Gold is uniformly chosen as the normal metal contact material.

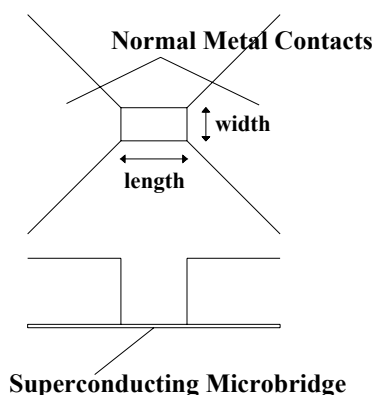


Figure 6.1. Schematic diagram of a superconducting diffusion-cooled HEB. In the research described in this dissertation, the superconducting material is a film of niobium between 100 - 150 Å thick. The normal metal contacts are composed of a layer of gold between 1000 - 3000 Å thick. An upper limit on the length L of the device is set by the electron-phonon interaction time in the superconducting film, which in this case limits $L \leq 0.3$ μm. The microbridge is typically between 0.1 - 0.3 μm wide.

Electron-beam lithography (EBL) is the standard method used to fabricate these devices [Skalare95, Ganzevles02, Bass04], but the absence of an EBL tool at UVA at the onset of this research encouraged the development of an alternative process using a gallium focused-ion beam (FIB) [Datesman99]. This approach had previously not been reported in the literature. While the two tools are similar in many ways, the vastly greater mass and energy of 30 keV gallium ions makes the FIB a tool for sculpting or milling rather than for photoresist patterning, which is the actual function of an EBL system. How the fabrication of a diffusion-cooled HEB is accomplished using an FIB is the topic of the next section. Subsequent sections of this chapter will discuss attempts to control

the stress of sputtered niobium films, the scope and effects of gallium contamination caused by the fabrication procedure, and some relevant materials issues relating both to niobium and to gold.

Although this dissertation is concerned with the fabrication of HEB receiver arrays on silicon wafers covered with silicon nitride, much of the HEB fabrication research was performed on quartz wafers. There are two reasons for this. First, the established and successful procedures for SIS junction fabrication which previously existed in the UVML [Clark03, Lea97] use quartz wafers. It was hoped to apply this knowledge to the HEB effort. Second, it was initially desired to build a single-element receiver using an existing waveguide block designed for 585 GHz operation and an HEB mixer on a quartz chip. While reasonable results with devices fabricated on quartz wafers were achieved, and sample devices were tested and will be described, in the course of this research no mixer chips on quartz were successfully diced, removed from the dicing carrier, packaged, and tested. ESD is likely responsible for this difficulty.

Finally, the idea for the FIB3 process which will be described in the next section is due entirely to Jon Schultz of the UVML [Schultz04], and the author would like to reiterate his gratitude to him for that suggestion.

2. FIB1-3 Process

A gallium focused-ion beam, interfaced with CAD control, can be used to mill away portions of a target substrate according to a user-defined pattern. The system used for this research, the FEI Inc. Series 200, is pictured in **Figure 6.2**. This FIB uses an accelerating voltage of 30 kV. The beam is addressable over a 12-bit DAC interface

(4096 positions) in both the x- and y-directions, and at the lowest beam current setting of 1 pA has a beam waist as narrow as 80 Å. This makes the FIB a very fine and controllable fabrication tool, as has been recognized for some time.

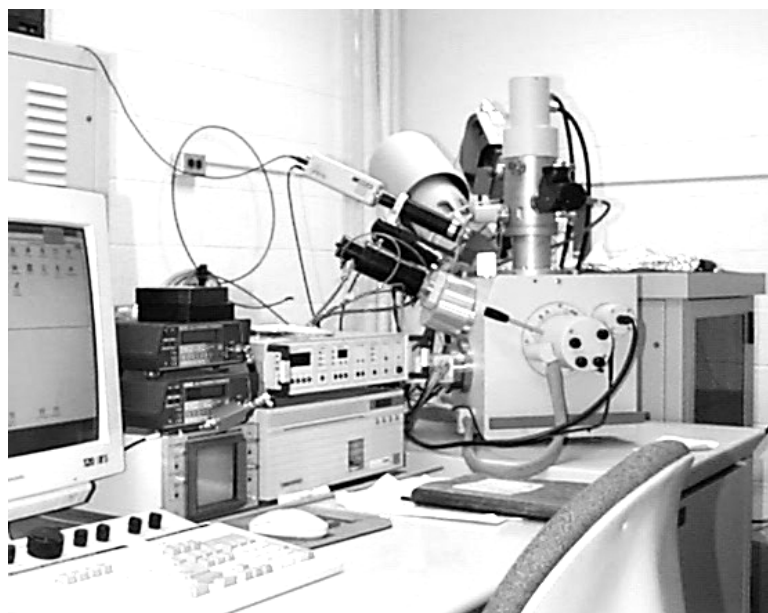


Figure 6.2. The FEI Inc. Series 200 FIB in the UVA MSE Department. The sample chamber is the second item from the right. Principally, this technology is used for the manufacture of TEM membranes, milling cross-sections for failure analysis, and IC repair. In addition to milling functions such as the ones described, this system also features both metal and insulator deposition and chemically enhanced etch capabilities, end-point detection, secondary-ion mass spectroscopy (SIMS), and a hot/cold stage.

The use of a focused-ion beam to manufacture arbitrary geometries has been reported by Vasile et. al. [Vasile97] and many others. Its application to the fabrication of both high-temperature superconducting (HTS) circuits [Mizuno99] and to the fabrication of structures from low-temperature superconducting (LTS, such as niobium) materials [Akaike92] is also a topic of reasonably long standing. More recently, Kang et. al. [Kang01] fabricated ion damage barriers in YBCO using an FIB to define a very narrow (approximately 80 Å) channel in a gold layer which acts as an implantation mask, and

scientists at IRAM [Frommberger01b] used a hybrid EBL-FIB process to fabricate diffusion-cooled niobium HEBs.

The UVML superconducting HEB FIB fabrication process evolved continuously for many years, and the final iteration described in this section is quite different from that described in earlier reports [Datesman01]. For the sake of clarity, only the most up-to-date protocol for the fabrication of HEB arrays on Si/Si₃N₄ is described below. Some information about earlier protocols is presented in the **Chapter 7**, along with the most recent results.

After RCA cleaning, the Si/Si₃N₄ wafer is patterned with a trilevel liftoff stencil similar to that used for SIS junction fabrication [Bass00]. This stencil consists of a hard-baked layer of polyimide, covered with 1000 Å of sputtered niobium, and capped with a layer of AZ5206E photoresist, which is patterned. The photoresist is developed in the negative of the image exposed, after which its features are transferred into the niobium and polyimide layers by reactive ion etching. The photoresist is removed by the oxygen plasma required to etch polyimide, so that the thickness of the finished poly-Nb liftoff stencil is approximately 5000 Å.

Layers of Nb(100 Å), Au(3000 Å), and Nb(300 Å) are sputtered on to the wafer under a single vacuum using the UVML multitarget sputtering system. The thin layer of niobium serves for the HEB microbridge, while the gold layer serves for both the HEB normal metal contacts and the mixer microwave circuitry. Because these films are deposited in succession without breaking vacuum, the interface between them is as clean and as transparent to the flow of heat as possible. The thicker layer of niobium on top is

intended to serve as a mask during an RIE gold etch which follows the FIB1-3 steps. It is nearly all removed at the end of the fabrication process (refer to **Table 5.1**).

The multitarget sputtering system operates with five 3" diameter guns in a confocal up-sputter configuration, with the niobium sputtering gun in the 0° position. The gold and ion guns are at 45° to the rotating substrate. The wafer is cleaned with the ion gun prior to deposition, which removes water vapor and volatiles, and a rigorous protocol of warming and cleaning the sputtering guns is followed. A great deal of effort was expended to discover and maintain the optimum sputtering conditions for the niobium films used in this work, which will be discussed in the next section. Typically the niobium gun was operated with a constant power of 500 Watts, at a sputtering pressure somewhere in the range between 4.15 and 5.25 μm (depending upon the age of the target). The background pressure of the sputtering chamber is in the low- to mid- 10^{-8} torr range.

After deposition of the Nb/Au/Nb metal films, the wafer is carefully dismounted from the wafer block, and thoroughly cleaned. The circuit features are revealed by liftoff of the trilevel resist stencil. N-methyl-2-pyrrolidinone (NMP) at 120° C, which dissolves polyimide, followed by swabbing with ethylene glycol, is suitable for this purpose. Once the circuit features have been fabricated, a series of steps are performed which define and release the silicon nitride membranes underlying the mixer circuitry (refer to **Chapter 5**). Then the wafers are diced and cleaned, which results in a small collection of about 30 individual arrays and sample test pads.

Before the FIB processing may be undertaken, the front of these chips must be covered by a thin (typically 150 Å) layer of gold which is called the "imaging gold"

layer. This is standard procedure when insulating materials (such as silicon or quartz wafers) are imaged with an electron- or ion-probe. The thin conductive layer prevents the accumulation of static charge on the substrate, which would otherwise interfere with the proper functioning of the instrument. The UVML RF diode sputter-etcher, which operates in a down-sputter configuration, is used for this quick deposition. After this point, the HEB arrays and sample test pads are handled either individually (during FIB processing), or in groups of a few lightly greased down to a clean glass slide (during the bridge etch).

FIB1-3 refers to three steps, all performed in one instrument session under a single vacuum. The FIB1 mill covers a relatively large area of about $20 \mu\text{m}^2$ using a beam current of 350 pA, while the FIB2 and FIB3 steps cover very small areas using a low beam current of only 11 pA. Because the second and third steps utilize the same beam current, which is different than that used for the first step, during the FIB session all of the FIB1 mills are performed at their locations before the beam current is changed. The FIB2 and FIB3 steps are subsequently performed in pairs before moving the stage to the next location. This minimizes disturbances associated with stage motion and focusing.

Out of a larger, sacrificial patch of material called the kernel⁴, the FIB1 step mills a waveguide probe transition too fine to create reliably by conventional lithography and liftoff (see **Figure 5.3**), at the apex of which lies a short, relatively narrow bridge (see **Figure 6.3**, top). The FIB1 mill must proceed to a reasonable depth into the silicon

⁴ The term “kernel” here denotes the meaning of **Figure 5.3**, a surfeit of material at the throat of the waveguide probe intended to be milled away. The term will also be used to refer to the structure resulting after the FIB3 step, when the microbridge is still covered with gold which will be removed by argon RIE. The use should be clear from context.

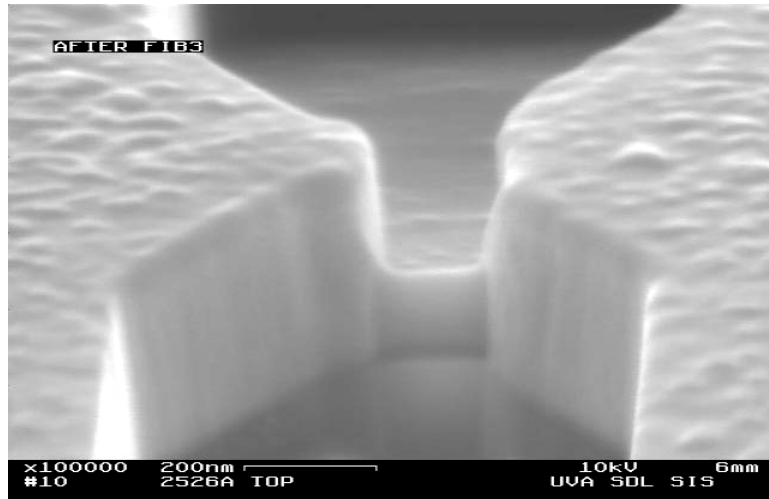
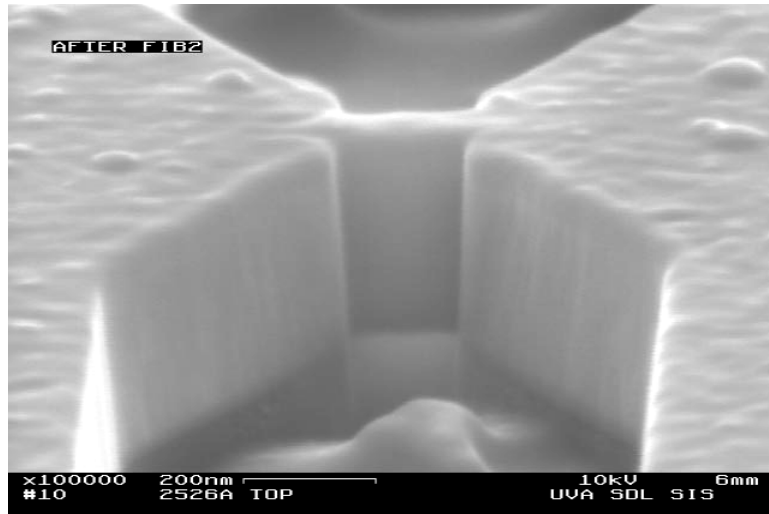
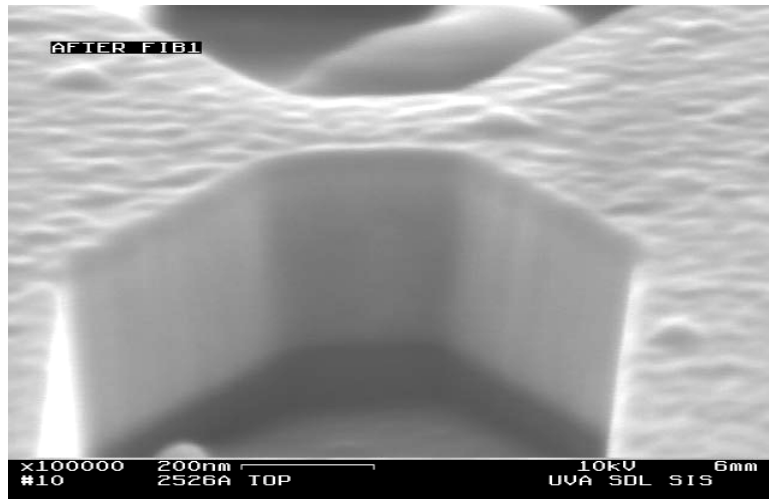


Figure 6.3. The FIB1, FIB2, and FIB3 steps, from top to bottom.

nitride membrane in order to sever any electrical connection which might remain to short out the finished microbridge. More information on this topic may be found in **Section 6.5**.

The FIB1 mill is performed with a nominal beam current of 350 pA, at a magnification of 20 kx. Normally, the FIB stream file does not quite fill the kernel area, so the FIB is used to trim the edges of the kernel before the FIB1 pattern is milled. With these operating settings, the nominal beam waist is 550 Å, and the field of view is approximately 14.4 µm on a side. With this information, the pixel overlap in the FIB1 stream file pattern can be calculated to exceed 80%. A milling time of 40 seconds is used with a dwell time at each pixel of 1 µs, representing about 180 passes over each of 221,000 pixels. The microbridge kernel which remains is 0.3 µm long by 0.3 µm wide.

Because the FIB1 mill kicks up a great deal of material, which tends to adhere to exposed gold surfaces, the FIB2 step is included to clear away this debris by trimming the edges of the kernel (see **Figure 6.3**, middle). The FIB2 and FIB3 steps are performed with a nominal beam current of 11 pA at a magnification of 50 kx. The FIB2 pattern consists of two rectangles, separated by a gap the dimension of the finished niobium microbridge, as shown in **Figure 6.4**. Typical dimensions for these rectangles are 0.35 µm long by 0.28 µm wide, with the gap between them specified by a pixel value of between 20 - 40. The length of the rectangles is chosen to be somewhat greater than the desired length of the microbridge, so that there is some margin for error in the FIB3 machine alignment which follows. The two rectangles are milled together, in parallel, for between 5 -7 seconds.

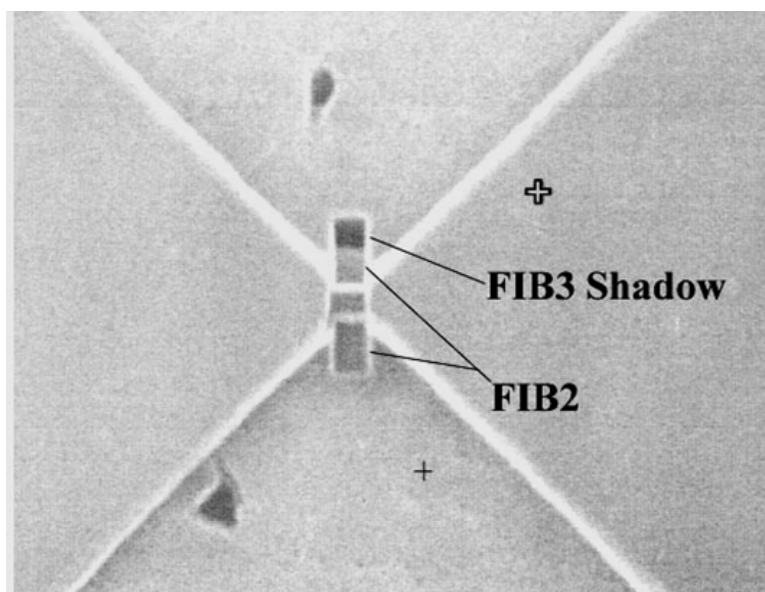


Figure 6.4. FIB image (at normal orientation, 50 kx magnification) of a microbridge kernel after the FIB3 step. The areas where the FIB2 and FIB3 steps cut into the substrate may be easily discerned. The regions milled during the FIB2 step correspond to the FIB2 pattern, since the stage is not tilted in that case. The angle of the stage tilt during the FIB3 places the milled shadow far away from the edge of the microbridge. In this case, the FIB3 pattern could have cut more deeply into the kernel without ill effect.

At 50 kx magnification, one pattern file pixel (linearly one pixel in a .pat file corresponds to 4 stream file pixels) covers about 56 Å. A setting for the gap between the rectangles of 22 pixels is found to produce a microbridge about 0.10 μm wide, while a gap of 28 pixels yields a width of about 0.15 μm. The former is somewhat narrower than one would expect, but such small dimensions are difficult to measure accurately, and the FIB magnification calibration can vary significantly from run to run (refer to **Section 7.4**). The result of the FIB2 step is a microbridge kernel of the appropriate final width, with clean sides of exposed gold, where the niobium microbridge is covered with 3000 Å of gold and still capped with an undesired 300 Å mask of niobium.

The FIB3 step defines the length of the microbridge by removing the niobium mask and 1500 - 2000 Å of gold from the kernel (see **Figure 6.3**, bottom). Because the

ion beam is not selective between materials, and because implantation with gallium changes the properties of the niobium microbridge, the FIB3 step is performed with the stage tilted. This removes the microbridge from the path of the ion beam, so that it will be neither milled away nor contaminated. After the FIB3 step, RIE bombardment with low-energy argon ions selectively removes the remaining gold (in a step denoted the “bridge etch”), finishing the HEB microbridges. The FIB3 pattern is a single rectangle, between 0.2 - 0.3 μm long (the intended length of the device) by 0.15 - 0.20 μm wide. The step is performed with a beam current of 11 pA at a magnification of 50 kx, with a short mill time of typically only 2 seconds.

As already described, the FIB3 step shears off the top of the kernel without risk of harming the underlying niobium microbridge because the stage and sample are tilted at an angle of 45° to the ion beam at this point [Schultz04]. With the top edge of the FIB3 pattern aligned to the top visible edge of the kernel, as shown in **Figure 6.5**, ion flux directed at the target area travels in nearly a straight line over the microbridge and comes to rest in the substrate behind. Because implanting gallium into the niobium microbridge alters the characteristics of the superconducting HEB device (as discussed in **Section 6.4**), this is a highly positive attribute of the FIB3 step. The trajectory of the gallium flux is illustrated by **Figure 6.4**.

Given the known dimensions of the kernel, simple geometry dictates what maximum value for the width of the FIB3 pattern is acceptable. This dimension is between 0.18 - 0.25 μm , depending upon whether the top of the FIB3 pattern is aligned to the front or to the rear edge of the kernel, respectively (refer to **Figure 6.5**). In practice, the FIB user cannot usually resolve these two separate edges distinctly, so that a

relatively shallow cut is typically chosen. A deeper cut may be accomplished either by increasing the width of the rectangle milled, or by aligning it somewhat lower on the kernel feature, but increasing the pattern milling time will not change the amount of gold remaining in the kernel.

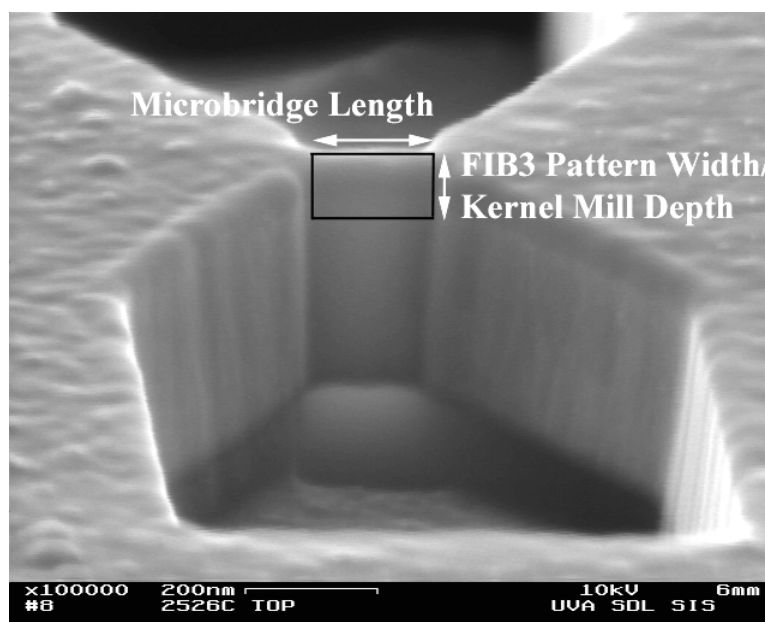


Figure 6.5. Alignment of the FIB3 pattern, using an SEM photo of a FIB2 kernel tilted at 75° (the stage tilt is 45° during the actual FIB3 process). The gallium ions will be normally incident to the plane of the photo, removing only the top of the kernel and avoiding implantation into the niobium microbridge. The width of the FIB3 pattern corresponds to the depth of the kernel milled away.

Choosing the width of the FIB3 rectangular pattern involves a trade-off between minimizing the possibility of milling away the edge of the HEB microbridge during this step and the desirability of leaving only the smallest amount of gold possible in the kernel for subsequent bridge etch removal. Pixelation of the image, its indistinctness, and the erosion of the kernel during imaging and alignment combine so that a reasonable allowance for misalignment of the FIB3 pattern to the kernel (which is about $0.35 \mu\text{m}$ high) is about $0.02 \mu\text{m}$. Aligning the FIB3 pattern to the higher rear edge of the kernel, and choosing a shallower cut than the $0.25 \mu\text{m}$ width dictated by geometry, maintains the

safe margin illustrated in **Figure 6.4**. FIB3 widths of 0.20 μm and 0.15 μm were used in this work at different times.

The kernel resulting from the FIB1-3 process is covered by approximately 1000 \AA of gold, which must be removed by a low-power argon ion bridge etch (see **Sections 6.5 and 7.4 - 7.6**). The height of this gold layer does not closely follow the slicing angle of the FIB3 ion beam across the width of the microbridge, although it may in general be somewhat higher (100 - 200 \AA) on one side than on the other. This is attributable to the poor milling characteristics of gold, discussed in **Section 6.5**. The gold thickness variation between kernels fabricated within the same FIB session may be as great as 200 \AA , or about 20%, but is likely somewhat less when the machine is operating well. If the FIB image is distinct and steady, so that the FIB3 pattern alignment can be accomplished quickly and well, then the contribution to this variation owing to the image pixellation alone is less than 70 \AA .

To conclude, the width of the kernel and of the microbridge is determined by the gap between the two FIB2 rectangles, and its length by the length of the FIB3 rectangle. HEB microbridges as small as 0.15 μm long by 0.10 μm wide have been fabricated using this method. Further results are discussed in **Chapter 7**.

3. Film Stress

The internal film stresses which result from sputter deposition on to a substrate are well known to affect the properties of devices made from those films [**Kuroda87**]. While working pressure, deposition power, operation mode (constant power, voltage, or current bias) and even deposition rate must all be examined in order to obtain optimal

conditions, the continual erosion of the magnetron sputtering target over its lifetime requires that these parameters be continually re-examined [Iosad98]. Discovering and maintaining the proper near-zero stress conditions for niobium films deposited in the UVML multitarget sputtering chamber was an important part of the HEB research. The internal film stresses of 2000 Å thick niobium films DC magnetron sputtered on to Si/SiO₂ and Si/Si₃N₄ substrates were examined.

Using the bending plate method [Finegan61], the stress within a deposited thin film layer may be deduced from the substrate's radius of curvature according to the relation [Zecchino]

$$\sigma = \frac{1}{6} \left(\frac{1}{R_{post}} - \frac{1}{R_{pre}} \right) \frac{E t_s^2}{1 - \nu t_f}, \quad (6.1)$$

where σ is the stress in the film after deposition, R is the substrate radius of curvature, pre- or post-deposition, E is the value of Young's modulus, and ν of Poisson's ratio, for the substrate material, t_s is the substrate thickness, and t_f is the film thickness. A negative value represents a compressive stress (i.e., the post-deposition substrate becomes more convex), while a positive value represents a tensile (concave) stress. The radius of curvature, before and after deposition, was measured using either laser interferometry or stylus profilometry.

The internal stresses found in magnetron sputtered metal films have been a subject of research interest for many years. Films deposited with a low working pressure are compressive, although their character quickly changes to tensile as the pressure is increased. If the working pressure is increased still further, however, the film stress will ultimately decrease toward zero [Hoffman76]. Computer simulations of refractory

metal film growth utilizing molecular dynamics [Müller87] successfully model this observation.

Working with glass substrates, Wu reported that niobium films can be prepared in any stress state by varying the argon sputtering pressure [Wu79]. At working pressures somewhat above the tensile peak the transition temperature of the superconducting film is strongly reduced. Kuroda and Yuda also report that small area niobium SIS junctions fabricated using a lift-off process have characteristics much improved over devices made from stressed films by other means, because lift-off patterning relaxes the stress field within the niobium film [Kuroda87]. Finally, for very thin films the film stress is found to depend upon the thickness of the film. Films thinner than about 100 Å are compressive, most likely due to the diffusion of oxygen into the film, and become tensile as the thickness increases [Murakami85].

Because the HEBs are fabricated by lift-off from niobium films only about 100 Å thick, it is difficult to say whether working to control the stress of deposited films actually has any effect upon the characteristics of finished devices. However, in order to maintain some basis for comparison between device runs spread apart in time, it is necessary to compensate in some way for changes in the measured stress of sputtered films caused by target erosion. The most sensible way to do this is to deposit high-quality films by maintaining the sputtering parameters at near-zero stress conditions.

The effects of oxidation, the incorporation of impurities into the sputtered film, and the very small changes in wafer curvature which must be measured in order to infer the stress state of very thin films all conspire to make it very difficult to work confidently with films a few hundred Ångstroms or less thick. It is therefore customary to measure

and control the stress of relatively thicker films, anticipating that the benefits of this effort will extend to thinner layers. Therefore, the stress results discussed in this section apply to sputtered films of niobium 2000 Å thick.

Ultra-flat silicon wafers covered with 1000 Å of thermal SiO₂ were used as substrates for many of the stress measurements described here in place of the quartz wafers on which devices were actually fabricated because a blank quartz wafer is transparent and cannot be scanned with a laser. Profilometry measurements [Cecil04] later demonstrated that, given identical deposition conditions, niobium films sputtered on to quartz wafers have the same stress as those sputtered on to Si/SiO₂ substrates. If a strict protocol of preparing the chamber, warming the sputtering guns, and cleaning the substrate is followed, sputter deposition of niobium on to Si/SiO₂ substrates is highly controllable and repeatable.

The Si/SiO₂ wafers used were 2” in diameter, ultra-flat, and 300 µm thick. After the initial pre-deposition scan, each was mounted in a “float block” designed to eliminate any stress effects caused by other methods of clamping the wafer to the block. In order to bring the levels of water vapor and other contaminants to the lowest levels possible, each wafer was allowed to sit overnight in the sputtering chamber before deposition. The chamber base pressure was in the mid- to low-10⁻⁸ torr range.

After the overnight chamber preparation, the niobium gun was run for 8 minutes in order to clean it, after which the substrate was cleaned for 7 minutes by ion milling with a beam voltage of 150 Volts. Next the niobium gun was warmed for an additional seven minutes. Only after this protocol was followed were 2000 Å of the metal deposited on the substrate. The DC magnetron gun was operated in a constant power mode, at a

power of 500 W, producing a deposition rate of approximately 4 Å/sec. The working pressure was adjusted from run to run in order to achieve a slightly compressive target stress of between -50 to -100 MPa. An identical protocol was followed for the deposition of HEB material.

For deposition on to Si/SiO₂ substrates, a change in working pressure of 0.05 μm reliably corresponded to a change in the film stress of a bit less than 50 MPa. This is demonstrated at several locations (s3-212 compared to s3-215, as well as s3-241 vs. s3-243) within **Table 6.1**, where the working pressures and corresponding stress measurements over 30 months (and several sputtering gun targets) for both Si/SiO₂ and Si/Si₃N₄ substrates are presented.

The Si/Si₃N₄ wafers used were 2” in diameter, flat to 1 μm TTV, 127 μm thick, and covered with about 7500 Å of LPCVD silicon nitride. The stress runs performed on these substrates were conducted exactly as just described for the depositions on Si/SiO₂ wafers, but the results were very different. The measured film stresses were often highly compressive, were not repeatable from wafer to wafer under identical deposition conditions, and did not reliably show a trend toward zero stress with increasing working pressure. The relevant results from **Table 6.1** are summarized in the graph of **Figure 6.6**.

Before the permanent magnets in the sputtering gun had been replaced (i.e., prior to s3-248), the stress of films deposited on to Si/Si₃N₄ did not appear repeatable by comparison to films deposited on to Si/SiO₂. However, the 50 MPa/0.05 μm rule of thumb did approximately apply (refer to the open circles in **Figure 6.6**), and three successive trials over four months did yield zero-stress material. Each of these trials used a working pressure 0.30 μm greater than the optimal working pressure determined for

Run	Date	SiO ₂ pressure (μm)	Stress (MPa)	Si ₃ N ₄ pressure (μm)	Stress (MPa)
s3-212	12/11/02	4.95	5		
s3-215	12/17/02	4.85	-71		
s3-218	1/31/03	4.85	-131		
s3-222	2/5/03			4.85	-453
s3-224	2/10/03			4.85	-357
s3-225	2/10/03			5.10	-241
s3-227	2/13/03			5.20	-55
s3-232	3/19/03	4.85	-61		
s3-234	4/9/03			5.15	28
s3-241	6/4/03	4.80	64		
s3-243	6/10/03	4.65	-51		
s3-244	6/20/03			4.95	-48
*s3-248	9/12/03	4.65	371		
s3-249	9/15/03	4.20	15		
s3-255	1/4/04			4.45	-364
s3-257	1/6/04	4.45	-115		
s3-258	1/7/04			4.80	-384
s3-260	1/9/04			4.80	-228
s3-261	1/12/04	4.50	-82		
s3-262	1/13/04			5.10	-251
s3-264	1/16/04			5.20	-320
s3-274	6/3/04	4.60	-71		
s3-275	6/4/04			4.60	-354/-386

Table 6.1. Summary of niobium stress runs over 30 months deposited on both Si/SiO₂ and Si/Si₃N₄ substrates. The permanent magnets in the sputtering gun were replaced just before s3-248 (*). The stress is consistent, repeatable, and controllable for deposition on to Si/SiO₂ substrates; this is not at all true for deposition on to silicon nitride.

deposition on to a Si/SiO₂ substrate at a corresponding time (i.e., for a given state of target erosion), which seemed also a useful rule of thumb.

Out of six trials performed after the rehabilitation of the sputtering gun (refer to the filled squares in **Figure 6.6**), none came close to a zero stress result. Both of the rules of thumb just referenced do not apply to the new data; in fact, it is reasonable to ask whether the appearance of meaning in the earlier results is merely a statistical fluke. After s3-248, depositions on to Si/SiO₂ substrates continued to be controllable and follow the same trends as previously.

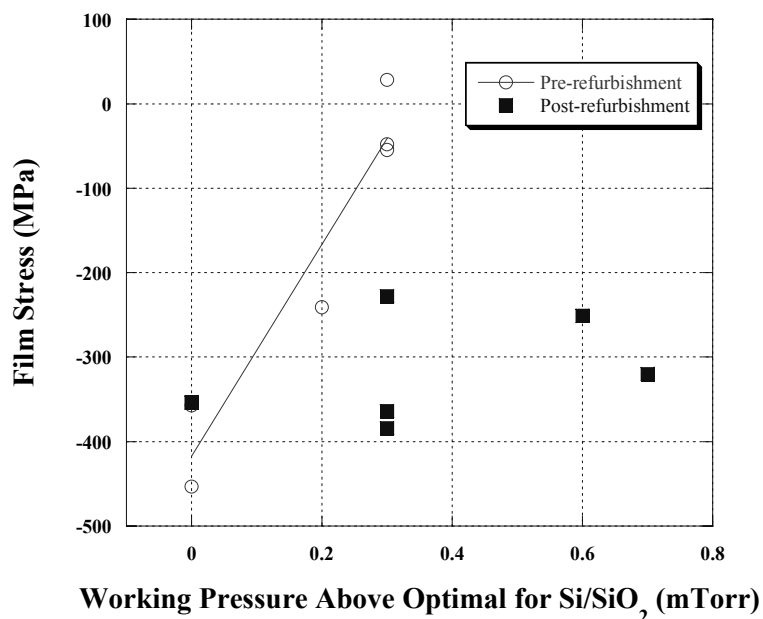


Figure 6.6. Summary of stress results on Si/Si₃N₄ substrates from **Table 6.1**. The “optimal” working pressure is the near zero stress pressure determined for Si/SiO₂ substrates in corresponding runs - i.e., “0” working pressure in this figure indicates that the deposition on to a Si/Si₃N₄ substrate was performed at the same pressure as a deposition on to a Si/SiO₂ substrate just prior which was measured to be zero stress. The open circles represent stress runs before the replacement of the gun magnets; the filled squares, runs after. A line fit to the earlier data shows a slope of approximately 65 MPa/0.05 mTorr.

Thick LPCVD silicon nitride is certainly less smooth, less flat and more chemically active than a relatively thin thermal oxide layer on silicon, and as such is

clearly a difficult choice of substrate for this thin-film device application. No other explanation for the results presented here can be offered at this time.

For the results presented for measured devices in **Chapter 7**, the niobium HEB material was sputtered at a pressure 0.30 μm above the optimal working pressure determined for deposition on Si/SiO₂ substrates, in an attempt to compensate for the highly compressive film stresses which were observed.

4. Gallium Implantation

Because the FIB fabrication method by its nature implants some gallium into the niobium HEB microbridge, it is worthwhile to quantify the degree and possible effect of this contamination. To this end, simulations of 30 keV gallium ion implantation into relevant materials were performed using SRIM [SRIM]. In addition to the results for range and straggle presented in **Table 6.2**, these simulations confirmed that no backscattering of incident gallium ions from quartz or silicon nitride surfaces should be expected.

A significant applicable literature exists. Ion implantation into thin niobium films, either for purposes of fundamental study [Camerlingo85], or for the fabrication of superconducting weak links [Arrington74], has been a subject of interest for some time. Further discussion of this topic may be found in **Chapter 8**. In addition, at one time high-T_C (20 K) Nb_xGa_{1-x} [Foner72] and Nb₃Ga [Sosnowski77] compounds were an area of active study. Interest in Nb-Ga binary superconductors was eventually eclipsed by the development of Nb₃Ge and Nb₃Sn, which are more stable and easier to produce, but even

in the present day there is active interest in the beneficial use of gallium as a dopant in Nb_3Sn conductors for high-field applications [Rudziak01].

Target	Long. R (Å)	Long. ΔR (Å)	Lat. R (Å)	Lat. ΔR (Å)
Silicon Nitride	384	126		
Quartz (SiO_2)	263	86		
Germanium	182	94		
Niobium	125	69	49	64
Gold	95	56	48	61
Qtz/Nb(100 Å)/Au(100 Å)	109	77		

Table 6.2. Ion implantation ranges (R) and standard deviations, or straggles (ΔR), for 30 keV gallium ions under normal incidence, obtained using SRIM. According to standard Gaussian statistics, 68% of the dose lies within one standard deviation of the peak; almost 96% of the dose lies within twice the straggle. The quartz/Nb/Au structure listed in the last row is that of the sample described later in this section.

Considering that the range of 30 keV gallium ions in gold is slightly less than 100 Å, examination of the FIB1-3 fabrication process reveals that the FIB1 step cannot implant any gallium into the niobium microbridge at all. The FIB2 and FIB3 steps, however, are likely to implant gallium into the edges of the HEB device.

Although the incident doses per unit area may be easily calculated, the actual concentration of gallium contaminant which results from either step is quite difficult to quantify. In the FIB2 case, this is true in part because the bombarded portion of the sample sputters away dynamically, completely, and unevenly during the process. The adjacent edges of the HEB microbridge which remain are implanted as a result, but the implanted dose must arrive in those regions obliquely, after scattering through a swiftly

but irregularly decreasing thickness of gold. No dose arrives in the microbridge by backscattering out of the substrate.

According to **Table 6.2**, the lateral range and straggle of 30 keV gallium ions in niobium are 49 and 64 Å, respectively, with nearly the same results for gold. (These SRIM results are depicted graphically in **Figure 6.7**.) Noting that 96% of the ion flux scattered laterally into the microbridge due to the FIB2 mill just adjacent lies within two standard deviations of the dose peak, all but 4% of the dose lies within 128 Å of the microbridge edge. Since the HEB device is typically at least 0.10 μm, or 1000 Å, wide, therefore much or most of the microbridge width should be free of significant contamination after the FIB2 step.

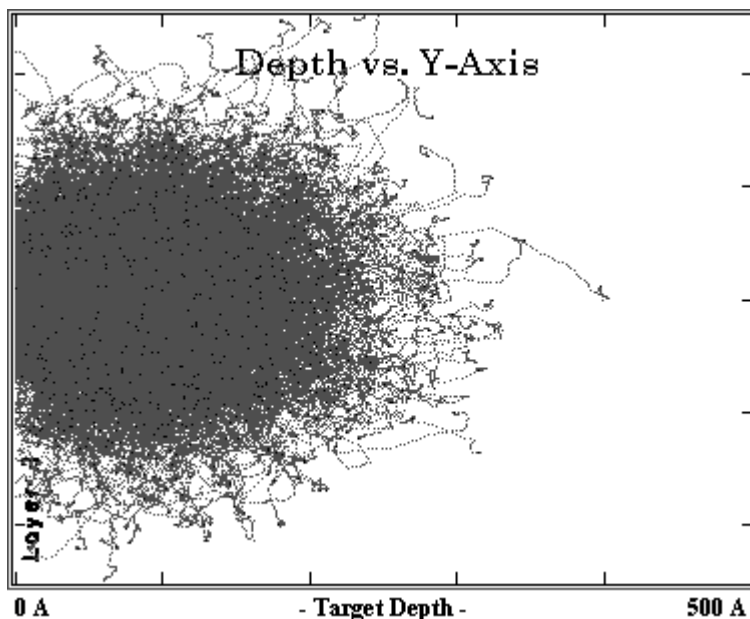


Figure 6.7. Results of an SRIM simulation of the implantation of 30 keV gallium ions into a gold target. The vertical axis represents the lateral ion displacement, while the horizontal axis represents the longitudinal displacement. The lateral and longitudinal ranges are 47 and 95 Å, respectively.

This assertion can be quantified somewhat. A dose of 10^{19} cm^{-3} will be seen to reduce the transition temperature of a 100 Å Nb/100 Å Au film by about 0.5 Kelvins.

Although this is a significant reduction, gallium contamination at or below this level will certainly not prevent successful HEB fabrication, as the transition temperature of the device will still lie above the 4.2 Kelvin temperature of liquid helium. Assuming a peak dose of 10^{21} cm^{-3} at the microbridge edge, a gallium concentration of 10^{19} cm^{-3} is found at a distance of 194 Å from that edge. Therefore 60% of the microbridge width (for a 1000 Å wide microbridge) lies below this contamination threshold. The corresponding widths for thresholds of 10^{18} cm^{-3} and 10^{16} cm^{-3} are 50% and 40%, respectively.

The FIB2 pattern consists of two $0.28 \text{ }\mu\text{m} \times 0.35 \text{ }\mu\text{m}$ rectangles, milled to a depth of about 4600 Å (the Nb/Au/Nb/imaging gold material stack, plus about 1000 Å of substrate) using an 11 pA beam current for 5 seconds. Assuming incorrectly that all of the milled material is removed uniformly at equal rates, all of the ions which strike within the niobium layer and laterally are directed to a point less than 100 Å (twice the lateral range) away from the microbridge edge (that is, ions which are likely to scatter into the microbridge) can be counted up, according to the proportion of this small volume to the total milled volume. In this way, a simple estimate of the gallium concentration in the implanted edges of the microbridge may be obtained.

Pixellating the 100 Å wide strip adjacent to the microbridge according to the magnification and applying simple range statistics, it is found that 24% of the ions which strike this area scatter out beyond the pattern edge. This analysis suggests therefore that 59,000 gallium ions are distributed within the microbridge edge interaction volume. Since this volume measures 100 Å thick by 3500 Å long by about 128 Å wide (twice the lateral straggle), a rough but reasonable estimate of the volume dose is $10 \times 10^{20} \text{ cm}^{-3}$, or 2% by atomic composition. Whether this estimate is realistic is impossible to judge,

because the assumption of uniform milling which underlies it is not at all accurate. Specifically, since the gallium ion beam tends to melt the gold layer where it strikes the sample, the actual physical process which occurs involves not only gallium ion scattering and implantation, but possibly also the melting and re-freezing of a small volume of liquid gold contaminated with a concentration of gallium which might increase with time.

The FIB3 step itself is intentionally carefully designed to avoid contaminating the microbridge, which is viewed at a 45° angle with one edge of the HEB device exposed. Therefore no implantation occurs during the quick removal of the niobium mask from the microbridge kernel. Some implantation into the visible edge of the microbridge doubtless does occur, however, during focusing, imaging, and alignment of the FIB3 pattern to the kernel. It is possible to put a bound on the degree of the contamination at issue, without calculating the specific dose captured by the niobium layer.

The FIB3 step is performed using an 11 pA beam current at a magnification of 50 kx; the field of view is 5.74 μm on a side. The niobium microbridge, covered by the gold in the kernel, is 0.3 μm long and 100 Å thick. Because the sample is tilted at an angle, the microbridge presents an ion capture section of $2.1 \times 10^{-3} \mu\text{m}^2$. (Refer to **Figure 6.8**.) If the operator takes 10 seconds to align the FIB3 pattern to the kernel, then it is easy to calculate that the edge of the HEB microbridge captures approximately 40,000 incident gallium ions. The time required to focus and align, however, is quite variable from device to device within a fabrication set - in practice, it ranges from as little as 5 to as long as 20 seconds.

Assuming for the sake of argument that this flux impinges normally upon the edge of the microbridge, and that none of it scatters out of the top or bottom surfaces of

the 100 Å thick niobium layer, an upper bound on the gallium concentration may easily be calculated. As shown in **Figure 6.8**, the captured gallium ions are spread throughout a volume 0.30 μm long, 0.01 μm (100 Å) high, and approximately 0.02 μm (200 Å) deep. (Neglecting backscattering, 84% of the incident dose lies between the film's edge and a depth of $R+\Delta R = 194$ Å). The upper bound which results from this calculation is 7×10^{20} cm⁻³, with the 10^{19} cm⁻³ contamination threshold extending 330 Å inward from the microbridge edge (not including the contribution of the FIB2 step).

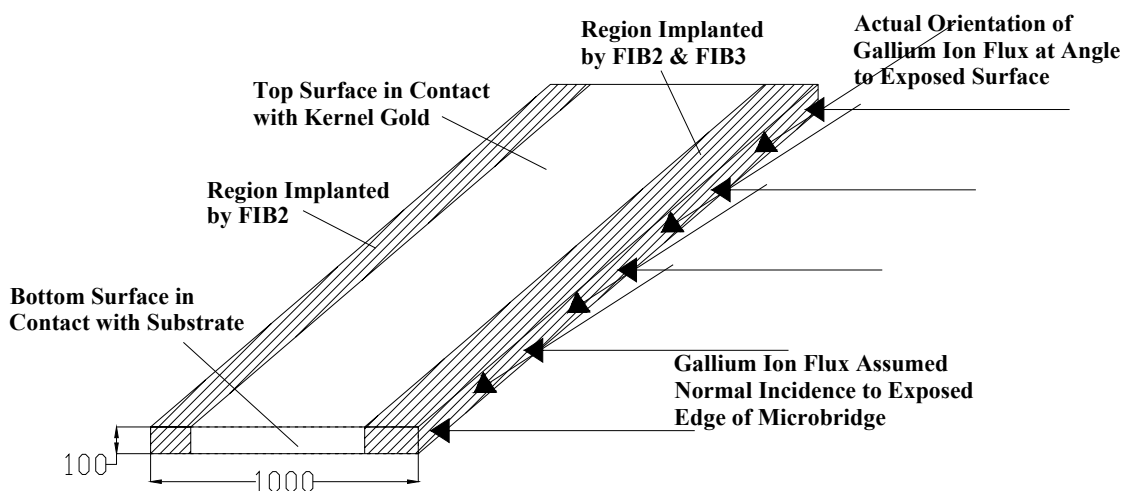


Figure 6.8. Scale diagram of the niobium HEB microbridge, detailing the gallium contamination which results from the FIB fabrication process. Shading indicates those volumes which are implanted with gallium. Because the sample is tilted at 45° to the beam during the FIB3 step, the ion capture section is not the same as the physical area of the exposed surface, and only one edge of the microbridge is implanted during the imaging preceding that step. The stated dimensions are in Ångstroms.

The actual gallium concentration within the affected volume is significantly lower than this 7×10^{20} cm⁻³ figure, in part because the ion beam in fact strikes the edge of the microbridge at an angle, and in part because the assumption of no scattering out of the top and bottom microbridge surfaces is incorrect. Based upon the 64 Å lateral straggle in niobium, simple range statistics indicate that, assuming normal incidence, at least 35% of incident ions exit from those surfaces.

Therefore the contamination resulting from the FIB2 step probably dominates, although the greater range of the FIB3 dose within the microbridge suggests that this may not be the case more than 200 Å away from the microbridge edge irradiated during the FIB3 step. Beyond this point, however, the implanted concentration has decreased significantly from its maximum value. Even though the magnitude of the FIB3 dose may be negligible, the dose is not so small that its variability, caused by the operator's need to align and focus, can be ignored as a concern. Unfortunately, no data which addresses this issue concretely is available.

In order to quantify the effect that gallium contamination has on the superconducting properties of 100 Å thick niobium films, samples of Nb(100 Å)/Au(100 Å) on quartz substrates were prepared, irradiated with gallium using the FIB, and measured. The films were prepared according to the protocol described in the previous section. The thin layer of gold on top of the niobium serves as a sacrificial layer for ion implantation, prevents the superconducting film from sputtering away under bombardment, provides good contact between the dipstick pogos and the superconducting film, and prevents oxidation of the refractory metal film. The thickness of the gold layer is chosen to approximately coincide with the range of the energetic gallium ions in that material. More information about these experiments can be found in **Chapter 8**.

For the structure just described, a simulation with SRIM predicts that 35% of the incident gallium ions will stop within the niobium layer, although with a very non-uniform dose profile. The average volume dose within the film is therefore estimated to be on the order of 10^{19} cm^{-3} , which corresponds to an atomic concentration of around

0.02%. The correlation between average dose and transition temperature for two sets of samples is shown in **Figure 6.9**.

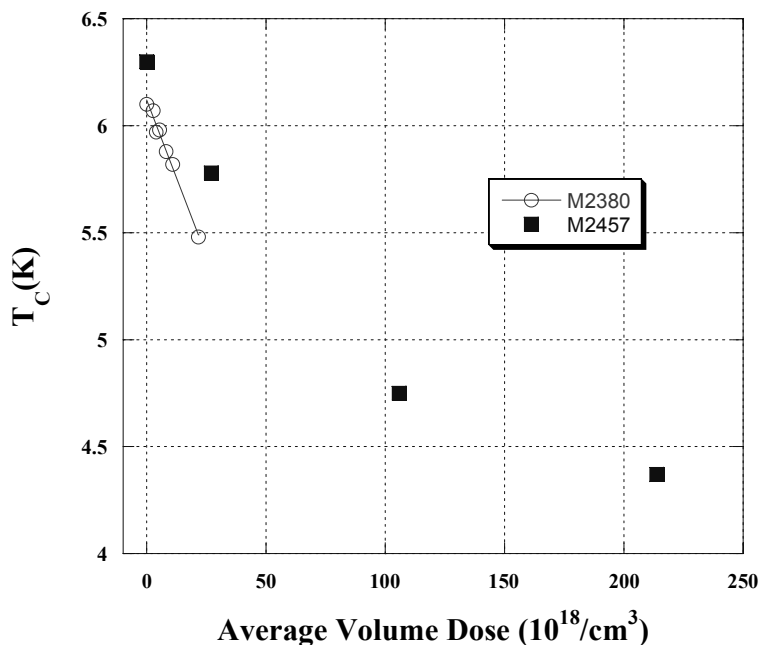


Figure 6.9. Measurements of the critical temperature of Nb(10 nm)/Au(10 nm) films vs. FIB-implanted gallium dose. Even a dose above 10^{20} cm^{-3} (0.2% atomic substitution) does not destroy superconductivity in the film, instead merely suppressing the transition temperature of the sample. The two sets of samples were deposited in the UVML multitarget sputtering system many months apart. Changes in the sputtering conditions or the thickness monitor settings probably explain the discrepancy between the two sets of data.

High doses (i.e., long FIB exposures) do seem to roughen up the 100 Å sacrificial layer of gold on these samples somewhat, but under simple SEM examination the films do not appear to be significantly sputtered away. Because the proximity effect [Kain02] dictates that removing a certain thickness of gold from above the niobium microbridge ought to increase the transition temperature of the sample, the real T_c suppression effect caused by gallium implantation may in fact be somewhat greater than shown by the data in **Figure 6.9**. The general trend, however, is accurately represented.

While the FIB3 mill itself does not implant any gallium into the microbridge, the dose which results from imaging prior to the operation was found to be of the order of

10^{20} cm^{-3} . An implanted dose of this magnitude was shown to suppress, but not destroy, superconductivity in a 100 Å niobium film. By contrast, the estimated dose implanted by the FIB2 step equaled 10^{21} cm^{-3} . No T_C vs. dose data is available for such a large dose, which might very well cause implanted regions to fail to superconduct at 4.2 K, or at all. Because gold congeals under bombardment, however, the assumption upon which this estimate is based is not physically realistic; what the true concentration might be is not reliably known.

In conclusion, both the FIB2 and FIB3 steps are likely to implant significant amounts of gallium into the HEB microbridge, though only into its edges. Most of the width of the device should be largely free of significant contamination, so that undesired implantation of gallium should not prevent the successful application of the FIB1-3 HEB fabrication method.

5. Further Materials Issues

In addition to its excellent thermal and electrical conductivity, gold has many desirable material properties. It may be plated, etched with wet chemicals, and reactively etched in a chlorine plasma [**Ranade93**]. In addition, it is soft enough to be etched non-reactively using an ion gun, or in an RIE chamber using an inert gas such as argon. In the micro-scale, however, gold may accurately if unscientifically be described as a “sticky” and “clumpy” material. This presents significant challenges for the HEB fabrication, which will be discussed as they relate to the FIB1 and bridge etch steps.

Since the FIB1 step uses a 350 pA beam current, 30 kV accelerating potential, and a 1 μs dwell time at each pixel, it is easy to calculate the energy delivered to the target by

the ion flux. Assuming the bulk values for the density and heat capacity of gold, and an interaction volume based upon the beam waist and ion range, by a reasonable estimate the energy delivered by the ion beam causes the temperature of that small volume to increase by approximately 20,000 Kelvins. Obviously nearly all of this heat is either shared with adjacent regions of the film and substrate by diffusion, or lost as kinetic energy imparted to sputtered particles, but a small volume of gold likely melts under the impact of the ion beam. This volume of liquid then re-freezes as the ion beam is steered to another location. According to this analysis, surface adhesion at a liquid/solid interface seems a reasonable explanation for the “clumpy” behavior illustrated in **Figure 6.10**.

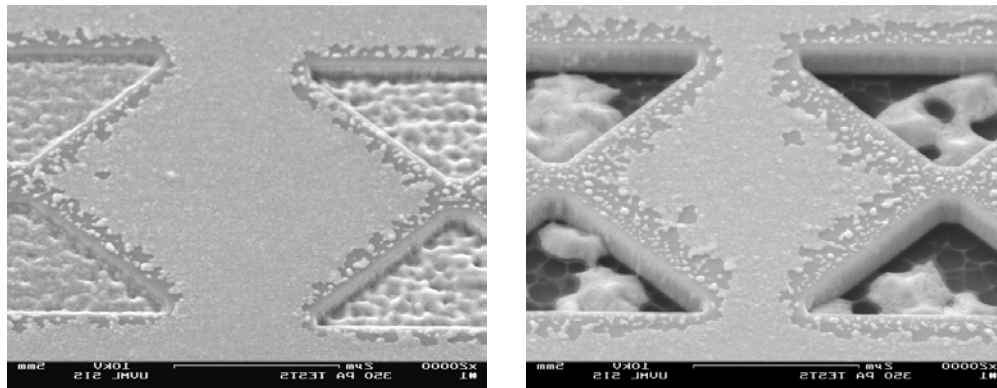


Figure 6.10. Test FIB1 patterns (for HEBs on quartz substrates) for increasing mill times (3, 4, 7 and 8 seconds, respectively), illustrating the tendency of the gold layer to clump together during bombardment. The material within the milled patterns congeals because it melts when struck by the ion beam and re-freezes when the ion beam moves away. The imaging gold near the un-milled edges of the patterns is degraded for the same reason, as the local temperature at the edges of the pattern is elevated due to heat deposited by the ion beam. The FIB1 mill time applied to these patterns for the manufacture of real devices was 20 seconds

Because gold cannot be removed smoothly and uniformly by ion beam milling, the FIB1 step must mill quite deeply into the substrate in order to avoid leaving material behind which shorts out the HEB device. Therefore the FIB1 step sputters up a great deal

of inert material, which coats the sidewalls of the kernel and must be removed before the bridge etch. The FIB2 step would not be necessary if the 3000 Å gold layer could be removed smoothly and uniformly, and the gallium contamination which accompanies it could be avoided.

To remove the 1000 - 2000 Å of gold remaining on top of the niobium microbridge after the FIB3 step, a physical etch with argon ions works reasonably well. This bridge etch process and its results are described in more depth in **Section 7.3 - Section 7.5**. However, the “clumpy” behavior which gold exhibits under ion milling with energetic gallium ions also applies to bombardment with low-energy argon ions, as illustrated in **Figure 6.11**.

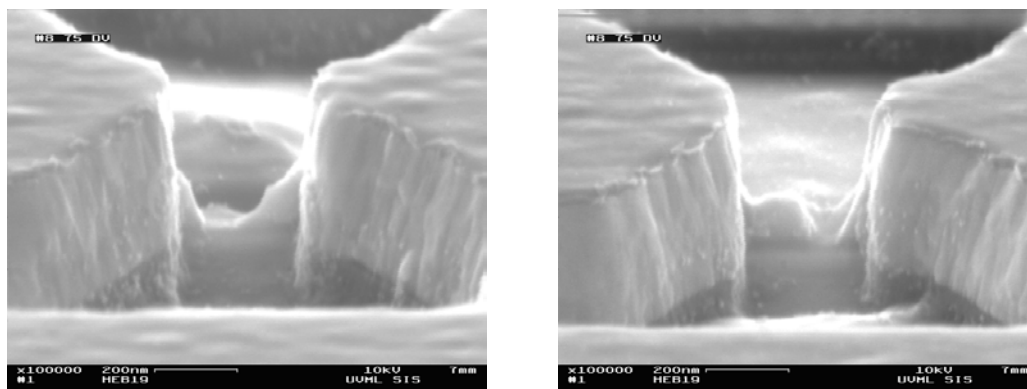


Figure 6.11. Two HEB microbridges from HEB19 top, which were etched together at 150 Volts for 2 hours and 15 minutes. The results of the bridge etch vary greatly, even though the kernel structures following FIB processing are basically the same.

The photographs of **Figure 6.11** exhibit two important features, which will be discussed in turn. The first is that the microbridge kernel, like the material in the FIB1 pattern volume, clearly does not etch away evenly and uniformly. (There is no data to support or refute this assertion for a 300 Volt bridge etch.) Instead, it seems that a small gap first opens in the gold layer - not even necessarily in the center of the structure. Once the gap has formed, the short length of exposed niobium slowly grows as the overlying

gold film creeps toward the masked gold surfaces at each end of the microbridge. This has interesting implications for the properties of the niobium microbridge, since the total cumulative exposure to argon ion bombardment varies along the length of the microbridge, and this argon bombardment profile is furthermore not consistent from device to device within a single fabrication set.

The manner in which the gold layer creeps off of the microbridge toward the ends of the structure explains the results of an experiment in which a series of microbridges of increasing lengths (0.2, 0.3, up to 0.6 μm) were fabricated and etched. Every microbridge turned out to be about 0.10 μm shorter than its expected length, the length of the gap in the niobium mask milled by the FIB3 pattern, as shown in **Figure 6.12**. This is a very consistent result of the bridge etch process, at 300 Volts and at 150 Volts, for the microbridge lengths which were examined (FIB3 lengths between 0.20 - 0.30 μm).

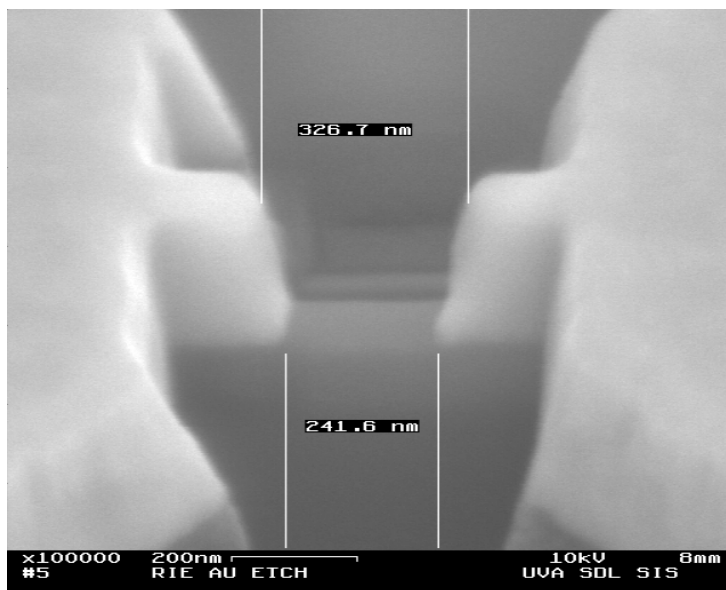


Figure 6.12. SEM photograph showing that the microbridge turns out to be shorter than the FIB3 pattern specification. The gold on top of the HEB microbridge creeps toward the masked ends of the kernel during the bridge etch, with the result that the finished device is about 80 nm shorter than the corresponding gap in the etch mask.

The second important issue suggested by **Figure 6.11** is that the bridge etch may not produce consistent results from device to device within a fabrication set. This is confirmed in **Figure 6.13**, which shows two identical devices on quartz substrates, etched at 150 Volts, which are nominally complete. Although in both cases the FIB3 pattern was 0.30 μm long, in one case the exposed length of the microbridge was 0.24 μm , while in the other, it was only 0.17 μm . The room temperature sheet resistances of these microbridges, calculated using the measured dimensions, are about the same - 50 Ω/\square - so that the resistances of the two devices were quite different. Essentially, the bridge etch should be considered complete in the case of the first device, and incomplete for the second.

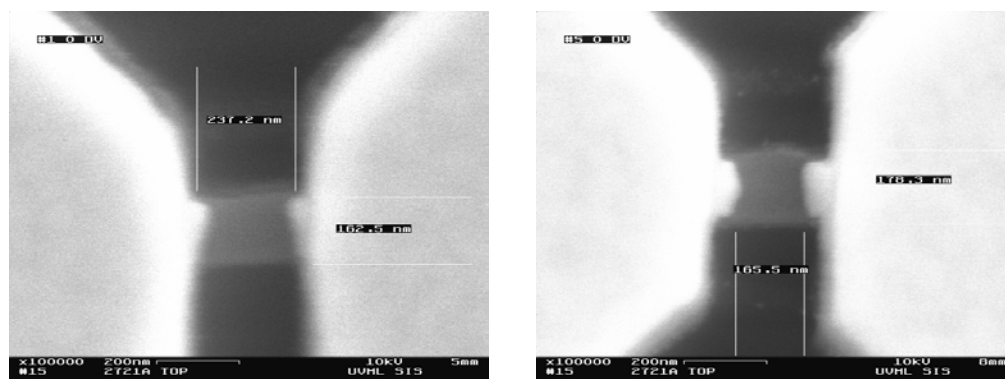


Figure 6.13. Two devices from the same fabrication set (M2721A top) showing the inconsistent progress of the bridge etch between identical devices. The device on the left is basically finished, while the device on the right is not.

Several possible explanations for this problem exist, including cold spots in the RIE chamber, exposure of L-grease squeezed out from beneath a sample die during the bridge etch, non-uniform kernel thicknesses, variability of the RIE chamber conditions, or perhaps non-uniformity of the thermal mounting between samples. How well the samples are thermally sunk has a substantial influence on the gold etch rate, as may be seen in **Table 6.3**.

Power (W)	Self-Bias (V)	Mask	Condition	Rate ($\text{\AA}/\text{min.}$)
80	320	Cr	Pyrex dish, no grease	75
40	205	Cr	Pyrex dish, no grease	22
25	150	Nb	Pyrex dish, slide, greased down	9
25	150	Nb	Pyrex dish, slide, no grease	3

Table 6.3. Gold etch rates in the UVML Semi-RIE system using 50 sccm flow of argon, a fixed pressure of 20 μm , and a pyrex dish for a platter. In less recent work, sometimes chromium was used in place of niobium as the mask layer in the HEB material stack.

The process variability may even simply be unavoidable when processing thin gold films in this manner. Therefore, the most direct solution to the problem just described is to over-etch substantially. This is only an option, however, if the exposed areas of the microbridge can withstand the additional etching necessary to remove all of the gold from the kernel. In order to address this issue, a set of 100 \AA Nb/250 \AA Au samples were deposited, masked, and etched. **Figure 6.14** presents the results of that series of experiments. A 100 \AA niobium film responds fairly robustly to bombardment with 300 V argon ions, as its critical temperature is reduced from 6.35 K to 5.78 K as a result of 12 minutes of etching. During that time, the 10 Kelvins resistance of the samples increased by 12 Ω . No corresponding data is available for etching at 150 Volts self-bias.

It will be seen in **Chapter 7** that 30 minutes is a typical duration for the bridge etch if a 300 V self-bias is used. Therefore it seems clear that the niobium films are robust enough to withstand a substantial over-etch. However, because over-etching also increases the resistance of exposed areas, the very non-uniform way in which the bridge etch has been shown to progress causes significant variation in the resistances of finished

HEB devices. It may be that the microbridge which suffers the greatest accumulated exposure over the duration of the bridge therefore exhibits the greatest resistance, even though every finished device from the same given set of devices outwardly appears identical.

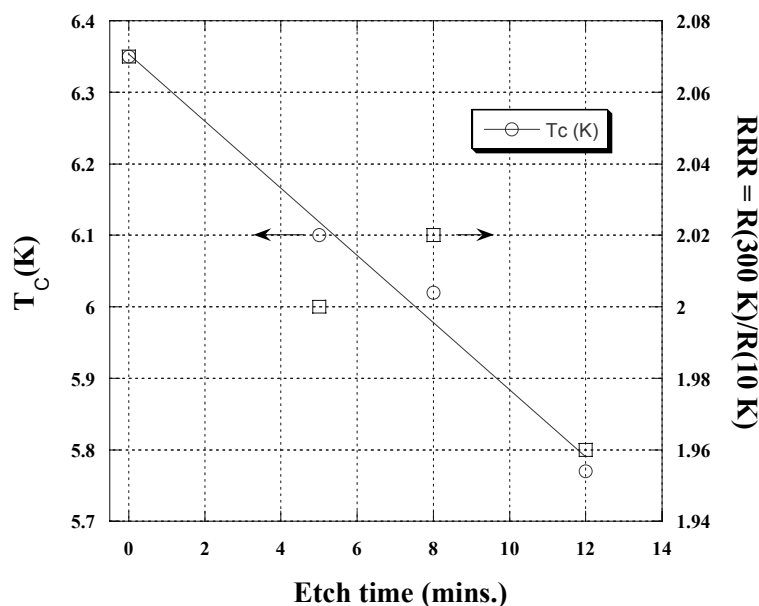


Figure 6.14. Argon etching robustness results for M2012B, showing the decrease of transition temperature and resistance ratio with etch time for a 100 Å niobium film. The samples were etched on a quartz platter at 300 Volts self-bias. The “etch time” is the number of minutes after the measured length of time required to remove the 250 Å thick layer of gold from the unmasked area.

For example, a set of four samples on a quartz substrate after two hours of etching at 150 Volts had resistances of 6, 32, 19, and 24 Ω at room temperature. The variation among these values is most likely due to incomplete removal of the gold from the microbridge kernel, as shown in **Figure 6.13**. An additional 75 minutes of etching removed all of the undesired gold, but the resistance variation remained - 95, 108, 87, and 121 Ω.

While there are many factors contributing substantially to the resistance non-uniformity of finished HEB devices, on the simple criterion of having a sample device

which can be tested and which superconducts, the yield of the process described in this chapter is quite good (perhaps 90%). The results of this fabrication protocol are presented in the next chapter.

CHAPTER 7 - FABRICATION RESULTS

1. Overview

The understanding developed in the last chapter involving the bridge etch, the effects of argon ion bombardment, and gallium implantation are used in this chapter to examine the actual characteristics and behavior of finished HEB microbridges. Among the properties which are investigated, which include R(T) and I(V) traces, the resistance ratio, and the ability of the superconducting thin film devices to absorb RF power, the normal state resistance and the uniformity of that trait among a set of devices fabricated identically are a principal concern. The resistance uniformity is introduced with respect to an alternate protocol to the FIB1-3 process, called the BtA/BtB process, which is self-aligned but ultimately not as well suited to the fabrication challenge as the method already described.

Because the FIB1-3 process sculpts microbridge kernels which are basically identical to each other, the bulk of this chapter is taken up by examination of how the bridge etch delivers (or fails to deliver) an acceptable degree of uniformity of device resistance. Bridge etches with argon plasmas at self-biases of both 300 Volts and 150 Volts were explored, the latter using test devices on both quartz and silicon/silicon nitride substrates. Ultimately, a deviation among a group of devices of $\pm 25\%$ or less seems representative of what the FIB1-3 fabrication process can achieve.

This chapter also details the methods of ESD suppression which were developed, and it will be seen that the yield of the FIB1-3 fabrication process (on the simple criterion of obtaining a device with a resistance similar to others in the same fabrication set) is extremely good. Of the three groups of HEB microbridges which were fabricated

(discussed in **Sections 7.3, 7.4, and 7.5**), the ratios of “good” devices were 37/38, 32/35, and 12/13, respectively. These compare to a published value for the fabrication process yield (based upon the DC device characteristics) by a method using EBL of 5% [**Ganzevles02**]. It will furthermore be shown that the target resistance of 50 Ω at 10 Kelvins can be met, and that niobium microbridges passivated with layers of sputtered germanium are stable and do not oxidize away.

Several possible reasons why the fabrication process fails to achieve consistent results between sets will be presented. Finally, it is suggested in this chapter that the structure of a completed device, although a superconducting HEB is merely a thin, narrow, short strip of metal, is quite complicated. This framework is employed to explain the behavior of three devices which were measured cryogenically, in data presented at the end of the chapter.

2. BtA/BtB Process

In addition to the three-step FIB1-3 procedure described in **Section 6.2**, in the early stages of this research a two-step procedure was also investigated [**Datesman99**]. This effort, using a “BtA/BtB” process, focused on the fabrication on quartz substrates of HEB devices with 1000 \AA thick layers of gold (much less than the 3000 \AA thickness subsequently adopted). A review of these attempts illustrates several of the fabrication issues discussed earlier.

The BtA and BtB patterns, shown in **Figure 7.1**, are basically each FIB1 patterns, except that the BtA pattern includes the microbridge kernel. This pattern, milled first, is intended to remove the niobium or chromium mask and a few hundred \AA of the

gold just beneath it. The appropriate BtA milling time is obtained through observation, either in real time or by measurement of a series of test patterns, or by use of a marker layer. The BtB pattern which follows mills down into the substrate, leaving behind a kernel very similar to that which results from the FIB1-3 process.



Figure 7.1. The BtA (left) and BtB patterns, used together, sculpt a microbridge kernel very similar to what results from the FIB1-3 process, but the patterns are self-aligning. (“Bt” stands for “bow-tie”).

The BtA/BtB procedure is different from the FIB1-3 process in several obvious ways, including some which represent advantages. The most significant of these is that the BtA/BtB process is self-aligned (both because the BtA and BtB patterns are registered to each other, and because the design of the patterns leaves some allowance for stage drift and other sources of error), whereas the FIB1-3 process is machine-aligned. There exist a few disadvantages, too: the potential for gallium contamination of the microbridge seems greater, it is probably not possible to manufacture narrow ($< 0.10 \mu\text{m}$ wide) microbridges by this technique, and the process includes no FIB2-type step to clean off material redeposited on the sides of the microbridge kernel. A hybrid BtA/BtB/FIB2 process might preserve the advantages of self-alignment while addressing these other concerns. An HEB microbridge fabricated using the BtA/BtB protocol is pictured in **Figure 7.2**, demonstrating that the process just described can produce desirable results. A set of samples prepared in this way (533B) had very uniform resistances at room temperature

all between 23-25 Ω , although similarly excellent results using this technique could not be reliably replicated in later attempts.

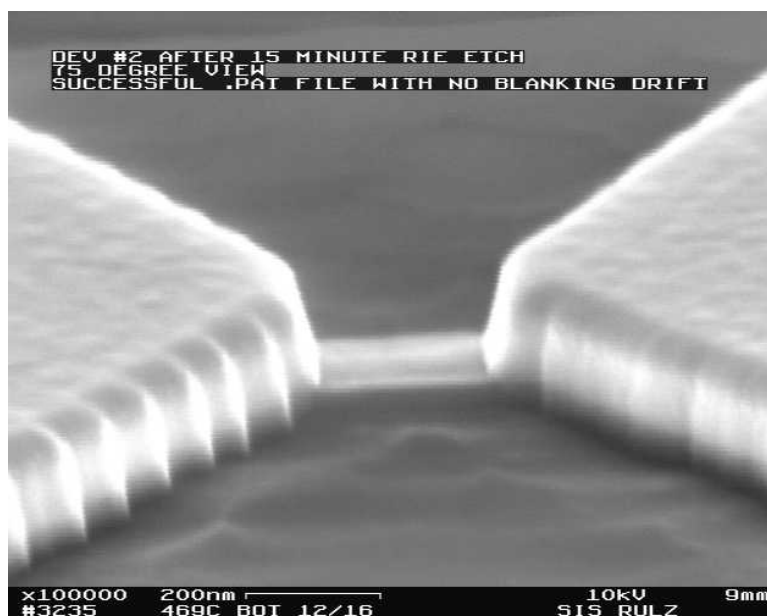


Figure 7.2. An HEB microbridge fabricated using the BtA/BtB process. The argon ion bridge etch was performed at 80 Watts using a quartz platter.

The fabrication efforts just described, predating the FIB1-3 process, involved quite wide microbridges and thin layers of gold, compared to the devices fabricated recently which are characterized in **Section 7.7**. A direct comparison between the two FIB fabrication methods is therefore not available, in part because the applicable knowledge about the bridge etch and methods of ESD suppression evolved considerably over time, but a few salient points may be noted.

Most significantly, the thinner 1000 Å layer of gold seem to mill more uniformly than the thicker layer used in its place at later times, so that it was possible for the BtB step usually to proceed less far into the substrate than the FIB1 step must. Therefore a FIB2-type cleaning of the edges of the microbridge kernel was sometimes not necessary

with the BtA/BtB process. In other cases this step would have been useful, had the idea existed at that time.

Self-alignment of the BtA and BtB patterns is a significant advantage of the previous process over the FIB3 machine alignment, which is difficult (and which would not work with thinner gold layers, due to simple geometrical considerations). However, the FIB1-3 process was judged to be a better accommodation to the difficult material properties of gold, as discussed in **Section 6.5**. As the BtA mill progresses, for instance, the tendency of the gold film to clump together under bombardment causes voids to form in the surface of the film, as shown in **Figure 7.3**. Since the formation of a void on top of the microbridge kernel might destroy the HEB device, the BtA step cannot be allowed to mill very deeply. Therefore the angled FIB3 mill removes more gold from the kernel than would likely be possible to remove safely with the BtA/BtB process.

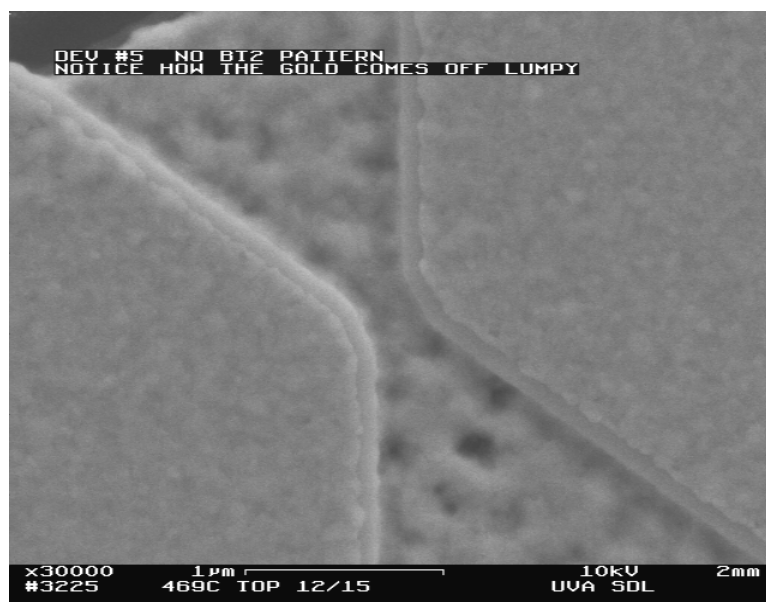


Figure 7.3. SEM photograph of a milled BtA bow-tie, clearly showing the non-uniformity of the milled surface, and the beginning of the formation of voids in the film. A void which formed in the location of the microbridge kernel could allow the entire surface of the microbridge to be contaminated with gallium, or even allow the device to be milled away.

Despite the avoidable uncertainty introduced by machine alignment, then, the FIB1-3 process is most likely superior even to an adapted BtA/BtB/FIB2 process. No direct comparison of results, either between the BtA/BtB and FIB1-3 processes, or between devices with 1000 Å and 3000 Å gold layers, is available

3. 300 Volt Argon Bridge Etch - Samples on Silicon/Silicon Nitride Substrates

A series of six sets of test HEB devices were fabricated between late January and early March, 2004, using a 300 Volt, 80 Watt, argon ion bridge etch. The RIE chamber was cleaned with a high-pressure ash for 30 minutes prior to each bridge etch, followed by an additional 25 minutes of conditioning. The etches were performed with a 50 sccm argon flow, at a pressure of 20 µm. In cases where the bridge etch was interrupted in order to monitor its progress, the sample was allowed to oxidize in atmosphere for 15 minutes before it was replaced in the RIE chamber. The argon plasma in the empty chamber was maintained during these intervals.

The sets of devices discussed in this section came from four Si/Si₃N₄ wafers, HEB10, HEB11, HEB12, and HEB14, which were manufactured according to the process described in **Section 6.2**. All were fabricated after the refurbishment of the niobium sputtering gun, when the stress of films deposited on to Si/Si₃N₄ substrates was found to be impossible to control, and low-stress films could not be obtained. Therefore, the HEB devices discussed in this section (and later, in **Sections 7.5 - 7.7**) are likely to have been fabricated from niobium films which were highly compressive and whose stress was not uniform between wafers (refer to **Section 6.3**).

The etch mask used in this case was 300 Å of chromium, not niobium, and the niobium microbridges were 100 Å thick. Since wet etchants suitable for chromium investigated during the course of this research turn out to undercut Ge-Cr interfaces and to damage niobium thin films, this material was later abandoned as a mask in favor of niobium, which can be removed simply by RIE. The bridge etch was performed on whole wafers (in some instances half of a wafer was masked with a clean glass slide), not on single dies. The Si_3N_4 membranes had not been released.

In order to maintain a clean etch, a pyrex dish was used as a platter. The wafer was held down within the dish using two 1" glass cover slips; half of each slip was greased down to the dish, so that the clean half of the slip functioned as a clip. This prevented the wafer from sliding around inside the RIE chamber. The wafer itself was not greased down, primarily because it would have been impossible to remove safely from the platter if it had been. The pyrex dish, cover slips, and slides (when they were used) were carefully prepared prior to the bridge etch by soaking in TCA and methanol for five minutes each, followed by a 10 minute cleaning in an oxygen plasma. The surface of the HEB wafer was also cleaned in an oxygen plasma prior to the bridge etch.

Handling the pyrex dish platter instead of the wafer was one important accommodation to the delicate nature of the HEB devices. Some adjustments to the use of the RIE were also made, with the purpose of minimizing the possibility of damage caused to the devices by electrostatic discharge (ESD). The first of these changes was that the active microwave tuners were locked into position during the chamber conditioning, before the beginning of the bridge etch. Therefore no adjustments to the electrical conditions of the plasma were made during the bridge etch. The second was

that the operator turned off the power input to the RIE plasma by turning it down to zero manually, rather than simply switching the power off. These protocols were instituted in order to minimize unnecessary electrical disturbances in the volume surrounding the HEB devices. While the results of the bridge etch which will be presented are neither precise nor accurate, it will be seen that a process which avoids the catastrophic failure indicative of ESD damage has been successfully developed.

The length and 10 Kelvin resistance (just above the transition temperature) of the HEB microbridges are the two most important parameters by which the devices are initially characterized. Although the HEB microbridge should superconduct at the operating temperature of 4.2 K, the 850 or 1450 GHz operating frequency exceeds the energy gap of the niobium thin film material, so that those areas of the device which absorb submillimeter radiation operate resistively. Therefore the normal state impedance of the microbridge must match the impedance of the microwave circuit in which the mixing element is embedded. This resistance is 50 Ω .

Because the residual resistance ratio

$$RRR = \frac{R(300K)}{R(10K)} \quad (7.1)$$

of 100 Å niobium films was found in **Section 6.5** to be approximately 2.1, it was assumed that the device target resistance at room temperature was about 105 Ω . In practice, HEB devices fabricated by the FIB1-3 method, on both silicon/silicon nitride and on quartz substrates, exhibit a resistance ratio of around 1.5. Therefore, the target resistance at room temperature should be about 75 Ω . The resistance of the contact pads, excluding the HEB device, is less than 1 Ω .

The first set of samples to use a 300 Volt bridge etch, HEB08, used a FIB2 pattern with a gap of 54 pixels (corresponding to the bridge width) and a FIB3 pattern 0.2 μm long (which determines the bridge length) by 0.2 μm deep. After etching in three stages for a total duration of 45 minutes, the average room temperature resistance among these five devices was $31 \pm 3 \Omega$. This $\pm 10\%$ uniformity suggests that it may be possible by the FIB1-3 method to fabricate a batch of devices with 10 Kelvin resistances of $50 \pm 5 \Omega$, although achievement of this goal has not been conclusively demonstrated.

The HEB08 microbridges were measured to be approximately 0.32 μm wide and are assumed to measure about 0.12 μm long (based upon the information presented in **Figure 6.12** and upon the 0.2 μm length of the FIB3 pattern). Based upon these HEB08 results, increasing the FIB3 length (to 0.3 μm) and decreasing the FIB2 gap (to 40 pixels) should yield a microbridge 0.22 μm long by 0.24 μm wide, with a room temperature resistance of 75 Ω . This fabrication was not undertaken, because it was believed at the time that the appropriate room temperature target resistance was 105 Ω . Typical dimensions for a niobium DHEB reported in the literature are around 0.25 μm long by 0.15 μm wide [Skalare95].

Therefore, for subsequent fabrication sessions, the FIB3 length was increased (to 0.3 μm) as described, but the FIB2 gap distance was chosen to be quite narrow (28 pixels). The results of the 300 Volt bridge etch tests are shown in **Figure 7.4**. Between 4 and 8 individual samples were included in each set of test devices. No devices described in this section were cryogenically tested.

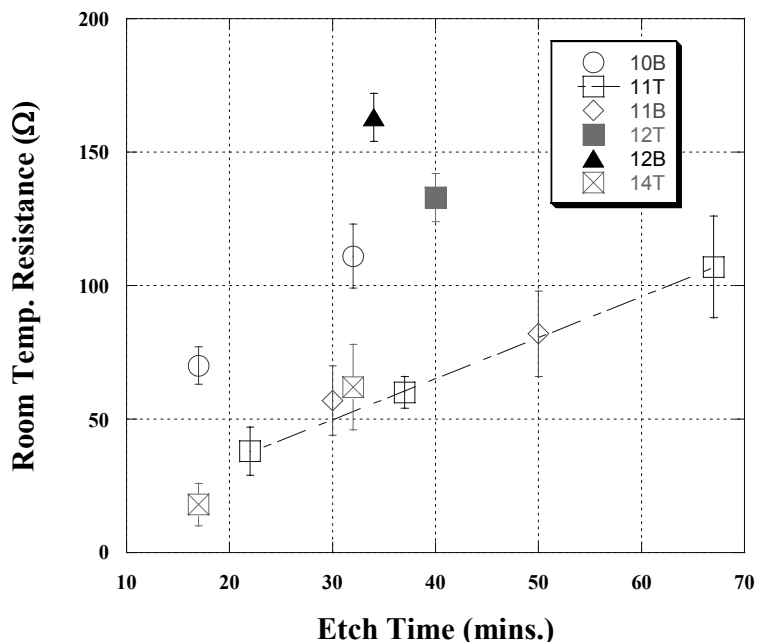


Figure 7.4. Results of the 300 Volt bridge etch tests for the HEB10T - HEB14T sets. Several marks for one set indicate that the wafer was removed from the RIE and measured, after which the bridge etch was resumed. The two solid marks indicate sets which were etched continuously without interruption. The experiments were intentionally extended beyond the 75 Ω target resistance.

Noting that the six sets of devices represented in **Figure 7.4** were fabricated under nominally identical conditions, the results obtained with the FIB1-3 process and the 300 Volt bridge etch were not terrifically consistent between the distinct sets. Several useful observations may be made regarding these results, however.

1. Within individual sets, device resistance uniformity of $\pm 26\%$ or better was obtained in every case. The data points for three of the four sets etched in stages lie on nearly the same resistance vs. etch time line. These three sets came from two different wafers (HEB11 and HEB14), and were fabricated and etched a few weeks apart.

2. HEB11T, which was etched in three stages, showed a linear increase in the device resistance with increasing etch time. About 20 minutes of etching was required to clear the microbridge kernels of gold.
3. It seems advantageous to break the bridge etch up into stages, rather than to etch without interruption for times exceeding 20 minutes. A short (15 minute) pause, during which time the etched sample devices are held in atmosphere, allows exposed regions of the niobium microbridge to oxidize slightly. This treatment hardens the material and increases its resiliency to argon ion bombardment. The two sets which were etched continuously (HEB12T and HEB12B) remained unoxidized during the bridge etch, were therefore less resilient, and exhibited much higher resistances than sets etched in stages for equal cumulative durations.
4. Every one of the four sets etched in stages was measured at a point where the average resistance among the devices in the set lay within 20% of the 75 Ω target resistance (specifically, between 60 - 82 Ω).
5. Out of the 38 devices belonging to the HEB10T - HEB14T sets, all but one survived without showing the sudden increase in resistance which indicates possible ESD damage (this one was removed from the results presented). While these wafers were neither membrane etched nor diced, this was a very promising development at the time. When the membrane etch and dicing were moved within the processing order to precede the bridge etch (refer to **Table 5.1**), this advance brought the ESD issue largely under control (for devices on Si/Si₃N₄).

With reference to **Figure 7.4**, comparing individual sets of devices to other sets, there are several possible reasons why three of the sets under discussion (HEB10B, HEB12T, and HEB12B) fail to lie on the indicated line. The first of these explanations, which has already been mentioned, is that the HEB12 sets were not bridge etched in stages, as the others were. Lacking the protection of a thin layer of oxidized material as the bridge etch continued, the devices in the HEB12 sets did not respond to argon ion bombardment as robustly as did the other sets of microbridges.

It was found in **Section 6.3** that the stress of niobium films deposited on silicon/silicon nitride substrates cannot be reliably controlled. Therefore, a second plausible explanation for the variation between sets which was observed is that the niobium film stress varied greatly between the four wafers which were examined.

Because only the HEB14T set was actually examined in the SEM, it is also possible that the microbridges in separate sets, while nominally identical, in fact possessed different dimensions. Although the calibration protocol was improved just before these experiments were undertaken, this could still result from an incorrect magnification calibration. For instance, using the old protocol (calibrating the magnification at 50 kx), it had been observed that the magnification can vary from its nominal value by as much as 20%. Because the actual width of the microbridge decreases much faster than its specified width in pixels (refer to **Section 7.4**) if the microbridge is narrow (less than 0.20 μm wide), an error of this degree could change the device resistance by as much as 30%. With the new calibration protocol (calibrating only once per session, at 10 kx), such a large error is unlikely to occur. But it was

nevertheless observed during the FIB session for HEB12B that the magnification calibration seemed somewhat different than it had been during previous sessions.

Since the bridge etch has been observed to be more aggressive when the RIE chamber has been recently cleaned, a fourth and final possible explanation for the observed discrepancy between the sets is that the condition of the RIE chamber evolves continuously over time. Because the RIE system is shared between many lab users, who utilize fluorine- and chlorine-based chemistries in a number of fairly dirty processes (including for silicon nitride etching), the RIE chamber condition is a difficult variable to control or even to quantify.

Among the four possible explanations for the observed variation between sets just offered, it is not possible to settle the issue conclusively given the data available. However, SEM measurements ought to settle the magnification calibration issue, and additional experience with the fabrication process should reveal what contribution to the variation between sets is due to the niobium film stress and whether interrupting the bridge etch to oxidize the samples in atmosphere really does have the described effect.

Even if the RIE chamber condition is in fact an important source of the observed non-uniformity between sets, it should still be possible to create a robust and controllable fabrication process by working in parallel with two or three sets of test devices. The bridge etch and measurement of the first two sets could be used to establish the RIE conditions (i.e., a line such as that shown in **Figure 7.4**) for the subsequent “money run”.

Because the HEB10B and HEB12 sets failed to fall on the line in **Figure 7.4**, it is not quite clear what FIB1-3 parameters (i.e., FIB2 gap and FIB3 length) should be chosen in order to achieve a 75Ω RT target resistance. According to the information presented

in **Figure 7.4**, the dimensions which were used were about appropriate for the HEB11 and HEB14T sets. The resistances of the devices belonging to the HEB10B and HEB12 sets, however, were much too great, indicating that in those instances the chosen FIB2 microbridge dimension was too narrow. It may be that the appropriate microbridge width must be empirically determined for each fabrication run by working in parallel with several sets of devices in the manner just described, because the stress of the thin niobium film from which the HEB is fabricated cannot be controlled (and is not known), and because the condition and cleanliness of the RIE chamber is also not known and cannot be quantified.

The approximately 25% variation within sets of devices also merits examination. Two sets of wider microbridges (HEB08, with a FIB2 gap of 54 pixels, and HEB10T, 32 pixels) exhibited standard deviations within their sets of only 10%. (This was also true of HEB10B, and at one point in the trace for HEB11T; both sets of HEB12 were in fact better than 10%. The FIB2 gap for all of the HEB10B - HEB14T sets was 28 pixels.) It will be seen in **Section 7.4** that microbridges within a set, while nominally identical, in fact vary in width rather significantly. Two devices belonging to the M2721A set, for instance, with a FIB2 gap also of 28 pixels, were measured to be 0.16 and 0.18 μm wide. This represents a $\pm 6\%$ variation in the width and in the device resistance, assuming that the microbridge is homogenous across its width (which it is not). It is possible that this variation is the result of the microbridge kernel being worn away during the focusing and alignment prior to the FIB3 step, since the actual duration of that exposure can vary significantly from device to device within a set.

The information presented in **Section 6.5** regarding the robustness of thin niobium films also helps to explain the non-uniformity which is observed within a set of devices. Because the FIB3 step is user-aligned to the FIB image, the thickness of gold remaining in the microbridge kernels after the FIB3 step varies significantly - as much as 200 Å, or 20% of the approximately 1000 Å total - within a set of devices (see **Section 6.2**). Even if one assumes (wrongly) that gold is sputtered away from the microbridges evenly and uniformly, during the bridge etch some niobium microbridges within the set will be fully exposed while others are still partially covered with gold. These devices suffer a greater cumulative duration of argon ion bombardment than the others, and therefore will exhibit a greater resistance.

Section 6.5 presented relevant information about the increase in resistance of a 100 Å niobium thin film with a large area (more than 10 µm on a side) under 300 Volt argon ion bombardment. **Table 7.1** presents that data along with similar information for two HEB microbridges which were etched in stages. The results, obtained by applying a linear fit to the resistance vs. etch time data, show that the room temperature sheet resistance of a 100 Å thick niobium HEB microbridge increases by between 1 - 3 Ω/□ per minute of etching with argon ions at 300 Volts self-bias.

Sample	Slope (Ω/min.)	Time (mins.)	Squares (□)	Rate (Ω/□/min.)
HEB10T	2	32	0.63	3.1
HEB11T	1.5	45	1.2	1.2
M2012B	2.3	12	1.2	1.9

Table 7.1. Effect of 300 Volt argon ion bombardment upon the sheet resistance of thin niobium films at room temperature. HEB10T and HEB11T are sample HEB devices on Si/Si₃N₄ substrates which were etched in stages. M2012B is a large-area niobium film on a quartz substrate which was etched without interruption.

Using the measured gold etch rate of $75 \text{ \AA}/\text{minute}$, a 200 \AA thickness of gold, and the rate of increase found in **Table 7.1** ($1.5 \text{ \Omega}/\text{min.}$ for HEB11T), one concludes that a 4 \Omega variation in the microbridge resistance may result from the variation of the FIB3 alignment. This represents a further 5% variation for a 75 \Omega device. This may understate the case somewhat, since the other rates listed in **Table 7.1** are significantly higher than that found for HEB11T, and the effective gold etch rate on the microbridge kernel is probably slower than that stated, for reasons described in **Section 6.5**.

In addition to the two non-uniformities just analyzed, of course the HEBs are fabricated from a rather delicate thin film sputter deposited over a large area. The properties of this film should be expected to vary somewhat over the surface of the wafer, which perhaps explains the variation which remains beyond those contributed by FIB fabrication uncertainties. Although the device uniformity within a set should therefore never be expected to be perfect, and will perhaps never be much better than $\pm 25\%$ using the FIB1-3 process, a method for trimming finished HEB devices to the desired value is suggested in **Appendix C**.

Figure 7.5 tracks the time evolution of the resistivity (that is, the data presents the device resistances normalized to the microbridge areas) of a set of wide microbridges (HEB08, 0.12 \mu m long by 0.32 \mu m wide) next to that of a set of narrow bridges (HEB10T, 0.12 \mu m long by 0.19 \mu m wide, 32 pixel FIB2 gap), and the HEB10B and HEB11T (0.18 \mu m wide) data points from **Figure 7.4**. This graph reveals several interesting things.

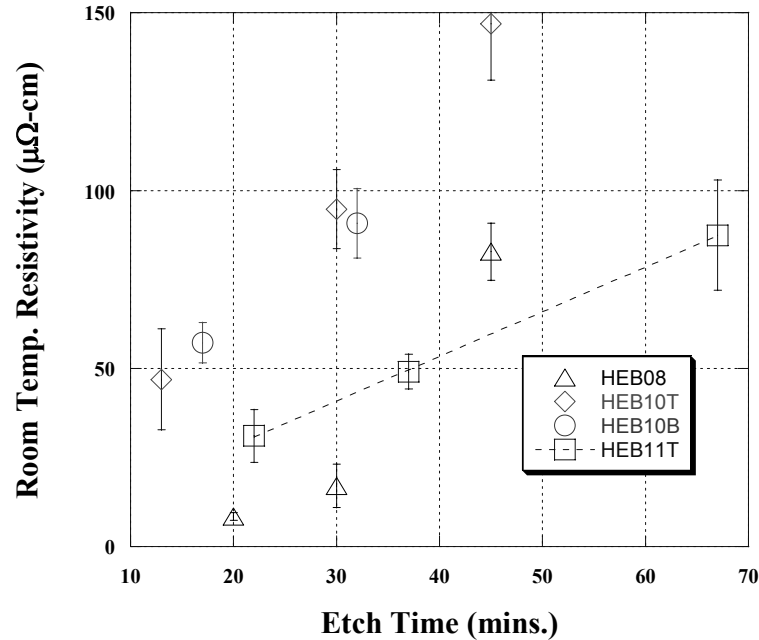


Figure 7.5. Time evolution of the resistivity ($\rho = RA/\ell$) of wide (HEB08 - 0.32 μm) and narrow (HEB10T - 0.19 μm) microbridges. Two of the curves from **Figure 7.4**, HEB10B and HEB11T (0.18 μm), are included for reference.

First, the HEB10T data points nearly coincide with the HEB10B data points, and do not lie near the HEB11T line from **Figure 7.4** which is included for reference. This suggests very strongly that, while niobium film stress or chamber conditioning (HEB10T and HEB10B were bridge etched only two days apart) might each be responsible for the observed variation between sets of devices, an incorrect magnification calibration is not responsible.

The second interesting feature of **Figure 7.5** has to do with the HEB08 set. Unlike the other two sets etched in three stages (HEB10T and HEB11T), the three points of HEB08 fail to lie on a line. This suggests that the HEB08 microbridge kernels were not etched clear of gold even after approximately 30 minutes of etching. This compares to a time of 20 minutes (or less) to completely etch narrower microbridges, after which their increase in microbridge resistance (resistivity) is seen to be linear with time.

Because the gold in the microbridge kernel withdraws toward the protected ends of the structure as it is sputtered away, the problem of determining just when the bridge etch is finished is not completely obvious. This issue is discussed further in **Section 7.4**.

Because all of the microbridge kernels (ideally) possess the same thickness of gold, whatever their width, this observation regarding the wide HEB08 microbridges suggests that the effective gold etch rate under argon ion bombardment depends upon the lateral dimension of the etched structure. With the understanding developed in **Chapter 6** that gold layers under bombardment (by argon or by gallium ions) are deformed dynamically at the same time that a portion of the film is sputtered away, this observation seems plausible. However, it is also possible that the FIB3 mill leaves a greater thickness of gold behind if the kernel is wider.

Finally, **Figure 7.6** shows an SEM photograph of one of the HEB10T microbridges just discussed, along with two photos of a microbridge from the HEB14T set. These two photographs represent the devices in the HEB10B - HEB14T sets, which were all fabricated under identical conditions, and which comprised the principal focus of this section.

To conclude, the RIE bridge etch using a 300 Volt self-bias produces HEB microbridges which seem to be quite robust with respect to ESD damage and reasonably uniform results (within a single set of devices, the uniformity of device resistance is not worse than $\pm 26\%$, and often better). The results were also seen to vary significantly between the sets, for which variable RIE chamber conditioning and/or the poorly controlled stress of niobium films on silicon/silicon nitride substrates are likely responsible. Variation of the microbridge width and of the thickness of gold remaining in

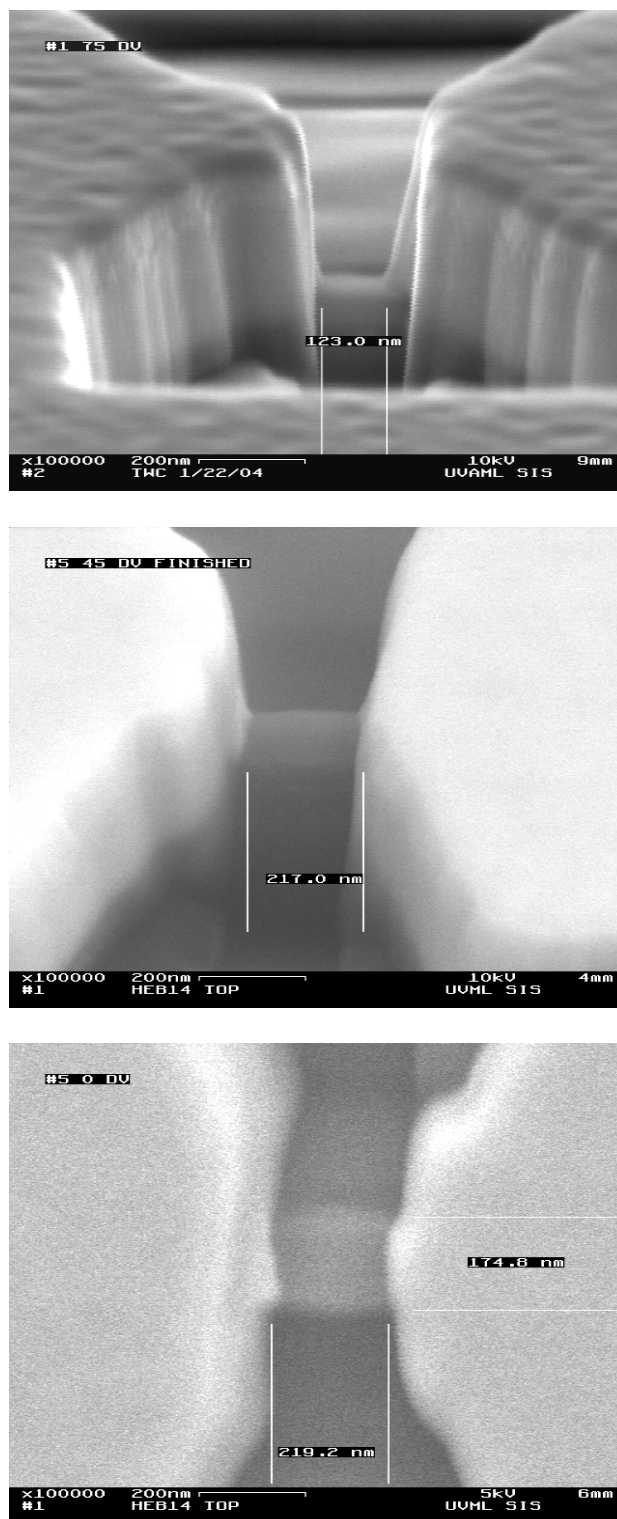


Figure 7.6. SEM photographs of HEB microbridges fabricated with 300 V argon ion bridge etches. From top to bottom, HEB10T (0.20 μm long FIB3), HEB14T (0.30 μm long FIB3), and the same device in a straight-on view, showing its true dimensions.

the microbridge kernel after the FIB3 step were shown to account for a significant portion of the non-uniformity observed within a set.

The sheet resistance at room temperature of HEB microbridges fabricated from 100 Å films was found to be between 50 - 67 Ω/\square (HEB10B, HEB11, and HEB14T), and devices exposed to argon ion bombardment were found to increase in resistance at a rate of approximately 2 $\Omega/\square/\text{min}$. once clear of gold. Microbridges as small as 0.12 μm long by 0.18 μm wide were successfully fabricated, and devices reasonably close to the 75 Ω target resistance were obtained.

4. 150 Volt Argon Bridge Etch - Samples on Quartz Substrates

It was proposed in **Section 7.3** that the variation of microbridge resistance observed among the single devices comprising one fabrication set may in part be caused by argon ion bombardment of the niobium films exposed during the course of the bridge etch. According to this explanation, the variation arises because the FIB3 step leaves behind thicknesses of gold in the microbridge kernels which are not quite uniform from device to device. With the expectation that lower energy ions should treat thin niobium films more gently than the 300 Volt etch described in **Section 7.3**, an argon ion bridge etch using 150 Volts self-bias was also examined. The results of these experiments are compiled in **Table 7.2** (for devices on quartz substrates) and in **Section 7.5** for sample devices on Si/Si₃N₄ substrates.

The etch conditions were similar to those examined previously, although with lower power: 20 Watts, 150 Volts with 50 sccm argon gas flow and a fixed pressure of 20 μm . A clean pyrex dish was again used for an etch platter, and the same protocols of

ESD suppression explained previously were employed. However, for the experiments described in this section, it was possible to thermally sink the samples with L-grease, and this was done. Therefore, during the bridge etch, the wafers or samples were greased down to a clean glass slide which sat inside the pyrex dish. Thereafter, the samples were never handled until dismounted from the glass slide after passivation, which helped to minimize the possibility of ESD damage. Only one set of test samples were diced and subsequently mounted on the slide (M2747CT); the other sets included 2, 3, or 4 samples together on a piece of the wafer which had been broken away with the edge of a metal ruler, and were mounted on the slide.

In a final change, every fabrication discussed in which a 150 Volt bridge etch was employed used a FIB3 depth of 0.15 μm , compared to the 0.20 μm depth used in the experiments described in **Section 7.3**. Therefore the slower etch at 150 Volts was used to reveal microbridges covered with somewhat greater thicknesses of gold. The relevant etch rates for gold at 300 Volts and at 150 Volts, as discussed in **Section 6.5**, are 75 and 9 $\text{\AA}/\text{min}$, respectively.

The results for 150 Volt bridge etching of samples on quartz substrates are presented in **Table 7.2**. Because these sets mostly include only a few samples, not many statements with true statistical validity can be made. A series of comments regarding the data presented in **Table 7.2** follows.

Sample	RT Resistance (Ω)	Etch time (mins.)	FIB2 width (pixels)
M2721AT 1,4,5	73,56,42	200	28
ditto T 3,6,7,8*	62 ± 4	240	28
M2747BT 2,6	110,121	150	18
ditto T 4,5*	118,143	150	18
ditto B 1,4,5	195,215,161	135	18
ditto B 2,3,6,8	157 ± 7	105	18
M2721B T 1,2	148,133	150	18
ditto T 3,8,7	67,74,82	210	24
ditto T 4,5,6	52,50,48	210	30
M2781BT 1,3*	124,86	135	22
M2747CT 1-4(B)	103 ± 15	195	25

Table 7.2. Results of the 150 Volt argon ion bridge etch for HEB devices on quartz substrates. The FIB3 length was 0.30 μm in every case. An asterisk (*) indicates that one test device in that set was damaged by ESD and is not listed. Device (B) is discussed in **Section 7.7**. Etch time refers to the total cumulative time, although in every case the bridge etch was broken down into as many as six stages.

1. There are several general comments about the data shown in **Table 7.2**. First, M2721A,B possessed a chromium layer for the etch mask, while M2747B,C and M2781B each used an equal thickness of niobium for that purpose. Second, at the time that these sets were fabricated, it was still believed that the target resistance was 105 Ω . Third, out of the 35 devices described in this section, three were lost due to ESD, which is somewhat more severe than the problem encountered for devices on Si/Si₃N₄ substrates (1 out of 38 lost). Finally, the four samples of M2747CT were

- diced before being mounted on a clean glass slide for the bridge etch. One of these devices was cryogenically tested.
2. Three sets included four devices, which is just enough to provide some statistical validity. These sets exhibited standard deviations of the device resistances within the individual sets of 6% (M2721AT 3,6,7,8, 28 pixels wide), 4% (M2747BB 2,3,6,8, 18 pixels wide), and 15% (M2747CT 1-4, 25 pixels wide). This is promising by comparison to the corresponding result with a 300 Volt etch and samples on silicon/silicon nitride substrates (not worse than 26%).
 3. The bridge etch of the M2721AT 1,4,5 set was not quite completed; these samples are pictured in **Figure 6.13**. The samples of M2721AT 3,6,7,8 possessed the same dimensions (FIB2 gap 28 pixels, FIB3 length 0.30 μm), and were etched completely. These dimensions were the same as those used for the HEB10B - HEB14T sets described in **Section 7.3**. The M2721AT 3,6,7,8 set (62 Ω) is nearly identical to the HEB11 and HEB14T sets (60, 57, 62 Ω) represented in **Figure 7.4**. The sheet resistance at room temperature of the M2721A HEB microbridges is about 50 Ω/\square .
 4. The measured widths of the devices in the M2721AT 1,4,5 set were between 0.16 - 0.18 μm (28 pixel FIB2 gap). For the M2781BT 1,3 set, where the FIB2 gap was reduced to 22 pixels, the measured microbridge widths lay between 0.08 - 0.11 μm . The uncertainty in the microbridge width (for a microbridge of any width) is therefore at least $\pm 0.01 \mu\text{m}$. Realistically, the width of the actual thin and narrow niobium film is quite difficult to measure.
 5. Extremely narrow microbridges were successfully fabricated. Because a 22 pixel FIB2 gap produced a microbridge measured to be 0.08 μm wide, if the magnification

- calibration operated consistently, then the 13 microbridges which were fabricated using a FIB2 gap of 18 pixels may have been as narrow as 700 Å. However, none were measured directly by SEM.
6. A set of samples (M2721BT 3,7,8) were fabricated at the 75 Ω target resistance, spread between 67 - 82 Ω.
 7. The data in **Table 7.2** seem to describe a process which is quite repeatable for samples sets taken from the same wafer and FIB session (M2721AT and M2747BT), not repeatable for nominally identical samples from different wafers (M27221BT 3,7,8 vs. M2747CT 1-4), and not even repeatable for sets taken from the same wafer but fabricated in separate FIB sessions and etched a few days apart (M2747BT and M2747BB, discussed shortly). Because the stress of niobium films deposited on to quartz substrates was carefully controlled during the course of this work, this suggests that an inconsistent magnification calibration, the variable condition of the RIE chamber, or both, are at fault. Because many of the microbridges described in this section are much narrower than those described in **Section 7.4**, the magnification calibration issue is a very likely explanation.

Photographs of an HEB microbridge fabricated on a quartz substrate are shown in **Figure 7.7**.

Two other features of these experiments deserve mention. The second relates to the three M2721BT sets, which were fabricated in a single FIB session using different FIB2 widths. The first relates to the M2747B sets, where the top and bottom halves were fabricated in separate FIB sessions, and turned out rather dissimilarly. A graph showing

how the four separate bridge etches of those sets developed with time is shown in **Figure 7.8**. This graph possesses one noteworthy feature.

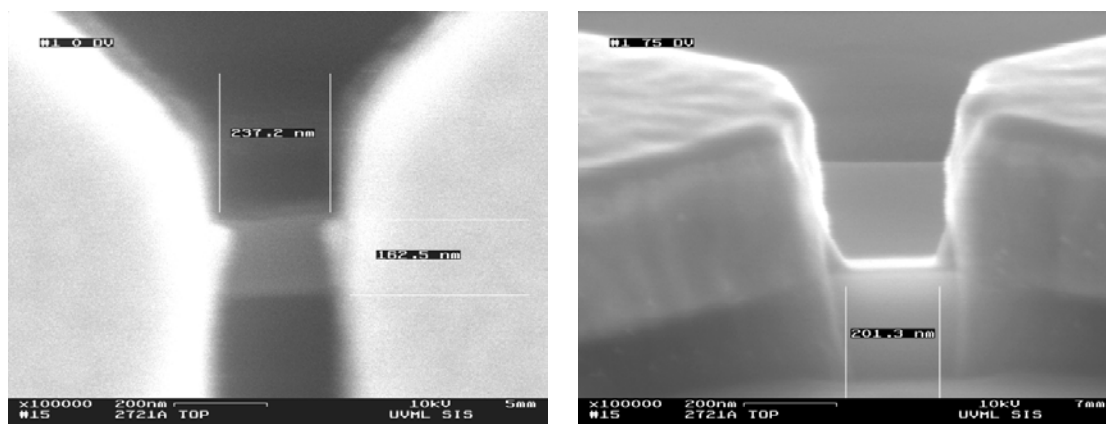


Figure 7.7. SEM photos of M2721AT #1, fabricated with a 28 pixel FIB2 gap and a 150 Volt bridge etch.

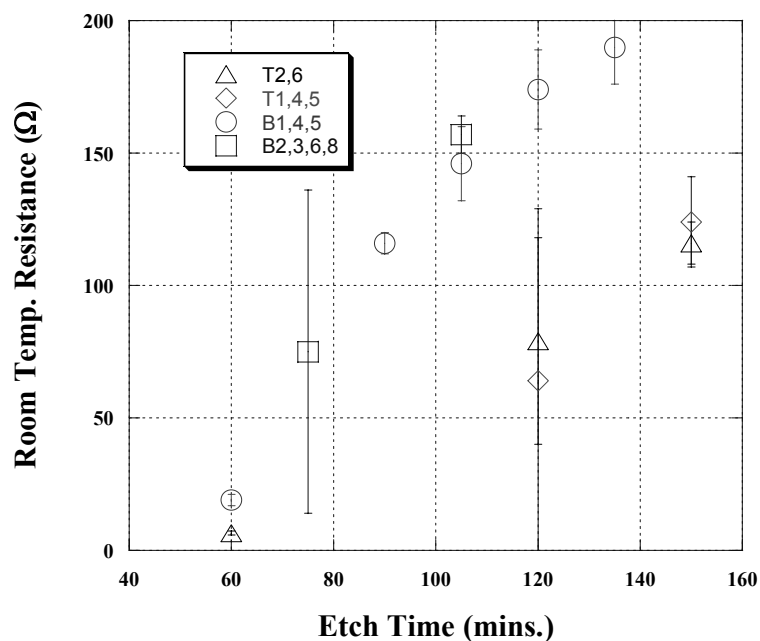


Figure 7.8. Results of the 150 Volt bridge etch of the M2747B sets. The sets from the top half of the wafer were fabricated in the FIB together, separately from the two sets from the bottom half of the wafer, which were also fabricated together, but etched separately.

The curves for the M2747BT (“T2,6” and “T1,4,5”) and M2747BB (“B1,4,5” and “B2,3,6,8”) sets coincide with themselves (so that the bridge etch itself is repeatable), but

not with each other, even though the FIB fabrication process was nominally identical for both the top and bottom sections. Because niobium film stress should not be an issue for devices fabricated on quartz, and because this result is extremely unlikely to have arisen due to the variable condition of the RIE chamber, one must conclude that the magnification calibration is not perfectly consistent from session to session. The inconsistency of the calibration has a significant effect when the microbridge is very narrow (in this case, less than 0.10 μm wide).

The three sets which comprise M2721B were all fabricated in a single FIB session, but with different widths, in order to obtain some perspective on the difficulty which exists in estimating what dimensions are desired based upon the target resistance and a trial run. The results of this experiment are displayed in **Table 7.3**, which also includes information about the two sets of samples described in this section which were measured by SEM.

Width (pxls)	Msrd. width (μm)	RT R (Ω)	Rw (Ω -pixel)	Rw (Ω - μm)
28	0.17	62	1700	10.5
22	0.10	105	2310	10.5
18		141	2500	
24		74	1800	
30		50	1500	

Table 7.3. Results of the resistance vs. microbridge width experiment of M2721BT. The Rw product, where w is measured in pixels, increases for narrower microbridges, although it should be constant. The measured widths (for M2721AT and M2781BB) are accurate $\pm 0.015 \mu\text{m}$.

Given that the resistance of a thin metallic strip is described by the equation $R = \rho\ell/wt$, if one assumes that the length, thickness, and resistivity of every

microbridge belonging to a group of samples is the same (as they ideally should be), then the product of the resistance and the width, Rw , should be constant. This is in fact the case for the two sets of samples whose physical dimensions were measured by SEM, shown in the first two lines of **Table 7.3**.

For the two samples whose physical dimensions are known, it is interesting to note that the Rw product is not constant if w is measured in pixels, replacing the physical width; instead, Rw_{pixels} increases as the width decreases. This is also the case for the three sets belonging to M2721BT. This indicates that narrow microbridges are not physically as wide as their corresponding specification in FIB pattern pixels, which occurs because the ion beam melts a small volume of gold where it strikes, rather than sputtering the film away evenly, because of edge sputtering, and because of other non-ideal effects. Assuming the measured Rw product of $10.5 \Omega\text{-}\mu\text{m}$, the microbridges with an 18 pixel FIB2 gap should physically measure only about $0.07 \mu\text{m}$ across. The size of the FIB2 gap in this case, measured on the FIB screen, is $0.10 \mu\text{m}$.

To conclude this discussion, the results just described for 150 Volt bridge etching of devices on quartz substrates show a process which seems somewhat more uniform (perhaps better than 15% within a set) than the 300 Volt bridge etch of devices on silicon/silicon nitride substrates discussed in **Section 7.3**. Comparing sets from different wafers, and from different FIB sessions, the 150 Volt bridge etch examined in this section does not seem to be much more consistent or controllable than the previously described 300 Volt etch. However, the samples fabricated in this section were much narrower (as small as $0.07 \mu\text{m}$) than those fabricated in **Section 7.3** ($0.18 \mu\text{m}$ wide), so a true comparison is not available. The effects of inconsistent magnification calibration were

shown to be significant for such very narrow samples, and it was also observed for narrow devices that the physical width of the niobium microbridge decreases as the FIB2 microbridge width in pixels is reduced faster than linearly.

In addition to changing the etch power and voltage, the substrate, the thermal anchoring of the samples during the bridge etch, and the size of the FIB2 gap from the conditions used during the experiments described in **Section 7.3**, the depth of the FIB3 mill was also reduced from 0.20 μm to 0.15 μm . Nevertheless, after a long etch (4 hours), basically identical results (62 Ω) were obtained with a set of microbridges using the same 28 pixel width. A set of samples fabricated with a 24 pixel width met the target resistance of 75 Ω , although they were not cryogenically tested.

One device from M2747CT was successfully tested at cryogenic temperatures. Its R(T) and I(V) traces are included in **Section 7.7**.

5. 150 Volt Argon Bridge Etch - Samples on Silicon/Silicon Nitride Substrates

HEB devices were fabricated on Si/Si₃N₄ substrates and on silicon nitride membranes over a time span of four months using a 150 Volt bridge etch as described in **Section 7.4** for devices on quartz substrates. The samples came from only two wafers, HEB19 and HEB21, were diced prior to imaging gold deposition, and were processed through the FIB in sets of only two or three. Two 1x5 arrays were fabricated concurrently with the samples described in this section. The samples and array dies were affixed to clean glass slides using L-grease prior to the bridge etch. Until the samples and arrays were passivated, only the glass slide, used as a carrier, was handled. This minimized the risk posed to the delicate HEB devices by ESD.

The results which were obtained for 150 Volt bridge etching of HEB devices on Si/Si₃N₄ substrates are tabulated in **Table 7.4**. Since so few devices were fabricated, no statement with statistical weight can be made. Of the runs outlined in **Table 7.4**, HEB19T 8-10 was not etched completely. HEB19T2 and HEB19B5, which turned out reasonably similar to each other, were in fact fabricated in the same session and bridge etched together, and so comprise a set (except that one sits on a membrane, and the other does not).

Sample	RT R (Ω)	Etch time (mins.)	FIB3 length (μm)	RRR
19T 8-10	46, 21,81	135	0.30	
19T 6 (A),7	116, 100	120	0.30	1.57, 1.70*
19T 2	80	90	0.30	1.47
19B 5 (m)	95	90	0.30	
19B 3 (m)	146	90	0.30	
19B 8-10 (m)	(170), 94, 71	135		1.47, 1.40
21T7(C),8 (m)	63, 71	220	0.25	1.44*

Table 7.4. Results of the 150 V argon ion bridge etch for HEB devices on Si/Si₃N₄ substrates and on silicon nitride membranes. The etch mask for both the HEB19 and HEB21 wafers was 300 Å of niobium. An asterisk (*) indicates that the measured devices were passivated, and (m) denotes that the indicated set of devices was fabricated on released membranes. Devices (A) and (C) are discussed in **Section 7.7**. The FIB2 width was 22 pixels; the FIB3 depth was 0.15 μm .

Out of the thirteen sample devices fabricated, the resistances of four lie within 10% of the 75 Ω target resistance. (None of these were successfully measured cryogenically.) The resistance ratios, between 1.40 - 1.70, are in line with the value of RRR = 1.59 for the single device on a quartz substrate which was measured. Aside from these two observations, the only obvious conclusion that one may draw from the data

presented in **Table 7.4** is that the results are rather inconsistent. This might be caused by an inconsistent magnification calibration, as discussed in **Section 7.4**, by changes in the condition of the RIE chamber, or even by stage drift in the FIB. The issue of stage drift must be addressed carefully when individual dies are processed, since it is necessary to re-align the sample stage for every individual die.

Several of the finished devices listed in **Table 7.4** were passivated. Deposition of a layer of sputtered germanium on to a finished niobium microbridge does not alter its resistance, and the resistance of an HEB device passivated with this material remains stable over a long period of time (months). Therefore, a sample which is passivated almost immediately after the bridge etch will maintain the resistance which was measured upon removal from the RIE chamber. If the device is left unpassivated, on the other hand, in most cases its resistance will increase by between 5 - 10% over a time of about 24 hours. Left exposed to atmosphere after this point, in some cases the resistance will not increase further; in other cases, unpassivated devices eventually open-circuit. HEB19T2, after a week left unpassivated, did not change in resistance beyond the first 24 hours, but it was found not to superconduct at 4.2 Kelvins. Because devices fabricated identically to HEB19T2 did superconduct at LHe temperature, the failure of that device to superconduct is most likely the result of oxidation of the unprotected film.

Cryogenic results for samples "A" and "C" are presented in **Section 7.7**. SEM photographs of HEB19B9 are shown in **Figure 7.9**. The room temperature sheet resistance of this device is about $44 \Omega/\square$; at 10 Kelvins, $32 \Omega/\square$.

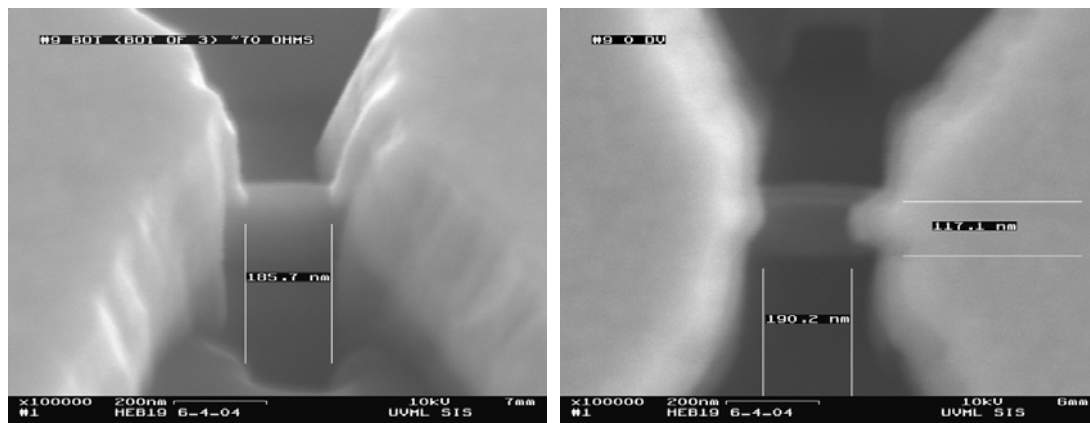


Figure 7.9. SEM photographs of HEB19B #9, a device on a silicon nitride membrane bridge etched at 150 Volts.

In summary of the discussions about the bridge etch contained in the last three sections, the most important point to be made is that the fabrication process seems to work about as well for devices on silicon nitride and on silicon nitride membranes as it does for devices on quartz substrates. Because slight modifications to the fabrication process were made, and because of the small number of samples fabricated on Si/Si₃N₄ using a 150 Volt bridge etch, a truly accurate comparison between the effectiveness or success of the bridge etch at 150 Volts and the 300 Volt bridge etch results presented in **Section 7.3** is not possible. However, it seems clear that the 150 Volt bridge etch does not offer a dramatic improvement.

Analysis of the cryogenic results begins in the next section, with an examination of the residual resistance ratio of completed HEB devices.

6. Resistance Ratio

Films of niobium 100 Å thick on quartz substrates possess highly uniform values of the resistance ratio around RRR = 2 (refer to **Figure 6.14**), so the reduction in and variability of the resistance ratio exhibited by finished HEB microbridges (as shown in

Table 7.4, between 1.4 - 1.7, with 1.6 measured for a device on a quartz substrate) is a result of the fabrication process. This section examines why this variation might occur.

The behavior of thin niobium films irradiated with 30 keV gallium ions is more complicated than described in **Section 6.4**, although the finding that implantation of large doses of gallium into 100 Å niobium thin films lowers their transition temperature is certainly correct. In addition to T_C suppression, implantation into these films changes their resistance and lowers their resistance ratio. To determine the extent of this reduction, a sample curve from the gallium implantation experiments discussed in **Chapter 8** is reproduced in **Figure 7.10**. This graph shows the resistive transition of a test sample on a quartz substrate of 100 Å of niobium, covered by 100 Å of gold. The central portion of the sample (refer to **Figure 8.1**) was irradiated with an average gallium dose equal to $2 \times 10^{20} \text{ cm}^{-3}$, so that two separate transitions result: one for the irradiated portion, and one for the remainder of the sample.

Good quality thin films of niobium such as those used in this work possess sharp resistive transitions which are then flat as the temperature increases past 10 Kelvins. It is therefore reasonable to infer from the graph of **Figure 7.10** that the resistance at 10 Kelvins of the irradiated and non-irradiated portions of the sample under discussion are 11.5 Ω and 14.5 Ω, respectively. The resistance ratio of the sample as a whole is $RRR = 1.50$. Since an identical but un-implanted 100 Å Nb/100 Å Au sample (M2457T #2) possessed a resistance ratio $RRR = 1.60$, it is clear that implantation changes the resistance ratio of affected areas, and that an average value over the entire sample is not physically sensible. Using the value of $RRR = 1.60$ from a separate, “clean” sample as appropriate for the 14.5 Ω un-implanted portions of this sample, one concludes that the irradiated central

portion of M2457T #4, with an average dose in the niobium layer of $2 \times 10^{20} \text{ cm}^{-3}$, exhibits a reduced value of $\text{RRR} = 1.38$.

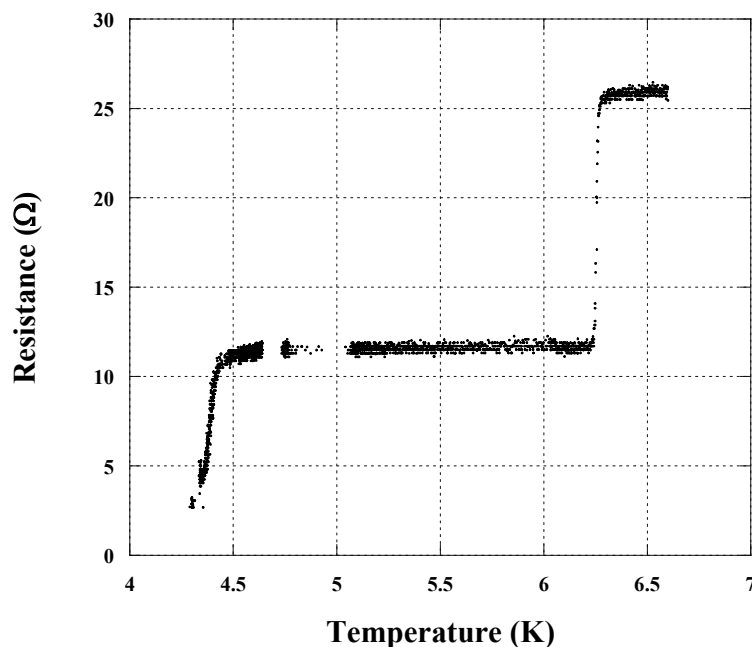


Figure 7.10. Resistive transition of a 100 Å Nb/100 Å Au thin film (M2457T #4) where the niobium layer in the central portion of the sample has been irradiated with a gallium dose of $2 \times 10^{20} \text{ cm}^{-3}$. The first transition corresponds to the implanted portion of the sample; its 10 Kelvin resistance is 11.5 Ω. The second transition, corresponding to non-irradiated portions of the sample, has a 10 K resistance of 14.5 Ω (26 Ω total, as shown in the graph). The 300 K resistance of the entire sample is 39.1 Ω.

Based upon this analysis, it is not possible to say exactly what the resistance ratio of a 100 Å thick niobium film, contaminated with gallium but not covered by a thin layer of gold, would be. It is clear, however, that the value of RRR would be reduced from its undamaged value of approximately two in regions with large implanted doses of gallium. Because the edges of the HEB microbridge are contaminated with gallium at a concentration on the order of $10^{20} - 10^{21} \text{ cm}^{-3}$, this effect contributes to the reduction in RRR which is observed.

Argon bombardment of the thin film niobium microbridges likely also plays a role in the decrease of the resistance ratio. It was shown in **Section 6.5** that bombardment

with 300 Volt argon ions reduced the resistance ratio of a 100 Å thick niobium film from 2.07 to 1.96 over twelve minutes of etching. While the HEB devices discussed in **Section 7.7** were etched at 150 Volts, they were etched for very long durations (several hours). Therefore, the contribution to the reduction in the resistance ratio from this source is unknown, but may be substantial. Additionally, in contrast to the effects of gallium contamination, which affects only the edges of the microbridge, the entire area of the structure is exposed to bombardment with 150 V argon ions (although not uniformly).

Many of the same issues which contribute to the non-uniformity of the bridge etch both between fabrication sets and among the devices which comprise a set likely also influence the resistance ratio, its reduction from the expected bulk value, and its variability (between 1.40 - 1.70). A full list of these issues includes:

1. The uneven manner in which the bridge etch progresses.
2. Inconsistency of the magnification calibration.
3. Variability of the RIE chamber condition.
4. Inability to control the stress of niobium films deposited on silicon nitride.
5. Uncertain microbridge width, perhaps caused by wear during FIB3 focusing and alignment.
6. Non-uniformity of the gold thickness in the kernel after the FIB3 step.
7. Possible variation of the thin niobium film across the wafer surface, and
8. The uncertain effects of thin film oxidation.

However, **Figure 7.11**, which exhibits the relationship between the resistance of the HEB microbridges and their 300 K/10 K resistance ratio as reported in **Section 7.5**, suggests that the reported values of RRR are not as variable as they appear. Instead, it seems likely that the resistance ratio is correlated to the device resistance. With two exceptions, these devices all share the same dimensions - a FIB2 gap of 22 pixels (for the device on a quartz substrate, 25 pixels was used), and a FIB3 length of 0.30 μm (for device “C”, this was 0.25 μm).

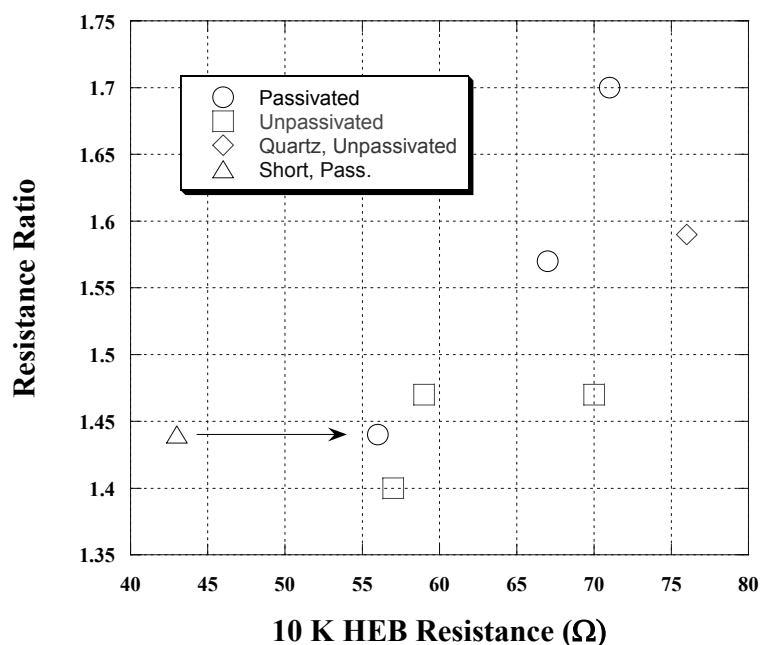


Figure 7.11. Relationship between the resistance ratio RRR and the 10 Kelvins device resistance for all of the HEBs measured cryogenically presented in this dissertation. The “short, pass.” data point is device “C”, with a 0.25 μm long FIB3. In the graph, it is normalized to the length of the other devices (0.30 μm long FIB3) and also presented in the “passivated” category for a meaningful comparison.

That the resistance ratio of FIB-manufactured HEB devices is reduced from the expected value of approximately 2.0 is undoubtedly a result of the fabrication process, but the source of the correlation between RRR and the device resistance demonstrated in **Figure 7.11** is obscure. Although the nominal dimensions of the microbridge devices discussed in this section were all nearly identical, because these devices were quite

narrow (around 0.11 μm), geometry may still explain the observed effect. If microbridges with higher resistances are in fact narrower than others (due to issue #2 or #5), for instance, then it may be that the resistance ratio really depends upon the lateral width of the structure. (In this case, perhaps the increase in RRR with decreasing width is caused by the low-level gallium contamination - on the order of 10^{16} cm^{-3} - which extends across most or all of the width of very narrow microbridges.) On the other hand, if the microbridges appear to be physically identical, then perhaps it is interesting from a theoretical perspective to ask what mechanism is responsible for the resistance variation, and why the resistance ratio is correlated to the resistance.

To conclude with a practical point, because the approach to the target resistance (50 Ω at 10 Kelvins) is monitored during the bridge etch at room temperature, **Figure 7.11** suggests that the appropriate value of the resistance ratio to use is about $\text{RRR} = 1.44$.

7. Results and Analysis

The three devices described in this section were all fabricated using a 150 Volt bridge etch, but are otherwise not identical in some significant ways. Devices “A”, HEB19T6, and “C”, HEB21T7, were both fabricated on silicon/silicon nitride wafers, but only the latter device sat on a membrane. Device “B”, M2747CT, was fabricated on a quartz wafer. Of the three, only device “C” was passivated as quickly as possible. Device “B” was allowed to oxidize for 16 hours between its completion and when it was measured, while device “A” oxidized for 13 hours before it was passivated, and was only measured another two days after that. The device dimensions and etch times were not greatly different and may be found in **Table 7.2** and **Table 7.4**.

Because the niobium microbridges which were fabricated are far from homogeneous, uniform thin films, it is worthwhile before progressing to review a few aspects of the fabrication process which will bear upon the results under discussion. These have to do with the non-uniform manner in which the bridge etch progresses, the effects of argon ion bombardment of thin niobium films, and gallium contamination.

Niobium microbridges fabricated by the FIB1-3 process are non-uniform along their length because (in many cases) the gold in the microbridge kernel is not removed evenly during the bridge etch. Instead, as shown in **Figure 6.13**, the niobium microbridge is first exposed when a small gap opens in the gold layer which covers it. The microbridge is then slowly uncovered as the gold layer creeps back toward the masked ends of the structure and the gap expands. The cumulative exposure to argon bombardment suffered by the niobium microbridge therefore varies along its length. It is also clear from **Figure 6.13** that the total exposure and exposure profile also vary substantially among the separate devices which make up a set, and that it is not necessarily the geometrical center of the microbridge which receives the greatest total exposure.

Under bombardment with 300 Volt argon ions, the transition temperature of a film of niobium 100 Å thick decreases at an approximate rate of 0.05 K/min. Therefore, the profile of exposure to argon ion bombardment likely creates a gradient of the critical temperature along the length of the microbridge. The intrinsic transition temperature should be lowest at the point first exposed during the bridge etch, increasing toward each end of the microbridge. (This is not at all the case for HEBs fabricated by other means; it

is particular to this research that the intrinsic transition temperature of an incremental length of the niobium microbridge may not be independent of location.)

It is not quantitatively known how bombardment with 150 Volt argon ions affects the transition temperature of these thin films. While the lower power etch undoubtedly has a smaller influence on the transition temperature per unit of time, greater cumulative exposure (due to far longer bridge etch times) might cause the total effect to be about the same as or greater than that found for 300 Volt bridge etches.

As outlined in **Section 6.4**, the microbridge is implanted with gallium along both of its exposed edges during both the FIB2 and FIB3 steps. Simple calculations suggest that the FIB2 contamination, at a concentration of 10^{21} cm^{-3} , is much greater. The measured trend (refer to **Figure 6.9**) suggests that a dose above about $3 \times 10^{20} \text{ cm}^{-3}$ suppresses the transition temperature of implanted regions below 4.2 Kelvins. It must therefore be considered that, in addition to the longitudinal variation in transition temperature just described, the edges of the microbridge may not superconduct at an operating temperature of 4.2 K. Since much or most of the width of the microbridge is free of large doses of gallium (greater than 10^{18} cm^{-3}), the HEB device will still be found to be superconducting if this is the case.

The resistive transitions of two devices, one fabricated on a quartz substrate and the other on a silicon nitride membrane, are shown in **Figure 7.12**. Each curve is normalized to the 10 Kelvins normal state resistance of the device.

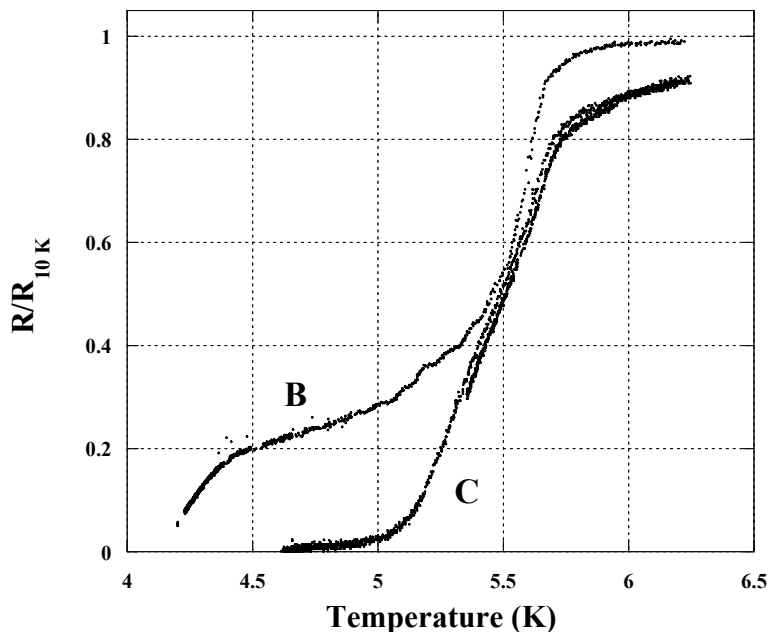


Figure 7.12. Resistive transitions of a device fabricated on a quartz substrate (“B”) and on a silicon nitride membrane (“C”), normalized to the 10 Kelvins resistance of each. The resistance was measured using a 4-point configuration with a 10 μ A bias current.

HEB devices fabricated from niobium films deposited on quartz substrates typically exhibit higher transition temperatures than the 5.5 Kelvins T_C of device “B”. This is partly due to the fabrication process, and partly due to oxidation. An unpassivated sample (HEB19T2), for instance, after one week exposed to atmosphere was found not to be superconducting down to 4.2 K, although its properties and fabrication were basically the same as those of the devices under discussion here which were found to superconduct. Aside from this observation about oxidation, for HEB devices of these short lengths, the shape of the $R(T)$ curve is largely dictated by the presence of the nearby normally conducting gold pads, and largely not by the intrinsic properties of the superconducting niobium film [Wilms Floet98]. Therefore the discussion moves to current-voltage characteristics of HEB devices.

From among the samples available, it was not possible to test two devices from the same fabrication set, so there is no data available which might illustrate how much the

I-V characteristics between nominally identical devices may or may not vary. A comparison between the three devices from different runs which were measured, however, does offer useful insight. This comparison is shown in **Figure 7.13**.

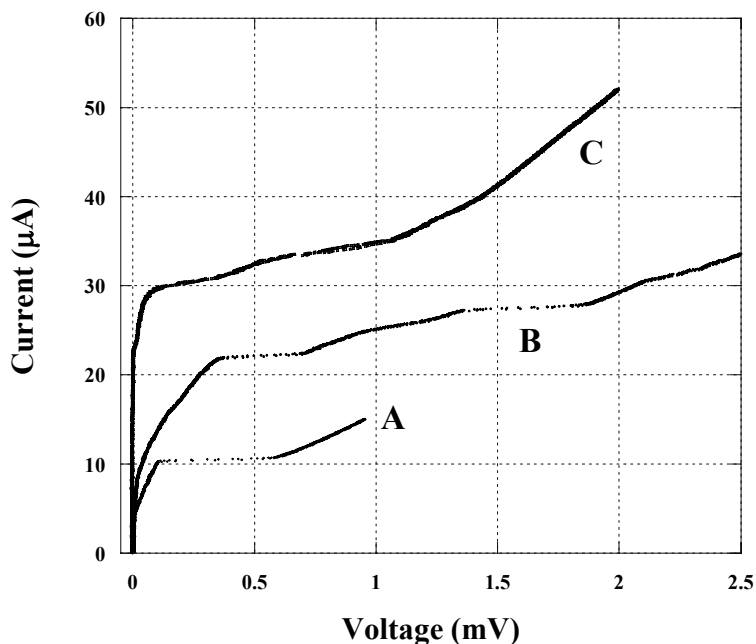


Figure 7.13. I-V curves at 4.2 Kelvins for the three devices “A” - “C”.

Devices “A” and “B”, which were allowed to oxidize, each exhibit a critical current of around 5 μA , while device “C” possesses a critical current of nearly 25 μA . It is therefore reasonable to conclude that it is important to passivate the niobium microbridges quickly once they are etched clear.

The traces in general do not reproduce all of the features of I-V curves reported by others for diffusion-cooled HEBs in the literature. [Karasik97] Still, some features of the curves in **Figure 7.13** can be sensibly interpreted in terms of the framework already developed. Curve “A”, for instance, exhibits behavior typical of a superconducting film, except for the resistive branch between 5 - 10 μA and the absence of hysteresis (refer to **Figure 8.6**). Curves “B” and “C” mostly do not.

Considering the I-V characteristic of a superconductive film, hysteresis and an abrupt transition between the superconducting and resistive states are properties of samples which possess single, well-defined critical temperatures. This is not likely to be the case for the devices under discussion. Instead, the existence of a transition temperature gradient along the length of the microbridge may prevent these effects by working against the expansion of the resistive hot spot (once it forms) by self-heating. Although the hot spot still expands due to the heat generated Ohmically within it, this expansion is limited by the gradient of increasing T_C more strongly than would be the case if T_C were uniform everywhere within the film. Therefore the I-V characteristic is perfectly reversible (not hysteretic) and, for the case of curve "C", at least, does not suffer abrupt, non-incremental changes.

The flat regions of curves "A" and "B"⁵ can perhaps be explained by oxidation. The range of 150 Volt argon ions in niobium is 7 Å, so that the damage caused by the bridge etch is really confined to only the topmost portion of the thin niobium film. This very thin damaged layer, which reduces the transition temperature of the entire 100 Å thin film through the proximity effect, is also the portion of the film which oxidizes first. This oxidation extends to a depth of less than or about 30 Å over a time of about one day [Halbritter87]. As the superconducting Nb layer damaged by argon ion bombardment oxidizes away to insulating Nb₂O₅, only the undamaged metal underneath (which possesses a single, uniform transition temperature) remains to carry superconducting

⁵ It is possible that the flat regions of these curves are in fact regions of negative differential resistance. These measurements were made under current bias with an integrator circuit which included a voltage follower. This circuit may have been unable to respond to an increase in the resistance of the DUT with a decrease in the output current.

current. This hypothesis both explains the reduction in critical current with oxidation, and suggests that a critical temperature gradient caused by surface damage effects may disappear as oxidation is allowed to continue. If this hypothesis is true, then the I-V traces for devices “C” (were it not passivated) and “B” should come to resemble curve “A” as their exposure to atmosphere continues.

The I-V curves obtained for device “C” will be compared to the characteristic expected for diffusion-cooled HEB devices in the context of **Figure 7.14**, which shows the I-V traces of device “C” at three different temperatures. These curves are different from the most relevant set of data published in the literature [**Burke97**] in only one significant respect: they fail to show regions of negative differential resistance. Allowing the exception just noted, in the temperature range available during this research, the traces shown in **Figure 7.14** are quite similar in character to those recorded by Burke. Measuring additional I-V traces down to 2 Kelvins might therefore be revealing.

A region of negative differential resistance appears in the I-V characteristic when the current falls as the voltage increases. Qualitatively, this occurs to a diffusion-cooled HEB under bias when the heat generated within the hot spot expands the length of the resistive region. This increases the resistance of the device and causes the current to fall at a given bias voltage. It may be that negative differential resistance is not be seen in devices fabricated by the FIB1-3 method because the critical temperature gradient restricts expansion of the hot spot, as explained earlier.

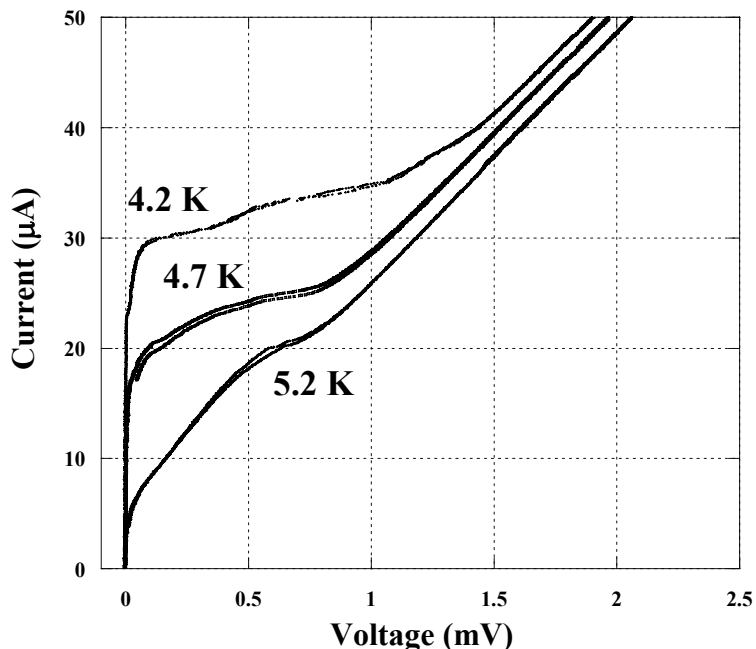


Figure 7.14. I-V traces of device “C” at three different temperatures. Each current-controlled trace was swept both up and down. What appears to be hysteresis is due to temperature drift during the measurement.

If the foregoing analysis is correct, it has interesting implications for the performance of the device as a mixer. A typical diffusion-cooled HEB must be biased with a combination of DC and LO power, because a stable bias point cannot be obtained using DC power alone. This would not seem to be the case with FIB1-3 manufactured devices. Since more heat is required to move the edges of the hot spot outward, however, it is likely that the conversion efficiency of these devices would be worse than that of HEB devices fabricated by other means.

If the hypothesis based upon the variation in the intrinsic transition temperature of the niobium thin film does not happen to be correct, or is not wholly responsible for the observed phenomenon, another plausible explanation exists. If the gallium-implanted edges of the microbridge are not superconducting, then in addition to the superconducting current, there is a normally conducting component to the current for all non-zero

voltages. It is possible that, subtracting off this shunt contribution to the current, the I-V trace of the superconductive portions of device “C” do indeed exhibit negative differential resistance above the critical current knee.

Assuming for the sake of argument that device “C” is 1000 Å wide, that its normally conducting edges are each 100 Å wide, that the entire microbridge shares the same sheet resistance, and noting that the 10 K resistance of the device is 43 Ω, the shunt resistance of the normally conducting regions comes to about 215 Ω. The flat region of the I-V curve at 4.2 Kelvins in **Figure 7.14**, extending from about 0.2 mV to 1 mV, has a slope of 180 Ω, which represents reasonable agreement to this proposal. That a similar shunt normal conductance fails to mask the flat portions of the I-V traces of devices “A” and “B” in **Figure 7.13** does cast doubt on this explanation, however. (Perhaps the microbridge oxidizes inward from its edges as well as downward from its top surface, removing the shunt path.)

Finally, it should be noted that the three curves in **Figure 7.14** fail to coincide in their (nearly) normal states because the temperature profile along the length of the bridge is not the same in each case (for a representation of the temperature profile, refer to **Figure 2.8**). The stated temperatures in **Figure 7.14** refer not to the temperature of the microbridge (which is not uniform), but to the sunk temperature at the microbridge ends. Because the critical current density decreases with increasing temperature and is zero at T_C , the devices are driven normal first because the critical current is exceeded in the small central region of the microbridge where the temperature is greatest (the hot spot). This hot spot expands subsequently due to thermal propagation and increasing current. According to this model, the ends of the microbridge continue to superconduct even

when most of the structure does not, as they remain below the transition temperature and the corresponding critical current density until the bias current is quite large. For increasing heat sink temperature (4.2 - 5.2 Kelvins), the portion of the microbridge which superconducts is reduced, and the amount of current carried by the device at a given voltage is lessened.

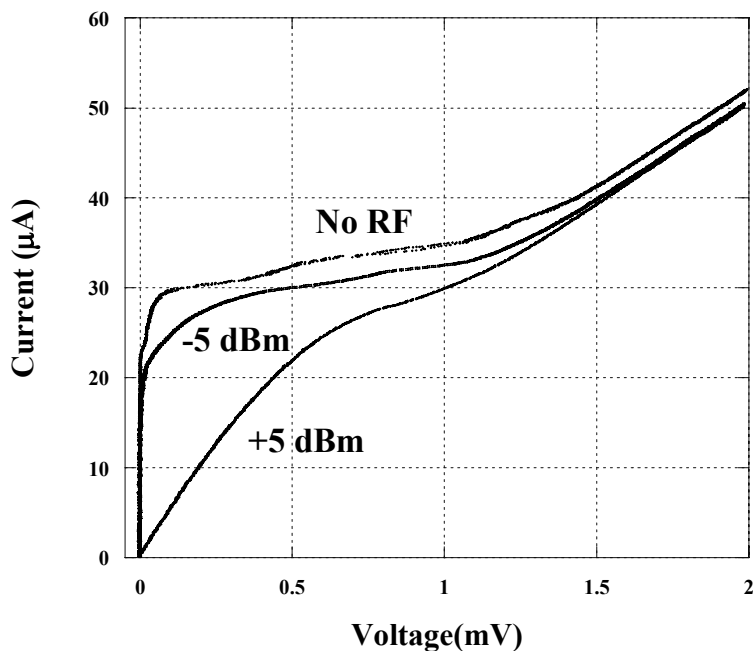


Figure 7.15. I-V characteristics for device “C” with 10 GHz RF applied through a capacitively-coupled antenna. The power measurements refer to the supply, not to the amount of power absorbed by the device, which is not known. The temperature was 4.2 Kelvins.

Current-voltage traces were also taken for device “C” under irradiation with 10 GHz RF energy using a test fixture designed and built by the author, as shown in **Figure 7.15**. Although 10 GHz is far below the gap frequency of the material (around 700 GHz), this sub-gap radiation is absorbed by unpaired electrons (whose presence is guaranteed for $T > 0$). [van Duzer99] Additional absorption occurs in areas immediately adjacent to normally conducting regions, since in these regions $T \approx T_C$ and the energy gap goes quickly to zero according to the relation

$$\Delta(T) = 3.2k_B T_C \sqrt{1 - \frac{T}{T_C}}. \quad (7.2)$$

For this reason, the absorption of 10 GHz radiation is not uniform across the surface of the microbridge, as it would be if an RF frequency above the gap were used, but the experiment demonstrates that the microbridge which was fabricated responds appropriately to RF radiation. HEBs may be used for detection and mixing below the gap frequency, but work most efficiently above it.

8. Conclusion

A great deal of data was presented in the foregoing chapter regarding the results of niobium diffusion-cooled HEB fabrication following FIB definition of the microbridge kernel. Bridge etches at both 300 Volts and 150 Volts self-bias were investigated, using devices fabricated on quartz and silicon/silicon nitride substrates, as well as on silicon nitride membranes. Although not enough HEB devices were fabricated to offer true statistical rigor, the data indicates that the FIB1-3 process produces devices which are uniform in resistance within $\pm 25\%$, and perhaps better. Several explanations for the observed non-uniformity between fabrication sets and between the individual devices which make up a set were proposed. Of these, non-uniform microbridge widths and inconsistent magnification calibrations were shown to occur. Others which were suggested may contribute to the non-uniformity, but bear further examination. Additionally, it may be possible to improve the uniformity by trimming finished devices in the FIB, which is discussed in **Appendix C**.

The FIB1-3 fabrication process results in a very complicated structure: the critical temperature of the thin niobium microbridge varies simultaneously in both lateral

dimensions due to the bridge etch and to implantation with gallium ions. It is possible to estimate the extents of these effects, but detailed and specific calculations in this regard cannot meaningfully be made and were not attempted. Likely because the bridge etch opens fissures in the niobium thin film, emphasizing its columnar structure, finished HEB microbridges oxidize rather quickly and must be passivated in order to preserve their superconductivity at 4.2 Kelvins. Passivation with a film of sputtered germanium was successfully demonstrated.

The research goal of fabricating arrays of niobium diffusion-cooled hot-electron bolometers on silicon nitride membranes was achieved, and sample devices with reasonably good characteristics were measured at cryogenic temperatures. Developing a better understanding of the uses and limitations of the focused-ion beam as a fabrication tool, and operator habits and a fabrication process which circumvented or suppressed ESD problems, were very important pieces of that success. The behavior of the device which was characterized most thoroughly significantly resembled reports published in the literature, except that negative differential resistance was not observed. A hypothesis which explained this difference in terms of the reduction of critical temperature due to argon ion bombardment and/or the creation of shunt normally conducting regions due to gallium implantation was presented.

The most important point to make, however, is that a fabrication process which may possess an exceptionally high yield (better than 90%) was demonstrated. Without the benefit of good yield statistics, a working five-element array of mixers on a chip would be virtually impossible to manufacture successfully. Thanks to this advance, as of

this writing, 1x5 arrays of superconducting diffusion-cooled HEB mixers operating at 1450 GHz await receiver testing at the University of Arizona.

CHAPTER 8 - ANOMALOUS RESULTS WITH 10 nm NIOBIUM FILMS

1. Introduction

While investigating the effect which gallium contamination has upon the properties of thin niobium films (discussed in **Section 6.4**), an interesting phenomenon was uncovered: the transition temperature of regions of the sample which were not irradiated with the ion beam actually increased as a result of implantation elsewhere on the sample. This anomalous behavior occurs only for gallium doses below a certain threshold, and appears to be quite consistent as long as the samples are not electrically grounded to the FIB stage during implantation. This chapter surveys the experimental technique, the ion implantation statistics, and the results of these experiments. No plausible explanation for the phenomenon which was observed can be offered at this time.

2. Description of the Experimental Technique

Samples of Nb (100 Å) covered by Au (100 Å) were deposited onto quartz wafers under low-stress conditions using DC magnetron sputtering and patterned using liftoff. Deposition took place under a single vacuum, in a sputtering chamber with a base pressure in the mid 10^{-8} torr range, following an in-situ ion clean. Bare, unoxidized samples of niobium prepared in this manner exhibited a resistance ratio $R(300\text{ K})/R(10\text{ K})$ above 2.0.

The actual sample structures for implantation consisted of two 3 mm x 1.5 mm contact pads, connected in the middle by a bridge 10 μm wide by 5 μm long. Two sets of experiments were conducted. In the first set (M2380), the samples were not protected

from the stray doses of gallium which result from imaging during stage alignment within the FIB chamber. Processing in the FIB was performed individually and included focusing, alignment, and implantation steps. Neglecting the stray imaging dose, the implanted area was constrained to the center of the sample by increasing the system magnification. Only imaged regions were implanted.

The experimental procedure for the M2380 samples just described is not ideal, both because of the stray imaging dose and because the actual region of the sample implanted probably varied somewhat from sample to sample. These issues were addressed in another set of samples (M2457), where the implantation area was defined with a photoresist window. A negative photoresist (AZ 5214E-IR, 1.4 μm thick), intended for implantation applications, covered all of the area of the sample except for an open window over its center, as shown in **Figure 8.1**. For the M2457 set of samples, the implanted region was defined by this open area in the layer of photoresist. After FIB implantation, the resist was removed with acetone. The gold layer was not removed at any time from either set of samples.

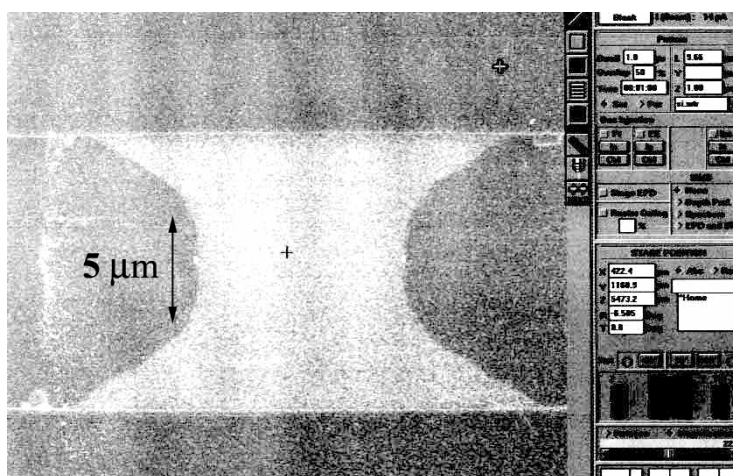


Figure 8.1. A screen shot from the FIB during implantation. The indicated central section of the sample measures 10 μm wide by 5 μm long. The adjoining portions connect to the 3 mm contact pads, which are covered by photoresist, and are therefore obscured in this image.

The FIB was used to implant gallium into the samples simply by focusing on the sample for a set length of time. The process is not very exact for short exposures, due to the need to find and focus on the area to be exposed with the same Ga-ion beam used to image the sample. The samples were held down on the sample stage with a small amount of vacuum grease, and were not fastened with a metal clip. Therefore they were not electrically grounded. Different results were obtained with samples which were held down by a clip (refer to **Appendix D**). That approach was not deemed preferable, because it was difficult to obtain good electrical contact to the very thin films used in these experiments. Aside from the exposure time, the thickness of the sacrificial gold layer and the FIB beam current and magnification all served to control the dose implanted in the niobium layer of the exposed section of each sample. The energy of the implanted gallium ions was 30 keV. All measurements reported here were performed using a 4-point configuration with 10 μA of bias current.

3. Theoretical Analysis Using SRIM

The software program SRIM (the Stopping and Range of Ions in Matter) was used to develop predictions regarding the distribution of gallium dopants within the quartz/Nb/Au structure [SRIM]. As shown in **Table 6.2**, the predicted range of 30 keV Ga ions in gold is 95 Å, with a 56 Å straggle. The range increases to 109 Å in a quartz/Nb(100 Å)/Au(100 Å) structure because of the greater range of the energetic gallium ions in niobium and quartz, as compared to gold. Simply by counting the number of ions in the proper range of depths, the percentage of the ion flux incident upon the structure which will be caught in the niobium layer may be calculated. The results of

this calculation for varying thicknesses of the gold layer are shown in **Figure 8.2**.

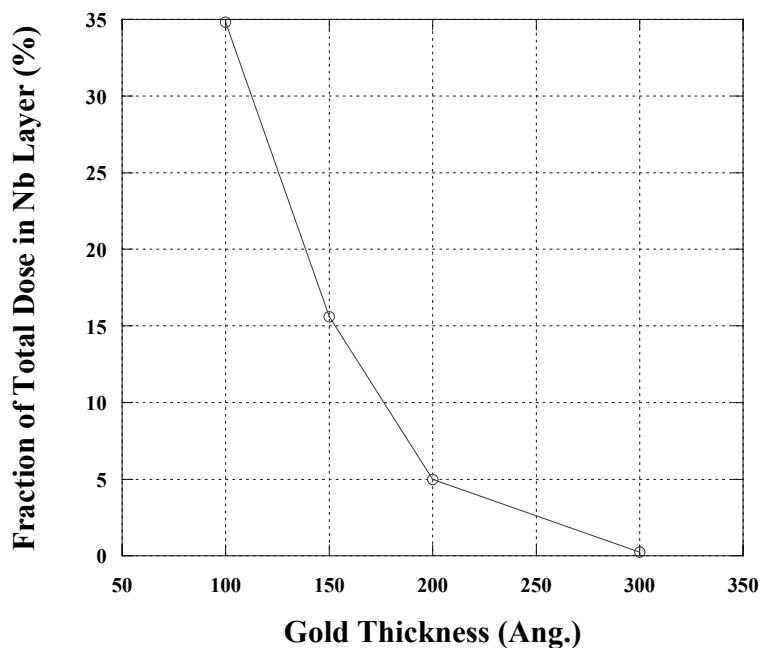


Figure 8.2. Capture percentages of incident Ga^+ flux within the 100 Å Nb layer depend strongly upon the thickness of the gold layer on top, according to simulations with SRIM using 10^5 ions.

The actual distribution of the contaminant gallium ions within the niobium layer is not uniform, as may be seen in **Figure 8.3** for the case of a 100 Å gold layer. Therefore results in this work refer to an average concentration of gallium, based upon the total capture percentage for the entire thickness of the niobium layer and the ion flux (in units of per cm^2) incident upon the structure. The capture percentage for 100 Å Nb/100 Å Au films is 35%, so that a typical volume dose in this discussion is about 10^{20} cm^{-3} , or 0.2% by atomic composition.

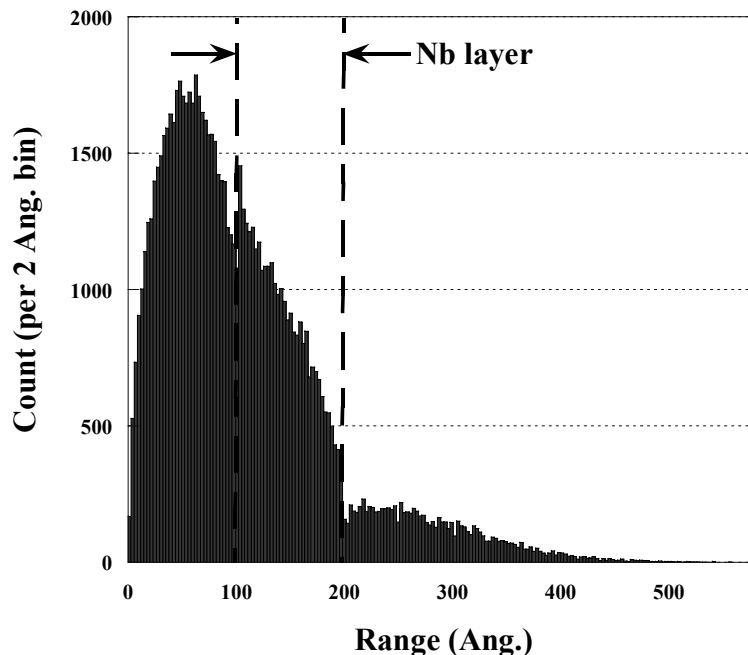


Figure 8.3. Distribution of implanted gallium, according to an SRIM simulation utilizing 10^5 ions in 2 Å bins. The gold layer on top of the 100 Å niobium layer is also 100 Å thick. Analysis of this data reveals that about 35% of the ion flux incident on the sample will stop in the Nb layer, although clearly its distribution within that layer is not uniform.

4. Experimental Results

Figure 8.4 shows the results of the experiments outlined in **Section 8.2** on the M2457 set of samples, which were masked with photoresist. Curves “B” and “C” were implanted using a 13 pA beam current, with a magnification of 10,000x (corresponding to a field of view of 29 microns on a side), for periods of 30 and 60 seconds, respectively. Sample “0”, which did not undergo implantation, is included for reference. Its transition to the superconducting state occurs at 6.30 Kelvins and is quite narrow, indicating that the thin films used for this work were of high quality.

Curve “A”, which exhibits the anomalous behavior which is the subject of this chapter, was also implanted at a magnification of 10,000x, but with a lower 4 pA beam current, for a time of 25 seconds. The average volume dose in the niobium layer of this sample

was $2.7 \times 10^{19} \text{ cm}^{-3}$. The entire transition of sample “A” was inadvertently not measured and is not pictured in **Figure 8.4**, as its 10 K resistance was measured to be 19.5Ω . The nature of the remainder of transition “A”, taking place above 6.6 K , is not known. The results presented in the graph of **Figure 8.4** are summarized in **Table 8.1**.

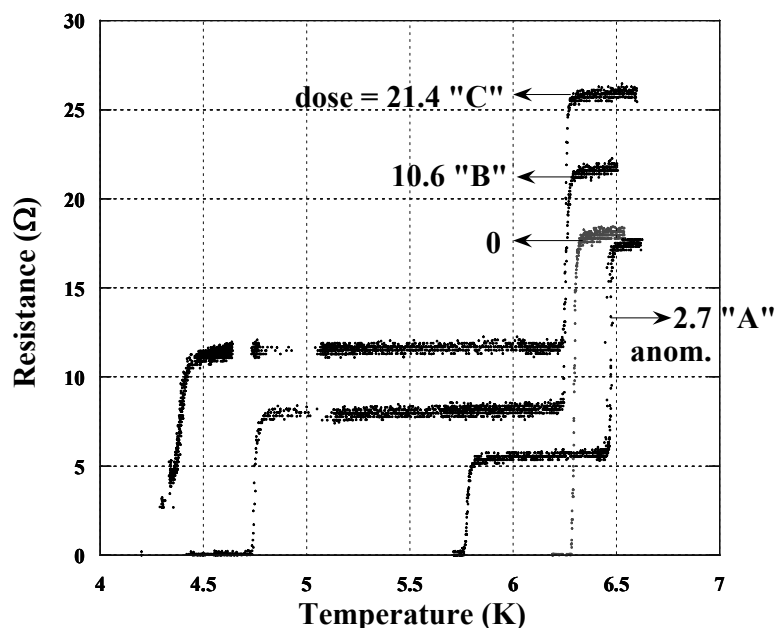


Figure 8.4. Results of the implantation experiments on samples masked with photoresist (M2457), showing the resistive transitions of Ga-irradiated Nb(100 Å)/Au(100 Å) films. The stated doses are in units of 10^{19} cm^{-3} . Curve “A” (the anomalous curve) exhibits an odd feature: the portions of the sample which were not irradiated actually show an increase in T_c as a result of the implantation.

Curve	Dose (10^{19} cm^{-3})	T (K)	R (Ω)	10 K R (Ω)	ΔR (Ω)
0	0	n/a	n/a	18.2	n/a
A	2.7	6	5.5	19.5	14
B	10.6	5.5	8.1	22.3	14.2
C	21.4	5	11.5	26	14.5

Table 8.1. Summary of the measurements illustrated in Figure 4. The T(K) and R(Ω) columns both refer to the first (lower temperature) steps in the measured transitions of the irradiated samples - T(K) is the temperature at which the sample resistance is R(Ω). ΔR is the difference between the 10 K resistance and the figure in the R(Ω) column; i.e., the height in Ohms of the second transition.

Using the data in **Table 8.1**, the results of this experiment may be easily understood. Examining only the irradiated samples “A”-“C”, the first steps in the transitions of **Figure 8.4**, occurring between 4 and 6 Kelvins, correspond to the irradiated portions of the samples. These exhibit decreasing transition temperature and increasing resistance with increasing dose. The contact pads, which are covered in photoresist and which do not receive any gallium dose, are represented by the second transitions, between 6.25 and 6.5 Kelvins. These regions all exhibit very similar resistances ΔR between 14-14.5 Ω (the uncertainty on this measurement is at least $\pm 0.2 \Omega$). Comparing this figure to the 18.2 Ω resistance of an uncontaminated sample, one may deduce that the resistance of the exposed area shown in **Figure 8.1** before irradiation is approximately 4 Ω . This is perfectly consistent with the other data presented, since it may be interpreted to mean that the resistance of the irradiated portion of sample “A” increased by about 1.5 Ω as a result of the implantation.

Additional support for this interpretation is offered by the second transitions of curves “B” and “C”, which occur at the same temperature as the transition of the reference sample “0”. That is, the masked, non-irradiated portions of samples “B” and “C” (the contact pads), which are physically identical to the same regions of the reference sample “0”, possess the same transition temperature and resistance (about within the measurement error) as that sample. This is only to be expected, as nothing was done to the contact pads. However, although the same analysis should extend to sample “A”, it is clear from **Figure 8.4** that it does not. The second transition of sample “A” is elevated about 0.17 K above the transition temperature of sample “0”, which is wholly unexpected.

To re-state: for the anomalous sample “A”, the transition temperature of the non-irradiated portion of the sample (the contact pads) clearly increases as a result of implantation elsewhere on the sample. This anomalous behavior does not occur with the higher-dose samples “B” and “C”.

The anomalous behavior has been verified on a second set of samples, M2380, with lower implanted doses from $0.3 - 2.2 \times 10^{19} \text{ cm}^{-3}$. This set of samples was irradiated using an 11 pA beam current and a magnification of 1200x, for exposure durations between 60 - 480 seconds. The lower implanted doses in this set of samples were the result of the lower magnification which was used, as a given ion flux per unit of time was spread over a larger area of implantation. This set of samples was not masked with photoresist. The transitions of the M2380 samples are shown in **Figure 8.5**.

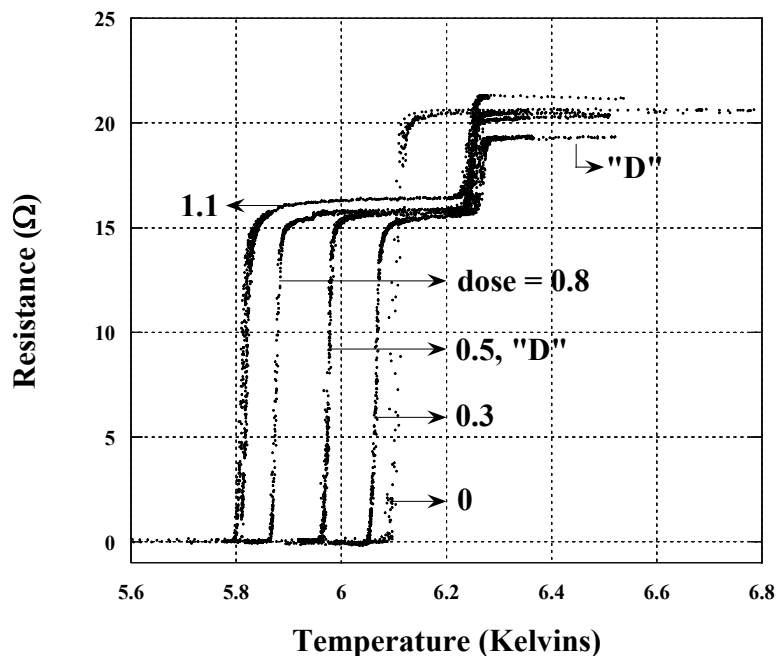


Figure 8.5. Results of the implantation experiments on samples which were not masked with photoresist (M2380). The stated doses of gallium are again in units of 10^{19} cm^{-3} , and so are much lower than the doses utilized with the other set of samples.

The most important observation to be made through examination of **Figure 8.4** and **Figure 8.5** is that every sample implanted with a dose less than $10 \times 10^{19} \text{ cm}^{-3}$ (in fact, less than 3×10^{19}) exhibits the anomalous increase of the transition temperature of non-irradiated regions, with an increase of approximately 0.15 Kelvins. It is also interesting to note that sample “D” of **Figure 8.5** possesses a 10 Kelvin resistance of 20.4Ω , so that curve “D” must possess an unrecorded transition above 6.5 Kelvins. This is similar to the unrecorded portion of curve “A” above 6.6 Kelvins, from about 17.5Ω up to the sample’s measured 10 K resistance of 19.5Ω . However, the other curves of **Figure 8.5** do not exhibit a third portion of their respective superconductive transitions.

The reference “0” samples for M2380 and M2457, while nominally identical, in fact possess rather different transition temperatures and resistances. Because the films are so thin, this likely indicates simply that the two sets of samples possess slightly different thicknesses of gold and of niobium.

Lastly, the curves of **Figure 8.4** are quite different from those of **Figure 8.5**, although the experimental technique is basically the same. Comparing curve “A” to curve “D”, for instance, curve “A” exhibits much less resistance in the irradiated region (the first transition), and much more resistance in the contact pads than does curve “D”. This difference arises simply because a much smaller area of the M2457 samples (the group including sample “A”) was irradiated, due to the higher magnification which was used (10,000x, instead of 1200x).

Although the M2380 samples were not masked with photoresist, it is important to note that nevertheless only the small portion of the sample imaged by the FIB was implanted. Without the photoresist, a very small concentration of Ga was undoubtedly

implanted in the contact pads while the samples were being imaged and aligned. With the photoresist mask (the M2457 samples), this unwanted stray dose was vastly reduced. Therefore, the anomalous second transition cannot be caused by stray doses implanted in the contact pads. This conclusion is supported by the observation that the samples “B” and “C” do not exhibit the anomalous behavior, although those samples received about the same tiny stray dose that sample “A” did, whatever that may have been.

The current-voltage characteristic of the exposed portion of sample “C” at 4.2 Kelvins is shown in **Figure 8.6**. The sample becomes resistive immediately once the critical current of $168 \mu\text{A}$ is exceeded, corresponding to a critical current density $J_C = 3.4 \times 10^5 \text{ A/cm}^2$. Once in the resistive state, the I-V curve is linear with a slope corresponding to the 10 K resistance, $(11.5 \Omega)^{-1}$. Heat generated by Ohmic losses in the

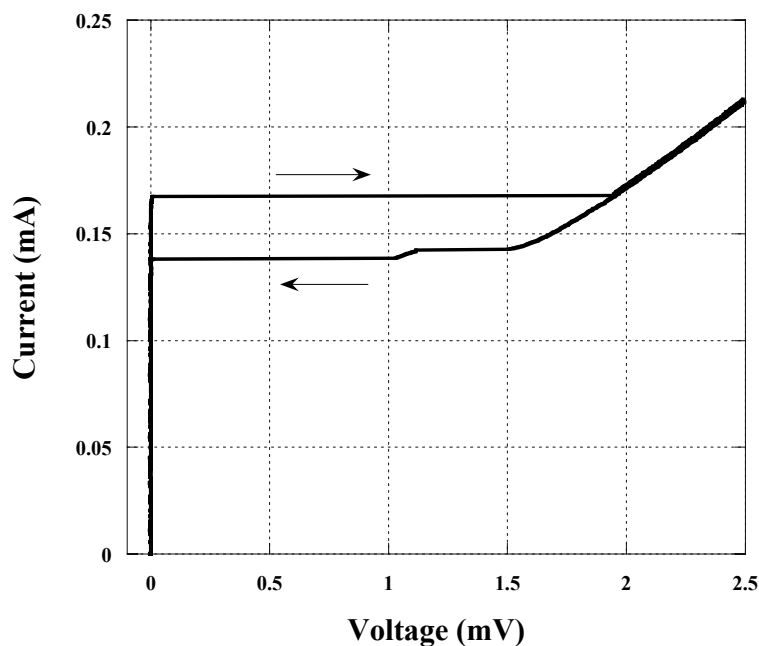


Figure 8.6. I-V characteristic of the exposed central region of sample “C”, with an implanted dose of $21.4 \times 10^{19} \text{ cm}^{-3}$, taken at 4.2 Kelvins. The small bump in the middle of the downward branch is caused by the taper in the sample, since the critical current density is a function of the area through which the bias current travels. The transition of the contact pads is not represented here and was not recorded.

resistive state causes the resistivity of the sample to remain while the current decreases below I_C , which explains the hysteresis of the I-V curve. These are typical characteristics of superconducting thin films. Samples “A” and “B”, with lesser implanted doses, possessed critical currents above 1 mA. Their I-V characteristics were not recorded.

Outside of the anomalous behavior of the non-irradiated regions, the results presented in this section are summarized in **Figure 8.7**. Some of the increase in sample resistance shown in the figure may be due to removal of gold by the ion beam, but visual inspection of the samples by SEM shows the gold layer to be largely intact. “Anomalous behavior” refers to the finding that the implantation of gallium into a small region of the sample increases the transition temperature of masked, much larger regions elsewhere on the sample. These non-irradiated regions received, at most, a tiny stray dose of implanted gallium, but this effect is not caused by that stray dose.

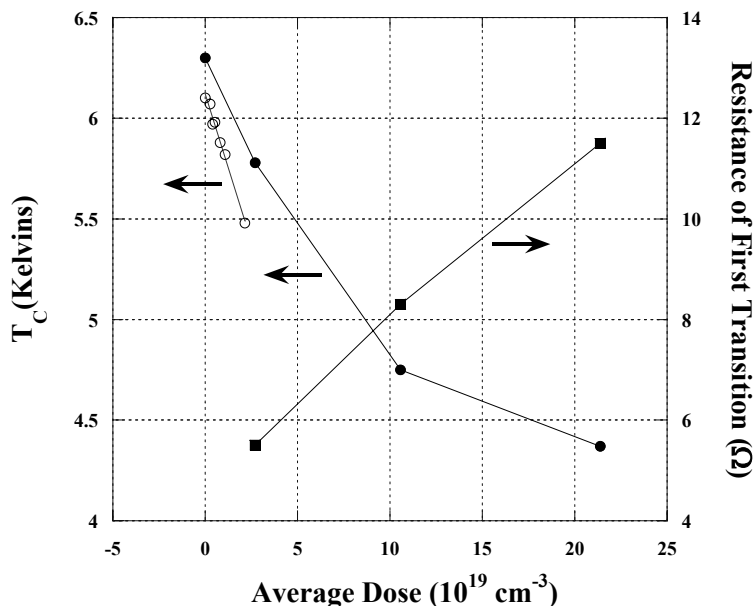


Figure 8.7. Summary of the gallium implantation experimental results, on Nb(100 Å)/Au(100 Å) films. The circles (open, M2380, no photoresist mask; closed, M2457, masked) detail the suppression of critical temperature with increasing dose; the squares, the increase in 10 Kelvin sample resistance of the irradiated area (M2457). Since the gold was not removed from the sample, it is not certain that the second effect is not at least in part due to thinning of the gold layer by the FIB during implantation.

Prior to the experiments just described in this section, other samples from M2380 were implanted and tested, with different results than those shown - one sample even exhibited an anomalous decrease in the contact pad transition temperature. This data is included in **Appendix D**. In that experiment, the samples were secured to the FIB stage with a metal clip, so that there was at least some electrical contact with the sample, and some possibility that charge deposited on the sample by the ion beam might be drawn off to ground. For the experimental results presented in **Figures 8.4 - 8.6**, however, there was no electrical contact with the sample during implantation. Even so, the accumulation of static charge upon the substrate is not a likely cause of the anomalous behavior which was observed, because the high-dose samples “B” and “C” failed to exhibit this behavior.

There is furthermore some indication that Nb/Au samples which are masked, similar to those of M2457, and etched at low power with argon ions, show an anomalous change in the test pad transition temperature (M1865A). That data is preliminary, however, and is therefore included in **Appendix D**.

5. Conclusion

The decrease in transition temperature undergone by a 100 Å Nb film as a result of implantation with gallium ions using a focused-ion beam has been examined. Most of this information was also presented in **Section 6.4**, in the context of diffusion-cooled HEB fabrication. Because the investigation discussed in this chapter also revealed that the resistance of implanted regions increases with gallium dose, it is worthwhile to consider trimming HEB devices by FIB implantation of gallium. This possibility is discussed in **Appendix C**.

The principal topic which was discussed is the anomalous behavior of the large, masked portions of the sample at doses below $3 \times 10^{19} \text{ cm}^{-3}$, which show an increased transition temperature above that of a non-irradiated reference sample. This increase is not due to any stray dose of gallium, but is instead caused by the irradiation of the exposed central portion of the sample. Especially noteworthy is that this behavior does not occur if the concentration of implanted gallium exceeds a certain limit, which lies between $3 - 10 \times 10^{19} \text{ cm}^{-3}$.

The experiments described in this chapter were refined over time, in the hopes of developing an explanation or theoretical framework for the surprising phenomenon which was uncovered. More measurements than were taken in the course of this research are necessary, however, as no plausible explanation for the anomalous behavior is currently available. For that reason, some data from earlier, less refined, experiments is included in **Appendix D**. This data suggests that a) grounding the samples to the FIB stage during implantation affects the anomalous behavior of the samples, and b) masked Nb/Au samples from which the gold is removed by argon RIE may also exhibit an anomalous change of the contact pad transition temperature. Neither conclusion should be regarded as definitive, however.

Examining only the data from the best-controlled experiment, that shown in **Figure 8.4**, it is at least possible to construct a conceptual framework with which to consider these results. Examining the SRIM calculation displayed in **Figure 8.3**, it's clear that implantation creates a complicated graded Nb-Ga structure down through the vertical profile of the exposed area. It is also clear that some mechanism within the irradiated region exerts an influence over the entire superelectron gas throughout the

entire sample volume. An excessive concentration of implanted gallium seems to degrade the structure and destroy this effect.

It is not clear to the author what mechanism within the exposed area of the sample, which measures about 15 μm in length, might encourage the persistence of the superconductive state in the contact pads, 3000 μm across, above their nominal transition temperature. Nor can any explanation at all be offered for the third transitions of samples “A” and “D”. A measured curve with a third transition is pictured in **Figure D.1**, for a sample from the M2380 set. More measurements will be necessary to develop a theoretical explanation for this phenomenon: $R(T)$ curves at different bias currents, $I(V)$ curves with applied RF power, and the fabrication of additional samples with thicker gold layers, of samples from which the gold layers have been removed after implantation, and of samples with oxidized niobium layers (which eliminates the proximity effect influence of the gold layer by reducing the interface transparency), as a beginning.

The behavior of very thin films of niobium is quite different from the behavior of bulk superconductors (to cite one example, these films exhibit hot-electron effects). Therefore, further investigation of the anomalous behavior may be found to be very rewarding.

CHAPTER 9 - CONCLUSIONS

This dissertation discussed the use of a focused-ion beam to fabricate diffusion-cooled superconducting hot electron bolometers, and the construction of a 1x5 receiver array operating at 1450 GHz which utilizes these devices as mixers. How the FIB was employed as a tool to pattern these very small structures was examined in detail. Its influence upon the characteristics of finished sets of HEB devices (in terms of uniformity within the set) and of individual devices (due to contamination with stray gallium from the ion beam) was also covered. It is clear that FIB patterning of superconducting microbridges is a promising method of realizing arrays of mixers for THz applications.

The FIB1-3 process which was developed by the author allows the fabrication of stable, robust superconducting niobium DHEBs with a high (apparent) yield, which is absolutely necessary in order to manufacture a five-element array. A very important additional aspect of this research was the elaboration of an overall fabrication process and specific operator protocols which minimized the potential for ESD damage to finished devices. The development of a passivation scheme using a layer of sputtered germanium, not reported elsewhere, was still another significant development. The devices described in this dissertation were the first niobium HEBs to be fabricated successfully in the UVML.

The use of a gallium focused-ion beam to pattern the small superconducting HEB microbridge structure was examined in depth. On a larger dimensional scale (of several microns), its application to define the probe throat transition was demonstrated, and incorporated into the FIB1-3 process. It was further suggested that the FIB can be usefully employed in several other capacities (among them trimming of HEB devices and

PCJ deposition) related to the construction of the 1x5 receiver array. It was shown that the FIB is certainly a very versatile and useful tool for sub-micron patterning, in particular of superconducting devices.

The complications which arise from the application of the FIB tool, which include the uneven manner in which gold mills away and the problem of gallium contamination of the finished niobium microbridge, were examined in detail. The FIB1-3 process evolved significantly over time primarily in response to these concerns. For instance, an earlier version of the FIB fabrication process, called the BtA/BtB process, was briefly discussed in this context. The FIB1-3 fabrication process is quite successful judged by these criteria, because this technique confines gallium contamination to the edges of the HEB microbridge, and is robust enough to allow for the undesirable materials properties of gold. It was suggested, however, that the device resistance uniformity of $\pm 25\%$, and the significant width variation ($\pm 0.01 \mu\text{m}$) in the microbridge width which was observed, may be in part due to the use of the focused-ion beam tool.

In order to explore the issue of how robustly thin niobium films respond to the prolonged bombardment with low-energy argon ions necessary to remove the gold layer from the microbridge kernel, bridge etches at both 300 Volts and 150 Volts were examined. Although a lower-voltage etch might be expected to be more gentle, there is no data to support the contention that the 150 Volt etch is preferable. Devices with the same dimensions (three sets on silicon/silicon nitride substrates at 300 Volts, and another set on quartz at 150 Volts) came out basically the same - about $50 \Omega/\square$ at room temperature. Sets of devices with resistance uniformity of about $\pm 25\%$ at or near the target resistance of 50Ω at 10 Kelvins were successfully fabricated.

Narrow (about 0.11 μm wide by 0.22 μm long) devices fabricated with a 150 Volt bridge etch were measured cryogenically. The resistance ratio of these devices was found to lie between 1.4 - 1.7 (while the RRR of unprocessed 100 \AA niobium films is around 2.0). Down to 4.2 Kelvins, the I-V characteristics of these devices do not exhibit hysteresis, and the one passivated device which was measured did not exhibit a region of negative differential resistance. In these respects, the devices fabricated in this work using the focused-ion beam are different from those described in other reports in the literature. This suggests that DHEBs manufactured by the FIB1-3 method may be stably biased more easily than other DHEB devices, which would be advantageous.

The I-V characteristics of unpassivated devices appear to change with time as a result of oxidation, and microbridges which remain unpassivated for more than several days no longer superconduct down to liquid helium temperature. Devices passivated with layers of sputtered germanium, first reported in this research, are stable, and seem to be reasonably robust with respect to ESD damage.

A finished HEB device was shown to absorb 10 GHz RF radiation applied through a capacitively-coupled antenna, which indicates that the microbridge should operate as intended as a terahertz hot-spot mixer. Several 1x5 arrays of HEB mixers on silicon nitride membranes and backshort blocks fabricated by the author now await receiver testing at the University of Arizona.

Finally, the anomalous increase of the contact pad transition temperature was presented and explored. Although no explanation for this phenomenon can be offered at this time, this peculiar topic may prove of interest to other researchers.

APPENDIX A - RECEIVER NOISE TEMPERATURE CHARACTERIZATION

Because the noise temperature is the primary figure of merit for an HEB receiver, this appendix examines how the receiver noise temperature is calculated and the relevant models which apply.

The receiver noise temperature in fact refers to the temperature of an equivalent blackbody radiator. The total power emitted by this radiator per unit of bandwidth equals the noise power present in the signal under discussion, and is given by Planck's Law,

$$P(T_{eq}, f) = \frac{hf}{e^{hf/kT_{eq}} - 1}. \quad (\text{A.1})$$

where T_{eq} is the equivalent noise temperature, f is the frequency, h is Planck's constant, and k is Boltzmann's constant. This reduces to $P(T_{eq}, f) = kT_{eq}$ in the Rayleigh-Jeans limit $hf \ll kT_{eq}$, which however does not necessarily apply at terahertz frequencies.

When examining the noise characteristics of a circuit element, it is conceptually simpler to assume that the element is ideal, or noiseless, and to refer the noise added to the output signal by the device to the input. This is illustrated in **Figure A.1**, where it can be seen that the noise power P_{noise} has been replaced by an additional noise power at the input, P_{eq} . The HEB receiver is therefore represented by its gain G , bandwidth Δf , and equivalent noise power referred to its input, P_{eq} .

Because, according to **Figure A.1**, $P_{out} = GP_{in} + P_{noise}$, in theory all that is needed to measure the receiver noise temperature is a matched load at 0 Kelvins attached to the input of the receiver (so that $P_{in}=0$) [**Pozar98**]. In reality, the measurement cannot be

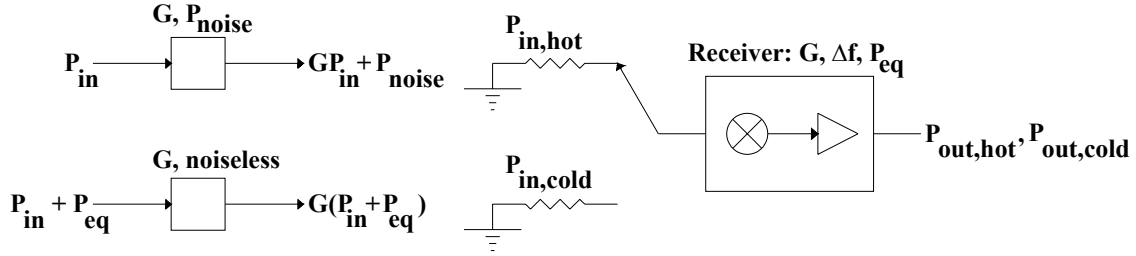


Figure A.1. Definition of the equivalent noise power referred to the input of an arbitrary device (left), and schematic diagram of the experimental setup for a Y-factor measurement (right). $P_{in,hot}$ and $P_{in,cold}$ are the noise powers generated by loads matched to the receiver input held at room temperature and 77 K, respectively. Measurement of the hot and cold load output powers allows the receiver noise temperature to be calculated.

accomplished in precisely this manner, but the same information may be obtained using two separate matched loads held at different temperatures. This procedure is referred to as a Y-factor measurement. Referring again to **Figure A.1**, one may write

$$P_{out,hot} = G(P_{eq} + P_{in,hot}), \text{ and}$$

$$P_{out,cold} = G(P_{eq} + P_{in,cold}). \quad (\text{A.2})$$

The Y-factor is defined as the ratio of the measured hot and cold output powers, or

$$Y = \frac{P_{out,hot}}{P_{out,cold}}. \quad (\text{A.3})$$

Combining Equations (A.2) and (A.3), the equivalent noise power is then

$$P_{eq} = \frac{P_{in,hot} - YP_{in,cold}}{Y - 1}. \quad (\text{A.4})$$

The equivalent noise temperature T_{eq} is therefore

$$T_{eq} = \frac{T_{in,hot} - YT_{in,cold}}{Y - 1} \quad (\text{A.5})$$

if the Rayleigh-Jeans approximation applies, and

$$T_{eq} = \frac{P_{eq}}{k} \quad (\text{A.6})$$

if it does not. (In radio astronomy, the equivalent noise power and noise temperature are typically defined for a 1 Hz bandwidth).

For Y-factor measurements of HEB receivers, the matched loads are typically an absorbing material held at the window of the cryogenic dewar. This material is at room temperature for the hot load measurement ($T_{\text{in,hot}} = 293 \text{ K}$), and at liquid nitrogen temperature ($T_{\text{in,cold}} = 77 \text{ K}$) for the cold load measurement.

APPENDIX B - PROCESS SHEETS

This appendix contains process sheets for the HEB block fabrication (**Table 5.1**) and the backshort block fabrication (**Table 4.2**). The backshort block fabrication process outlined here will result in the destruction of the backside markers immediately after their deposition and patterning. This issue is discussed in **Appendix C**.

2" Si/Si₃N₄ HEB ARRAYS - 850 and 1500 GHz WAFER # _____

1. Polyimide spin on one 2" Si wafer, 127 μm/5 mils thick

Substrate: _____

Date: _____

A. Si RCA Clean w/short jars & baskets:

ETM spin clean

* note! Use filter paper on chuck! *

NH₄OH Si clean sol'n 80 C 12 min

Running DI rinse 1 min

BOE 10:1 dip 15 sec

Running DI 1 min

HCl Si clean sol'n 80 C 12 min

Running DI 1 min

Blow dry

B. Poly Spin:

ETM spin clean, unless immed. following step A

* note! Use filter paper on chuck! *

Ozone 5 min

120 C HPB 5 min

Pause 2 min

Spin OCG primer 0.2 μm filter, 6 krpm 30 sec

Spin unthinned OCG 285, 1 μm filter as 6 krpm 30"

160 C HPB 10 min

2. Sputter-Etcher Nb depo. for poly-Nb Date: _____

Deposit approximately 1000 Å of niobium for the poly-Nb layer; the chamber and shutter accommodate two wafers at one time. No need to grease the wafers down or use a platter.

Mode	Shutter	Load	Tuning	Voltage	Power	Pressure	Time
S	C			600		15	2 mins.
S	O			600		15	20 mins.

3. Liftoff litho., "HEB Block" Mask Date: _____

ETM clean

* note! use filter paper on chuck! *

Ozone 5 min

120 C HPB 5'

HMDS vapor 5'

Spin AZ5206E 6 krpm 30 sec

Pause 4 min

HPB 100 C 2 min

Pause 2 min

Align carefully to wafer flat

Expose EVG 15 sec 5 mW/cm², V+H

HPB 130 C 60 sec (PEB)

Flood expose EVG 60 sec

Develop AZ400K 1:4 plastic tweezers

t = _____ (flash + 20 sec)

* careful!! *

3 DI, 20 sec each

Blow dry

Examine - OK? _____

WAFER # _____

4. Nb – Poly RIE

Date: _____

A. ASH 50% O₂, 200 um, 200 W, > 10 minutes

FPD = _____ V = _____

B. CONDITION 50% SF₆, 20% CHF₃, 0.6 sccm N₂, 30 um, 170 FPD, 10 min

* be sure to flush CF₄ line if necessary, before turning valve to CHF₃ *

P = _____ V = _____

C. ETCH in clean medium Petri dishes flash + 20 sec (2'30" typical)

t = _____

D. ASH again, as above

E. Insert quartz platter. CONDITION 30% O₂, No VO, 700 V, 10 min

FPD = _____ P = _____

F. ETCH in clean medium Petri dishes, 17 minutes (more if necessary)

t = _____

G. Measure with Tencor and examine.

thickness = _____

5. HEB Material Deposition and Lift-Off, 2" Float Block

Date: _____

SiO₂ Stress: _____

Base Pressure: _____

Run & Date: _____

Material	Pressure (μm)	Power (W)	Voltage (V)	Current (A)	Rate ($\text{\AA}/\text{min}$)	Thickness (nm)	Time (min:sec)
μ bridge Nb							
Gold							
Mask Nb							

A. Sputt-3 Deposition of Nb & Au

Chamber must pump overnight

Wafer stage to cold stage; Cold stage water on

Degas 2'; record pressure

Flush Ar lines, MFC #1 and #3

Clean Nb gun 8 min

*** NOTE! The proper Ar pressure for sputtering on to Si₃N₄ is different than for SiO₂! ***

Warm up IG; Source 5 min, Beam 4 min

Cold stage water off; bring wafer into position

Ion mill 7 minutes

Retract wafer and close sycon shutter

Zero baratron gauge

Warm Au gun 2 minutes; record rate

Warm Nb gun 7 minutes; record rate

Deposit Nb, Au, Nb

B. Remove and clean wafer

Dismount 2" Float Block

Heat in oven approx. 100 C at least one hour

Remove wafer * carefully * with pins

Rinse with TCE

Clean in 2x TCE bottles 40 sec each *carefully*

Use tweezer with flat blade and agitate wafer up and down. Do not swish!

WAFER # _____

5C. Lift-Off

Date: _____

NMP 120 C 1 hr
Eglycol scrub
NMP 120 C 1 hr, new solution
Eglycol scrub

Return to same NMP solution for 5 min
4 DI, 20 sec each * carefully *
Blow dry
Tencor Thickness: _____

6. "HEB Membrane Etch" Mask Litho.

Date: _____

Backside ETM clean
* note! use filter paper on chuck! *
Ozone 5 min
120 C HPB 5'
HMDS vapor 5'
Spin AZ5214E-IR 4 krpm 30 sec 0.45 μ m filter
Pause 4 min
HPB 100 C 2 min
Pause 2 min
DUV 2" burnoff 18 sec
Develop AZ400K 1:4 flash + 20 sec

3 DI, 20 sec each + BD
EVG backside align
Expose EVG 30 sec 5 mW/cm², VAC
HPB 130 C 60 sec (PEB)
Flood expose DUV 30 sec
Develop AZ400K 1:4 plastic tweezers
t = _____ (flash + 20 sec)
* careful!! *
3 DI, 20 sec each
Blow dry
Examine - OK? _____

7. Silicon Nitride Etch & Clean

Date: _____

A. ASH 50% O₂, 200 μ m, 200 W, > 10 minutes

FPD = _____ V = _____

B. CONDITION 3.5% CHF₃, 10 sccm N₂, 20 μ m, 200 FPD, 10 min

* be sure to flush CF₄ line if necessary, before turning valve to CHF₃ *

P = _____ V = _____

C. ETCH 60 minutes and examine.

t = _____

D. PHOTORESIST STRIP & CLEAN

March plasma etch 200 W 1 hr.

NMP + Pglycol 120 C 1 hr

Eglycol scrub

4 DI 20 sec each + BD

E. EXAMINE AND MEASURE WITH TENCOR thickness = _____

8. Membrane Etch

Date: _____

Heat a 4:1 solution of 45% KOH (in water):IPA to 80° C in a short jar with no stir bar. Place the wafer in the meniscus etch jig with the bottom side (the side with the membrane windows) facing away from the frame and the O-ring between the top face of the wafer and the frame. Place the frame on the edge of the jar, so that the bottom of the wafer faces the solution. Add more solution until the meniscus jumps up and the entire wafer surface is coated with etchant. The etch takes about four hours and must be continuously monitored. Check carefully to ensure that the membranes are etched completely clear of silicon.

WAFER # _____

9. Dice

Date: _____

A. Spin Black Wax and Mount

1. Spin unthinned black wax on back of wafer (* note! use filter paper on chuck! *)
2. Mount wafer on carrier

B. Dice

1. Use a blade for silicon and Kerfaid
2. The wafer must be diced in segments: first the test pads, removed, mounted again separately, and diced, then the 850 arrays (same), and finally the 1x5 arrays.
3. The dicing markers indicate a space 25 μm wider on each side (50 μm for the die) than the intended die size - it was intended to use a blade with a 25 μm kerf. Line up the edge of the cut with the markers, and then jog the blade position by 0.03 mm.

C. Clean

1. Rinse thoroughly in d-Limonene
2. March etch 100 W 20 minutes

10. Sputter-Etcher Imaging Gold Depo.

Date: _____

Deposit approximately 150 \AA of gold on the chips just diced and cleaned. No need to grease them down or use a platter.

Mode	Shutter	Load	Tuning	Voltage	Power	Pressure	Time
S	C			600		20	2 mins.
S	O			600		20	

11. FIB1-3

A. FIB Run Procedures

1. Change beam current; Home AVA. Align X-Y.
2. Use spot for focus and eucentric adjustment.
3. Calibrate magnification at 10 kx.
4. Move stage in only one direction at a time.
5. Jog stage controller to relieve backlash.
6. Let stage relax for five minutes after complex motions.
7. Mill all finishing squares and FIB1s at 20 kx.
8. Move to unused portion of wafer before changing beam current; then home AVA.
9. Mill all FIB2 and FIB3 at 50 kx.

B. Milling individual devices

1. Move to new position.
2. Perform eucentric and focus adjustment.
3. Mill finishing squares & FIB1 (20 kx).
4. Move on to next device. Finish all FIB1s.
5. Mill FIB2 and FIB3 together.
6. Adjust eucentric looking at bridge at 50 kx.
7. Trim mill (FIB2).
8. Tilt stage to 45 degrees.
9. Draw FIB3 rectangle; adjust upper right corner to right-top point on microbridge. Mill.
10. Tilt stage back to zero and move to next location.

WAFER # _____

11 (cont'd). FIB1-3

Date: _____

C. Dies Included: _____

Fin. sqs. filename		FIB2 patt. filename	
Fin. sqs. time		FIB2 beam current	
FIB1 patt. filename		FIB2 time	
FIB1 beam current		FIB3 width	
FIB1 time		FIB3 height	
# FIB1 passes		FIB3 time	

Finishing Squares

Dimensions:

Separation:

Pixel specifications:

FIB2 Pattern

Dimensions:

Separation:

Pixel specifications:

Comments:

Dies Included: _____ **WAFER #** _____

12. Bridge Etch

Date: _____

A. ASH 50% O₂, 200 um, 200 W, > 30 minutes

FPD = _____ V = _____

B. Prepare etch platter

Dunk Pyrex Petri dish and glass slide in TCA, Methanol, each 5 mins., BD

Clean dish, slide, and dies in March plasma 200 W 10 minutes.

Secure dies with small dabs of L-grease on glass slide.

* Do not allow any grease to peak out!!! *

B. CONDITION Ar 35%, 20 mTorr, 170 FPD, 600 V

* open Ar line but keep bottle closed tightly - pump out line*

P = _____ V = _____ t = 25 mins _____

* LOCK TUNERS! *

C. ETCH in dish in center of chamber. * TURN POWER DOWN, THEN OFF! *

time = _____ (2 - 4 hrs. typical at 300 Volts reading - 150 V actual)

D. Measure

E. Continue etching by increments to hit Target Resistance of _____ Ohms

Do not remove dies from slide.

ROOM TEMPERATURE RESISTANCE MEASUREMENTS

Date & Time →						
A.						
B.						
C.						
D.						
E.						
F.						
G.						
H.						
Previous Step						

Dies: _____ WAFER # _____

13. Sputter-Etcher Germanium Deposition Date: _____

Deposit approximately 1000 Å of germanium on the dies and the glass slide carrier for the passivation layer. Once the deposition is finished, it is important ***** TO TURN THE POWER DOWN BEFORE CLOSING THE SHUTTER. ***** Measure the device resistances both just before and just after passivation.

Mode	Shutter	Load	Tuning	Voltage	Power	Pressure	Time
S	C			600		15	2 mins.
S	O			600		15	10 mins.

14. Spot Exposure Passivation Litho. Date: _____

Drip AZ5214E-IR on to dies; spin 4 krpm 30 sec
 Pause 4 min
 HPB 100 C 2 min
 Pause 2 min
 Spot expose μ scope 30 sec each location 100x
 Develop AZ400K 1:4 flash + 20 sec
 HPB 130 C 60 sec (PEB)
 Flood expose DUV 30 sec

Develop AZ400K 1:4 plastic tweezers
 $t =$ _____ (flash + 20 sec)
 * careful!! *
 3 DI, 20 sec each
 Blow dry very gently
 Examine - OK? _____
 Measure resistance

15. Ge/Nb RIE Etch Date: _____

A. ASH 50% O₂, 200 μ m, 200 W, > 10 minutes

$$\text{FPD} = \underline{\hspace{2cm}} \quad \text{V} = \underline{\hspace{2cm}}$$

B. CONDITION 50% SF₆, 20% CHF₃, 0.6 sccm N₂, 30 μ m, 170 FPD, 10 min* be sure to flush CF₄ line if necessary, before turning valve to CHF₃ *

$$\text{P} = \underline{\hspace{2cm}} \quad \text{V} = \underline{\hspace{2cm}}$$

C. ETCH flash + 20 sec (2'30" typical)

$$t = \underline{\hspace{2cm}}$$

D. Measure

16. Dismount & Package Date: _____

HPB 100 C 60 sec

Dismount with carbon fiber tweezers & package in static-dissipative gelpak

** Place something under the arrays to decrease the contact area ***

BACKSHORT BLOCK WAFER**WAFER #** _____**1. RCA Clean****Substrate:** _____**Date:** _____

Using short jars & baskets:

ETM spin clean

* note! Use filter paper on chuck! *

NH₄OH Si clean sol'n 80 C 12 min

Running DI rinse 1 min

BOE 10:1 dip 15 sec

Running DI 1 min

HCl Si clean sol'n 80 C 12 min

Running DI 1 min

Blow dry

2. "BS Block Pyramids" Mask Litho.**Date:** _____

ETM clean unless immed. after step 1

* note! use filter paper on chuck! *

Ozone 5 min

120 C HPB 5'

HMDS vapor 5'

Spin AZ5214E-IR 4 krpm 30 sec 0.45 μ m filter

Pause 4 min

HPB 100 C 2 min

Pause 2 min

DUV 2" burnoff 18 sec

Develop AZ400K 1:4 flash + 20 sec

3 DI, 20 sec each + BD

Align carefully to flat

Expose EVG 30 sec 5 mW/cm², VAC

HPB 130 C 60 sec (PEB)

Flood expose DUV 30 sec

Develop AZ400K 1:4 plastic tweezers

t = _____ (flash + 20 sec)

3 DI, 20 sec each

Blow dry

Examine - OK? _____

3. Silicon Nitride Etch & PR Strip**Date:** _____A. ASH 50% O₂, 200 μ m, 200 W, > 10 minutes

FPD = _____ V = _____

B. CONDITION 3.5% CHF₃, 10 sccm N₂, 20 μ m, 200 FPD, 10 min* be sure to flush CF₄ line if necessary, before turning valve to CHF₃ *

P = _____ V = _____

C. ETCH 60 minutes and examine.

t = _____

D. PHOTORESIST STRIP & CLEAN

March plasma etch 200 W 1 hr.

NMP + Pglycol 120 C 1 hr

Eglycol scrub

4 DI 20 sec each + BD

E. EXAMINE AND MEASURE WITH TENCOR Si₃N₄ thickness = _____

BACKSHORT BLOCK WAFER**WAFER #** _____**4. Backside Markers****Date:** _____**A. Niobium Deposition**

Deposit approximately 1000 Å of niobium on the back side of the wafer. No need to grease the wafers down or use a platter.

Mode	Shutter	Load	Tuning	Voltage	Power	Pressure	Time
S	C			600		15	2 mins.
S	O			600		15	20 mins.

B. "BS Block Metallization" Lithography

Backside ETM clean

* note! use filter paper on chuck! *

Ozone 5 min

120 C HPB 5'

HMDS vapor 5'

Spin AZ5214E-IR 4 krpm 30 sec 0.45 µm filter

Pause 4 min

HPB 100 C 2 min

Pause 2 min

DUV 2" burnoff 18 sec

Develop AZ400K 1:4 flash + 20 sec

3 DI, 20 sec each + BD

EVG backside align

Expose EVG 30 sec 5 mW/cm², VAC

Develop AZ400K 1:4 plastic tweezers

t = _____ (flash + 20 sec)

* careful!! *

3 DI, 20 sec each

Blow dry

Examine - OK? _____

C. Backside Markers Etch & PR Strip**A. ASH 50% O₂, 200 um, 200 W, > 10 minutes**

FPD = _____ V = _____

B. CONDITION 50% SF₆, 20% CHF₃, 0.6 sccm N₂, 30 um, 170 FPD, 10 min* be sure to flush CF₄ line if necessary, before turning valve to CHF₃ *

P = _____ V = _____

C. ETCH flash + 20 sec (2'30" typical)

t = _____

D. PR Strip

March etch 100 W 20 mins.

NMP + Pglycol 120° C >20 mins.

Eglycol scrub, 3 DI 20 sec. each, BD

E. Measure niobium thickness _____

BACKSHORT BLOCK WAFER**WAFER #** _____**5. Silicon Etch****Date:** _____

Heat a solution of 4:1 KOH 45 % in water:IPA to 80 C in the large etching pot in the heater sleeve using a stir bar. The teflon insert and one of the blocks which fit in the insert should be in the jar too. Once the temperature has been reached and is stable, place just the wafer in the solution on top of the blocks; there should be no need to monitor the solution if the reflux unit is used. The etch to a depth of 127 μm requires about 3 hours. When the etch is nearly over, the wafer should be removed (dipped in running water for 60 secs + BD), evaluated at several points by Tencor, and returned to the jar for additional etching. The measured etch rate is about 0.69 $\mu\text{m}/\text{minute}$.

The etch starts more easily if the wafer is dipped in BOE for 15 seconds before etching begins. Tencor measurements should be taken in both stylus directions for best accuracy.

→	←	→	←	→	←
Etch Time					

6. Silicon Nitride Removal**Date:** _____A. ASH 50% O₂, 200 μm , 200 W, > 10 minutes

FPD = _____ V = _____

B. CONDITION 3.5% CHF₃, 10 sccm N₂, 20 μm , 200 FPD, 10 min* be sure to flush CF₄ line if necessary, before turning valve to CHF₃ *

P = _____ V = _____

C. ETCH 60 minutes and examine.

t = _____

APPENDIX C - SUGGESTIONS FOR FABRICATION PROCESS ENHANCEMENT

This appendix elaborates upon a number of possible fabrication process improvements and presents some alternative approaches which were touched upon in the main body of this dissertation. Several of these suggestions would utilize the FIB in ways which emphasize its applicability and flexibility as a fabrication instrument. A strategy adapted to circumvent difficulties caused by ESD, for fabricating a single-element mixer on a quartz substrate, is also presented.

1. In **Section 3.2**, it was noted that the fabrication of photonic crystal junctions and other features (50 μm deep cutouts corresponding to the locations of the IF circuitry on the HEB block) on the bottom edge of the feedhorn block has not yet been demonstrated. While laser micromachining would certainly be faster, the PCJs could be fabricated by FIB deposition of platinum. Fixturing and aligning the feedhorn block for PCJ fabrication would actually be easier in the FIB than in the LMM system, although the processing which follows would be much slower.

It might be also be possible to accomplish the cutouts using the enhanced etch capabilities of the FIB, but the volume of material to be removed might be too large for this to be practical. Using a 5900 pA beam current with the enhanced etch, in one trial it required 60 minutes to mill a 25 μm by 100 μm rectangle to a depth of 12 μm in brass. This corresponds to a rate of material removal of about 8 $\mu\text{m}^3/\text{s}$, compared to removal rates of silicon using LMM of approximately $10^5 \mu\text{m}^3/\text{s}$. For the 1450 GHz design, the IF cutout in the feedhorn block measures about 200 μm wide x 280 μm long x 50 μm deep, for a volume of $2.8 \times 10^6 \mu\text{m}^3$. If silicon mills away at twice the rate of brass, then the

time required to fabricate the feature using FIB is an impractical but not impossible 48 hours.

2. The FIB could similarly be used to fabricate PCJs and backshort cavities on the top surfaces of backshort block pyramidal stubs (**Section 4.4**), which has likewise not yet been demonstrated using laser micromachining. However, if the PCJs are deposited on top of the pyramidal backshort stubs, instead of the intended process of fabrication by milling away using LMM, the finished backshort stub will end up a few microns too tall. (To fix this would require only a trivial compensating change, revising the target depth of the pyramidal stub silicon etch downward from 127 μm to 120 μm .) The backshort block cavity in the 1450 GHz design has a volume of 490,000 μm^3 , and so could be fabricated in less than nine hours under the conditions assumed above.

3. The backshort block fabrication procedure outlined in **Table 4.2** suffers from a process incompatibility issue: the niobium backside markers deposited and defined in step 5 are removed by the hot KOH silicon etch in step 6. The order of these two steps cannot be reversed because the bulk silicon etch obliterates the front-to-backside alignment markers on the front side of the wafer, which are crosses 110 μm in size. These features work very well as alignment markers, but possess four convex corners and as a result are etched away to a square shape bounded by $\{111\}$ planes. It is possible that this issue could be resolved by replacing the mask with an updated version which substitutes an array of squares (which the silicon etch would not distort) for the crosses,

so that the backside alignment markers (currently step 5) could be deposited and defined after the bulk micromachining step (currently step 6).

There are other options short of replacing the mask, however. It is possible that a metal less susceptible to hot KOH can be found (chromium and titanium are two candidates). It might also be possible to replace the process of immersion etching, despite the very good accuracy and uniformity which it was found to produce, with meniscus etching, as discussed for the HEB block in **Section 5.3**. This has been shown to protect the circuitry on the front of an HEB block wafer very well. Either of these approaches would solve the process incompatibility issue which currently exists.

4. Phosphoric acid is preferable to RIE for silicon nitride removal in step 7 of the backshort block fabrication process (**Section 4.4**). It cannot be used if there are features on the bottom side of the backshort block wafer, however, as the H_3PO_4 etch would remove those features along with the silicon nitride layer upon which they were deposited. It is furthermore impossible to use the wafer protection jig for this application, as phosphoric acid at 180°C etches stainless steel. Removal of the front-side silicon nitride by RIE has of course been demonstrated, so that currently this issue is not a significant impediment, but there are two other options which are worth considering.

The first is meniscus etching of Si_3N_4 , which seems quite plausible, if somewhat dangerous due to the elevated temperature of the etchant. The second possibility arises if one considers fabricating the pyramidal stub PCJs by FIB deposition of platinum, while fabricating the backshort cavities by LMM. In that case, it would be required only to remove the $0.75\ \mu\text{m}$ thick silicon nitride layer from the small area ($70\ \mu\text{m} \times 140\ \mu\text{m}$) of

the backshort cavity, exposing the silicon underneath to chemical attack by chlorine in the LMM system. This could be very easily done in the FIB, and would even take advantage of the superior alignment and registration capabilities of the FIB system, compared to the LMM apparatus.

5. Dicing the HEB block wafer before fabricating HEB devices (refer to **Table 5.1**) makes it impossible to use the passivation layer mask, as discussed in **Section 5.4**. While this issue could be addressed with a new mask design, the FIB could also conceivably be usefully applied in this situation. A small patch of SiO deposited by FIB on top of the passivation layer of germanium which covers a finished device would serve very well as a mask for the Ge/Nb etch which defines the passivation layer (step 13). There is an additional opportunity present in this proposal, however.

It was shown in **Figure 8.7** that implantation of gallium into a thin niobium film increases its resistance (a dose of about $20 \times 10^{19} \text{ cm}^{-3}$ was found to cause an increase of $5 \Omega/\square$ at 10 Kelvins). It may be possible to use the FIB to trim an array of HEB devices to nearly identical (room temperature) resistances, not by physically shaving off a bit of their widths, but by implanting them with gallium through a sacrificial/passivation layer of germanium.

This could be attempted with an HEB block which is already mounted (refer to **Figure 3.15**) and wire-bonded, in which case the device resistance could easily be monitored in-situ during implantation if the proper feedthrough were installed in the FIB chamber. Following this process, it would be necessary to place the entire copper mount with the HEB/backshort block chips installed in it into the RIE to perform the Ge/Nb etch

(using an FIB-deposited SiO mask), but there is no obvious reason that this should cause any difficulties. HEB trimming was not attempted during the course of the research described in this dissertation.

6. No mixers on quartz substrates were successfully fabricated during the course of this research. ESD is likely to blame for this failure, as small chips are very vulnerable to static (they often weigh less than the static attractive forces they experience, for instance) and difficult to handle. Experience furthermore suggests that ESD damage of HEBs is harder to control for devices on quartz substrates than for devices on Si/Si₃N₄ substrates. In view of the previous suggestion about placing the array mount in the RIE, however, it might be possible to fabricate a single-element mixer in a waveguide block by mounting the mixer chip in the block after the FIB1-3 processing but before the bridge etch. The device could then be bridge etched while the chip was sitting in the waveguide channel, and even passivated with germanium and patterned using the FIB and Ge/Nb RIE.

This is a recent idea of the author's which was not attempted in the course of the dissertation research.

APPENDIX D - PRELIMINARY RESULTS REGARDING THE ANOMALOUS BEHAVIOR OF THIN Nb/Au FILMS

This appendix contains preliminary results relevant to the anomalous behavior of thin Nb/Au films which were not included in **Chapter 8**. These data are considered preliminary in two respects. First, the graphs presented here are the results of experiments which were not as carefully structured as those discussed in **Chapter 8**, and which are therefore more difficult to meaningfully interpret. Second, the results presented here have not been verified by repetition.

Three graphs are included in this appendix. **Figure D.1** presents the results of implantation experiments on a set of samples from M2380, which were not masked with photoresist. The experiment represented by this information is the same in all respects as the experiment summarized in **Figure 8.5**, except that in this case the samples were held down to the FIB sample stage with a metal clip. Because the samples were very thin films, however, it is likely that the electrical contact to the sample may not have been equally good in every case. The samples were irradiated individually, with an 11 pA beam current and at a magnification of 1200x, with exposures between 60 - 480 seconds.

All of these samples exhibit the anomalous change in the transition temperature of the contact pads, although not in the uniform manner nor to the same degree shown by ungrounded samples in **Figure 8.5**. Sample "E" even shows an anomalous decrease, along with a dropback in resistance at the peak of the second transition. Sample "F" shows a third transition, of about 1.4 Ω in height, above the contact pad transition, across the range from 6.3 - 6.5 Kelvins. Samples "A" and "D" in **Chapter 8** possessed similar third transitions.

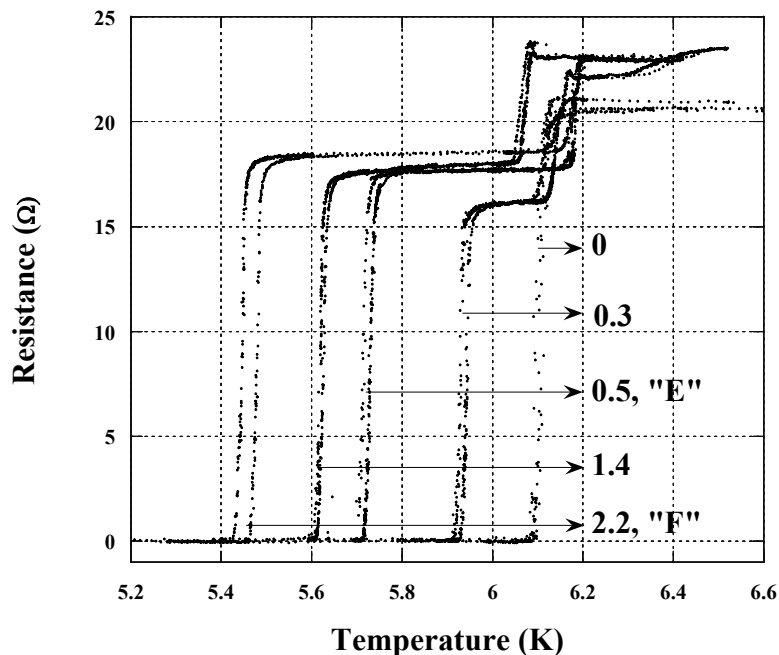


Figure D.1. Results of gallium implantation experiments on Nb (100 Å)/Au (100 Å) samples belonging to the M2380 set where the samples were grounded to the FIB stage with a metal clip. The implantation doses are given in units of 10^{19} cm^{-3} ; sample “0” was an unimplanted reference.

Figure D.2 presents the results of the implantation of another M2380 sample, using a low dose of only $2 \times 10^{16} \text{ cm}^{-3}$. This implantation was performed using an 11 pA beam current, an exposure time of 17 seconds, and a magnification of 226x, corresponding to a field of view (and implantation region) about $1300 \mu\text{m}$ across. Therefore, in this case approximately the central one-fifth of the sample by area was implanted. According to **Figure D.2**, the transition temperature of the implanted area of this sample increased above the transition temperature of the reference sample, by about 0.06 Kelvins.

Although the contact pad resistance of this sample is quite small (because the irradiated central region is so large), a transition of about 1.7Ω does occur at a temperature elevated above even the enhanced T_C of the irradiated region. Therefore this sample exhibits the anomalous behavior discussed in **Chapter 8**. In this case, the second

transition is quite broad, about 0.30 K, and exhibits an increase of about 0.40 Kelvins above the transition temperature of the irradiated region.

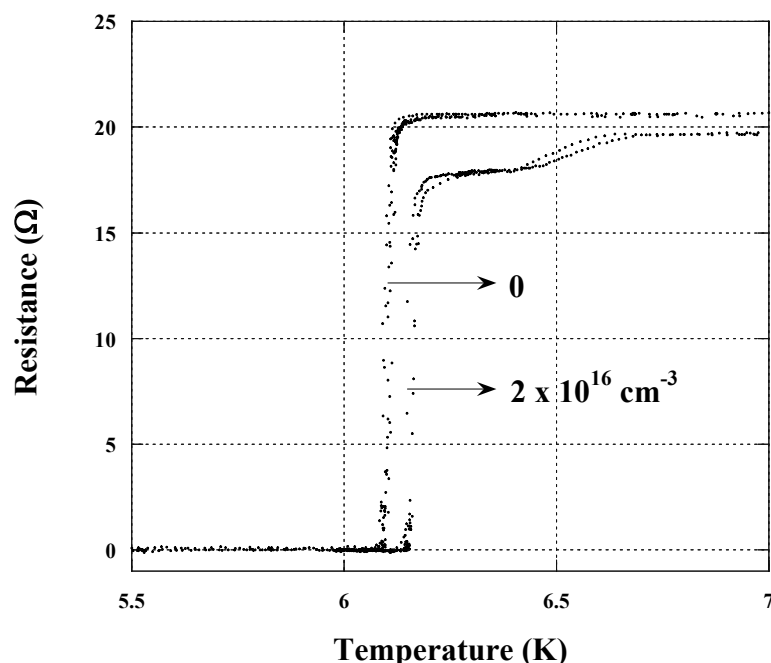


Figure D.2. Results of low dose gallium implantation on another sample from the M2380 set. The different 10 K resistances of these two samples indicates that the resistance ratio of the low-dose implanted sample increased slightly, to RRR = 1.68 from RRR = 1.64 for the unimplanted reference.

Figure D.3 suggests that bombardment with low-energy (300 Volt) argon ions can also cause the anomalous behavior. In this case, the samples were thicker - Nb(150 Å)/Au(250 Å) - masked with photoresist in the manner of **Figure 8.1**, and etched in the RIE using a quartz platter, an argon flow of 50 sccm, and a pressure of 20 μm. Several features of the information presented in the figure require explication.

In this case, the first transition represents the contact pads, which is different than what was found in **Chapter 8, Figure D.1**, and **Figure D.2**. Sample “H” exhibits an anomalous decrease, and sample “G” an anomalous increase, of the contact pad transition temperature with respect to the transition temperature of reference sample “0”. The

contact pads were masked with photoresist in this experiment, and did not suffer argon ion bombardment.

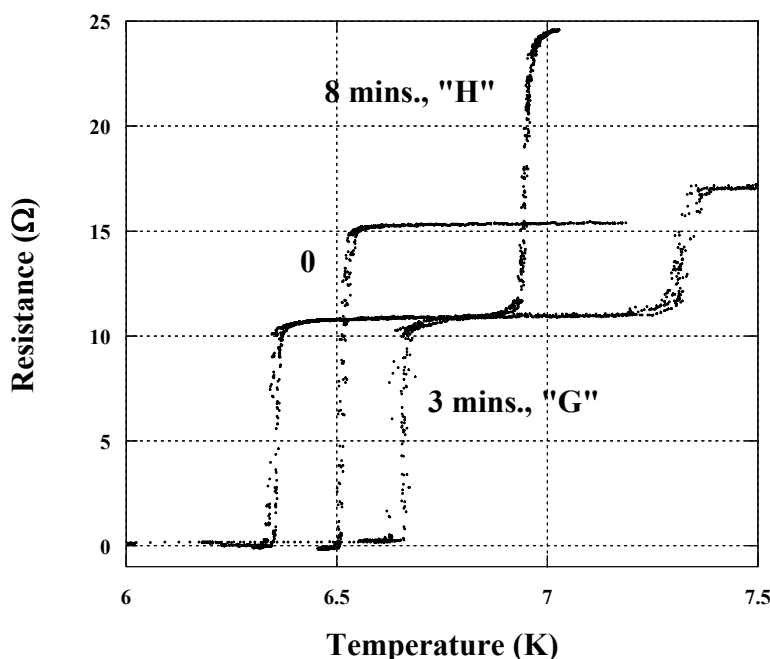


Figure D.3. Example of anomalous behavior shown by Nb(150 Å)/Au(150 Å) films, masked with photoresist and etched with argon at 80 Watts/300 Volts self-bias. In this case, the first transitions represent the contact pads. Therefore the 3 minute etch causes an anomalous increase, and the 8 minute etch an anomalous decrease.

The transition temperature of the etched portions of both samples “G” and “H” increased, which appears to be contrary to the findings of **Figure 6.14** using 100 Å thick niobium films. However, this observation is at least partially explained by the removal of the 250 Å thick gold layer, which increases the transition temperature by lessening the proximity effect suppression of T_C . Data from the period of time before the gold layer was completely removed from the sample by argon etching were not included in **Figure 6.14**.

Three minutes of etching was probably not sufficient to remove the entire gold layer, while eight minutes likely was; therefore the transition temperature of the 150 Å

niobium film of **Figure D.3** was found to decrease with increasing etch time, in accord with expectations.

Due to a fabrication error, however, it is necessary to repeat the experiment just described before relying on these results or designing a course of future research based upon them. After the wafer from which samples “G” and “H” were taken was fabricated, it was found that the gold target used to deposit the sample had partially worn through. Therefore, the gold layer in this case contained many other elements, including, significantly, indium. Because indium is chemically quite similar to gallium, the meaning of the third experiment is not at all clear from the information presented.

In conclusion, provisional data indicate that a) grounding the sample to the FIB stage during implantation has a significant effect upon the anomalous behavior, b) the anomalous behavior occurs even at quite low doses, and at low doses is even enhanced in terms of the temperature increase, and c) that bombardment with low energy argon ions might also cause the anomalous behavior, although in that case matters are perhaps complicated by the additional variation in the gold film thickness. The author can offer no explanation for the anomalous behavior or for these observations as of this writing.

BIBLIOGRAPHY

- [ACES] Anisotropic Crystalline Etch Simulation, available at <http://mass.micro.uiuc.edu/research/completed/aces/pages/home.html>.
- [Akaike92] H. Akaike, A. Fujimaki, Y. Takai and H. Hayakawa, "Submicrometer-Scale Patterning of Superconducting Nb Films Using Focused Ion Beam", *Jpn. J. Appl. Phys.*, Vol. 31, Part 2, No. 4A, April 1992, pp. L410-L412.
- [Arams66] F. Arams, C. Allen, B. Peyton, and E. Sard, "Millimeter Mixing and Detection in Bulk InSb", *Proc. of the IEEE*, Vol. 54, No. 4, pages 612-622, April 1966.
- [Araujo98] H. Araujo and G.J White, "Numerical Modelling of the Diffusion Cooling Response in Superconducting Hot-Electron Mixers", *IEEE Transactions on Applied Superconductivity*, Palm Desert, CA, 1998.
- [Arrington74] C.H. Arrington III and B.S. Deaver, Jr., "Superconducting weak links formed by ion implantation," *Applied Physics Letters*, Vol. 26, No. 4, pp. 204-206, February 1975.
- [Baselmans03] J.J.A. Baselmans, M. Hajenius, J.R. Gao, T.M. Klapwijk, P.A.J. de Korte, B. Voronov and G. Gol'tsman, "Noise performance of NbN Hot Electron Bolometer mixers at 2.5 THz and its dependence on the contact resistance," *Proceedings of the 14th Intl. Symp. on Space Terahertz Technology*, Tucson, AZ, April, 2003, pp. 11 - 19.
- [Bass00] Robert B. Bass, Master's Thesis, University of Virginia Dept. of Electrical Engineering, 2000.
- [Bass04] Robert B. Bass, Ph.D. Dissertation, University of Virginia Dept. of Electrical and Computer Engineering, 2004.
- [Baubert03] J. Baubert, H. Merkel, M. Salez, and P. Khosropanah, "A Hot Spot Model for Membrane-Based HEB Mixer", *Proceedings of the 14th Intl. Symp. on Space Terahertz Technology*, Tucson, AZ, April, 2003, pp. 393-404..
- [Burke96] P.J. Burke, R.J. Schoelkopf, D.E. Prober, A. Skalare, W.R. McGrath, B. Bumble, and H.G. LeDuc, "Length scaling of bandwidth and noise in hot-electron superconducting mixers", *App. Phys. Lett.*, Vol. 68, page 3344, 1996.
- [Burke97] Peter J. Burke, "High Frequency Electron Dynamics in Thin Film Superconductors and Applications to Fast, Sensitive THz Detectors," Ph.D. Dissertation, Yale University Dept. of Applied Physics, 1997.
- [Camerlingo85] C. Camerlingo, P. Scardi, C. Tosello and R. Vaglio, "Disorder effects in ion-implanted niobium thin films," *Physical Review B*, Vol. 31, No. 5, pp. 3121-3123, March 1985.

- [Cecil04]** Thomas W. Cecil, University of Virginia Microfabrication Laboratory, private communication.
- [Clark03]** W. Clark, J.Z. Zhang and A.W. Lichtenberger, "Ti Quadlevel Resist Process for the Fabrication of Nb SIS Junctions," *IEEE Transactions on Applied Superconductivity*, Vol. 13(2), pp. 115-118, June 2003.
- [Collins02]** A.F. Collins, *Electrical World and Engineer*, Vol. 39, 1902. Via **[Lee98]**, p. 4.
- [Datesman99]** Aaron M. Datesman, Master's Thesis, University of Virginia Dept. of Electrical Engineering, 1999.
- [Datesman01]** A. Datesman, J. Zhang, A. Lichtenberger and C. Walker, "Fabrication of a Superconducting Hot-Electron Bolometer Receiver with Micromachined Waveguide Components," *Proc. of the 14th Biennial University/Government/Industry Microelectronics Symposium*, Richmond, VA, pp. 186-189, June 2001
- [Echternach99]** P.M. Echternach, H.G. LeDuc, A. Skalare and W.R. McGrath, "Fabrication of an Aluminum Based Hot Electron Mixer for Terahertz Applications," *Proc. Tenth International Symposium on Space Terahertz Technology*, University of Virginia, March 1999, pp. 261-268.
- [Finegan61]** J.D. Finegan and R.W. Hoffman, "Stress and Stress Anisotropy in Iron Films," *8th Nat'l Symp. on Vacuum Technology Transactions*, pp. 935-942, 1961.
- [Foner72]** S. Foner, E.J. McNiff, Jr., G.W. Webb, L.J. Vieland, R.E. Miller and A. Wicklund, "Upper Critical Fields of Nb_xGa_{1-x} : A Binary High Temperature Superconductor," *Physics Letters*, Vol. 38A, No. 5, pp. 323-324, February 1972.
- [Frommberger01a]** Michael Frommberger, "Characterization of NbN thin films produced on quartz substrates using MgO seed layers for phonon cooled hot-electron bolometer devices", *Proc. 12th International Symposium on Space Terahertz Technology*, San Diego, CA, February 2001.
- [Frommberger01b]** Michael Frommberger, "Herstellung und Charakterisierung supraleitender Nb und NbN Hot-Electron Bolometer Mischerelemente," Ph.D. Dissertation, University of Cologne, 2001.
- [Ganzevles02]** Walter Ganzevles, "A Quasi-Optical THz Mixer Based on a Nb Diffusion-Cooled Hot-Electron Bolometer," Ph.D. Dissertation, Delft University of Technology, 2002.
- [Gerecht02]** E. Gerecht, C.D. Reintsema, E.N. Grossman, A.L. Betz, and R.T. Boreiko, "Noise Temperature for Nb DHEB Mixer Receiver for Far-Infrared Spectroscopy", *Proceedings of the 13th Intl. Symp. on Space Terahertz Technology*, Cambridge, MA, March, 2002, pp. 235 - 234.

- [Gerecht04]** E. Gerecht, S. Yngvesson, J. Nicholson, Y. Zhuang, F.R. Morales, X. Zhao, D. Gu, R. Zannoni, M. Coulombe, J. Dickinson, T. Goyette, B. Gorveatt, J. Waldman, P. Khosropanah, C. Groppi, A. Hedden, D. Golish, C. Walker, J. Kooi, R. Chamberlin, A. Stark, C. Martin, R. Stupak, N. Tothill and A. Lane, "Deployment of *TREND* - A Low-Noise Receiver User Instrument at 1.25 THz to 1.5 THz for AST/RO at the South Pole," *Proceedings of the 14th Intl. Symp. on Space Terahertz Technology*, Tucson, AZ, April, 2003, pp. 179 - 188.
- [Gershenson90]** E.M. Gershenson, G.N. Gol'tsman, I.G. Gogidze, Y.P. Gousev, A.I. Elant'ev, B.S. Karasik and A.D. Semenov, "Millimeter and Submillimeter Range Mixer Based on Electronic Heating of Superconductive Films in the Resistive State," *Soviet Physics: Superconductivity*, Vol. 3, p. 1582, 1990.
- [Gershenson91]** E.M. Gershenson, G.N. Gol'tsman, Y.P. Gousev, A.I. Elant'ev, and A.D. Semenov, *IEEE Trans. Magn.*, Vol. 27, page 1317, 1991.
- [Greene-Tweed]** Available through www.allorings.com.
- [Hajenius03]** M. Hajenius, J.J.A. Baselmans, J.R. Gao, T.M. Klapwijk, P.A.J. de Korte, B. Voronov and G. Gol'tsman, "Improved NbN Phonon Cooled Hot Electron Bolometer Mixers," *Proceedings of the 14th Intl. Symp. on Space Terahertz Technology*, Tucson, AZ, April, 2003, pp. 413-423.
- [Halbritter87]** J. Halbritter, "On the Oxidation and on the Superconductivity of Niobium," *Applied Physics A*, Vol. 43, pp. 1-28, 1987.
- [Harnack99]** O. Harnack, B. Karasik, W. McGrath, A. Kleinsasser and J. Barner, "Microwave Mixing and IF Bandwidth in Sub-Micron Long High-T_C Hot-Electron Bolometers," *Proc. Tenth International Symposium on Space Terahertz Technology*, University of Virginia, March 1999, pp. 169-179.
- [Held78a]** D.N. Held and A.R. Kerr, "Conversion Loss and Noise of Microwave and Millimeter Wave Mixers: Part 1 - Theory", *IEEE Trans. MTT*, Vol. MTT-26, No. 2, February 1978, pp. 49-54.
- [Held78b]** D.N. Held and A.R. Kerr, "Conversion Loss and Noise of Microwave and Millimeter Wave Mixers: Part 2 - Experiment", *IEEE Trans. MTT*, Vol. MTT-26, No. 2, February 1978, pp. 55-61.
- [Hesler01]** J.L. Hesler, "A Photonic Crystal Joint (PCJ) for Metal Waveguides," *Proc. of 2001 IEEE MTT-S Intl. Microwave Symposium*, Phoenix, AZ, June 21-25, 2001, pp. 783-786.
- [Hoffman76]** D.W. Hoffman and J.A. Thornton, "Internal Stresses in Sputtered Chromium," *Thin Solid Films*, 40, pp. 355-363, 1977.
- [Huang98]** L.-S. Huang, S.-S. Lee, E. Motamedi, M. C. Wu and C.-J. Kim, "MEMS Packaging for Micro Mirror Switches", *Proc. 48th Electronic Components & Technology Conference*, Seattle, WA, pp. 592-597, May 1998.

- [Hunt02] Matthew Hunt, University of Virginia Semiconductor Device Lab, private communication, 2002.
- [Iosad98] N.N. Iosad, E.K. Kov'ev, S.N. Polyakov, V.V. Roddatis, P.N. Dmitriev and T.M. Klapwijk, "Properties of DC Magnetron Sputtered Nb and NbN films for Different Source Conditions," *IEEE Transactions on Applied Superconductivity*, Vol. 9, No. 2, pp. 1720-1723, 1999.
- [Jasky33] K.G. Jansky, "Radio waves from outside the solar system," *Nature*, Vol. 132, No. 66, 1933.
- [Kain02] B. Kain, S.R. Khan and R.P. Barber Jr., "Tuning the transition temperature of superconducting Ag/Pb films via the proximity effect," *Physica C*, Vol. 382, pp. 411-414, 2002.
- [Kang01] D.-J. Kang, R. Speaks, N.H. Peng, R. Webb, C. Jeynes, W.E. Booij, E.J. Tarte, D.F. Moore and M.G. Blamire, "Nanometer scale masked ion damage barriers in $\text{YBa}_2\text{Cu}_3\text{O}_{7-\delta}$," *IEEE Transactions on Applied Superconductivity*, Vol. 11, No. 1, March 2001, pp. 780-783.
- [Karasik97] B.S. Karasik, M.C. Gaidis, W.R. McGrath, B. Bumble and H.G. LeDuc, "Low noise in a diffusion-cooled hot-electron mixer at 2.5 THz," *Appl. Phys. Lett.*, Vol. 71, No. 11, pp. 1567-1569, September 1997.
- [Karasik98a] B.S. Karasik, A. Skalare, W.R. McGrath, B. Bumble, H.G. LeDuc, J.B. Barner, A.W. Kleinsasser, P.J. Burke, R.J. Schoelkopf and D.E. Prober, "Low-noise and wideband hot-electron superconductive mixer for THz frequencies," *4th Int. Conf. on MM & SMM Waves and Applications*, San Diego, CA, 20-23 July 1998.
- [Karasik98b] B.S. Karasik, W.R. McGrath, and R.A. Wyss, "Optimal Choice of Material for HEB Superconducting Mixers", *IEEE Transactions on Applied Superconductivity*, Palm Desert, CA, September 1998.
- [Kawamura99] J.H. Kawamura, C.-Y.E. Tong, R. Blundell, D.C. Papa, T.R. Hunter, G. Gol'tsman, S. Cherednichenko, B. Voronov and E. Gershenzon, "An 800 GHz NbN Phonon-cooled Hot-electron Bolometer Mixer Receiver," *IEEE Transactions on Applied Superconductivity*, Vol. 9, 1999.
- [Kinch63] M.A. Kinch and B.V. Rollin, "Detection of millimetre and sub-millimetre radiation by free carrier absorption in a semiconductor", *Brit. J. Appl. Phys.*, Vol. 14, pages 672-676, 1963.
- [Kittel96] C. Kittel, Introduction to Solid State Physics. New York: John Wiley & Sons, 1996.
- [Kooi01a] J.W. Kooi, G. Chattopadhyay, F. Rice, J. Zmuidzinas, S. Withington and G. Yassin, "A Full Height Wave Guide to Thin Film Microstrip Transition," *9th International Conference on Terahertz Electronics*, Charlottesville, VA, September 15-16, 2001.

- [Kooi01b]** J.W. Kooi, California Institute of Technology, memo by private communication, "IF Considerations for a 1 μm Silicon Nitride ($\text{Er}=7$) Based Radial Probe with 0.3 μm Wiring," December 2001.
- [Kooi02a]** J.W. Kooi, California Institute of Technology, memo by private communication, "850 and 1450 GHz Designs Compared (Given a 1 μm Silicon Nitride ($\text{Er}=7$) Based Radial Probe with 0.3 μm Au Wiring)", January 2002.
- [Kooi02b]** J.W. Kooi, California Institute of Technology, private communication.
- [Kooi03]** J.W. Kooi, G. Chattopadhyay, S. Withington, F. Rice, J. Zmuidzinas, C.K. Walker and G. Yassin, "A Full Height Wave Guide to Thin Film Microstrip Transition With Exceptional RF Bandwidth and Coupling Efficiency," *Journal of IR & MM Waves*, Vol. 24, No. 3, pp. 261-284, 2003.
- [Kovacs98]** G.T.A. Kovacs, N.I. Maluf, K.E. Petersen, "Bulk Micromachining of Silicon," *Proceedings of the IEEE*, Vol. 86, No. 8, pp. 1536-1551, August 1998.
- [Kumar91]** S. Kumar and G.C. Vradis, "Thermal Conduction by Electrons Along Thin Films: Effects of Thickness According to Boltzmann Transport Theory", *Micromechanical Sensors, Actuators, and Systems*, DSC-Vol. 32, pages 89-101, ASME, 1991.
- [Kuroda87]** K. Kuroda and M. Yuda, "Niobium-stress influence on Nb/Al-oxide/Nb Josephson junctions," *J. Appl. Phys.*, Vol. 63, No. 7, pp. 2352-2357, April 1988.
- [Jansky33]** K.G. Jansky, "Radio waves from outside the solar system," *Nature*, Vol. 132, No. 66, 1933.
- [Lea97]** D.M. Lea, H.H. Huang, and A.W. Lichtenberger, "Use of a Negative Tone Photoresist to Improve Low-Tc Superconducting Tunnel Junction Fabrication Processes," *IEEE Transactions on Applied Superconductivity*, 1997.
- [Lee98]** T.H. Lee, *The Design of CMOS Radio-Frequency Integrated Circuits*. Cambridge, U.K.: Cambridge University Press, 1998.
- [Li95]** Y.X. Li, P.J. French, and R.F. Wolffenbuttel, "Selective reactive ion etching of silicon nitride over silicon using CHF_3 with N_2 addition," *J. Vac. Sci. Technol. B*, Vol. 13, No. 5, pp. 2008-2012, Sep./Oct. 1995.
- [Long99]** Mark K. Long, *Computer Aided Micro Machining*. Ph.D. Thesis, California Institute of Technology, 1999.
- [McGrath95]** W.R. McGrath, "Hot-Electron Bolometer Mixers for Submillimeter Wavelengths: An Overview of Recent Developments", *Proc. Sixth International Symposium on Space Terahertz Technology*, 1995.

- [Merkel01] H.F. Merkel, P. Khosropanah, S. Cherednichenko, K.S. Yngvesson, A. Adam, and E.L. Kollberg, "A Two-Dimensional Hot-Spot Mixer Model for Phonon-Cooled Hot Electron Bolometers", *IEEE Transactions on Applied Superconductivity*, Vol. 11, No. 1, pp. 179-182, March 2001.
- [Merkel02] H.F. Merkel, "A Hot Spot Model for HEB Mixers Including Andreev Reflection", *Proceedings of the 13th Intl. Symp. on Space Terahertz Technology*, Cambridge, MA, March 2002, pp. 53-64.
- [Mizuno99] Y. Mizuno, K. Miyahara, J.G. Wen, T. Utagawa and Y. Enomoto, "Asymmetrical FIB Junctions as Components for HTS SFQ Circuits," *IEEE Transactions on Applied Superconductivity*, Vol. 9, No. 2, June 1999, pp. 2882-2885.
- [Moore85] W.J. Moore, H.S. Newman, and D.C. Webb, "Minimization of the noise temperature of the free-electron bolometer mixer", *J. Appl. Phys.*, Vol. 58, No. 5, pages 1715-1718, September 1985.
- [Müller87] K.-H. Müller, "Stress and microstructure of sputter-deposited thin films: Molecular dynamics investigations," *J. Appl. Phys.*, Vol. 62, No. 5, pp. 1796-1799, September 1987.
- [Murakami85] M. Murakami and T. Yogi, "Strain in evaporated Nb thin films," *J. Appl. Phys.*, Vol. 57, No. 2, pp. 211-215, January 1985.
- [Prober93] D.E. Prober, "Superconducting terahertz mixer using a transition-edge microbolometer," *Appl. Phys. Lett.*, Vol. 62, No. 17, pp. 2119 - 2121, April 1993.
- [Phillips73] T.G. Phillips and K.B. Jefferts, "A Low Temperature Bolometer Heterodyne Receiver for Millimeter Wave Astronomy", *Rev. Sci. Instr.*, Vol. 44, No. 8, pages 1009-1014, August 1973.
- [Pozar98] D.M. Pozar, *Microwave Engineering*. New York, NY: John Wiley & Sons, 1998.
- [Puers90] B. Puers and W. Sansen, "Compensation Structures for Convex Corner Micromachining in Silicon," *Sensors and Actuators A21-A23*, pp. 1036-1041, 1990.
- [Putley65] E.H. Putley, "Indium Antimonide Submillimeter Photoconductive Detectors", *Applied Optics*, Vol. 4, No. 6, pages 649-657, June 1965.
- [Radford04] S.J.E. Radford, R. Blundell, S. Paine, H. Gibson and D. Marrone, "CO(9-8) in Orion," *Proceedings of the 14th Intl. Symp. on Space Terahertz Technology*, Tucson, AZ, April, 2003, p. 216.
- [Ranade93] R.M. Ranade, S.S. Ang and W.D. Brown, "Reactive Ion Etching of Thin Gold Films," *J. Electrochem. Soc.*, Vol. 140, No. 12, pp. 3676-3678, December 1993.

- [Richards94] P.L. Richards, "Bolometers for infrared and millimeter waves", *J. Appl. Phys.*, Vol. 18, No. 1, pages 1-24, July 1994.
- [Rohlf99] K. Rohlf and T.L. Wilson, Tools of Radio Astronomy. Berlin, Germany: Springer-Verlag, 1999.
- [Rudziak01] M.K. Rudziak and T. Wong, "Development of a Nb₃Sn Conductor Containing Ga and Mg Dopants," *IEEE Transactions on Applied Superconductivity*, Vol. 11, No. 1, pp. 3580-3583, March 2001.
- [Saleh71] A.A.M. Saleh, Theory of Resistive Mixers. Cambridge, MA: MIT Press, 1971.
- [Satow73] T. Satow, "Structure Change of Amorphous Germanium in the Annealing Process," *Phys. Stat. Sol. (A)*, Vol. 18, pp. K147-K150, June, 1973.
- [Schultz00] J. Schultz, D.V. Ivanov, and K.R. Farmer, "Meniscus Interface Etching of Silicon in KOH in a Hands-on Introductory Course in MEMS," *Proc. of the 14th Biennial University/Government/Industry Microelectronics Symposium*, Richmond, VA, pp. 153-157, June 2001.
- [Schultz03] Jonathan Schultz, University of Virginia Microfabrication Laboratory, private communication.
- [Schultz04] Jonathan C. Schultz, Master's Thesis, University of Virginia Dept. of Electrical and Computer Engineering, 2004.
- [Serapiglia04] G.B. Serapiglia, Y. Dora, M.S. Sherwin, M. Hanson, A.C. Gossard and W.R. McGrath, "Design, fabrication and testing of semiconductor tunable antenna-coupled intersubband Terahertz (TACIT) detectors," *Proceedings of the 14th Intl. Symp. on Space Terahertz Technology*, Tucson, AZ, April, 2003, pp. 119 - 120.
- [Skalare95] A. Skalare, W.R. McGrath, B. Bumble, H.G. LeDuc, P.J. Burke, A.A. Verheijen and D.E. Prober, "A Heterodyne Receiver at 533 GHz using a Diffusion-Cooled Superconducting Hot Electron Bolometer Mixer," *IEEE Transactions on Applied Superconductivity*, Vol. 5, No. 2, June 1995, pp. 2236-2239.
- [Skalare96] A. Skalare, W.R. McGrath, B. Bumble, H.G. LeDuc, P.J. Burke, A.A. Verheijen, R.J. Schoelkopf, and D.E. Prober, "Large bandwidth and low noise in a diffusion-cooled hot-electron bolometer mixer", *Appl. Phys. Lett.*, Vol. 68, No. 11, pages 1558-1561, March 1996.
- [Skalare03] A. Skalare, W.R. McGrath, B. Bumble, and H.G. LeDuc, "Transition Edge Operation of Tantalum Diffusion-Cooled Hot-Electron Bolometers", *Proceedings of the 14th Intl. Symp. on Space Terahertz Technology*, Tucson, AZ, April, 2003, pp. 427-430.

- [Skalare04] A. Skalare, W.R. McGrath, B. Bumble, and H.G. LeDuc, "Transition Edge Operation of Tantalum Diffusion-Cooled Hot-Electron Bolometers", *Proceedings of the 14th Intl. Symp. on Space Terahertz Technology*, Tucson, AZ, April, 2003, pp. 427-430.
- [Smith65] R.A. Smith, "Detectors for Ultraviolet, Visible, and Infrared Radiation", *App. Optics*, Vol. 4, No. 6, pages 631-638, June 1965.
- [SOFIA] From the website of the SOFIA project, <http://www.sofia.usra.edu/Gallery/data/TD20000004.html>.
- [SORAL] Stewart Observatory Radio Astronomy Laboratory, University of Arizona, Tucson, AZ. <http://soral.as.arizona.edu>.
- [Sosnowski77] J. Sosnowski, M. Drys and J. Szymaszek, "Properties of Superconducting Nb-Ga Alloys with A15 Type Structure," *Phys. Stat. Sol. (A)*, Vol. 42, pp. K159-K164, 1977.
- [SRIM] The Stopping and Range of Ions in Matter, www.srim.org.
- [SwissJewel] Swiss Jewel Company, Philadelphia, PA, www.swissjewel.com.
- [van Duzer99] T. van Duzer and C.W. Turner, *Superconductive Devices and Circuits*. Upper Saddle River, NJ: Prentice Hall, 1999.
- [Vasile97] M.J. Vasile, Z. Niu, R. Nassar, W. Zhang and S. Liu, "Focused ion beam milling: Depth control for three-dimensional microfabrication," *J. Vac. Sci. Technol. B*, Vol. 15, No. 6, Nov/Dec 1997, pp. 2350-2354.
- [Walker97] C.K. Walker, G. Narayanan, H. Knoepfle, J. Capara, J. Glenn and A. Hungerford, "Laser Micromachining of Silicon: A New Technique for Fabricating High Quality Terahertz Waveguide Components," *Proc. Eighth International Symposium on Space Terahertz Technology*, Harvard University, March 1997, pp. 358-376.
- [Walker00] C.K. Walker, C. Drouet D'Aubigny, C. Groppi, J. Papapolymerou, G. Chin, and A. Lichtenberger, "A New Laser Micromachining System for the Fabrication of THz Waveguide and Quasi-Optical Components", *Proceedings of the 11th Intl. Symp. on Space Terahertz Technology*, Ann Arbor, MI, May, 2000.
- [Whalen70] J.J. Whalen and C.R. Westgate, "Bulk Indium Antinomite Mixers for the Submillimeter Wave Region", *Symposium on Submillimeter Waves*, Polytechnic Institute of Brooklyn, March 31-April 2, 1970.
- [Wilms Floet98] D. Wilms Floet, E. Miedma, J.J.A. Baselmans, T.M. Klapwijk, and J.R. Gao, "Resistive States of Superconducting Hot-Electron Bolometer Mixers: Charge-Imbalance vs. Hotspot", *IEEE Transactions on Applied Superconductivity*, Palm Desert, CA, 1998.

- [Wilms Floet99a]** D. Wilms Floet, E. Miedema, T.M. Klapwijk, and J.R. Gao, "Hotspot Mixing: a Framework for Heterodyne Mixing in Superconducting Hot Electron Bolometers", *Appl. Phys. Lett.*, vol. 74, page 433, 1999.
- [Wilms Floet99b]** D. Wilms Floet, J.R. Gao, T.M. Klapwijk, and P.A.J. de Korte, "Comparison Between Electronic Hot Spot Model and Current-Voltage Characteristics of Superconducting Hot-Electron Bolometers", *Proceedings of the 10th Intl. Symp. on Space Terahertz Technology*, Charlottesville, VA, March, 1999, pages 580 - 588.
- [Wilms Floet01]** Danny Wilms Floet, "Hotspot Mixing in THz Niobium Superconducting Hot Electron Bolometer Mixers," Ph.D. Dissertation, Dept. of Applied Physics, University of Groningen, 2001.
- [Wu79]** C.T. Wu, "Intrinsic Stress of Magnetron-Sputtered Niobium Films," *Thin Solid Films*, 64, pp. 103-110, 1979.
- [Wu89]** X.-P. Wu and W.H. Ko, "Compensating Corner Undercutting in Anisotropic Etching of (100) Silicon," *Sensors and Actuators*, 18, pp. 207-215, 1989.
- [Yagoubov96]** P. Yagoubov, G.N. Gol'tsman, B. Voronov, S. Svechnikov, S. Cherednichenko, E. Gershenson, V. Belitsky, H. Ekstrom, E. Kollberg, A.D. Semenov, Yu.P. Gousev, and K.F. Renk, "The Bandwidth of HEB Mixers Employing Ultrathin NbN Films on Sapphire Substrate", *Proceedings of the 7th Intl. Symp. on Space Terahertz Technology*, Charlottesville, VA, March, 1996, pages 290-302.
- [Yngvesson03]** K.S. Yngvesson, "Review of HEB Heterodyne Detectors and Receiver Systems for the THz Range: Present and Future", *Proceedings of the 14th Intl. Symp. on Space Terahertz Technology*, Tucson, AZ, April, 2003, pp. 1-10.
- [Zecchino]** M. Zecchino and T. Cunningham, "Thin Film Stress Measurement Using Dektak Stylus Profilers," Veeco Inc. technical document, http://www.veeco.com/appnotes/AN516_Dektak_Stress_Measure.pdf.